Nucleosynthesis in Binary Stars

Robert G. Izzard

Institute of Astronomy

and

St. John's College,

Cambridge

This dissertation is submitted for the

Degree of Doctor of Philosophy

January, 2004

Nucleosynthesis in Binary Stars

Robert G. Izzard

Galactic chemical evolution models require stellar nucleosynthesis yields as input data. Stellar evolution models are used to calculate such yields but do not take into account the fact that many stars are in binaries. The computing time required to explore the binary star parameter space is usually considered to be prohibitively large. Therefore binaries, except for type Ia supernovae and novae which are included in an ad hoc way, are ignored in most Galactic chemical evolution models. In this dissertation synthetic nucleosynthesis models are developed which approximate full stellar evolution models. Cunning methods are employed to model shell burning in low- and intermediate-mass stars while high-mass stars have their surface abundances fitted to their mass. Explosive yields are fitted to published results. The synthetic nucleosynthesis model, with the addition of algorithms to deal with mass transfer in binaries, is coupled to a rapid binary star evolution code. The use of a synthetic model speeds up the calculation of stellar yields by a factor of about 10^7 and extends the analysis to binary stars.

Single- and binary-star yields are calculated for a range of initial mass and separation distributions. A change in the primary or single-star mass distribution is most significant. Changing the secondary mass or separation distribution has a smaller effect. Consideration is then given to variation of the input physics to determine which free parameters are important for the calculation of yields from single and binary stars. It is found that certain parameters are important for some isotopes. Future prospects are then briefly discussed.

Declaration

I declare that this dissertation is not the same as any I have submitted for a degree, diploma or any other qualification in other universities. This dissertation is the result of my own work and includes nothing which is the outcome of work done in collaboration except where specifically indicated in the text and Acknowledgements.

Robert G. Izzard

Some of chapter 2 has been published in

Izzard R. G., Tout C. A., Karakas A. I. and Pols O. R., *A New Synthetic Model for AGB Stars*, **MNRAS** in press,

and

Izzard R. G. and Tout C. A., *Nucleosynthesis in Binary Populations*, **PASA** volume 20, page 345.

This dissertation does not exceed 60,000 words.

Do not cross the binaries. . .

Acknowledgements

It's a cold, wintery night in Cambridge. The wine is mostly gone but Arsenal have won again. One must have priorities... Nearly three and a half years have passed during which time I have been lucky enough to work with some great people. It all started with a speculative lunch at Churchill with Chris Tout (more on him later). The food was, well, college food (and there was no wine!), but he had ideas, a dream, a research proposal which only a naive student slave would have considered. He didn't tell me how bloody difficult it would be! I have been lucky enough to work, and have fun, with some fine people at the IoA in Cambridge. In no particular order... Sverre you are a source of wisdom beyond my years, mainly relating to Alsace whites (and Blue Stragglers, not Blue Nun). Gijs thanks for taking me to La Palma to experience what *real* astronomers do – surf the web while it snows! Lynnette thanks for helping me with the massive stellar models. John (Eldridge) for moving out of the office so there's a spare desk, it really helps when mine is full. Richard you will solve the TPAGB stars problem before you know it and then your only problem will be what to do next! Maria, and Brett and Davidino of course, more gnocchi please! Pierre, and Huong-Mai, Claire and Appolline, enjoy the Cambridge weather. Also Mike Montgomery, Mark Wilkinson and the rest. John (Lattanzio) and Amanda, thanks for helping me to survive in Melbourne, and Amanda thanks for helping me so much with the AGB stars! Thanks Onno for reading the rubbish I kept sending you. Beware, there might be more! Thanks also to Graham Bell for the computer equipment.

Then there is the friends list: fortunately none of you will ever read this and *if you do* then you'll not read beyond the next page! So to all of you, thank you, especially Mike and Claire, I hope you're having fun in smelly London. Sten and Marie, thanks for the flat over the summer and the opportunity to experience Swiss beer! Mum and Dad thanks for everything, a house to live in, my education, supporting my drastic career change... life seems to be working out OK. Thanks also go to Little Bro for helping to put up the fence and texting the 1-1 draws to me.

Not last, and definitely not least, thanks to Chris for reassuring me in the hard times,
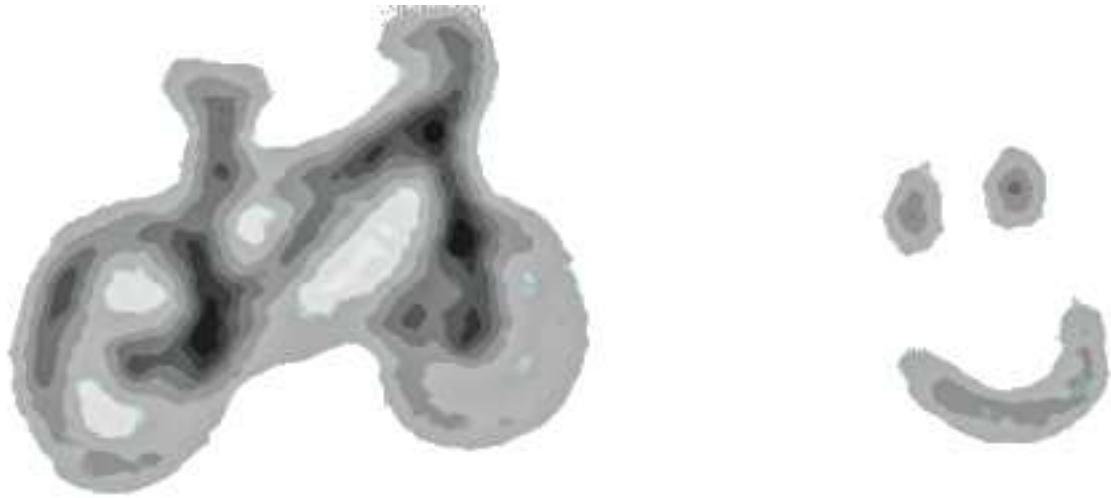
Figure 1: Sketch of the CNO bi-cycle (Ödman, 2004).

teaching me some grammar and being the best supervisor I have ever had. I am in no position to say you're the best supervisor in the department, but you probably are anyway.

And Carolina, I *could* have done this without you, *but I am so glad I didn't.* As long as you want me around, I shall be there for you. After all, you need an editor!

Three and a half years of PhD in Cambridge is enough, but it's better than living in Bracknell! See you in Roma. . .

Contents

Contents

Contents

List of Tables

List of Figures

1 Introduction

We used to think that if we knew one, we knew two, because one and one are two.

We are finding that we must learn a great deal more about 'and'. Arthur Eddington

1.1 The Popular-Science Blurb

One star is trouble enough! We think we know one particular star in detail, the Sun. From the earliest measurements of sunspots to `www.spaceweather.com`, we think we know about the Sun. *We* know, although the author of this dissertation does not. Certainly he does not understand exactly how convection works in the Sun despite his years of admiration of convection on the Earth. What causes the coronal mass ejections? Where does the magnetic field come from? Why does it flip every eleven years? Why did we, on Earth, get blasted by the strongest ever recorded solar flares last month when the solar cycle is near a minimum? Many questions remain unsolved, even for our nearest star.

Despite this, accurate models of the Sun can be made with some relatively simple assumptions. Spherical symmetry, local thermodynamic equilibrium, conservation of mass and neglect of radial acceleration lead to a reasonable Solar model. It remains to determine where the radiation that keeps the Sun luminous actually comes from and how it gets out. The source is the nuclear pyre burning in the core which primarily, as far as the energy budget is concerned, converts hydrogen to helium – a process called *nucleosynthesis*. Matter is converted to energy at a rate $L_\odot/c^2 \approx 4.3 \times 10^9 \, \mathrm{kg \, s^{-1}}$ in a core with temperature in excess of $1.5 \times 10^7 \, \mathrm{K}$ and a pressure of about 250×10^9 atmospheres. This energy generation

rate is unimaginably huge, but to burn the whole Sun, of total mass $1\,\mathrm{M}_\odot \approx 2 \times 10^{30}\,\mathrm{kg}$, to helium at this rate would take 2×10^{12} years.

How does the energy get out from the core? The photons can carry energy by diffusion through the Solar matter for most of their journey to the surface, a process so slow it can take millions of years for a photon to escape. For the final third or so of their journey to the solar surface, measured by the amount of mass they have travelled through relative to $1\,\mathrm{M}_\odot$, energy is transferred by a much faster method, convection. This is similar to thunderstorms on Earth. For most of the year, solar energy is transferred vertically upwards from the ground by either diffusion or advection. However, in the summer the rate of heating of the ground exceeds the amount which can be carried upwards by these mechanisms. The air becomes unstable to convective motion. Hot, rarefied blobs of air rise while cool, dense blobs fall and violent weather systems result. The rate of vertical motion in these systems can be many metres per second, compared to the tranquil centimetres per second associated with advective weather systems. The rate of energy flow, because energy moves with the hot blobs, is similarly increased. Solar convection is not so different. The outer layers are cooler than the core so their opacity, the measure of how resistant a gas is to light, rises. This impedes the flow of photons by diffusion so the only viable method of energy transport is convection. A simple model of convection is employed in models of stars, usually calibrated to this solar convection zone.

Models of the Sun incorporate all the above features and with tweaking of some free parameters all sorts of aspects of the Sun can be calculated such as its luminosity – both in photons and neutrinos – and composition. Because this composition varies as hydrogen burns to helium we can model a series of snapshots in time and eventually create a whole evolutionary sequence – starting from a ball of gas and ending with the death of the star. Thus *stellar evolution* is born. We estimate the Sun is about 4.5×10^9 years old, which agrees well with geological evidence. We know it is brightening as it ages. We also know it will expand to form a red giant in about 6 thousand million years, perhaps swallowing the Earth as it does so.

So much for our *one* star. There are other *ones* out there. What about those? Humans

have been observing stars for thousands of years, the earliest to do so were probably the Chinese although the Babylonians, were they around today, would also stake a claim. Such observations tell us there is a menagerie of stars of different colour and brightness. Later, astronomers analyzed spectra of the light from these stars to reveal they are basically black body emitters, but have both absorption and emission lines. These lines are indicative of the chemistry on the surface of the star. In 1868 observations of stellar absorption lines in the Sun's spectrum by Frankland & Lockyer led them to suggest the presence of a new element, which he called helium. It was not until 1895 that chemists finally isolated the gas in the laboratory (Ramsay, Collie & Travers, 1895). Other lines corresponding to isotopes of carbon, oxygen, magnesium, sulphur, silicon and other metals are commonly observed. In some red giant stars heavy-metal oxides and organic molecules have been detected. In some of the coolest stars there is more carbon than oxygen, very different to the solar C/O ratio of about 0.4. In these same stars technetium has been observed. This element is radioactive with a lifetime of 2.5×10^5 years so what we are seeing is real-time nucleosynthesis. There is something going on inside these other stars which does not happen in the Sun. It turns out that the initial mass of the star is the key to its evolution, with its initial composition also playing a part.

But then there is *one and one* – which is usually two! Most stars exist in some kind of multiple system, 57% according to Duquennoy & Mayor (1991). What is the effect of a companion star? This depends on a number of factors. Most important are the masses of the stars, conventionally measured in solar units, and the orbital period, or alternatively, the separation because they are related by Kepler's law. If the separation is large enough that the stars do not interact then their evolution is not affected and they behave like single stars. However, many binary systems have stars which are close enough to interact with each other. This usually happens when one of the stars becomes very large, such as during the red giant phase of evolution. Matter can leave the surface of the larger star and flow on to the companion, a process known as Roche-Lobe Overflow (RLOF). Such mass loss tends to make the mass-losing star expand further and so mass loss continues. The smaller star usually cannot accept the matter flowing on to it and the stars' envelopes

merge to form a common envelope. The fate of the stars after this depends on whether their cores merge – the case of *one and one is one* – or perhaps they survive as individuals and the envelope is lost from the system. This latter possibility is a crucial step to the progenitor of a type Ia supernova (SNIa). These thermonuclear explosions are critical to our understanding the expansion rate of the Universe and are the main source of iron in the Universe.

Interaction comes in other forms. Some stars have strong stellar winds, perhaps up to $10^{-3}\,\mathrm{M}_\odot\,\mathrm{yr}^{-1}$. The companion star travels in the wind, probably accreting some of it. But what if they have a wind themselves? Then the winds interact, shock and perhaps mix. Stars with these strong winds tend to be quite evolved and may have interesting surface chemistry, which pollutes the companion star. *Barium stars*, with strong Ba lines in their spectra, are thought to be made by this method. Explosions also tend to complicate matters. Apart from SNeIa there are also type Ib, Ic and II supernovae which result from explosions of stars initially eight or more times as massive as the Sun – or, in the case of binaries, perhaps from mergers of smaller stars. Such explosions are major sources of carbon, oxygen, neon, magnesium, sulphur and iron. Sometimes accretion of matter on to a very compact old star known as a white dwarf (WD) leads to thermonuclear explosions called novae, which are sources of minor isotopes such as ^{13}C, ^{15}N and ^{17}O.

Most of the stars we can identify exist in our Galaxy, the Milky Way, a vast gravitationally bound system of about 10^{11} stars, most of which lie in a disk about 7×10^5 light years across. The effect of stars on the chemistry of the Galaxy is the realm of Galactic Chemical Evolution (GCE) models. The first generation of stars had abundances of primordial matter left over from the Big Bang, about 76% hydrogen, 24% helium and a tiny fraction of heavier isotopes, which are known in astronomy as the metals. The fraction of these metals in matter, as measured by mass, is known as the *metallicity* and is denoted by the symbol Z, while the mass fractions of hydrogen and helium are denoted by X and Y respectively so $X + Y + Z = 1$. The first stars had $Z = 0$. They formed, grew old and lost their material, by wind or explosion, to the region between the stars known as the *Interstellar Medium* (ISM). The ISM contains the gas from which later generations of stars

form. Importantly, the primordial stars process their hydrogen (and helium) in their cores, converting them to heavier isotopes such as helium, carbon, oxygen and iron. The mass lost from the stars has a far higher Z than the input matter – for example the matter from a type Ib (Ic) supernova contains no hydrogen (or helium) at all. But the next generation of stars does not form directly from the processed material, rather there is dilution with the primordial material. The ISM material then goes on to form new stars with the mixed material and the cycle continues. The Sun has a metallicity $Z = 0.02$, so 2% of it is not hydrogen or helium. This metallicity is typical of Galactic disk stars, known as Population I. There is another population, imaginatively named Population II, with $Z \approx 0.001$ which inhabits a halo around the Galaxy. Population III stars have $Z = 0$ and are currently a theoretical construct – none has been observed.

The amount of each particular chemical isotope expelled from a star during its lifetime is its *chemical yield*. The yield is a function of a star's initial mass and composition. Stellar-evolution models are required to make these calculations for a wide range of initial Z, from zero to perhaps twice solar. Models of the Galaxy which take into account production and dilution of helium and metals and star formation from the interstellar gas are then constructed. The calculated chemical yields are a direct input to these GCE models. The yields are function of M, t and Z where M is the mass of the star and t is time since its birth.

The problem with the above scenario is that these stars are all assumed to be *single stars* – an approximation which does not look good when $60 - 80\%$ of stars are in multiple systems! Some of the binaries are wide systems and so do not interact, but this still leaves many in close binaries, most of which interact in some way during their lifetimes. What is the effect of having a companion star on the stellar yield? This is the primary question addressed in this work.

It should be noted at this point that in a system containing three or more stars, the system can usually only survive if it is hierarchical. Triples make up 9% and quadruples 2% of solar-type stars (Abt & Levy, 1976). In a system of three stars, two of them are in a close binary and the third orbits at some much larger distance. Similarly for a four-star

system there are probably two close binaries.

1.2 Stellar Evolution and Nucleosynthesis

Carter: "*Well, that means something inside this pyramid is slowing down neutrinos. Normally neutrinos pass right through ordinary matter, no matter how dense. I mean, something like five hundred million billion just passed through you.*"

O'Neill: "*No matter how dense.*"

Stargate "Crystal Skull"

The evolution of single stars depends primarily on two things, the initial mass, M, and metallicity, Z. The star commences its life as a ball of gas. It collapses under its own gravity until it is hot and dense enough to ignite hydrogen in the core. The heat and pressure generated by nuclear burning counteracts gravity, halts the collapse and a star is born. The following discussion is for solar metallicity stars, $Z = Z_\odot = 0.02$, although for stars considered in this work, with $10^{-4} \le Z \le 0.03$, the basic ideas are the same.

The lightest isotope, and the first to provide a significant energy source, is hydrogen, ^{1}H, which is burned to helium, ^{4}He. There are two ways to burn hydrogen, the pp chain and the CNO cycle. The pp chain operates at lower temperatures than the CNO cycle and follows one of the following reaction chains

$$^1\mathrm{H} + {}^1\mathrm{H} \longrightarrow {}^2\mathrm{D} + e^+ + \nu \,, \tag{1}$$

$$^2\mathrm{D} + {}^1\mathrm{H} \longrightarrow {}^3\mathrm{He} + \nu \,, \tag{2}$$

then either the pp-I chain

$$^3\mathrm{He} + {}^3\mathrm{He} \longrightarrow {}^4\mathrm{He} + 2\,{}^1\mathrm{H} \tag{3}$$

or the *pp*-II chain

$$^{3}\mathrm{He} + {}^{4}\mathrm{He} \longrightarrow {}^{7}\mathrm{Be} + \gamma \tag{4}$$

$$^{7}\mathrm{Be} + e^{-} \longrightarrow {}^{7}\mathrm{Li} + \nu \tag{5}$$

$$^{7}\mathrm{Li} + p \longrightarrow 2\,{}^{4}\mathrm{He} \tag{6}$$

or the *pp*-III chain

$$^{3}\mathrm{He} + {}^{4}\mathrm{He} \longrightarrow {}^{7}\mathrm{Be} + \gamma \tag{7}$$

$$^{7}\mathrm{Be} + p \longrightarrow {}^{8}\mathrm{B} + \gamma \tag{8}$$

$$^{8}\mathrm{B} \longrightarrow {}^{8}\mathrm{Be} + e^{+} + \nu \tag{9}$$

then

$$^{8}\mathrm{Be} \longrightarrow 2\,{}^{4}\mathrm{He} \,. \tag{10}$$
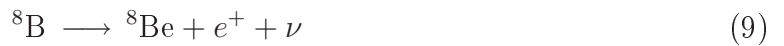
All three chains convert four protons to one helium nucleus, albeit by different routes. The three different chains operate at rates which are functions of the temperature and composition. For $X = Y$ the *pp*-I chain dominates at temperatures below $1.3 \times 10^{7}\,\mathrm{K}$ and above $3 \times 10^{7}\,\mathrm{K}$ the *pp*-III chain activates while between the two *pp*-II is most important. The energy liberated is calculated from $\Delta E = \Delta M\,c^{2} \approx 26.7\,\mathrm{MeV}$ per helium nucleus, where ΔM is the mass difference between four hydrogen nuclei and a helium nucleus. The *pp* chain powers the nuclear core of the Sun and the neutrinos produced can be directly observed because they pass through the Sun almost unimpeded. The reaction rates are a function of complex nuclear physics – fortunately for the purposes of stellar evolutionists, such reactions rates are tabulated (e.g. Angulo et al., 1999).

At high temperatures the CNO cycle operates. This involves a complicated series of reactions which can actually be split into two cycles, the CN and ON cycle, as in table 1 (see also section 2.8). The net effect of the cycle is the same as the *pp* chain, to convert

CN bi-cycle	ON bi-cycle
$^{12}\text{C} + p \longrightarrow {}^{13}\text{N} + \gamma$	$^{14}\text{N} + p \longrightarrow {}^{15}\text{O} + \gamma$
$^{13}\text{N} \longrightarrow {}^{13}\text{C} + e^+ + \nu$	$^{15}\text{O} \longrightarrow {}^{15}\text{N} + e^+ + \nu$
$^{13}\text{C} + p \longrightarrow {}^{14}\text{N} + \gamma$	$^{15}\text{N} + p \longrightarrow {}^{16}\text{O} + \gamma$
$^{14}\text{N} + p \longrightarrow {}^{15}\text{O} + \gamma$	$^{16}\text{O} + p \longrightarrow {}^{17}\text{F} + \gamma$
$^{15}\text{O} \longrightarrow {}^{15}\text{N} + e^+ + \nu$	$^{17}\text{F} \longrightarrow {}^{17}\text{O} + e^+ + \nu$
$^{15}\text{N} + p \longrightarrow {}^{12}\text{C} + {}^4\text{He}$	$^{17}\text{O} + p \longrightarrow {}^{14}\text{N} + {}^4\text{He}$
$^{12}\text{C} + 4p \longrightarrow {}^{12}\text{C} + {}^4\text{He} + 2e^+ + 2\nu + 3\gamma$	$^{14}\text{N} + 4p \longrightarrow {}^{14}\text{N} + {}^4\text{He} + 2e^+ + 2\nu + 3\gamma$

Table 1: The CNO cycle nuclear reactions. The left and right columns separate the two halves of the bi-cycle. The bottom row shows the net result of the bi-cycles.

four protons into one helium nucleus, but it requires other isotopes (^{12}C, ^{13}C, ^{14}N, ^{15}N, ^{15}O, ^{16}O and ^{17}F) to act as catalysts. The number of CNO and ^{17}F nuclei is conserved, although the CNO cycle acts to change their relative abundances. Careful analysis of the CNO cycle (Clayton, 1983) leads to the result that the main component ($\approx 98.5\%$) of CNO-processed material, if it has time to reach equilibrium, is ^{14}N.

Whatever the source of energy, all stars go through a phase called the *Main Sequence* (MS; stellar-type acronyms are defined in table 2). During this time steady hydrogen burning occurs in the stellar core, by the *pp* chain in low-mass stars or the CNO cycle in higher-mass stars. The length of time spent on the MS is a highly non-linear function of the initial mass, 1.1×10^{10} years for a $1\,\text{M}_\odot$ star, 6.8×10^7 years for a $6\,\text{M}_\odot$ star and 4.3×10^6 years for a $50\,\text{M}_\odot$ star. The MS ends when hydrogen in the core has been converted to helium. No more energy can be extracted, so the star resumes the course it took prior to hydrogen burning, and restarts its collapse under its own weight.

During the relatively short *Hertzsprung Gap* (HG) phase, which typically lasts for less than a few per cent of the MS time, the core contracts. At the same time the stellar envelope expands and cools. Cooler gas has a higher opacity so a convective envelope develops. Collapse is stopped by hydrogen ignition in a shell around the core, which provides a new source of energy, and for a while the star remains on the *Giant Branch* (GB). Because of its lower temperature the star is very red and because of its size it is very bright. Up to this point, the chemical abundances at the surface do not alter from their initial abundance. The convective envelope which forms on the GB changes this because it

	Stellar Type	Acronym
0	Low-mass Main Sequence	
1	Main Sequence	MS
2	Hertzsprung Gap	HG
3	First Giant Branch	GB
4	Core Helium Burning	CHeB
5	Early Asymptotic Giant Branch	EAGB
6	Thermally-Pulsing Asymptotic Giant Branch	TPAGB
7	Helium Main Sequence	HeMS
8	Helium Hertzsprung Gap	HeHG
9	Helium Giant	HeGB
10	Helium White Dwarf	HeWD
11	Carbon-Oxygen White Dwarf	COWD
12	Oxygen-Neon-Magnesium White Dwarf	ONeWD
13	Neutron Star	NS
14	Black Hole	BH
15	Massless Remnant	

Table 2: Stellar types as defined by SSE/BSE.

mixes material from the core to the surface, in an event known as *first dredge-up*. Section 2.3 examines this process in detail. Stars with $M \gtrsim 7\,\mathrm{M_\odot}$ have a very short GB phase and stars with $M \gtrsim 13.2\,\mathrm{M_\odot}$ have no GB at all because helium burning ignites in the core before shell hydrogen burning can begin.

A star leaves the GB when conditions in the core are hot and dense enough to allow ignition of the next nuclear-burning stage. It becomes a *Core Helium Burning* (CHeB) star, burning by the triple-α reaction,

$$3\,^4\mathrm{He} \longrightarrow {}^{12}\mathrm{C}\,. \tag{11}$$

There is also some α-capture on carbon to produce oxygen,

$$^{12}\mathrm{C} + \alpha \longrightarrow {}^{16}\mathrm{O}\,. \tag{12}$$

For *low-mass stars*, $M \lesssim 2.0\,\mathrm{M_\odot}$, helium ignition occurs in an electron degenerate core,

so a nuclear runaway occurs known as the *helium flash*. There are no consequences for surface nucleosynthesis (Stancliffe, private communication). *Intermediate-* and *high-mass stars* do not experience this flash but ignite helium gently because their cores are not highly degenerate. The star proceeds to evolve with a helium-burning carbon- and oxygen-rich core surrounded by a helium envelope and a hydrogen-rich envelope.

The evolution that follows is similar to that of the MS except helium takes the place of hydrogen. Eventually central helium runs out and the star contracts. Burning restarts in a helium-burning shell surrounding the core and the star expands again, this time on the *Early Asymptotic Giant Branch*. The expansion and cooling of the envelope again increases the opacity and causes a deep convection zone to develop. For stars with $M \gtrsim 4\,M_\odot$ the convective envelope becomes deep enough to mix processed material from the core to the surface in the *second dredge-up*. Surface abundances of both hydrogen- and helium-burned material increase (see section 2.4) and the helium-core mass is reduced as the convective hydrogen-rich envelope eats into it.

The helium shell eventually meets the hydrogen envelope either by core growth or inward movement of the hydrogen envelope. The hydrogen shell reignites and the two burn alternately, because a thin helium-burning shell is unstable (Schwarzschild & Härm, 1965), on the *Thermally Pulsing Asymptotic Giant Branch* (TPAGB). These stars are rich sources for nucleosynthesis because the particular twin shell geometry and convective envelope allow the products of helium burning, particularly ^{12}C, to reach the stellar surface. This is the favoured method of formation of *carbon stars*, stars with surface C/O > 1. The most massive TPAGB stars, $4 \lesssim M/M_\odot \lesssim 8$, have hot enough convective envelopes that hydrogen burning occurs at the base of the envelope, known as *Hot Bottom Burning* (HBB). The CNO cycle, as well as the NeNa cycle (section 2.9) and the MgAl cycle (section 2.10), process a wide variety of isotopes to give a *very* non-solar abundance at the surface. Slow neutron capture (the *s*-process) may occur in the region between the burning shells and leads to the production of heavy isotopes such as barium, yttrium and lead. TPAGB stars have enormous radii, up to $1000\,R_\odot$, so matter at the surface is not very strongly bound and mass-loss rates are high. This causes the hydrogen envelope to be lost, possibly form-

ing a *planetary nebula*, so further nuclear burning is impossible. All that is left is the now extinguished CO core, which cools to become a *Carbon-Oxygen White Dwarf* (COWD).

While most stars follow the above evolutionary sequence, *massive stars*, with $M \gtrsim 8\,\mathrm{M_\odot}$, ignite carbon as they contract after core helium burning. Further burning is relatively quick, through neon-, oxygen- and silicon-burning, until an iron core forms. Beyond iron, nuclear burning is endothermic, so the stellar core lacks an energy source and continues to collapse. At a density about three times that of an atomic nucleus the core rebounds due to the Pauli exclusion of neutrons and a shockwave moves outward through the star. Most of the energy is released as neutrinos which interact[1] with the envelope, driving it off in a type II supernova (SNII) explosion. Material both from the core and the envelope may escape to the ISM, so supernovae are another source of metals (section 3.7). What remains of the star forms either a *neutron star* (NS) or a *black hole* (BH) if it is massive enough.

Even more massive stars, $M \gtrsim 23\,\mathrm{M_\odot}$, are affected by severe mass loss during their evolution. They lose enough mass that their hydrogen envelopes are completely stripped off before their cores collapse, exposing their helium cores. Observationally, they are known as *Wolf-Rayet* (WR) stars (section 3.1). They evolve on the *Helium Main Sequence* (HeMS) because they are similar in structure to a normal MS star but with hydrogen replaced by helium. These then evolve on the *Helium Hertzsprung Gap* (HeHG) and *Helium Giant Branch* (HeGB) by analogy with the HG and GB. Wind loss is not strong enough (at solar metallicity) to prevent a core-collapse SN during these latter phases. Such a supernova does not contain any hydrogen so is observed as a type Ib (SNIb). Again, these stars are an important source of metals.

Binary stars complicate the above picture (see e.g. Batten, 1995 for a review). The presence of a companion may cause mass transfer. This alters evolution by either increasing or decreasing the stellar mass and, less importantly, pollution of the accreting star. Some phases of evolution are associated with large radii (e.g. GB, AGB and massive HG stars) so are likely to be truncated by the presence of a companion. Wolf-Rayet stars form owing

---

[1]The interaction is very weak but there are *a lot* of high-energy neutrinos in an exploding star.

to the removal of their massive progenitor's hydrogen envelope. Removal of a hydrogen envelope from a RG star leads to an exposed core which, lacking a source of nuclear fuel, cools to form a *Helium White Dwarf* (HeWD) star. On the other hand, mass lost from a star must go somewhere. Sometimes it is lost from the system but it can also accrete on to the secondary star or perhaps the stars merge.

As well as evolutionary effects on a companion, pollution leads to production of chemically peculiar stars. A few examples are presented in section 4.7, including a dwarf carbon star. The interested reader may wish to make his or her own by use of the online `binary_c/nucsyn` front-end at `http://www.ast.cam.ac.uk/~rgi/cgi-bin/binary2.cgi`.

There are also the binary-specific thermonuclear explosions such as novae (section 4.5.1) and type Ia supernovae (SNeIa, section 4.5) which contribute metals to the ISM.

1.3 Stellar Models

. . .

O'Neill: *"Weren't you listening? Nintendos pass through everything."*

Stellar evolution is thought to be reasonably well understood because of the success during the last 40 years in making detailed stellar models. Such models are really just solutions of the set of stellar structure equations (see e.g. Kippenhahn & Weigert, 1994 for in-depth discussion or Prialnik, 2000 for an introduction), one for hydrostatic equilibrium

$$\frac{dP}{dm} = -\frac{Gm}{4\pi r^4}\,, \tag{13}$$

mass conservation

$$\frac{dr}{dm} = \frac{1}{4\pi r^2 \rho}\,, \tag{14}$$

nuclear energy generation

$$\frac{dL}{dm} = \epsilon \tag{15}$$

and radiative transport of the energy flux F,

$$\frac{dT}{dm} = -\frac{3}{4ac}\frac{\kappa}{T^3}\frac{F}{(4\pi r^2)^2}\,. \tag{16}$$

Also required is a method to transform eq. (16) when material is convectively unstable, an equation of state for the gas and equations to follow each isotope as it is created or destroyed. Usually just a few isotopes are considered, such as ^{1}H, ^{4}He, ^{12}C, ^{14}N, ^{16}O and ^{22}Ne, because the structure of the star depends only on these. Implicit in these equations are tables of nuclear reaction rates and opacity data. Codes have been written to solve all the above equations and this is what leads to the stellar evolution story told above.

Single stars are usually modelled with two free parameters, the mass and metallicity[2]. A complete set of models from the MS to TPAGB may take minutes, hours or days to make depending on the required accuracy and the code used. The Eggleton code, for example, is quite capable of modelling the TPAGB phase quickly, if the resolution is deliberately kept low so that thermal pulses are avoided. This is not a particularly satisfactory situation from the nucleosynthesis point of view because the third dredge-ups will also be ignored. However, the same code does an good job of modelling the previous stellar evolution phases.

The time required to make detailed nucleosynthesis models containing many isotopes is even longer. The low- and intermediate-mass nucleosynthesis models used in this work require the output from the Mt. Stromlo Stellar Evolution Code (Frost, 1997; Wood & Zarro, 1981) to be coupled with the nucleosynthesis code of Cannon (1993). Such output can take weeks to produce, *per star*. This is not a problem on a grid of, say, 10 stars over 10 metallicities. Then 100 stars take a few hundred weeks of CPU time. Such calculations are not impossible given a dozen reasonable PCs and a little patience.

Binary stars are a far more difficult prospect. One way of making detailed binary models is to combine a single star evolution code with a prescription for binary mass transfer and orbital changes. Such an option has existed in the Eggleton code for some time and has recently been improved with Eggleton's `TWIN` code, which actually computes the stellar structure of both stars implicitly and at the same time. It does not take much more time to make 100 binaries than it does to make the 100 single stars described above. The problem is the number of parameters which go into binary evolution. As well as the mass and metallicity, there is the mass of the other star, the period (or separation) of the orbit, the orbital eccentricity and free parameters associated with binary-specific mechanisms such as RLOF, common envelope evolution, enhanced wind-loss, tidal effects, supernova kicks etc. Soon, instead of making 100 stars, 10^8 or more stars are required. If detailed nucleosynthesis is required for these stars, and each model takes a week to make, that is about 200,000 years of CPU time. The average PhD student, taking three years, would

---

[2]While the models actually contain many other free parameters, M and Z are by far the most important to describe the evolution of a single star.

require about 60,000 fast PCs (and competent support staff to manage them). Clearly such an undertaking is beyond current resources. A very limited parameter space study was made by De Donder & Vanbeveren (2002) using rather old detailed models although, at the time of writing, their chemical yields *still* remain unpublished.

Synthetic stellar models are a way around the problem. The idea is to fit the results of detailed single star models to simple analytic functions. The need to solve a system of coupled differential equations is removed and the code is sped up by a huge factor. To calculate nucleosynthetic yields for a $4\,\mathrm{M}_\odot$ star takes $0.09\,\mathrm{s}$ with the synthetic model but many days for a full evolution model. Appendix F gives some data on code runtimes. The other great advantage of a synthetic model is the ability to change some of the input physics. Many aspects of stellar evolution are quite uncertain such as mass-loss rates, angular momentum transfer between binary-star components, common envelope loss efficiency and supernova kick velocities to name just a few. All these can be varied in a synthetic model and the results will be ready before tea time (or at least by the time you get back from the pub!). A synthetic model should not suffer the numerical failures associated with detailed stellar evolution codes.

The main disadvantage of a synthetic model is a loss of accuracy. Fitted formulae can never exactly reproduce the detailed models and sometimes, especially when dealing with highly non-linear phenomena, slight differences between the models can change the outcome by a large amount. This problem is not so important when entire *populations* of stars are considered. Far more important is the distribution of mass (the *Initial Mass Function* or IMF), metallicity and separation in a whole population of stars (see chapter 5).

Synthetic models were introduced out of necessity in the late 1970s to model TPAGB stars (Wood & Cahn, 1977; Iben & Truran, 1978; Renzini & Voli, 1981). Computing power and understanding of the physics of the stars was more limited than today. However, the models included third dredge-up in an approximate way and led to some explanation of the formation of carbon stars. Improvements followed in the 1990s, with the purely synthetic models improved by Groenewegen & de Jong (1993) and van den Hoek & Groenewegen (1997) who included CNO HBB. More detailed nucleosynthesis was considered by Forestini

& Charbonnel (1997) although with a more limited evolutionary model. A slightly different route was taken by the Padova group (Marigo, Bressan & Chiosi, 1998; Marigo, 1999, 2001) who use a synthetic prescription for the stellar core but solve the stellar evolution equations in the envelope (so-called *envelope integration* models). Such models are probably still too slow to model a large parameter space.

Application to other phases of stellar evolution is not necessary, except when one would like to model multiple stars or globular clusters. A project to develop analytic fits to single star evolution was started by Tout et al. (1996) who fitted Zero-Age Main Sequence (ZAMS) radii and luminosities to detailed stellar models constructed with the Eggleton code. This was extended by Hurley, Pols & Tout (2000) who fitted stellar luminosities, radii and lifetimes over the entire evolution of the star to the detailed models of Pols et al. (1998). This is the basis of the *rapid Single Star Evolution* (`SSE`) code. Hurley, Tout & Pols (2002, H02) extended this to the *rapid Binary Star Evolution* (`BSE`[3]) model which includes prescriptions for orbital motion, RLOF, common envelope evolution, wind accretion, tides and supernova kicks. The algorithm has been included in Aarseth's `NBODY` code to produce models of small globular clusters such as M67 (Hurley et al., 2001, see also Jarrod Hurley's PhD thesis).

This dissertation extends `BSE` to include the `nucsyn` library, a comprehensive synthetic nucleosynthesis package. Fits to the detailed nucleosynthesis models of Karakas, Lattanzio & Pols (2002, K02; see also Amanda Karakas' PhD thesis) include first, second and third dredge-up. Intershell abundances are fitted to detailed models and extended to include *s*-process isotopes. A simple shell-burning HBB model is developed to deal with CNO, NeNa and MgAl burning cycles. The models of Dray et al. (2003) and Dray & Tout (2003, see also Lynnette Dray's PhD thesis) are used to fit surface abundances for massive stars. Supernovae and novae are included by fitting to published detailed explosion models. Mass transfer on to and mixing into a companion is dealt with in a consistent way. The `C` version of `BSE` in conjunction with `nucsyn` is known as `binary_c/nucsyn`.

---

[3]Madness!

A word of caution. *Many* approximations go into the `nucsyn` code. Every effort has been made to fit the detailed models as accurately as possible, but given realistic time constraints the fit is not always as good as one would like. Also, the detailed models are almost certainly wrong in some respect, notably the mass-loss rates, so a perfect fit is pointless.

It is very difficult to estimate the error on any output value from the synthetic code given the large number of input variables. All that can be done is to vary each of these variables within reasonable ranges to give an idea of the uncertainty.

The `nucsyn` model is a prototype but the only one of its kind and, in the case of binary stars, the only one capable of exploring the parameter space. It can be improved in many ways but for now, it will do.

1.4 Dissertation Outline

Mellon: *"Colonel, you seem pensive. . ."*
O'Neill: *"No. I was just thinking."*

Stargate "2001"

The synthetic model description is split into three chapters. Chapter 2 deals with low-and intermediate-mass single stars including first, second and third dredge-up, HBB, the *s*-process, radioactive decays, calibration of third dredge-up and comparison of yields to the detailed models. Chapter 3 contains fits to surface abundances in high-mass single stars and helium stars, yields from core-collapse supernovae and masses of NS/BH remnants. The effect of a binary companion is considered in chapter 4, notably wind accretion and mixing, RLOF, stellar mergers, novae and type-Ia supernovae.

The calculation of stellar yields follows in chapters 5 and 6. The former deals with changes in stellar distributions, the latter with changes in the input physics. Finally, in chapter 7 single and binary stars are compared for a solar metallicity population to finally answer the question, what is the effect of duplicity on chemical yields?

Appendix A details some useful algorithms. Appendix B contains the fitting formulae coefficients and solutions to the shell burning differential equations. Appendix C contains the calibration of the HBB stars to the detailed models. Appendices D1-D3, D4 and E detail the mass-loss prescriptions used, the default initial mass function (KTG93) and Pols' prescription for the free parameter λ_{CE}. Appendix F1 compares the runtime of the synthetic code to full evolution codes. Table 3 contains a list of useful acronyms.

Acronym/Symbol	Meaning	Notes
Z	ZAMS Metallicity	
Z_t	Current metallicity of the star	
M	Current mass of the star	
M_{ZAMS}	ZAMS mass of the star	Can be increased by accretion/merging on the MS
M_{i}	Initial mass of the star	
M_{HG}	Mass of the star when it leaves the MS	
X_j	Surface mass fraction of element j	
$X_{\mathrm{i},j}$	Initial surface mass fraction	Can be redefined by accretion/merging on the MS
X_j^{i}	Mass fraction of isotope j in the TPAGB intershell	

Table 3: Table of variables.

2 Low- and Intermediate-Mass Stars

From the point of view of nucleosynthesis, low- and intermediate-mass stellar evolution is dominated by a series of mixing events known as dredge-ups which bring nuclear processed material to the surface. First dredge-up occurs on the first giant branch, second dredge-up, if it occurs, at the beginning of the AGB and third dredge-up during the TPAGB. All three processes have their origin in convective mixing of processed material from near the core to the surface where the material can be lost in a stellar wind or binary interaction. Between the dredge-ups the surface layers are radiative so while nuclear burning continues in the core there is no connection between this processed material and the surface and enriched material cannot leave the star. Figure 2 shows a mass-coordinate vs time view of these dredge-up events.

The distinction between low- and intermediate-mass stars is that low-mass stars undergo degenerate helium ignition – the *helium flash* – at the tip of the GB while intermediate-mass stars do not. The effect of this flash on the surface abundances is thought to be negligible (Stancliffe, private communication). Intermediate-mass stars also ignite helium at the tip of the GB but in a non-degenerate core, so there is no flash rather a transition to steady burning. Typical mass ranges are $M \leq 2\,\mathrm{M_\odot}$ for low-mass stars, $2 \lesssim M/\mathrm{M_\odot} \lesssim 7-8$ for intermediate-mass stars, the uncertainty owes to a slight metallicity dependence. The upper mass limit depends on factors such as convective overshooting and wind-loss prescription, e.g. for the Padova models (see below) the upper mass is $5\,\mathrm{M_\odot}$.
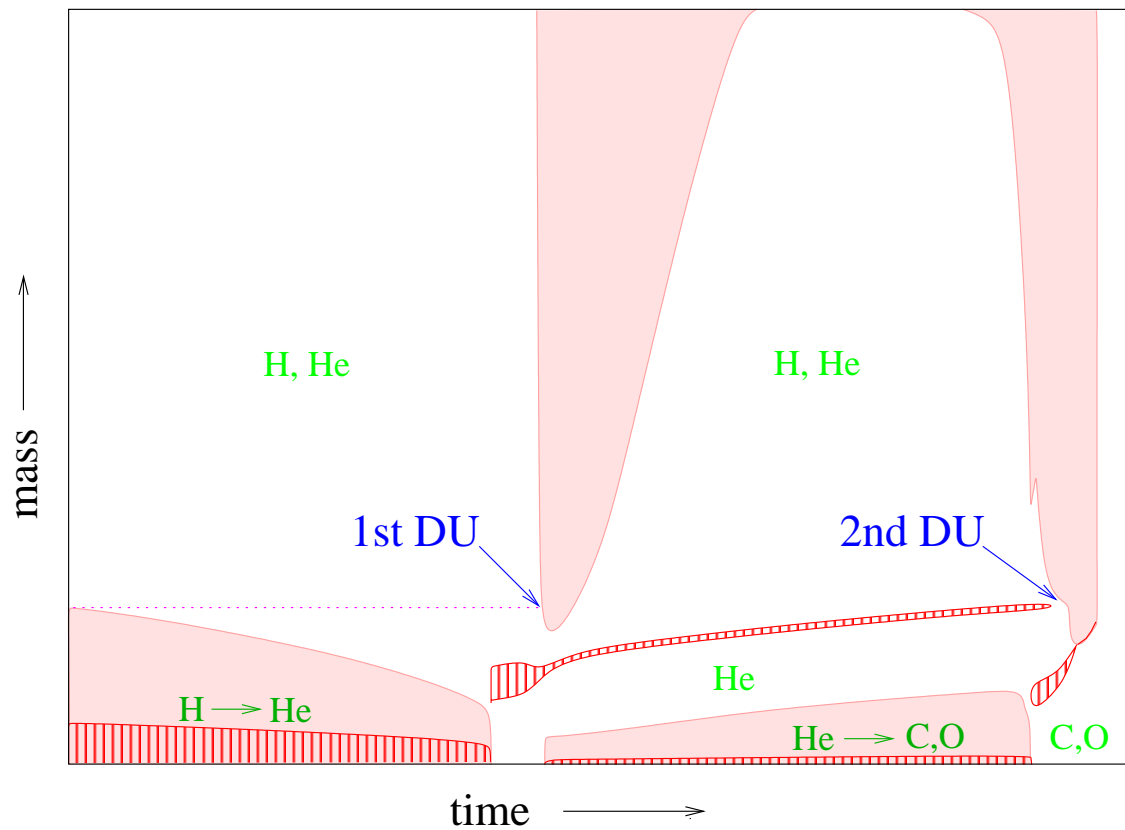
Figure 2: Mass co-ordinate vs time for an intermediate mass star with $M \gtrsim 4\,\mathrm{M_\odot}$. Pink regions are convectively mixed, vertically hatched regions are burning shells. This figure is based on real Eggleton code output, courtesy of Onno Pols.

2.1 The Model Sets

Four sets of full stellar evolution models are used to determine nucleosynthesis in low- and intermediate-mass stars.

- The *Monash* models (Karakas et al., 2002, K02) are the basis for the analytic fits in this chapter for all isotopes except those involved in the *s*-process. They were constructed using the Monash version of the Mount Stromlo Stellar Evolution Code and cover the mass range $1 \leq M/\mathrm{M}_\odot \leq 6$ and metallicity range $0.004 \leq M/\mathrm{M}_\odot < 0.02$, as well as $1 \leq M/\mathrm{M}_\odot \leq 2.25$, $Z = 10^{-4}$ and $M = 6.5\,\mathrm{M}_\odot$, $Z = 0.02$. These models are calculated with the wind-loss prescription described below (eq. 32) and without convective overshooting. The TPAGB phase, including third dredge-up and HBB, is modelled in detail. Nucleosynthesis for stable elements up to ^{56}Fe is calculated using the post-processing code of Cannon (1993, and Karakas, private communication). These models are the basis of the synthetic code described in this chapter because they provide evolution to almost the end of the TPAGB, detailed nucleosynthesis up to iron and cover a wide range of mass and metallicity.

- The *Eggleton* models (Pols et al., 1998) which are the basis for the `SSE` code of Hurley et al. (2000). Models with (OV) and without (NOV) convective overshooting were calculated in the mass range $0.5 \leq M/\mathrm{M}_\odot \leq 40$ with $10^{-4} \leq Z \leq 0.03$. While the mass and metallicity range covered by these models is greater than the Monash set nucleosynthesis is limited to ^{1}H, ^{4}He, ^{12}C, N, ^{16}O, Ne and ^{24}Mg where Ne $=^{20}$Ne $+^{22}$Ne and N represents everything else. The AGB is modelled but with insufficient time resolution to obtain thermal pulses so these models are not especially useful for creation of a synthetic TPAGB model.

- The *FRANEC* models (Gallino et al., 1998) were calculated specifically to model the *s*-process in TPAGB stars and are used to evaluate *s*-process abundances appropriate for intershell material at each third-dredge up (Lugaro, private communication, see

section 2.11 below). The models have masses $1.5\,M_\odot$, $3\,M_\odot$ and $5\,M_\odot$ and metallicities 0.02, 0.006, 0.002, 0.005 and 10^{-4}.

- The *Padova* group's models (Girardi et al., 2000) are probably the most popular set of models in current use and form the basis of the envelope integration code of Marigo (2001). They include convective overshooting (OV) except for one model set (NOV) at $Z = 0.019$ but not mass loss and cover the mass range $0.15 \leq M/\,M_\odot \leq 7$ and metallicity range $4 \times 10^{-4} \leq Z \leq 0.03$. The models include first and second dredge-up but do not extend to the TPAGB. Nucleosynthesis includes ^{1}H, ^{4}He, ^{12}C, ^{13}C, ^{14}N, ^{15}N, ^{16}O, ^{17}O and ^{18}O but no isotopes beyond this. Note that where the Padova models are used to compare with the others the $Z = 0.019$ sets are referred to as $Z = 0.02$.

2.2 Initial Abundance Sets

The traditional[1] choice of initial isotopic abundance mix in stellar models is to use the solar abundance set of Anders & Grevesse (1989, hereafter AG89) and to scale isotopes heavier than helium with a factor $Z/Z_\odot$. The Monash models adopt this approach for $Z = 0.02$ and $Z = 10^{-4}$ but use observed isotopic abundances from the Magellanic Clouds (Russell & Dopita, 1992) for $Z = 0.008$ and $Z = 0.004$. In order to fit the change in surface abundance to the Monash models it is necessary to use the same initial abundance set. Table 4 shows that the difference between the choices are quite significant, up to a factor of 4 for ^{14}N in the SMC.

2.3 First Dredge Up

Prior to ascent of the giant branch the products of internal nucleosynthesis are generally not visible at the surface of the star. The situation inside the star is different. During the

---

[1]Recently, at least!

	$Z = 0.02$	LMC $Z = 0.008$	$\frac{\text{LMC}}{\text{Scaled}}$	SMC $Z = 0.004$	$\frac{\text{SMC}}{\text{Scaled}}$
^{1}H	0.68720	0.73689		0.74840	
^{4}He	0.29280	0.25510		0.24760	
^{12}C	2.92593×10^{-3}	9.69593×10^{-4}	0.83	4.82297×10^{-4}	0.82
		1.17037×10^{-3}		5.85186×10^{-4}	
^{13}C	4.10800×10^{-5}	2.88281×10^{-5}	1.75	1.49927×10^{-5}	1.82
		1.6432×10^{-5}		8.216×10^{-6}	
^{14}N	8.97864×10^{-4}	1.42408×10^{-4}	0.40	5.10803×10^{-5}	0.28
		3.59146×10^{-4}		1.79573×10^{-4}	
^{15}N	4.14000×10^{-6}	2.90500×10^{-6}	1.75	1.51090×10^{-6}	1.82
		1.656×10^{-6}		8.28×10^{-7}	
^{16}O	8.15085×10^{-3}	2.63954×10^{-3}	0.81	1.28308×10^{-3}	0.79
		3.26034×10^{-3}		1.63017×10^{-3}	
^{17}O	3.87600×10^{-6}	2.72000×10^{-6}	1.75	1.41459×10^{-6}	1.82
		1.5504×10^{-6}		7.752×10^{-7}	
^{22}Ne	1.45200×10^{-4}	1.01894×10^{-4}	1.75	5.29927×10^{-5}	1.82
		5.8088×10^{-5}		2.904×10^{-5}	

Table 4: ZAMS abundances (mass fractions) used in the Monash models for $Z = 0.02, 0.008$ and 0.004 (top numbers) and the equivalent solar-scaled abundance (numbers below).

pre-main sequence and main-sequence CNO processing converts ^{12}C and ^{16}O to ^{13}C and ^{14}N. The exact amount of conversion depends sensitively on mass and metallicity. The isotopic profiles through the star are complex and impossible to follow synthetically. As the star evolves up the giant branch a deep surface convective envelope forms which dredges up material from below reducing the surface ^{12}C and ^{16}O and increasing the surface ^{13}C and ^{14}N. Figure 3 shows the hydrogen, helium and CNO abundances of a $1.25\,\mathrm{M}_\odot$, $Z = 0.02$, non-overshooting Eggleton model prior to first dredge-up and during the dredge-up. The increase in surface ^{14}N and decrease in ^{12}C is due to mixing of the CNO processed material at $M_r \approx 0.4\,\mathrm{M}_\odot$. Also apparent is that the change in surface abundance is sensitive to the depth of the surface convection zone and convective overshooting.

A $4\,\mathrm{M}_\odot$, $Z = 0.02$ star exists for the Monash, Eggleton (NOV) and Padova (OV and NOV) group model sets and the changes in surface abundance during first dredge-up are shown in table 5. Convective overshooting doubles the amount of ^{4}He dredged-up, consistent with overshooting at the base of the convection zone eating further into the helium core than the non-overshooting models. The effect on the other isotopes is less obvious but the Monash and Padova (NOV) models agree reasonably well. The Eggleton code consistently overestimates the changes relative to the other codes, perhaps owing to its different mixing scheme and perhaps the small number of isotopes considered. There are some minor changes to Ne, Na and Mg, owing to NeNa and MgAl cycling, according to the Monash models but these isotopes are not available for comparison from any other model set.

Fortunately the effect of first dredge-up is quite sudden on stellar evolutionary timescales, so can be fitted as an event rather than an ongoing process. Analytic fits to the changes in surface abundance from the Monash models are given in appendix B1.

2.4 Second Dredge-Up

After core helium burning has finished the star again climbs the giant branch. Shell helium burning begins, the helium exhausted core moves outward in mass and the surface con-
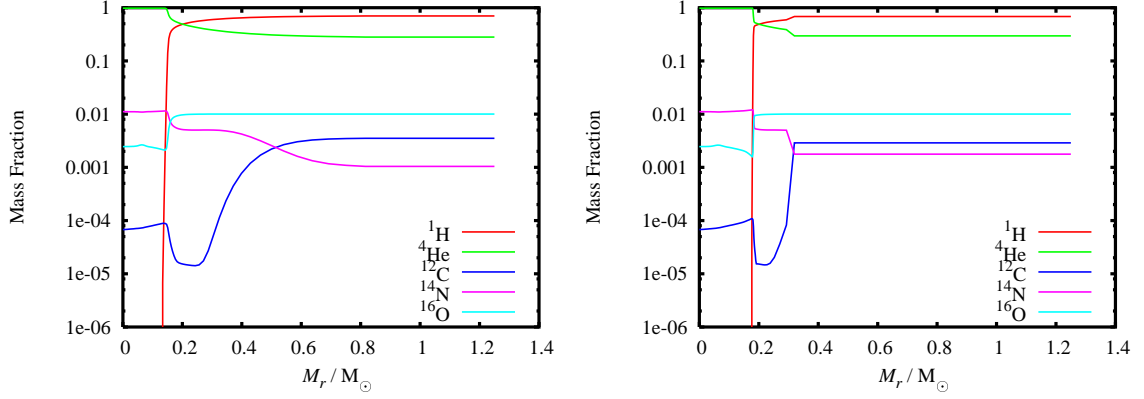
Figure 3: Abundance vs mass co-ordinate M_r inside a $1.25\,\mathrm{M}_\odot$, $Z = 0.02$ star just before and during first dredge-up.

Isotope	Monash	Eggleton (NOV)	Padova (OV)	Padova (NOV)
^{1}H	-1.01×10^{-2}	-2.28×10^{-2}	-2.6×10^{-2}	-1.2×10^{-2}
^{4}He	9.92×10^{-3}	2.28×10^2	2.6×10^{-2}	1.2×10^{-2}
^{12}C	-1.07×10^{-3}	-1.46×10^{-3}	-1.00×10^{-3}	-1.05×10^{-3}
^{13}C	4.99×10^{-5}	-	7.58×10^{-5}	6.58×10^{-5}
^{14}N	1.48×10^{-3}	2.09×10^{-3}	1.66×10^{-3}	1.48×10^{-3}
^{15}N	-2.19×10^{-6}	-	-1.86×10^{-6}	-1.89×10^{-6}
^{16}O	-3.31×10^{-4}	-7.0×10^{-4}	-6.7×10^{-4}	-4.0×10^{-4}
^{17}O	1.36×10^{-5}	-	1.12×10^{-5}	1.75×10^{-5}
^{18}O	-5.71×10^{-6}	-	-4.3×10^{-6}	-4.9×10^{-6}
^{19}F	-1.99×10^{-8}	-	-	-
^{20}Ne	-1.16×10^{-7}	0	-	-
^{21}Ne	1.29×10^{-7}	-	-	-
^{22}Ne	-1.53×10^{-5}	-	-	-
^{23}Na	1.59×10^{-5}	-	-	-

Table 5: Surface abundance changes at first dredge-up for a $4\,\mathrm{M}_\odot$, $Z = 0.02$ star.
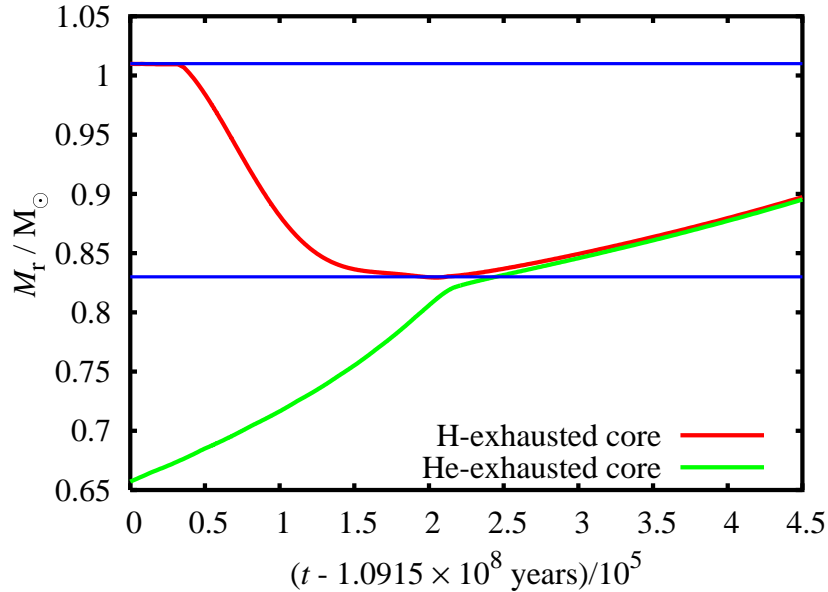
Figure 4: Second dredge-up in a $5\,M_\odot$, $Z = 0.02$ Eggleton model star. As the He-exhausted core (green line) grows the surface convection zone eats into and shrinks the H-exhausted core (red line). The hydrogen-burned matter between 0.83 and $1.01\,M_\odot$ (blue lines) is mixed into the convective envelope, altering surface abundances.

vection zone moves inward, eating into previously hydrogen-burned material (see figure 4). The products of hydrogen burning are mixed to the surface in the process known as second dredge-up. Stars with mass greater about about $4\,M_\odot$ experience significant changes in surface abundance at second dredge-up.

Table 6 compares the surface abundance changes during second dredge-up from the various model sets. Again the amount of convective overshooting is important, with the Padova overshooting models mixing more processed material to the surface. The non-overshooting models give similar results, with the Monash model changes generally lying between the Eggleton and Padova models. All the CNO isotopes except ^{14}N and ^{17}O drop as a result of CNO processing, ^{20}Ne and ^{22}Ne drop at the expense of ^{21}Ne and ^{23}Na owing to NeNa cycling, ^{25}Mg is destroyed in the MgAl cycle while ^{26}Mg is created. ^{24}Mg and Al barely change, nor do heavier isotopes.

As with first dredge-up, second dredge-up is a relatively quick process so is modelled

Isotope	Monash	Eggleton (NOV)	Padova (OV)	Padova (NOV)
^{1}H	-3.13×10^{-2}	-3.26×10^{-2}	-4.50×10^{-2}	-2.40×10
^{4}He	3.13×10^{-2}	3.27×10^{-2}	4.60×10^{-2}	2.40×10^{-2}
^{12}C	-1.17×10^{-4}	-1.40×10^{-4}	-1.90×10^{-4}	-1.10×10^{-4}
^{13}C	-2.45×10^{-6}	-	-3.00×10^{-6}	0
^{14}N	4.50×10^{-4}	5.40×10^{-4}	7.20×10^{-4}	4.00×10^{-4}
^{15}N	-1.31×10^{-7}	-	-1.80×10^{-7}	-1.20×10^{-7}
^{16}O	-3.56×10^{-4}	-4.50×10^{-4}	-5.70×10^{-4}	-3.10×10^{-4}
^{17}O	4.31×10^{-7}	-	7.00×10^{-7}	9.00×10^{-7}
^{18}O	-1.00×10^{-6}	-	-1.40×10^{-6}	-8.00×10^{-7}
^{19}F	-2.31×10^{-8}	-	-	-
^{20}Ne	-7.28×10^{-7}	0	-	-
^{21}Ne	7.70×10^{-7}	-	-	-
^{22}Ne	-7.25×10^{-6}	-	-	-
^{23}Na	7.57×10^{-6}	-	-	-
^{24}Mg	2.30×10^{-9}	0	-	-
^{25}Mg	-2.69×10^{-6}	-	-	-
^{26}Mg	2.75×10^{-6}	-	-	-
^{26}Al	2.93×10^{-8}	-	-	-
^{27}Al	2.23×10^{-8}	-	-	-

Table 6: Surface abundance changes during second dredge-up for a $5\,\mathrm{M}_\odot$, $Z = 0.02$ model.

as an instantaneous event which occurs at the start of the TPAGB. Analytic fits to the changes in surface abundance from the Monash models are given in appendix B2.

2.5 TPAGB Evolution

In order to synthetically model the Monash TPAGB model nucleosynthesis it is also necessary to model the stellar evolution: core mass, radius, luminosity etc. The prescription used in the SSE model, based on Eggleton models with convective overshooting and a larger timestep, is significantly different from the Monash models. The state of the star at the beginning of the TPAGB is known from the fit to the core mass at the first thermal pulse. The star is evolved forward in time pulse by pulse (see figure 5). Between pulses the star loses mass at a rate $\dot{M}$ from the envelope in a wind. The core grows owing to hydrogen burning and the envelope material may experience hot-bottom burning. At every timestep, usually coincident with a thermal pulse, the HBB algorithm is activated. If the time since the previous pulse exceeds the interpulse period this is immediately followed by third dredge-up. The change in core mass owing to nuclear burning and dredge-up combined with the effect of wind loss determines the time evolution of the star.

The fit for the core mass at the first thermal pulse, $M_{\mathrm{c,1TP}}$, valid for the range $0.004 \leq Z \leq 0.02$ and $1 \leq M_{\mathrm{1TP}}/\mathrm{M}_{\odot} \leq 6$, , where M_{1TP} is the stellar mass at the first thermal pulse, is taken from K02

$$
\begin{aligned}
M_{\mathrm{c,1TP}}/\mathrm{M}_{\odot} \;=\; & f_{17}(-a_{17}(M_{\mathrm{1TP}}/\mathrm{M}_{\odot} - b_{17})^2 + c_{17}) + \\
& (1 - f_{17})(d_{17}M_{\mathrm{1TP}}/\mathrm{M}_{\odot} + e_{17})\,,
\end{aligned}
\tag{17}
$$

where

$$
f_{17} \;=\; \left(1 + e^{\frac{M_{\mathrm{1TP}}/\mathrm{M}_{\odot} - g_{17}}{h_{17}}}\right)
\tag{18}
$$
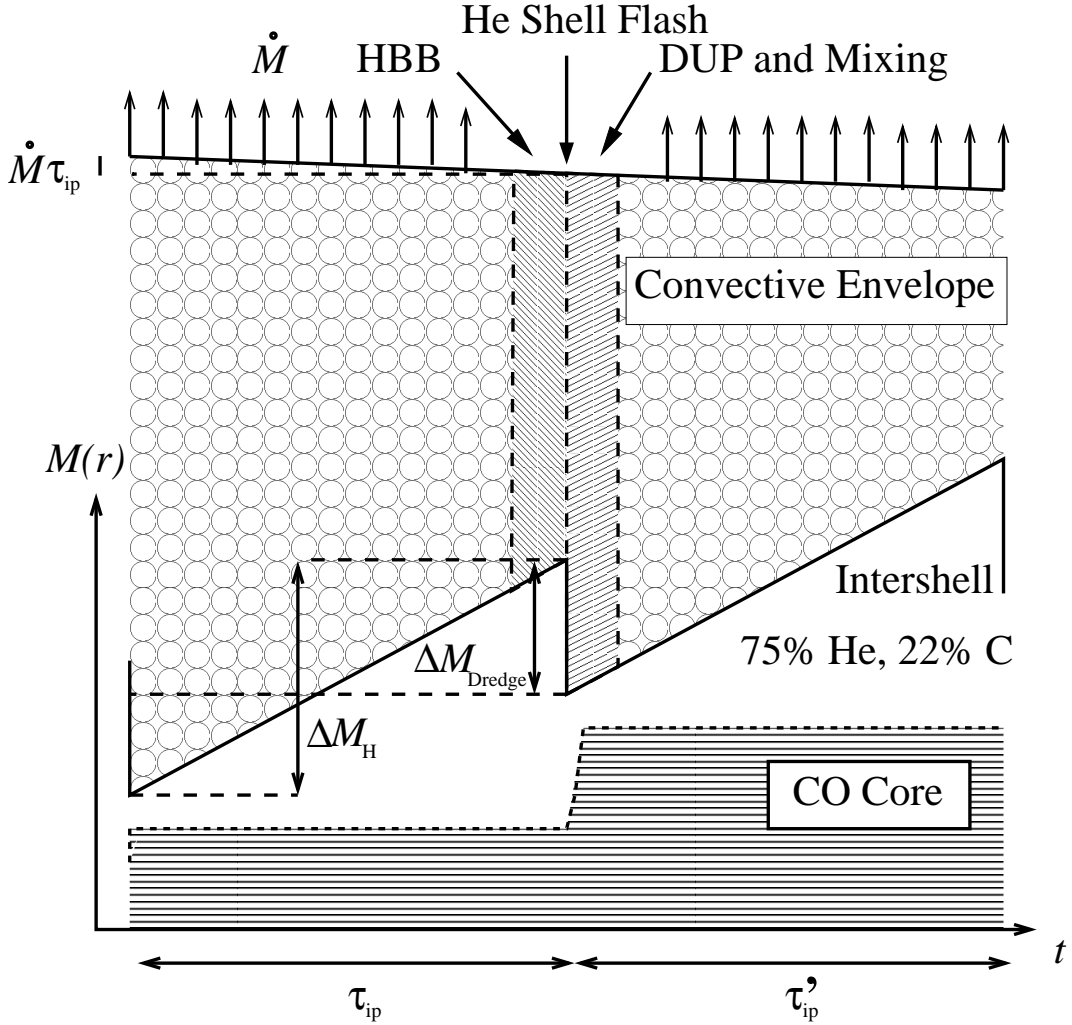
Figure 5: Time evolution of the synthetic AGB model ($\lambda > 0$, not to scale). During the interpulse period τ_{ip} the hydrogen-free core M_{c} (Intershell + CO Core) grows by ΔM_{H} and the envelope loses mass $\dot{M}\tau_{\mathrm{ip}}$. At the end of the interpulse period the envelope is burned using the HBB algorithm and then a He-shell flash occurs causing $\Delta M_{\mathrm{dredge}} = \lambda \Delta M_{\mathrm{H}}$ of material from the intershell region to mix with the convective envelope. The new interpulse period τ'_{ip} is calculated and the evolution continued. The CO core is shown here but is considered to have the same mass as the hydrogen-free core.

is metallicity dependent and is interpolated from the tables in K02 (see appendix B3). Upon extrapolation this function is well behaved for $0.02 < Z \leq 0.03$. Below $M = 1\,\mathrm{M_\odot}$ the relation flattens off so there is little mass dependence upon extrapolation, above $M = 6\,\mathrm{M_\odot}$ the relation is linear and is assumed to be correct – there is no way to test it. K02 find little change in $M_{\mathrm{c,1TP}}$ whether mass loss is included or not because the $M_{\mathrm{c,1TP}}(M_\mathrm{i})$ curve flattens off at low mass so GB mass loss is not important.

In order to evolve the star forward in time the interpulse period, luminosity and radius are required as functions of M, M_c and Z. A direct fit to the time, t, is avoided so the mass-loss rate can be varied and the code used for binary stars. For some of the fits $M_{\mathrm{c,nodup}}$, the core mass as it would be in the absence of third dredge-up, is used. It is defined by

$$M_{\mathrm{c,nodup}}(t) = M_{\mathrm{c,1TP}} + \int_{t_{\mathrm{1TP}}}^{t} \max(0, \frac{dM_c}{dt})\,dt\,, \tag{19}$$

where t_{1TP} is the time of the first thermal pulse. The use of $M_{\mathrm{c,nodup}}$ allows effects of an increase in degeneracy in the core during core growth to be taken into account.

The change in core mass is defined by

$$\Delta M_\mathrm{c} = M_\mathrm{c} - M_{\mathrm{c,1TP}} \tag{20}$$

and the change in core mass without third dredge-up

$$\Delta M_{\mathrm{c,nodup}} = M_{\mathrm{c,nodup}} - M_{\mathrm{c,1TP}}\,. \tag{21}$$

The interpulse period τ_{ip} is based on the formula in Wagenhuber & Groenewegen (1998) but modified to fit the Monash models (Pols, private communication) and includes a dependence on the dredge-up parameter λ (see section 2.6)

$$\log_{10}(\tau_{\mathrm{ip}}/\mathrm{yr}) = a_{22}(M_\mathrm{c}/\mathrm{M_\odot} - b_{22}) - 10^{c_{22}} - 10^{d_{22}} + 0.15\lambda^2, \tag{22}$$

where c_{22} and d_{22} are taken directly from Wagenhuber & Groenewegen (1998), α is the

mixing length parameter ($\alpha = 1.75$ for the Monash models) and $\zeta = \log_{10}(Z/0.02)$. The coefficients are given in appendix B3.

For low-mass stars the peak luminosity at each pulse (after the first few thermal pulses) follows a linear core-mass–luminosity relation (CMLR, Paczynski, 1970). For intermediate-mass stars ($M_i \gtrsim 3.5\,M_\odot$) this relation fails because of hot-bottom burning (Blöcker & Schönberner, 1991; Marigo et al., 1999; see also section 2.7). The peak luminosity is fitted as a sum of the core-mass luminosity L_{CMLR} and a term owing to HBB in the envelope, L_{env}, such that

$$L = f_d(f_t L_{CMLR} + L_{env})\, L_\odot\,. \tag{23}$$

The CMLR is given by a quadratic in M_c for high initial core masses otherwise a linear form is more suitable. If $M_{c,1TP} > 0.58$

$$
\begin{aligned}
L_{CMLR} \quad = \quad & 3.7311 \times 10^4 \times \\
& \max\left[(M_c/M_\odot - 0.52629)(2.7812 - M_c/M_\odot),\right. \\
& \left. 1.2(M_c/M_\odot - 0.48)\right]
\end{aligned} \tag{24}
$$

otherwise

$$L_{CMLR} = \max\left[4(18160 + 3980Z) \times (M_c - 0.4468) - 4000, 10\right]\,. \tag{25}$$

No fit exists for $M_c < M_{c,1TP}$ so the above expression is used for $M_c > 0.4468$ otherwise the expression from H02 is used [2].

The envelope luminosity is given by

---

[2]Stars with such a low core mass can only form in binary systems.
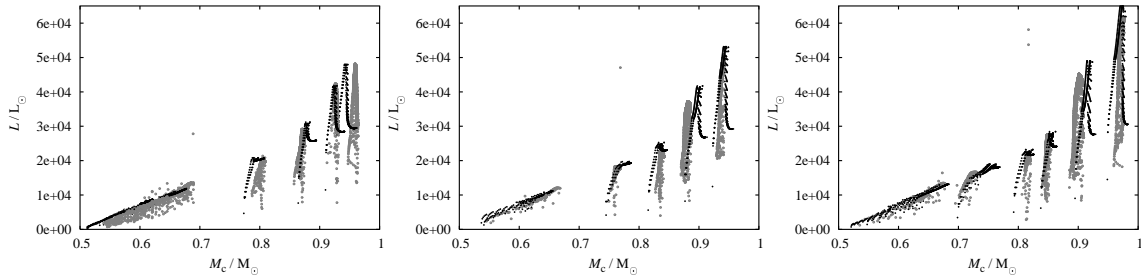
Figure 6: Luminosity vs core mass during the TPAGB phase for $Z = 0.02$ (left), 0.008 (centre) and 0.004 (right). The grey points are the Monash full stellar evolution models, the black points are the synthetic models with the same initial masses. The full stellar evolution models include post-flash dips while the synthetic models do not. Models with core masses above about $0.8\,\mathrm{M_\odot}$ show HBB.

$$
\begin{aligned}
L_{\mathrm{env}} \quad = \quad & 1.50 \times 10^4 (M_{\mathrm{env}}/\mathrm{M_\odot})^2 \times \left[1 + 0.75 \left(1 - \frac{Z}{0.02} \right) \right] \\
& \max \left[\left(M_{\mathrm{c}}/\mathrm{M_\odot} + \frac{1}{2}\Delta M_{\mathrm{c,nodup}}/\mathrm{M_\odot} - 0.75 \right)^2 , 0 \right] ,
\end{aligned}
\tag{26}
$$

where $M_{\mathrm{env}} = M - M_{\mathrm{c}}$ with a turn-on factor for the first few pulses

$$
f_{\mathrm{t}} = \min \left[\left(\frac{\Delta M_{\mathrm{c,nodup}}}{0.04} \right)^{0.2} , 1.0 \right] .
\tag{27}
$$

The short-timescale changes in luminosity which occur during the thermal pulse cycle are not modelled except to calibrate dredge-up, see section 2.6. However, it is necessary to correct for these to obtain an accurate evolution algorithm. This is done with the factor f_{d} given by

$$
f_{\mathrm{d}} = 1 - 0.2180 \exp \left[-11.613 (M_{\mathrm{c}}/\mathrm{M_\odot} - 0.56189) \right] .
\tag{28}
$$

Figure 6 shows the luminosity for the Monash full stellar evolution and synthetic models vs core mass.
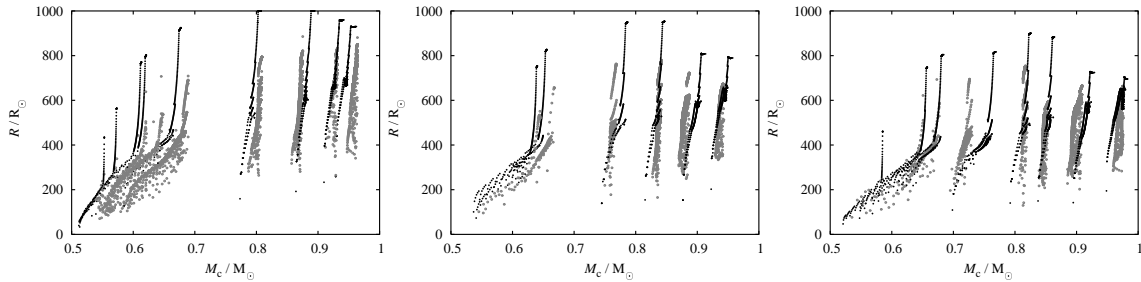
Figure 7: As figure 6 but for radius.

The radius R is defined by $L = 4\pi\sigma R^2 T_{\text{eff}}^4$ where σ is the Stefan-Boltzmann constant and T_{eff} is the effective temperature of the star, defined to be the mass shell where the gas temperature equals T_{eff}. The fit takes the basic form $\log R \approx A \log L$ with a correction for envelope mass loss

$$\log_{10}(R/R_\odot) \;\; = a_{29} \;\; + \;\; b_{29} \log_{10}(L/\,L_\odot) + c_{29} \log_{10}(M_{\text{env}}/M_{\text{env,1TP}}) \;\; . \tag{29}$$

The coefficients a_{29}, b_{29} and c_{29} are extrapolated from table B5. As M_{env} tends to zero this radius diverges so it is capped at $10^3\,R_\odot$. The `BSE` model also truncates the stellar radius as M_{env} becomes small to allow a smooth transition to the WD cooling track on the HR diagram (see appendix B5). Figure 7 shows the radius, without small envelope corrections, vs core mass from the Monash models and synthetic models.

Between pulses the hydrogen-deficient core grows owing to hydrogen burning. The luminosity is due mainly to this and so can be used to calculate the change in core mass during any timestep

$$\Delta M_{\text{c}} = \min(L, L_{\text{max}})Q\delta t \,, \tag{30}$$

where L is the luminosity, δt is the timestep and Q is the effective nuclear burning efficiency. The cap at $L_{\text{max}} = 3.0 \times 10^4\,L_\odot$ is introduced because an increase in core size beyond this rate is not seen in the Monash models (see figure 8, left panel). Q is set to

$$Q = 10^{-11}(2.72530 - 1.8629 X_{H1}) \tag{31}$$

as fitted to the Monash models, see the right panel of figure 8. The fit is not so good for models which experience HBB but these models undergo deep dredge-up so the net core mass growth, and any associated error, is small.

To compare the synthetic model to the Monash models the same wind-loss prescription is used (K02, section 2). Before the giant branch the mass-loss rate $\dot{M}$ is negligible. On the giant branch the formula of Kudritzki & Reimers (1978) with $\eta = 0.4$ is used. On the EAGB and TPAGB the mass-loss rate is according to Vassiliadis & Wood (1993, VW93), without the correction for masses above $2.5\,\mathrm{M}_\odot$, so

$$\log_{10}(\dot{M}/\mathrm{M}_\odot\,\mathrm{yr}^{-1}) = -11.4 + 0.0125(P/\mathrm{d}), \tag{32}$$

where P is the Mira pulsation period given by

$$\log_{10}(P/\mathrm{d}) = -2.07 - 0.9\log_{10}(M/\mathrm{M}_\odot) + 1.94\log_{10}(R/\mathrm{R}_\odot)\,. \tag{33}$$

A typical mass-loss rate is then about $10^{-9}\,\mathrm{M}_\odot\,\mathrm{yr}^{-1}$ for a $1.9\,\mathrm{M}_\odot$, $Z = 0.008$ star (a typical carbon star mass, with $L \approx 5 \times 10^3\,\mathrm{L}_\odot$, $R \approx 200\,\mathrm{R}_\odot$ and $P \approx 200\,\mathrm{d}$) prior to superwind. This is a little low compared to observations (e.g. Wallerstein & Knapp, 1998) although higher-mass stars have significantly higher rates (e.g. $\dot{M} \approx 4 \times 10^{-7}\,\mathrm{M}_\odot\,\mathrm{yr}^{-1}$ for $M = 6\,\mathrm{M}_\odot$, $Z = 0.02$) and as Wallerstein & Knapp (1998) point out it is more difficult to observe AGB stars with low mass-loss rates so there is some observational bias. The radius used in eq. (32) is that calculated in eq. (29) without the envelope correction of H02.

On the TPAGB and for $P \geq P_{\max}$ the rate in eq. (32) is truncated (if necessary) to a superwind given by

$$\dot{M} = \frac{L}{c\,v_{\exp}}\,, \tag{34}$$
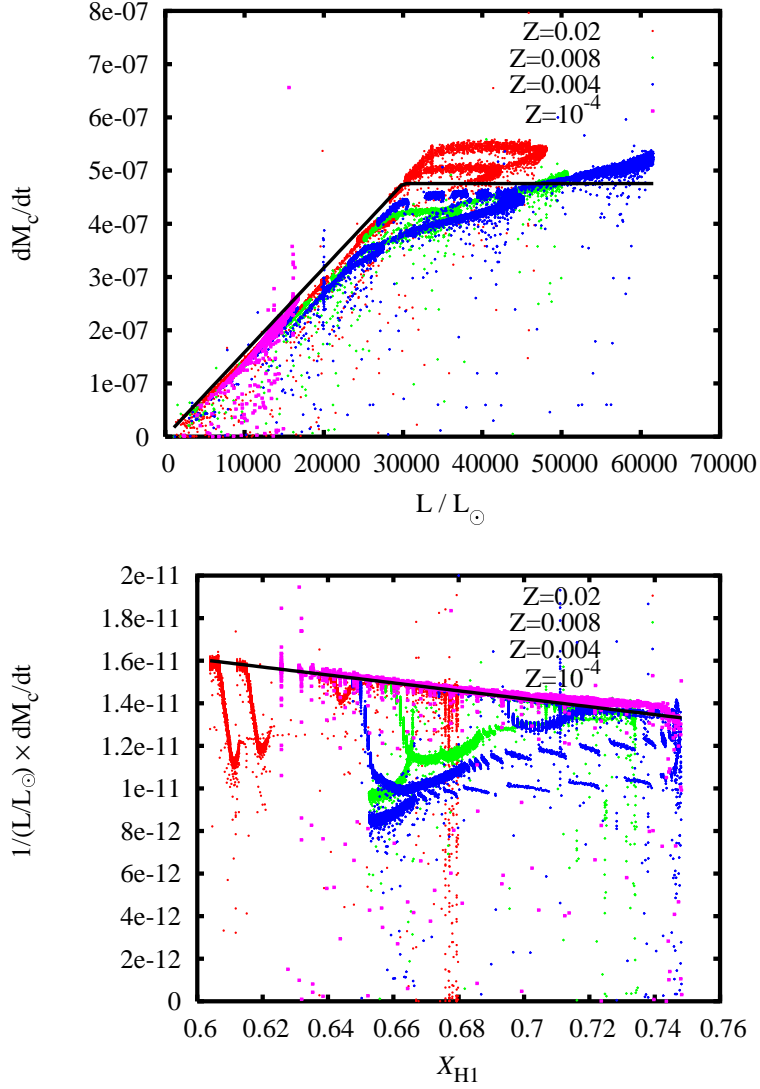
Figure 8: Left panel: $\frac{dM_c}{dt}$ vs L for the Monash models with $\frac{dM_c}{dt} > 0$. The black line is the fit used in the synthetic model. Right panel: $\frac{dM_c}{dt} \times \frac{1}{L/L_\odot} = Q$ vs surface hydrogen abundance for the Monash models with $\frac{dM_c}{dt} > 0$, the black line is the fit used in the synthetic model. Most of the model points below the synthetic fit are stars undergoing HBB so the linear fit fails but the error on M_c is small (see text for details).

where c is the speed of light and v_{exp} is the expansion velocity of the wind (VW93) given by

$$v_{\mathrm{exp}} = \min\left[(-13.5 + 0.056 P_{\mathrm{max}}/\mathrm{d}), 15\right] \, \mathrm{km\,s^{-1}}. \tag{35}$$

The Monash models have $P_{\mathrm{max}} = 500\,\mathrm{d}$ and this is used in the standard synthetic model. The superwind mass-loss rate is usually much greater than the rate given in eq. (32) and leads to a quick end for the star and probably a planetary nebula. For the $1.9\,\mathrm{M_\odot}$, $Z = 0.008$ star a typical superwind mass-loss rate is about $10^{-5}\,\mathrm{M_\odot\,yr^{-1}}$ which agrees reasonably with observations (Wallerstein & Knapp, 1998).

2.6 Third Dredge-Up

The efficiency of third dredge-up is parameterized by

$$\lambda = \frac{\Delta M_{\mathrm{dredge}}}{\Delta M_{\mathrm{H}}}, \tag{36}$$

where $\Delta M_{\mathrm{dredge}}$ is the mass dredged up from the intershell region and ΔM_{H} is the core mass increase owing to hydrogen burning during the previous interpulse period (see figure 5) so that over a whole interpulse period the core grows by $\Delta M_{\mathrm{c}} = \Delta M_{\mathrm{H}} - \Delta M_{\mathrm{dredge}} = (1-\lambda)\Delta M_{\mathrm{H}}$. The fitting of λ to M and Z is an approximation to the true, and unknown, form which would depend on M_{c}, M_{env}, Z and perhaps $M_{\mathrm{c,nodup}}$.

The dredged-up material is instantaneously mixed with the convective envelope of the star. There is a possibility of a degenerate thermal pulse in some stars (Frost, Lattanzio & Wood, 1998). However the effect is to increase the amount of $^{12}\mathrm{C}$ dredged-up by a factor of 4 so one degenerate pulse is equivalent to about four normal pulses. Frost et al. (1998) report degenerate thermal pulses in a $5\,\mathrm{M_\odot}$, $Z = 0.004$ star which would also undergo many dozens of non-degenerate third dredge-up events, so the effect of one or two degenerate pulses is small compared to the effect of non-degenerate pulses and such pulses are not modelled with the synthetic model.

K02 find third dredge-up for stars above a certain core mass M_c^{min}, a function of M_i, Z and M_{sdu}, where M_{sdu} is the mass above which second dredge-up occurs ($M_{sdu} \approx 4\,M_\odot$ for $Z = 0.02$ and $M_{sdu} \approx 3.5\,M_\odot$ for $Z = 0.004$). For $M < M_{sdu}$ the minimum core mass is given by K02

$$M_c^{min*}/M_\odot \;\; = \;\; a_{37} + b_{37}M/M_\odot + c_{37}(M/M_\odot)^2 + d_{37}(M/M_\odot)^3 \,. \tag{37}$$

For $M \geq M_{sdu} - 0.5\,M_\odot$ K02 find $M_c^{min} > 0.7\,M_\odot$ so $M_c^{min} = M_{c,1TP}$. Equation (37) diverges as M increases and so is capped at $0.7\,M_\odot$. A correction is subtracted for $Z < 0.004$ to force dredge-up in the low-metallicity models

$$\Delta M_{LZ} = -205.1Z + 0.8205. \tag{38}$$

Finally the above prescriptions are combined so M_c^{min} is given by

$$M_c^{min} = \max \left[M_{c,1TP}, \min(0.7\,M_\odot, M_c^{min*} - \Delta M_{LZ}) \right] \,. \tag{39}$$

The use of M rather than M_i is consistent with K02 but allows a reduced envelope mass to reduce λ. Below M_c^{min}, $\lambda = 0$. For $M_c > M_c^{min}$, λ reaches an asymptotic value $\lambda_{max}\,N_r$. λ_{max} is fitted with

$$\lambda_{max} = \frac{a_{40} + b_{40}M/M_\odot + c_{40}(M/M_\odot)^3}{1 + d_{40}(M/M_\odot)^3} \,, \tag{40}$$

with $a_{40} \ldots d_{40}$ functions of metallicity (K02, see also appendix B3). For $M \geq 3.0\,M_\odot$, λ reaches a value of $0.8 - 0.9$ with a slight metallicity dependence. At low metallicity dredge-up is efficient at low mass so for $Z \leq 0.004$ eq. (40) is used with M artificially increased by an amount $60 \times (0.004 - Z)$.

The dependence on pulse number since $M_c \gtrsim M_c^{min}$, N, is approximated by

$$\lambda(N) = \lambda_{max} \left(1 - \exp^{-N/N_r}\right) \,. \tag{41}$$
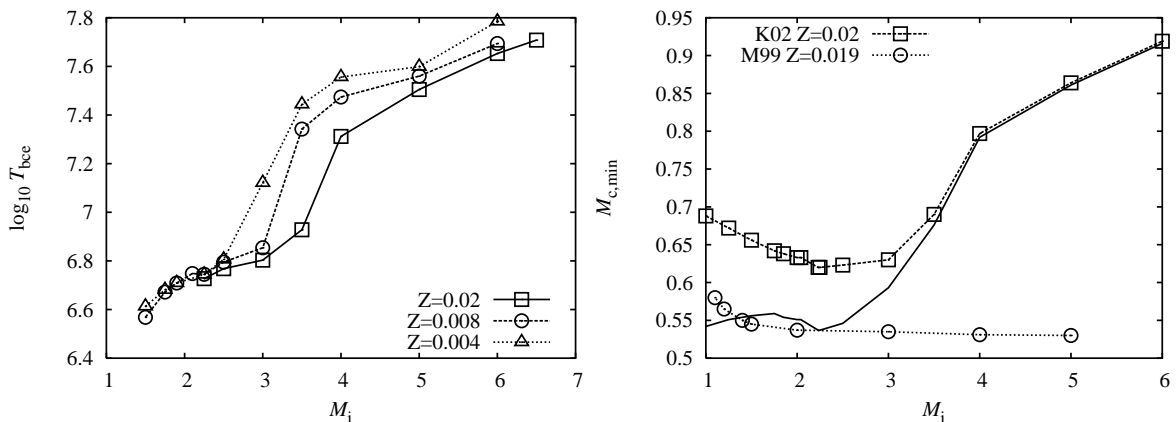
Figure 9: Left panel: Temperature at the base of the convective envelope at the first thermal pulse from the Monash models at various metallicities. Right panel: M_c^{min} from the Monash models (K02) and the model of Marigo et al. (1999). The solid line shows the core mass at the first thermal pulse in the Monash models.

Table 5 of K02 lists appropriate values for N_r but there is no systematic variation that is easily fitted with a simple function. The fit is

$$
\begin{aligned}
N_r &= (a_{42} + b_{42}Z) \times \exp\left(\frac{[M_{1TP} - c_{42}]^2}{d_{42}}\right) + \\
&\quad (e_{42} + f_{42}Z) \times \exp\left(\frac{[M_{1TP} - g_{42}]^2}{h_{42}}\right).
\end{aligned}
\tag{42}
$$

Figure 9 (left panel) shows the temperature at the base of the convective envelope at the first pulse from the Monash models. Note that use of the Marigo, Girardi & Bressan (1999) prescription for dredge-up above $\log_{10} T_{bce} = 6.4$ would lead to dredge-up in all the Monash stars. Also in figure 9 is a comparison of K02's M_c^{min} with Marigo et al.'s prescription (with $\log_{10} T_{bce} = 6.4$) for solar metallicity. Even allowing for calibration of the models by comparison to carbon star luminosity functions the Monash models still have a slightly higher M_c^{min}.

The intershell abundances are a mixture of hydrogen-burned material which is then

mixed into the intershell region and processed through helium burning. The abundances in the intershell region X^i are fitted to data taken from the final thermal pulse of the Monash models with $0.004 \leq Z \leq 0.02$ (Karakas, private communication). Coefficients are given in appendix B4.

Apart from ^{4}He, most of the intershell is ^{12}C and the abundance is fitted to M and Z,

$$
\begin{aligned}
X^i_{\mathrm{C12}} \;=\;& a_{43} + (b_{43} + c_{43}Z)M + (d_{43} + e_{43}Z)M^2 + \\
& (f_{43} + g_{43}Z)M^3 \,,
\end{aligned}
\tag{43}
$$

and further α capture leads to ^{16}O

$$
\begin{aligned}
X^i_{\mathrm{O16}} \;=\;& a_{44} + (b_{44} + c_{44}Z)M + (d_{44} + e_{44}Z)M^2 + \\
& (f_{44} + g_{44}Z)M^3 \,.
\end{aligned}
\tag{44}
$$

All CNO in the hydrogen shell is converted to ^{14}N in the hydrogen burning shell so

$$
X^i_{\mathrm{C13}} = X^i_{\mathrm{N13}} = X^i_{\mathrm{N15}} = X^i_{\mathrm{O15}} = X^i_{\mathrm{O17}} = X^i_{\mathrm{O18}} = 0 \,.
\tag{45}
$$

Some ^{19}F, ^{20}Ne and ^{21}Ne remain

$$
X^i_{\mathrm{F19}} = (a_{46} + b_{46}Z) \times \exp\left(-\frac{(M + c_{46} + d_{46}Z)^2}{(e_{46} + f_{46}Z)}\right) \,,
\tag{46}
$$

$$
X^i_{\mathrm{Ne20}} =
\begin{cases}
\frac{Z}{0.02}(a_{47} + b_{47}M) & M < 2.2\,\mathrm{M}_\odot \\[2mm]
\frac{Z}{0.02}(c_{47} + d_{47}M + e_{47}M^2) & M \geq 2.2\,\mathrm{M}_\odot
\end{cases}
\tag{47}
$$

and

$$
X^i_{\mathrm{Ne21}} = \chi_{21}\left(\frac{0.02}{Z}\right)^{0.4}\left(a_{48} + b_{48}\exp\left[-\frac{(M + c_{48} + d_{48}\log_{10}Z)^2}{e_{48}}\right]\right)
\tag{48}
$$

where $\chi_{21} = Z/0.02$ for $M > 4\,\mathrm{M}_\odot$, $\chi_{21} = 1$ otherwise.

This is then converted to ^{22}Ne by double-α capture in the helium burning shell prior to dredge-up. There is also some further processing of ^{22}Ne to ^{24}Mg, ^{25}Mg and ^{26}Mg. The fits are

$$
X^{\mathrm{i}}_{\mathrm{Ne22}} = \begin{cases} a_{49}Z + b_{49}M^{c_{49}} + (d_{49} + e_{49}Z)\times & \\ \quad \exp\left(\left(-\frac{(M+f_{49}+g_{49}Z)^2}{(h_{49}+i_{49}Z)}\right)\right) & M < 4\,\mathrm{M_\odot} \\ (j_{49} + k_{49}M) \times (1 + l_{49}Z) & M \geq 4\,\mathrm{M_\odot} \end{cases}, \tag{49}
$$

$$
\begin{aligned} X^{\mathrm{i}}_{\mathrm{Na23}} = {} & a_{50} + (b_{50} + c_{50}Z) \times M + (d_{50} + e_{50}Z) \times \\ & \exp\left[-\frac{(x + f_{50} + g_{50}Z)^2}{h_{50}}\right], \end{aligned} \tag{50}
$$

$$
\begin{aligned} X^{\mathrm{i}}_{\mathrm{Mg24}} = {} & a_{51} + b_{51}\log_{10}Z + (c_{51} + d_{51}\log_{10}Z) \times \\ & \left[1 - 1/(1 + e_{51}^{M+f_{51}+g_{51}Z})\right], \end{aligned} \tag{51}
$$

$$
X^{\mathrm{i}}_{\mathrm{Mg25}} = \max(0, a_{52} + b_{52}M + c_{52}M^{d_{52}} + e_{52}M\log_{10}Z), \tag{52}
$$

$$
X^{\mathrm{i}}_{\mathrm{Mg26}} = a_{53} + b_{53}M + c_{53}\log_{10}Z \times M^{d_{53}}, \tag{53}
$$

$$
X^{\mathrm{i}}_{\mathrm{Na22}} = X^{\mathrm{i}}_{\mathrm{Al26}} = 0, \tag{54}
$$

$$
X^{\mathrm{i}}_{\mathrm{Al27}} = a_{55} + b_{55}\log_{10}Z + \frac{c_{55}}{1 + 0.1^{M+d_{55}+e_{55}Z}}. \tag{55}
$$

Heavy *s*-process isotopes are fitted in section 2.11 below. All other isotopes heavier than ^{27}Al are set to their envelope abundances. The remaining material in the intershell is assumed to be ^{4}He. The above fits give typical intershell abundances, for a solar metallicity, $5\,\mathrm{M_\odot}$ model, of 74% ^{4}He, 23% ^{12}C, 0.5% ^{16}O and 2% ^{22}Ne.

There is some debate on the exact composition in the intershell region. The inclusion

of overshooting (Herwig, 2000) seems to increase the abundance of ^{12}C and ^{16}O at the expense of ^{4}He while other authors (Marigo et al., 2003) suggest little or no ^{12}C and ^{16}O in the intershell. The Monash models do not obtain high values of intershell ^{16}O such as the 2% reported by Boothroyd & Sackmann (1988).

Groenewegen & de Jong (1993) include nuclear burning of third dredge-up material (their eq. 35) as well as envelope burning (section 2.7 below). The reason for this is that material brought up by third dredge-up is preferentially exposed to high temperatures at the base of the convective envelope. The Monash models do not show this phenomenon though, in the low metallicity models, there is dredge-up of ^{13}C and ^{14}N that leads to a similar effect which cannot possibly result from helium burning. These isotopes are enhanced in the envelope by dredge-up of material previously in the hydrogen burning shell but not mixed into the intershell convective zone.

To account for this a fraction f_{DUP} of $\Delta M_{\mathrm{dredge}}$ is burnt for a fraction of the interpulse period $f_{\mathrm{burn,DUP}}$ and at the temperature and density at the base of the envelope extrapolated from eqs. 61 and 65. The hydrogen abundance of the material to be burned is set to the envelope hydrogen abundance even though it may be somewhat lower owing to interpulse hydrogen shell burning. Because f_{DUP} and $f_{\mathrm{burn,DUP}}$ are fitted to the full evolution models any problems are circumvented by the calibration. The burning algorithm is that used for HBB. The hydrogen-burned material is immediately mixed with both the helium-burned intershell material and the whole convective envelope to give the post third dredge-up envelope abundances.

Note that when normal HBB occurs it is the dominant burning mechanism. At metallicity greater than 0.004 the change of ^{13}C and ^{14}N in the envelope owing to the dredge-up of the H-burning-shell is negligible compared to the abundance of ^{13}C and ^{14}N already in the envelope. The model used here is only approximate and does not reflect the actual hydrogen burning process – improvement requires more low-Z detailed models.

2.7 Hot-Bottom Burning

If the hydrogen envelope of an AGB star is sufficiently massive, the hydrogen burning shell can extend into the convective region, a process known as hot-bottom burning (HBB). HBB is dealt with in the synthetic code by burning a fraction of the convective envelope f_{HBB} for a fraction of the interpulse period f_{burn} at the temperature and density as fitted below. The burned fraction is mixed with the rest of the convective envelope at the end of the timestep. Any dependence of HBB on mixing length should be small because the envelope is assumed to be fully mixed.

Between pulses the convective envelope of an AGB star turns over many thousands of times. It is impossible to model this using little CPU time because the burn $\rightarrow$ mix $\rightarrow$ burn $\rightarrow$ mix ... process is computationally expensive. Given the uncertainties involved in convective mixing and local mixing at the base of the envelope, it is simpler and preferable to approximate the burning many times of a thin HBB layer at the base of the convective envelope with a single burning of a larger portion of the envelope.

This can be justified by considering the size of the HBB region. For a $5\,\mathrm{M}_\odot$ star $d\log_{10}(T/\mathrm{K})/dm$ at the base of the envelope is typically $3\times 10^3\,\mathrm{M}_\odot^{-1}$. HBB ceases at $\log_{10}(T/\mathrm{K})\approx 7.6$ and the temperature at the base of the envelope is $\log_{10}(T/\mathrm{K})\approx 8$. So $\Delta M_{\mathrm{HBB}}\approx 10^{-4}\,\mathrm{M}_\odot$. This is much smaller than the size of the convective envelope (about $4\,\mathrm{M}_\odot$ for a $5\,\mathrm{M}_\odot$ star), so the HBB shell can be considered as thin.

When the thin HBB shell is burned and then mixed into the envelope the abundances in the envelope are essentially unchanged. Only once a significant number of mixing events (of the order $M_{\mathrm{env}}/\Delta M_{\mathrm{HBB}}$) have occurred will the envelope abundances change noticeably, so in this approximation a fraction of the envelope, f_{HBB}, is burned for a fraction of the interpulse period time f_{burn}. Fits are then made for f_{HBB} and f_{burn} to the Monash models. In reality, some parts of the envelope burn more than once but this is absorbed into the calibration of f_{HBB}. The following argument justifies this approximation. Figure 10 shows a schematic of the envelope of a hot bottom burning star. At time 0 the abundances in the envelope are $\mathbf{X}_0$, after a convective turnover time τ_{c} the abundances in the envelope

are converted by radioactive decay to $\boldsymbol{\alpha}\mathbf{X}_0$ and the HBB layer to $\boldsymbol{\alpha\beta}\mathbf{X}_0$ where $\boldsymbol{\beta}$ is due to HBB alone[3]. The envelope then mixes and the process is repeated. After one mixing the envelope abundances are given by

$$\mathbf{X}_1 = \frac{\boldsymbol{\alpha}\mathbf{X}_0(M_{\mathrm{env}} - M_{\mathrm{HBB}}) + \boldsymbol{\alpha\beta}M_{\mathrm{HBB}}\mathbf{X}_0}{M_{\mathrm{env}}} \tag{56}$$

and after N_c pulses, where $N_\mathrm{c} = \tau_{\mathrm{ip}}/\tau_\mathrm{c}$ is the number of convective mixing events during an interpulse period,

$$\mathbf{X}_{\mathrm{N_c}} = \mathbf{X}_0\left[\boldsymbol{\alpha} + \frac{M_{\mathrm{HBB}}}{M_{\mathrm{env}}}(\boldsymbol{\alpha\beta} - \boldsymbol{\alpha})\right]^{N_\mathrm{c}}. \tag{57}$$

which can be rewritten using a binomial expansion as

$$\mathbf{X}_{N_\mathrm{c}} = \mathbf{X}_0\boldsymbol{\alpha}^{N_\mathrm{c}}\left[1 + f_{\mathrm{HBB}}(\boldsymbol{\beta} - 1)\right] = \mathbf{X}_0\boldsymbol{\alpha}^{N_\mathrm{c}}\left[(1 - f_{\mathrm{HBB}}) + f_{\mathrm{HBB}}\boldsymbol{\beta}\right] \tag{58}$$

where

$$f_{\mathrm{HBB}} = N_\mathrm{c}\frac{M_{\mathrm{HBB}}}{M_{\mathrm{env}}} \tag{59}$$

under the assumption that the burning layer is thin ($M_{\mathrm{HBB}} \ll M_{\mathrm{env}}$) and that $\boldsymbol{\alpha}$ and $\boldsymbol{\beta}$ do not vary significantly during the interpulse phase. Radioactive decay is dealt with by the term $\boldsymbol{\alpha}^{N_\mathrm{c}}$, the unburned material by $(1 - f_{\mathrm{HBB}})$ and the multiple burnings of the thin shell by $f_{\mathrm{HBB}}\boldsymbol{\beta}$. The HBB shell mass f_{HBB} and burn time f_{burn} necessary to calculate $\boldsymbol{\beta}$ still have to be calibrated to the full evolution models but as long as the shell is thin this is justified. The radioactive decay term becomes $\exp -N_\mathrm{c}\tau_\mathrm{c}/\tau_{\mathrm{rad}}$ where τ_{rad} is the radioactive decay timescale. From the definition of N_c this becomes $\exp -\tau_{\mathrm{ip}}/\tau_{\mathrm{rad}}$ so knowledge of N_c is not required. If $\boldsymbol{\alpha}$ or $\boldsymbol{\beta}$ changes rapidly with time (this occurs when the nuclear timescale is similar to the convective timescale) the situation is more complex and a simple expression cannot be formulated. For this reason it is impossible to burn isotopes such as ^{7}Li or ^{8}Be with this technique.

---

[3]Both $\boldsymbol{\alpha}$ and $\boldsymbol{\beta}$ are matrices because they vary from isotope to isotope.
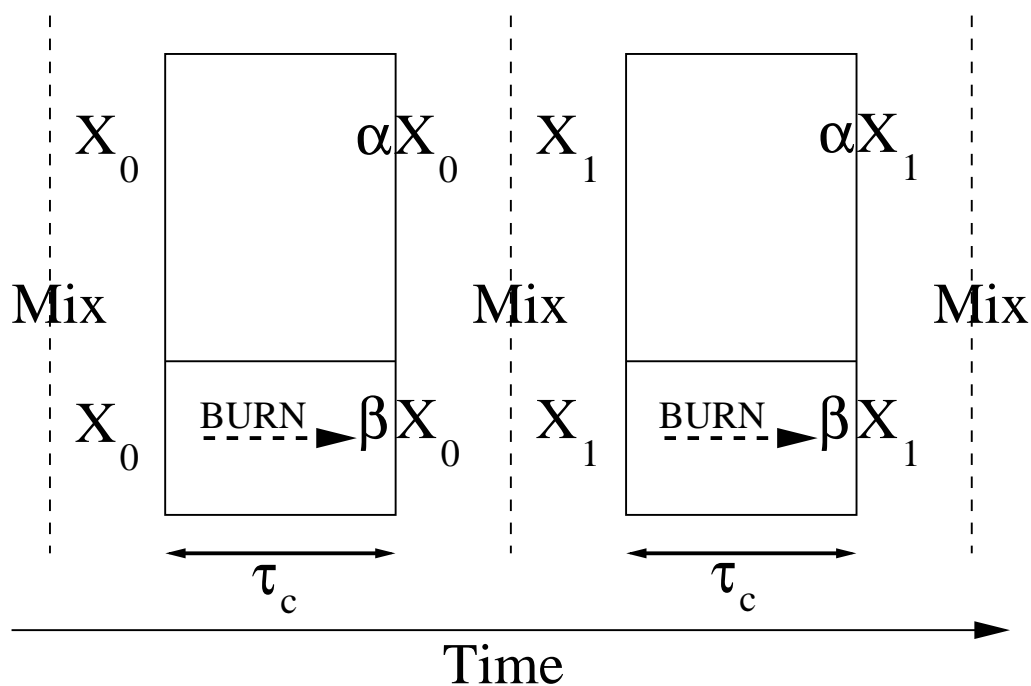
Figure 10: Synthetic convective mixing approximation: the region at the base of the envelope burns isotopes X to βX while radioactive decay in the envelope converts abundances **X** to **α**X.

The temperature at the base of the convective envelope T_{bce} is the critical factor which governs the rate of hot-bottom burning. If the temperature is sufficiently high ($T_{\mathrm{bce}} > T_{\mathrm{HBBmin}} \approx 10^{7.5}\,\mathrm{K}$) it is possible that hydrogen burning occurs in the convective envelope of the star altering the surface abundances. From the Monash models it is seen that the temperature rises quickly in these hot-bottom envelopes and then stays at a roughly constant value until the envelope mass becomes small. In order to model the HBB a fit to the temperature in the burning zone is needed.

The base of the convective envelope is defined as the innermost point in the envelope at which the Schwarzschild condition for stability is no longer satisfied. The rise at the beginning of the AGB and the fall owing to envelope mass reduction at the end of the AGB are extremely difficult to parameterize, so the maximum temperature over the lifetime of the star is fitted and modulated for the rise and fall. The logarithm of the temperature is then given by

$$\log_{10}(T_{\mathrm{bce}}/\mathrm{K}) = \log_{10}(T_{\mathrm{max}}) f_{\mathrm{Trise}} f_{\mathrm{Tdrop}}\,, \tag{60}$$

where T_{max}, f_{Trise} and f_{Tdrop} are defined below.

The logarithm of the temperature maximum is fitted to

$$\log_{10}(T_{\mathrm{max}}/\mathrm{K}) = \min(6.0379 + a_{61} M_{\mathrm{env,0}}/\mathrm{M_\odot} + B(\zeta, M_{\mathrm{c,1TP}}), 7.95)\,, \tag{61}$$

where a_{61} is a constant and

$$B(\zeta, M_{\mathrm{c,1TP}}) = (a_{62}\zeta^2 + b_{62}\zeta + c_{62}) \times (1 + d_{62} M_{\mathrm{c,1TP}}/\mathrm{M_\odot} + e_{62}(M_{\mathrm{c,1TP}}/\mathrm{M_\odot})^2)\,, \tag{62}$$

where $a_{62}\ldots e_{62}$ are constants. The maximum value of 7.95 was a limitation of the HBB code at the time it was calibrated[4]. Temperatures higher than this are only likely to be

---

[4]Above this temperature the burning algorithm became unstable, e.g. see figure C8 with $f_{\mathrm{T}} = 1.02$, possibly due to the roots of the quadratic eigenvalue equation being complex. The problem is not repeatable with the latest version of the code although it is not known why.

encountered in the envelopes of the lowest metallicity and highest-mass stars for which there are few Monash models available for calibration.

The rise in temperature during the first few thermal pulses is modelled by a factor

$$f_{\text{Trise}} = 1.0 - \exp\left(-\frac{N_{\text{TP}}}{N_{\text{rise}}}\right),$$ (63)

where N_{TP} is the thermal pulse number and N_{rise} is a rather arbitrary constant, of the order of 1 for $M_{\text{i}} \approx 6\,\text{M}_\odot$, a few for $M_{\text{i}} \approx 5\,\text{M}_\odot$, about 20 for $M_{\text{i}} \approx 4\,\text{M}_\odot$ and possibly infinite for $M_{\text{i}} < 3.5\,\text{M}_\odot$. No HBB occurs in the latter stars, at least for $Z \geq 0.004$, and the $T_{\text{max}} < T_{\text{HBB,min}}$ condition also prevents HBB.

The drop in temperature owing to the decrease in envelope mass is taken care of by

$$f_{\text{Tdrop}} = \left(\frac{M_{\text{env}}}{M_{\text{env,1TP}}}\right)^{\beta_{64}},$$ (64)

where β_{64} is another free parameter which is quite uncertain, especially for the high-mass stars, for which there is no data when $M_{\text{env}} \lesssim 1.0\,\text{M}_\odot$. Fortunately M_{env} falls quickly during the superwind phase near the end of the AGB so the uncertainty does not matter too much. A constant value $\beta_{64} = 0.02$ is used and this works well for most stars.

The density ρ at the base of the convective envelope is not as important for nucleosynthesis as the temperature but a reasonable value is required. The logarithm of the maximum density over the star's TPAGB evolution as a function of M_0 and Z is fitted by

$$\log_{10} \rho_{\text{max}} = a_{65} + b_{65}(M_{\text{1TP}}^{\text{c65}}/\text{M}_\odot) + d_{65}\zeta.$$ (65)

This function is modulated by f_{Trise} and $M_{\text{env}}/M_{\text{env,0}}$ to give

$$\rho = \rho_{\text{max}} f_{\text{Trise}} \frac{M_{\text{env}}}{M_{\text{env,1TP}}}.$$ (66)

This is a reasonable fit for $M_{\text{1TP}} > 3\,\text{M}_\odot$ and models with $M_{\text{1TP}} < 3\,\text{M}_\odot$ do not experience HBB.

The free parameters,

- f_{HBB} - the fraction of the star's envelope that is burned in the HBB shell,

- f_{burn} - the fraction of the interpulse period for which the HBB shell burns,

- f_{DUP} - the fraction of the dredged-up material which is burned before being mixed into the envelope,

- $f_{\text{DUP,burn}}$ - the fraction of the interpulse period for which the dredged-up material is burned and

- N_{rise} - the factor used to define how quickly the HBB temperature reaches T_{max}

are calibrated to the surface abundance vs time profiles of Monash models for ^{12}C, ^{13}C, ^{14}N and ^{16}O. Appendix C contains details of the calibration method, fits to the free parameters and a brief sensitivity study.

2.8 Rapid CNO burning

The CNO elements are burned according to Clayton's CNO bi-cycle (Clayton, 1983). He claims this is accurate to 1% for the temperature range considered ($\log_{10} T/\text{K} < 8$) and this was confirmed by Groenewegen & de Jong (1993) who used a similar approach. This technique is much faster than solving the differential equations of a complete nuclear reaction network.

The CNO cycle can be simplified from the full set of differential equations (see table 7) if ^{13}N, ^{15}N, ^{15}O and ^{17}F are in equilibrium. The cycle then splits into two at $^{15}\text{N}(p, \gamma)^{16}\text{O}$, the CN cycle and the ON cycle, with branching ratios $\alpha_{\text{CN}} = 1 - \alpha_{\text{ON}}$ and $\alpha_{\text{ON}} \simeq 7 \times 10^{-4}$ respectively (Angulo et al., 1999). The small value of α_{ON} reflects the fact that the timescales in the ON cycle are many thousands of times those required to bring the CN cycle into equilibrium so the cycles can be treated separately.

The CN cycle equations, with $\alpha_{\text{CN}} = 1$, become

i	Reaction	τ/s	Cycle
12	$^{12}\text{C} + {}^{1}\text{H} \rightarrow {}^{13}\text{N} + \gamma$	NACRE	CN
13β	$^{13}\text{N} \rightarrow {}^{13}\text{C} + e^{+} + \nu$	597.54	Equilibrium
13	$^{13}\text{C} + {}^{1}\text{H} \rightarrow {}^{14}\text{N} + \gamma$	NACRE	CN
14	$^{14}\text{N} + {}^{1}\text{H} \rightarrow {}^{15}\text{O} + \gamma$	NACRE	CN/ON
15	$^{15}\text{N} + {}^{1}\text{H} \rightarrow {}^{12}\text{C} + \alpha$	NACRE	Equilibrium
	$^{15}\text{N} + {}^{1}\text{H} \rightarrow {}^{16}\text{O} + \gamma$	NACRE	CN/ON branch
15β	$^{15}\text{O} \rightarrow {}^{15}\text{N} + e^{+} + \nu$	122.2	Equilibrium
16	$^{16}\text{O} + {}^{1}\text{H} \rightarrow {}^{17}\text{F} + \gamma$	NACRE	ON
17β	$^{17}\text{F} \rightarrow {}^{17}\text{O} + e^{+} + \nu$	64.78	Equilibrium
17	$^{17}\text{O} + {}^{1}\text{H} \rightarrow {}^{14}\text{N} + {}^{4}\text{He}$	NACRE	ON
17γ	$^{17}\text{O} + {}^{1}\text{H} \rightarrow {}^{18}\text{F} + \gamma$	NACRE	ON
18β	$^{18}\text{F} \rightarrow {}^{18}\text{O} + e^{+} + \nu$	0	Equilibrium
18α	$^{18}\text{O} + {}^{1}\text{H} \rightarrow {}^{15}\text{N} + {}^{4}\text{He}$	NACRE	Equilibrium

Table 7: Reactions used in the rapid CNO bi-cycle. The columns show the reaction number used in the text i, the corresponding nuclear reaction, the reaction timescale (NACRE indicates use of the analytic fit to the cross section from Angulo et al., 1999, beta-decay timescales are from Tuli, 2000) and synthetic cycle used.

$$\frac{d}{dt} \begin{bmatrix} ^{12}\text{C} \\ ^{13}\text{C} \\ ^{14}\text{N} \end{bmatrix} = \begin{bmatrix} -1/\tau_{12} & 0 & 1/\tau_{14} \\ 1/\tau_{12} & -1/\tau_{13} & 0 \\ 0 & 1/\tau_{13} & -1/\tau_{14} \end{bmatrix} \begin{bmatrix} ^{12}\text{C} \\ ^{13}\text{C} \\ ^{14}\text{N} \end{bmatrix} \tag{67}$$

which is of the form $\frac{d}{dt}\mathbf{U} = \Lambda\mathbf{U}$. Eigenvalues λ_i are given by $\Lambda\mathbf{U} = \lambda_i\mathbf{U}$ and $\mathbf{U}$ is a linear combination of the eigenvectors $\mathbf{U_i}$, so

$$\mathbf{U}(t) = Ae^{\lambda_1 t}\mathbf{U_1} + Be^{\lambda_2 t}\mathbf{U_2} + Ce^{\lambda_3 t}\mathbf{U_3}\,. \tag{68}$$

The timescales τ_i for the proton-capture reactions are defined by

$$\tau_i = \left(\langle\sigma v\rangle_i\, N_{\text{H1}}\right)^{-1} \tag{69}$$

where $\langle\sigma v\rangle_i$ is the velocity averaged cross section for the appropriate reaction i. The rate of change of each isotope (eq. 67) is proportional to the cross section, the hydrogen density and the isotope density.

The method of solution for eq. (67) is found in Clayton (1983). The timestep δt is substituted for t in eq. (68) to calculate the abundances at the end of the current timestep.

The ON cycle equations are identical to the CN cycle, with ^{12}C, ^{13}C and ^{14}N replaced by ^{14}N, ^{16}O and ^{17}O and with appropriate τ_i (see Clayton, 1983 and table 7). The amount of ^{17}O converted to ^{18}O (via ^{18}F) is too small to affect the surface abundance of ^{17}O and the associated ON cycle so is ignored. Similarly, because the ^{18}O abundance is always small feedback into the CN cycle via ^{15}N is also ignored. The minor species ^{13}N, ^{15}N, ^{15}O, ^{18}O and ^{17}F are then assumed to be in equilibrium such that

$$N_{\mathrm{N}13} = N_{\mathrm{C}12} \frac{\tau_{\beta 13}}{\tau_{12}}, \tag{70}$$

$$N_{\mathrm{N}15} = \tau_{15} \left(\frac{N_{\mathrm{O}15}}{\tau_{\beta 15}} + \frac{N_{\mathrm{O}18}}{\tau_{18}} \right), \tag{71}$$

$$N_{\mathrm{O}15} = N_{\mathrm{N}14} \frac{\tau_{\beta 15}}{\tau_{14}}, \tag{72}$$

$$N_{\mathrm{F}17} = N_{\mathrm{O}17} \frac{\tau_{\beta 17}}{\tau_{16}} \tag{73}$$

and

$$N_{\mathrm{O}18} = \frac{N_{\mathrm{O}17}}{\tau_{17\gamma}} \left(\frac{1}{\tau_{\mathrm{O}18\alpha}} + \frac{1}{\tau_{\mathrm{O}18\gamma}} \right)^{-1}. \tag{74}$$

For short burning times ($\delta t < \tau_{12}$) only the CN part of the cycle is necessary. For longer times, the CN cycle is burned to equilibrium before the ON cycle is activated. Even in the most massive AGB stars undergoing vigorous HBB, $X_{\mathrm{O}16}$ does not change much so the ON cycle never approaches equilibrium. Nuclear reaction rates are taken from the formulae in the NACRE compilation (Angulo et al., 1999) except the beta decay constants which are taken from compilation of Tuli (2000). The rates compare well to table 5.3 (page 393) of Clayton (1983).

Figures 11 to 18 show the synthetic models compared to the Monash models for stars which experience HBB ($M \geq 3.5\,\mathrm{M}_\odot$) for ^{1}H, ^{4}He, CNO and ^{17}F. The agreement is excellent for the major elements and the qualitative behaviour is correct for the others. In

cases where the synthetic and Monash models differ the mass of the star can be varied a little to obtain a better match so the effect on the yield from an integrated population of stars owing to these minor deviations is small.

2.9 Rapid NeNa and ^{19}F burning

The NeNa cycle is given by

$$
^{21}\text{Ne} \xrightarrow{(p,\gamma)} {}^{22}\text{Na}
$$

$$
(\beta^+) \uparrow \qquad \downarrow (\beta^+)
$$

$$
^{21}\text{Na} \qquad\qquad {}^{22}\text{Ne}
$$

$$
(p,\gamma) \uparrow \qquad \downarrow (p,\gamma)
$$

$$
^{19}\text{F} \xrightarrow{(p,\gamma)} {}^{20}\text{Ne} \xleftarrow{(p,\alpha)} {}^{23}\text{Na} \xrightarrow{(p,\gamma)} \text{MgAl}
$$

where the timescales for the reactions (eq. 69) are shown in figure 19. The cross sections are taken from the NACRE compilation and the previously fitted T_{bce} and ρ_{bce} are used.

As it stands, this is a complicated problem. However, entry via ^{19}F can be dealt with explicitly and exit via ^{24}Mg can be neglected because MgAl cycling is of greater importance (see section 2.10). The beta decays have lifetimes of $32\,$s for ^{21}Na, so this is assumed to decay instantly, and $3.74\,$yr for ^{22}Na which is assumed to be in equilibrium. The remainder of the cycle is

$$
^{21}\text{Ne} \xrightarrow{(p,\gamma)} {}^{22}\text{Ne}
$$

$$
(p,\gamma) \uparrow \qquad \downarrow (p,\gamma)
$$

$$
^{20}\text{Ne} \xleftarrow{(p,\alpha)} {}^{23}\text{Na}
$$

and the differential equations become

$$
\frac{d^{20}\text{Ne}}{dt} = -\frac{^{20}\text{Ne}}{\tau_{20}} + \frac{^{23}\text{Na}}{\tau_{23}} \,, \tag{75}
$$

$$
\frac{d^{21}\text{Ne}}{dt} = \frac{^{20}\text{Ne}}{\tau_{20}} - \frac{^{21}\text{Ne}}{\tau_{21}} \,, \tag{76}
$$

Figure 11: ^{1}H, ^{4}He, ^{12}C, ^{13}C and ^{14}N vs time (in units of 10^5 years) for the synthetic models (red) and the Monash models (green) with $M = 6\,\mathrm{M}_\odot$.
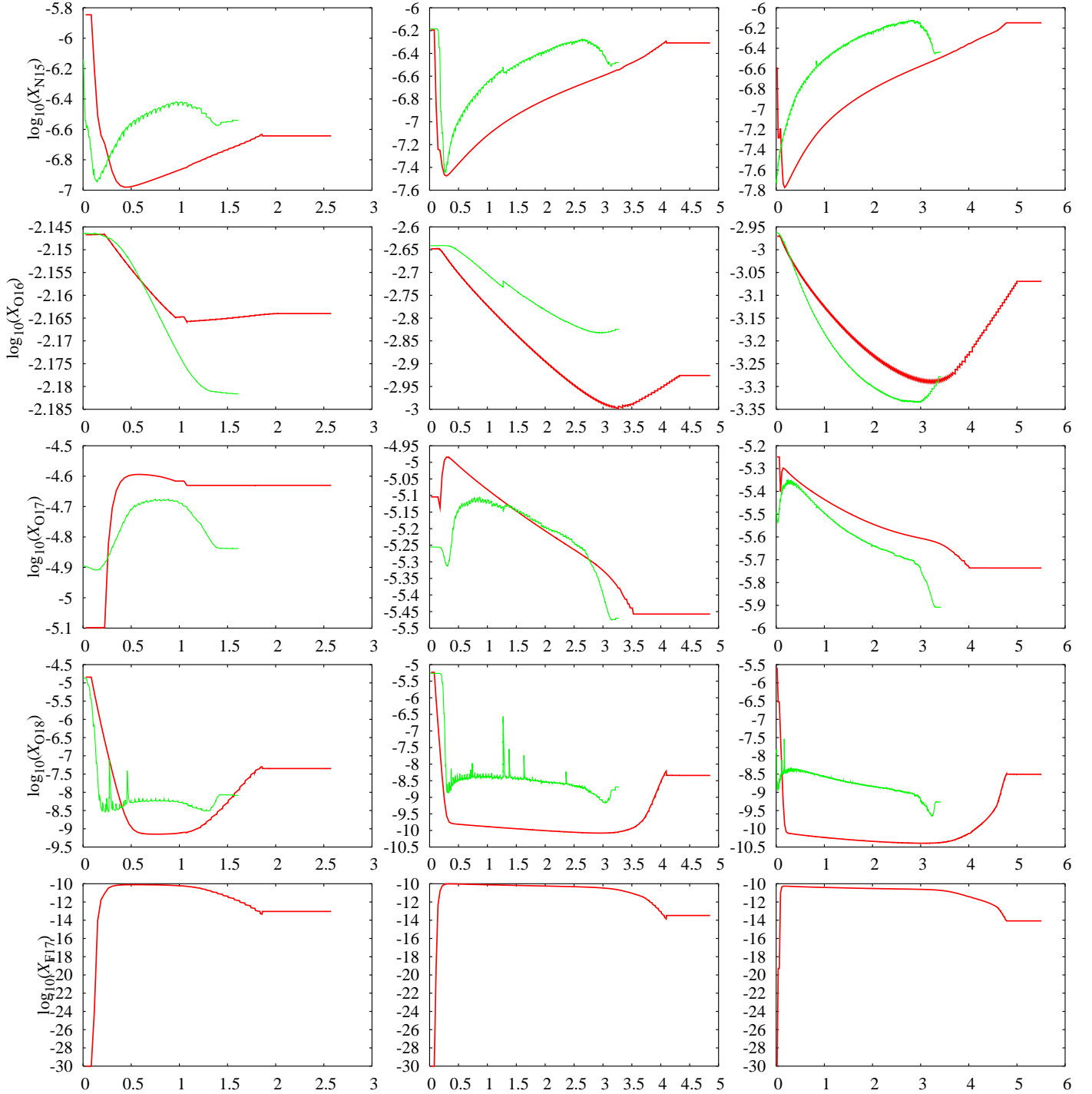
Figure 12: ^{15}N, ^{16}O, ^{17}O, ^{18}O and ^{17}F vs time (in units of 10^5 years) for the synthetic models (red) and the Monash models (green) with $M = 6\,M_\odot$.

Figure 13: ^{1}H, ^{4}He, ^{12}C, ^{13}C and ^{14}N vs time (in units of 10^5 years) for the synthetic models (red) and the Monash models (green) with $M = 5\,\mathrm{M}_\odot$.
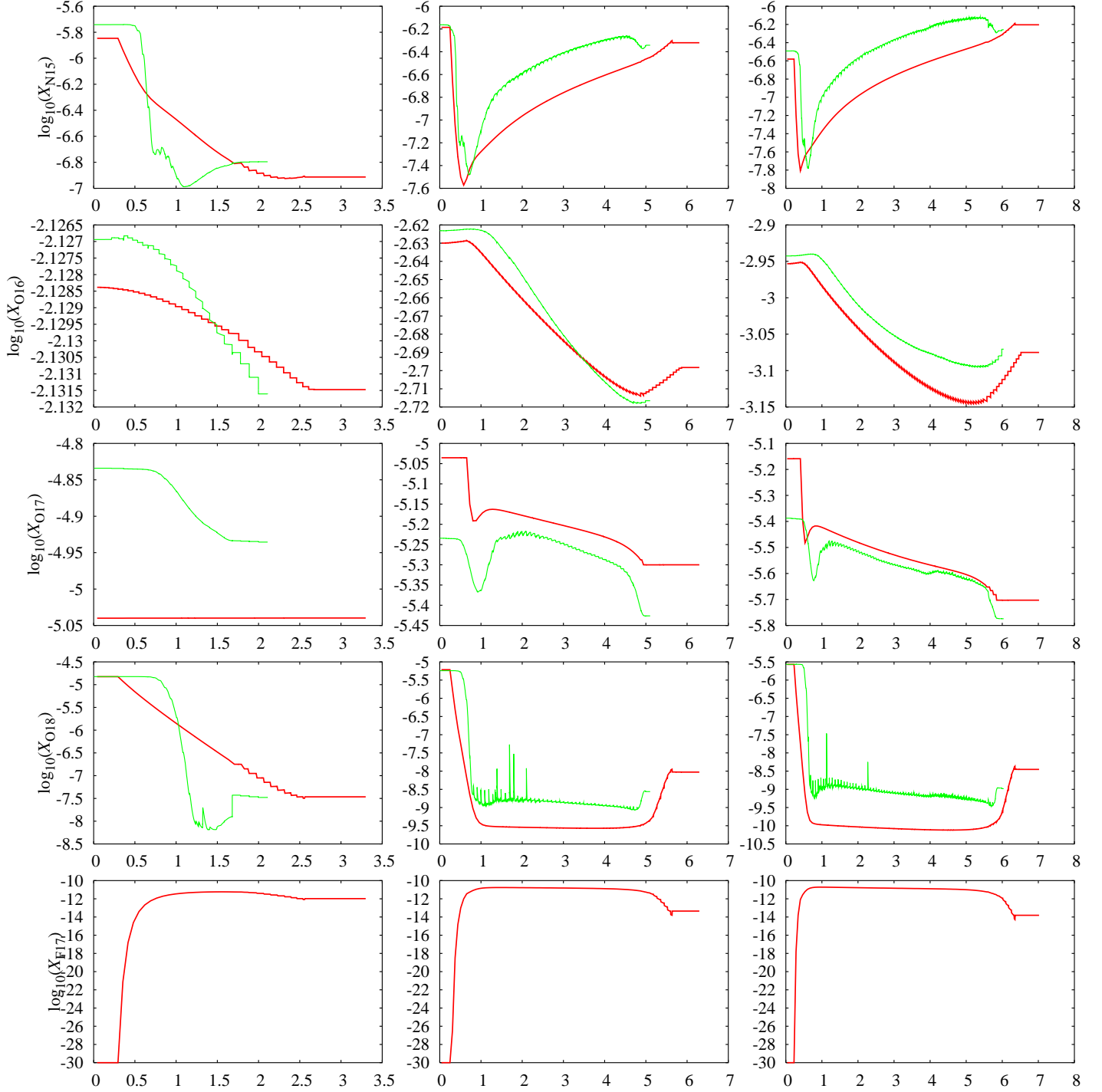
Figure 14: ^{15}N, ^{16}O, ^{17}O, ^{18}O and ^{17}F vs time (in units of 10^5 years) for the synthetic models (red) and the Monash models (green) with $M = 5\,\mathrm{M_\odot}$.

Figure 15: ^{1}H, ^{4}He, ^{12}C, ^{13}C and ^{14}N vs time (in units of 10^5 years) for the synthetic models (red) and the Monash models (green) with $M = 4\,M_\odot$.
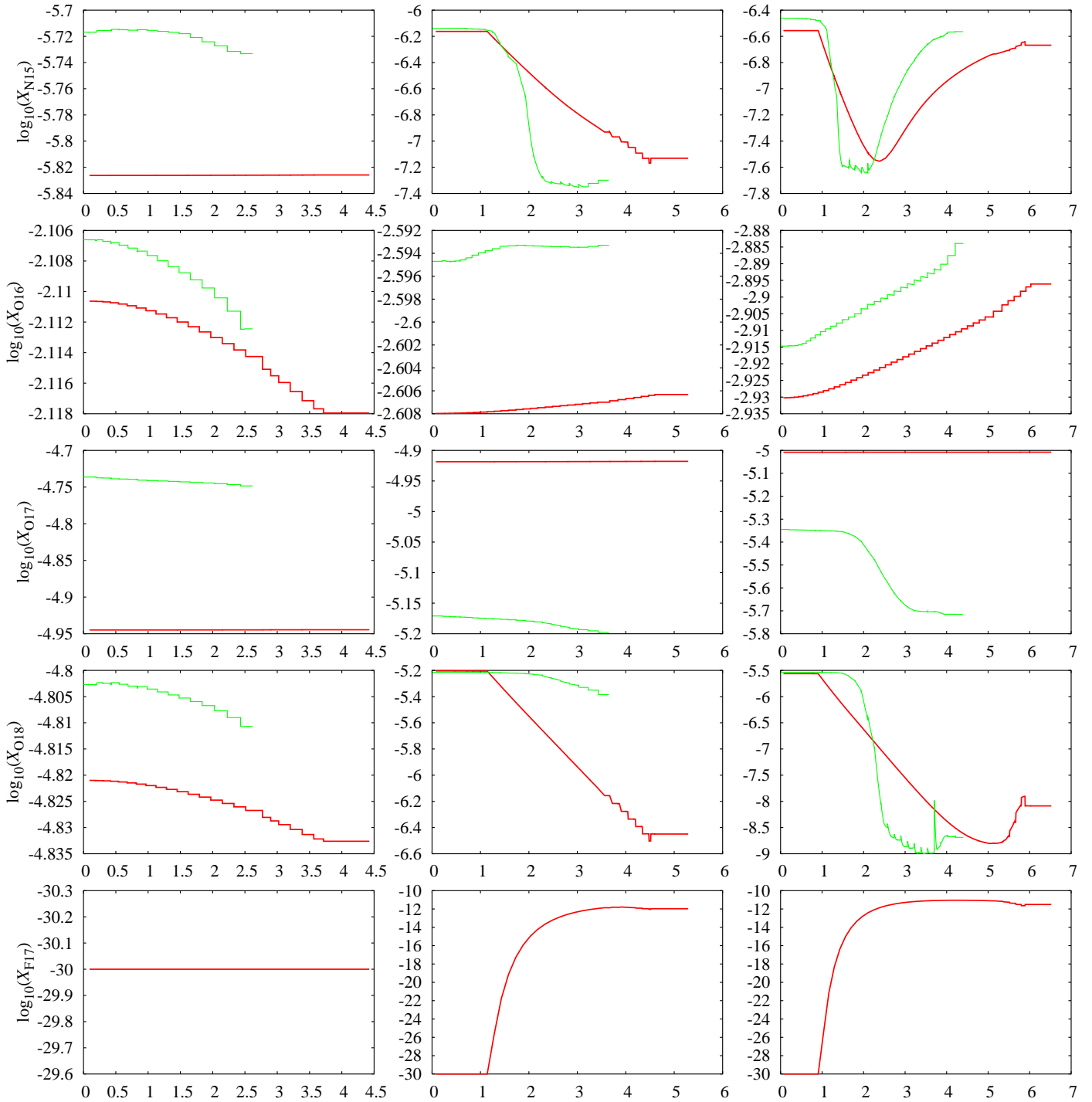
Figure 16: ^{15}N, ^{16}O, ^{17}O, ^{18}O and ^{17}F vs time (in units of 10^5 years) for the synthetic models (red) and the Monash models (green) with $M = 4\,\mathrm{M}_\odot$.

Figure 17: ^{1}H, ^{4}He, ^{12}C, ^{13}C and ^{14}N vs time (in units of 10^5 years) for the synthetic models (red) and the Monash models (green) with $M = 3.5\,M_\odot$.
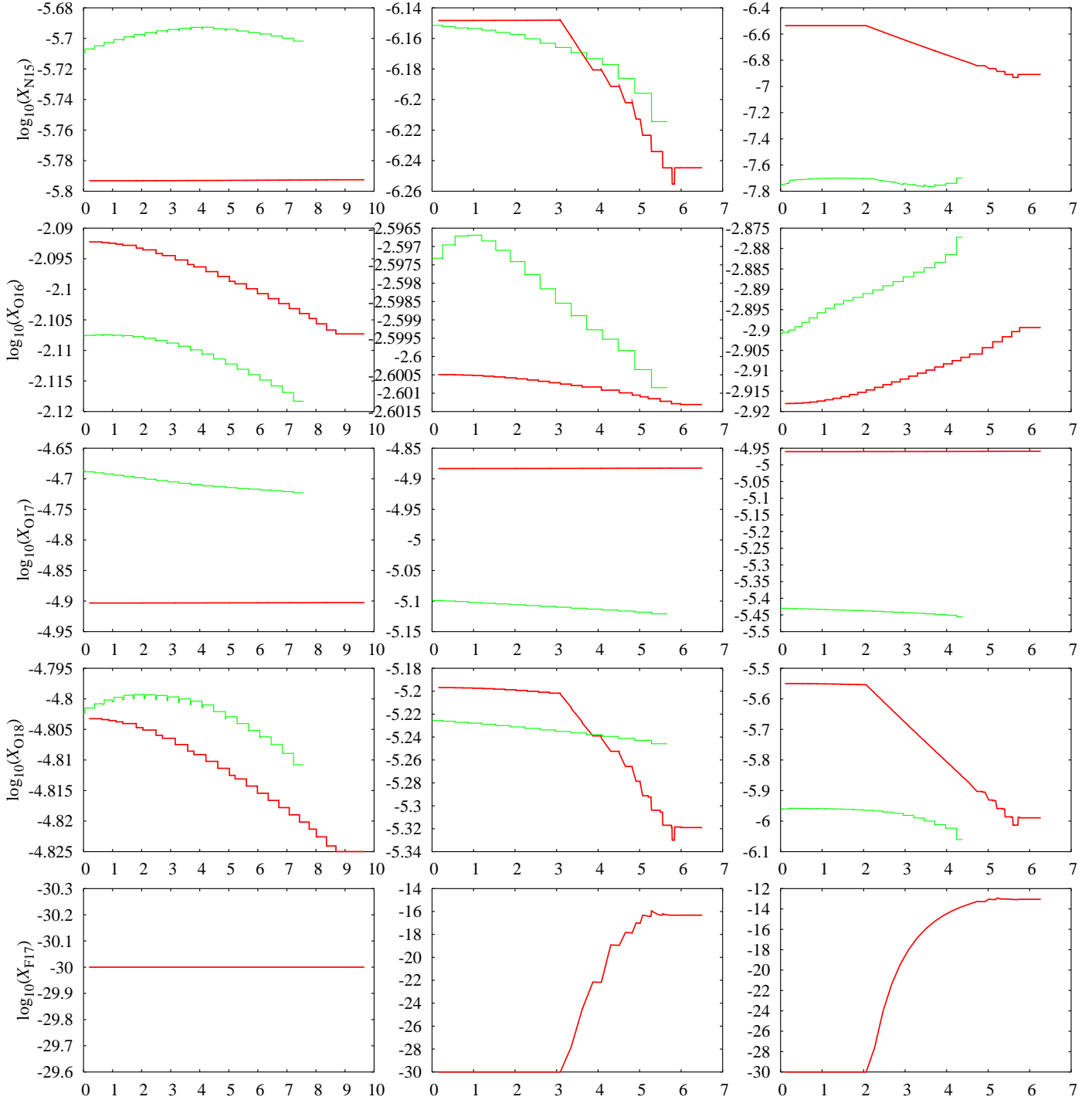
Figure 18: ^{15}N, ^{16}O, ^{17}O, ^{18}O and ^{17}F vs time (in units of 10^5 years) for the synthetic models (red) and the Monash models (green) with $M = 3.5\,\mathrm{M}_\odot$.
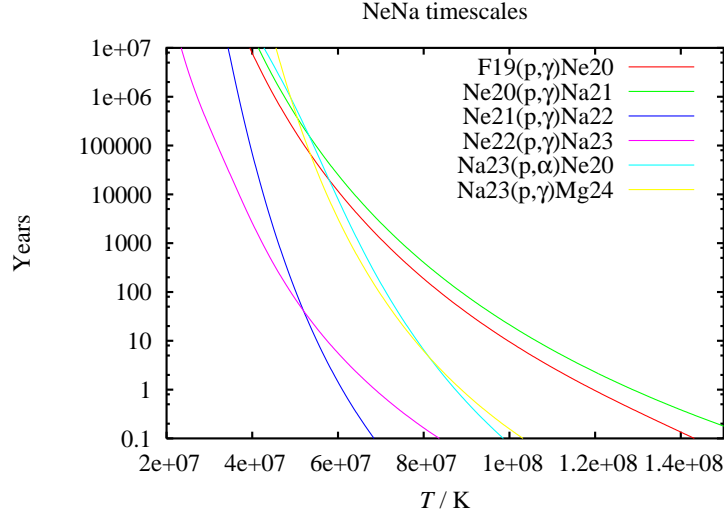
Figure 19: The timescales for the various NeNa reactions as a function of temperature.

$$\frac{d^{22}\text{Ne}}{dt} = \frac{^{21}\text{Ne}}{\tau_{21}} - \frac{^{22}\text{Na}}{\tau_{22}} \tag{77}$$

and

$$\frac{d^{23}\text{Na}}{dt} = \frac{^{22}\text{Ne}}{\tau_{22}} - \frac{^{23}\text{Na}}{\tau_{23}} \tag{78}$$

where the isotopes represent the number densities. These equations can be written in matrix form as

$$\frac{d}{dt}\begin{bmatrix} ^{20}\text{Ne} \\ ^{21}\text{Ne} \\ ^{22}\text{Ne} \\ ^{23}\text{Na} \end{bmatrix} = \begin{bmatrix} -\frac{1}{\tau_{20}} & 0 & 0 & \frac{1}{\tau_{23}} \\ \frac{1}{\tau_{20}} & \frac{1}{-\tau_{21}} & 0 & 0 \\ 0 & \frac{1}{\tau_{21}} & -\frac{1}{\tau_{22}} & 0 \\ 0 & 0 & \frac{1}{\tau_{22}} & -\frac{1}{\tau_{23}} \end{bmatrix} \begin{bmatrix} ^{20}\text{Ne} \\ ^{21}\text{Ne} \\ ^{22}\text{Ne} \\ ^{23}\text{Na} \end{bmatrix} = \frac{d}{dt}\mathbf{U} = [\Lambda]\,\mathbf{U}\,. \tag{79}$$

This is an eigenvalue problem with solutions of the form

$$\mathbf{U}(t) = A_0 e^{\lambda_0 t}\mathbf{U}_0 + \sum_{i=1,2,3} A_i e^{\lambda_i t}\mathbf{U}_i$$

where the eigenvalues are the solutions of

$$
\begin{vmatrix}
-\frac{1}{\tau_{20}} - \lambda & 0 & 0 & \frac{1}{\tau_{23}} \\
\frac{1}{\tau_{20}} & -\frac{1}{\tau_{21}} - \lambda & 0 & 0 \\
0 & \frac{1}{\tau_{21}} & -\frac{1}{\tau_{22}} - \lambda & 0 \\
0 & 0 & \frac{1}{\tau_{22}} & -\frac{1}{\tau_{23}} - \lambda
\end{vmatrix} = 0
\tag{80}
$$

which evaluates to

$$
(\frac{1}{\tau_{20}} + \lambda)(\frac{1}{\tau_{21}} + \lambda)(\frac{1}{\tau_{22}} + \lambda)(\frac{1}{\tau_{23}} + \lambda) - \frac{1}{\tau_{20}\tau_{21}\tau_{22}\tau_{23}} = 0 \,.
\tag{81}
$$

With $\alpha = 1/\tau_{20}$, $\beta = 1/\tau_{21}$, $\gamma = 1/\tau_{22}$ and $\delta = 1/\tau_{23}$ this can be simplified to

$$
(\alpha + \lambda)(\beta + \lambda)(\gamma + \lambda)(\delta + \lambda) = \alpha\beta\gamma\delta
\tag{82}
$$

i.e.

$$
\lambda(\lambda^3 + a\lambda^2 + b\lambda + c) = 0
\tag{83}
$$

where

$$
a = \alpha + \beta + \gamma + \delta \,,
\tag{84}
$$

$$
b = \gamma\delta + \alpha\delta + \beta\delta + \alpha\gamma + \beta\gamma + \alpha\beta
\tag{85}
$$

and

$$
c = \alpha\gamma\delta + \beta\gamma\delta + \alpha\beta\delta + \alpha\beta\gamma \,.
\tag{86}
$$

The first eigenvalue is the trivial solution $\lambda_0 = 0$. The eigenvector $\mathbf{U}_0$ is calculated from the set of equations

$$\begin{bmatrix} -\frac{1}{\tau_{20}} & 0 & 0 & \frac{1}{\tau_{23}} \\ \frac{1}{\tau_{20}} & -\frac{1}{\tau_{21}} & 0 & 0 \\ 0 & \frac{1}{\tau_{21}} & -\frac{1}{\tau_{22}} & 0 \\ 0 & 0 & \frac{1}{\tau_{22}} & -\frac{1}{\tau_{23}} \end{bmatrix} \mathbf{U}_0 = [\Lambda]\,\mathbf{U}_0 = 0 \tag{87}$$

which has the solution

$$\mathbf{U}_0 = \frac{1}{\tau_{20} + \tau_{21} + \tau_{22} + \tau_{23}} \begin{bmatrix} \tau_{20} \\ \tau_{21} \\ \tau_{22} \\ \tau_{23} \end{bmatrix}. \tag{88}$$

This can be rewritten by noting that

$$[\Lambda]\,\mathbf{U}_0 = \frac{d}{dt}\mathbf{U}_0 = 0 \tag{89}$$

so all the time derivatives are zero. This leads to the following equilibrium solution

$$\frac{^{20}\mathrm{Ne}}{\tau_{20}} = \frac{^{23}\mathrm{Na}}{\tau_{23}}, \tag{90}$$

$$\frac{^{20}\mathrm{Ne}}{\tau_{20}} = \frac{^{21}\mathrm{Na}}{\tau_{21}}, \tag{91}$$

$$\frac{^{21}\mathrm{Ne}}{\tau_{21}} = \frac{^{22}\mathrm{Na}}{\tau_{22}} \tag{92}$$

and

$$\frac{^{22}\mathrm{Ne}}{\tau_{22}} = \frac{^{23}\mathrm{Na}}{\tau_{23}}. \tag{93}$$

Substitution into $\mathbf{U}_0$ gives

$$\mathbf{U}_0 = \frac{1}{N_{\text{NeNa}}} \begin{bmatrix} {}^{20}\text{Ne}_e \\ {}^{21}\text{Ne}_e \\ {}^{22}\text{Ne}_e \\ {}^{23}\text{Na}_e \end{bmatrix} = \frac{\mathbf{U}_e}{N_{\text{NeNa}}} \tag{94}$$

where the subscript e refers to equilibrium and

$$N_{\text{NeNa}} = {}^{20}\text{Ne} + {}^{21}\text{Ne} + {}^{22}\text{Ne} + {}^{23}\text{Na} \tag{95}$$

is the total (conserved) number density of NeNa cycle isotopes.

It now remains to identify the other eigenvalues λ_1, λ_2 and λ_3. These are solutions of the cubic equation

$$\lambda^3 + a\lambda^2 + b\lambda + c = 0 \,, \tag{96}$$

which can be calculated using the cubic formula. All three roots are usually real and in the case where they are complex NeNa cycling is skipped for a timestep[5]. Given λ_1, λ_2 and λ_3 from above, substitution into the eigenvalue equation gives

$$\begin{bmatrix} -\frac{1}{\tau_{20}} & 0 & 0 & \frac{1}{\tau_{23}} \\ \frac{1}{\tau_{20}} & \frac{1}{-\tau_{21}} & 0 & 0 \\ 0 & \frac{1}{\tau_{21}} & -\frac{1}{\tau_{22}} & 0 \\ 0 & 0 & \frac{1}{\tau_{22}} & -\frac{1}{\tau_{23}} \end{bmatrix} \mathbf{U}_i = [\Lambda]\, \mathbf{U}_i = \lambda_i \mathbf{U}_i \,. \tag{97}$$

The solution is

---

[5]This situation is rare but can occur at low metallicity and high mass – the reasons for the failure seem to be numerical.

$$
\mathbf{U}_i = \begin{bmatrix} \tau_{20}(\lambda_i + \frac{1}{\tau_{21}}) \\ 1 \\ \frac{1}{\tau_{21}(\lambda_i + \frac{1}{\tau_{22}})} \\ \tau_{20}\tau_{23}(\lambda_i + \frac{1}{\tau_{21}})(\lambda_i + \frac{1}{\tau_{20}}) \end{bmatrix} \tag{98}
$$

and the NeNa abundances as a function of time are calculated from

$$
\mathbf{U}(t) = \mathbf{U}_e + \sum_{i=1,2,3} A_i e^{\lambda_i t} \mathbf{U}_i \tag{99}
$$

where the gory details of the solution for A_i are in Appendix A1.

There are three reactions which can destroy ^{19}F: ^{19}F$(p,\gamma)^{20}$Ne, ^{19}F$(p,\alpha)^{16}$O and ^{19}F$(p,n)^{19}$Ne. At $T_9 = 0.08$ they have reaction rates of $2.28{\times}10^{-10}$, $8.13{\times}10^{-7}$ and less than $10^{-22}\,\mathrm{cm^3\,mol^{-1}\,s^{-1}}$ respectively (Angulo et al., 1999) so only the ^{19}F$(p,\alpha)^{16}$O reaction is necessary. The change in ^{19}F is calculated from

$$
^{19}\mathrm{F} \to e^{-t/\tau_{19\alpha}}\,^{19}\mathrm{F}\,. \tag{100}
$$

The corresponding change in ^{16}O is neglected because the ^{16}O abundance is about 10^{-2} while the ^{19}F abundance is less than 10^{-7} so even if all the ^{19}F is converted to ^{16}O the effect is small.

Figures 20 to 23 show the synthetic model with and without NeNa cycling compared to the Monash models. Note that when the red lines are invisible they are hiding under the green lines. The qualitative and in some cases the quantitative agreement is good. ^{20}Ne is an exception. The reaction ^{23}Na$(p,\alpha)^{20}$Ne is extremely sensitive to temperature in the HBB regime, while ^{20}Ne$(p,\gamma)^{21}$Na$(\beta^+)^{21}$Ne is not. The difference in timescales leads to numerical errors which are as great as the change in ^{20}Ne seen in the detailed models owing to HBB or DUP. As is usual with numerical errors the effect is quite random hence the fluctuations in the ^{20}Ne yield as a function of mass. Also, as the temperature rises and the ^{23}Na$(p,\alpha)^{20}$Ne timescale becomes small it is comparable with the convective turnover time

so the assumptions of the synthetic HBB model – thin shell, constant temperature and density – are no longer valid and accurate synthetic burning proves difficult (in a similar manner to Li and Be). Still, most ^{20}Ne is thought to come from high-mass stars and their associated supernovae with only a small contribution from AGB stars so the worry is not warranted. The abundance of ^{22}Na is also poorly matched, but given the short timescale for decay of this isotope and its similarity to the convective turnover time again it is difficult to do any better.

Despite these small problems the temporal behaviours of ^{19}F, ^{21}Ne, ^{22}Ne and ^{23}Na are significantly improved with respect to the no-NeNa case and the equilibrium value for ^{22}Na is a reasonable assumption.

2.10 Rapid MgAl burning

The MgAl cycle is given by

$$
\begin{array}{ccccccc}
 & & ^{25}\mathrm{Mg} & \xrightarrow{(p,\gamma)} & ^{26}\mathrm{Al} & \xrightarrow{(p,\gamma)} & ^{27}\mathrm{Si} \\[4pt]
 & & (\beta^+)\uparrow & & \downarrow(\beta^+) & (\beta^+)\diagdown & \\
 & & ^{25}\mathrm{Al} & & ^{26}\mathrm{Mg} & \diagdown & \\[4pt]
 & & (p,\gamma)\uparrow & & \downarrow(p,\gamma) & & \\
^{23}\mathrm{Na} & \xrightarrow{(p,\gamma)} & ^{24}\mathrm{Mg} & \xleftarrow{(p,\alpha)} & ^{27}\mathrm{Al} & \xrightarrow{(p,\gamma)} & ^{28}\mathrm{Si}
\end{array}
$$

with the appropriate timescales shown in figure 24.

Assumptions are required to proceed:

- Entry into the MgAl cycle via ^{23}Na is neglected for simplicity. This works well even though the $^{23}\mathrm{Na}(p,\gamma)^{24}$Mg and $^{23}\mathrm{Na}(p,\alpha)^{20}$Ne cross sections are similar.

- The cycle is terminated at ^{27}Al because the timescale for conversion of ^{27}Al to ^{24}Mg or ^{28}Si is long compared to the burning time. This is justified when looking at the Monash models because the ^{28}Si abundance hardly changes.

Figure 20: ^{19}F, ^{20}Ne, ^{21}Ne, ^{22}Ne, ^{22}Na and ^{23}Na vs time (in units of 10^5 years) for the synthetic models with NeNa cycling (red), synthetic models without NeNa cycling (green) and the Monash models (blue) $M = 6\,M_\odot$. Note that when the red lines are invisible they are hiding under the green lines.
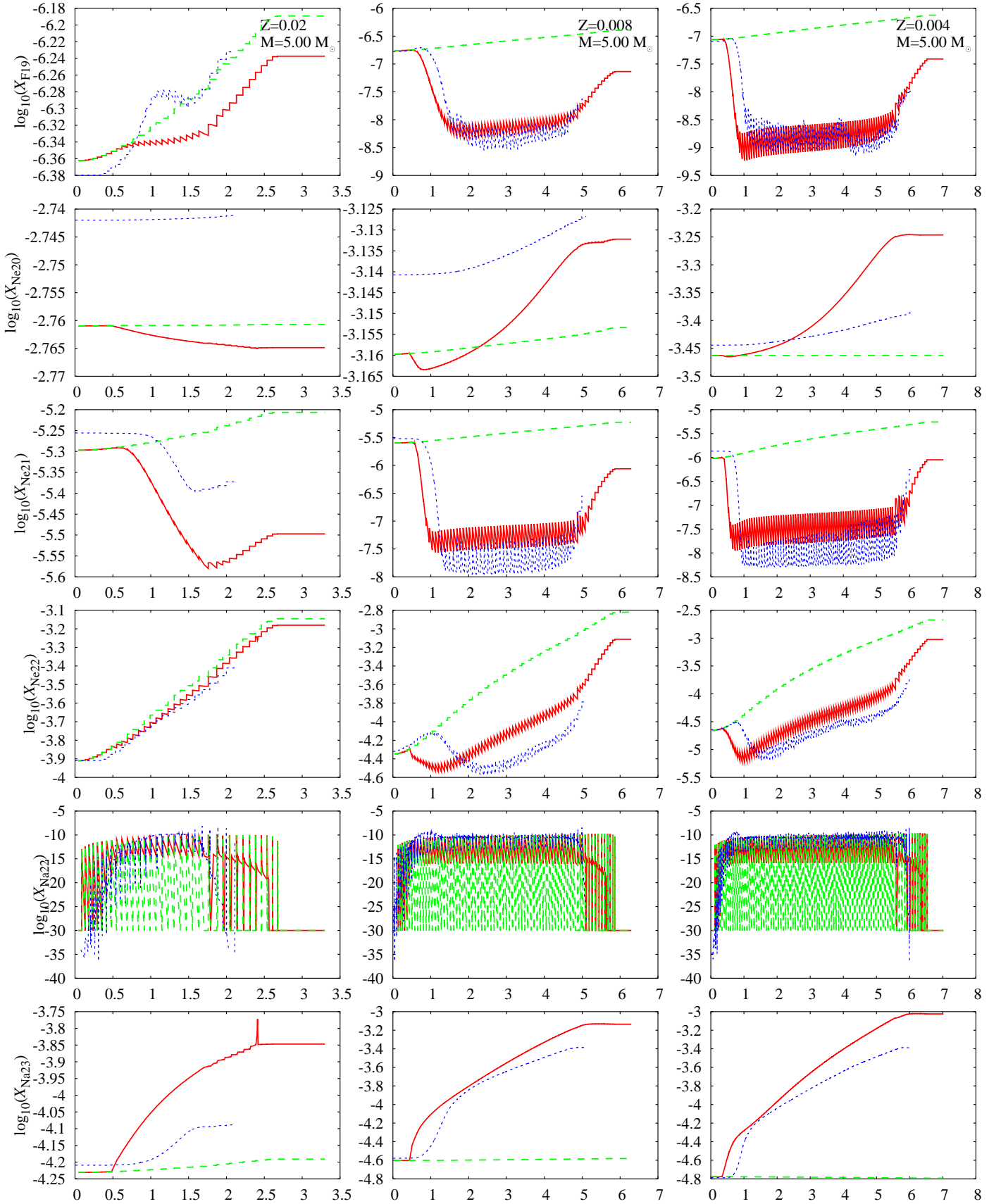
Figure 21: ^{19}F, ^{20}Ne, ^{21}Ne, ^{22}Ne, ^{22}Na and ^{23}Na vs time (in units of 10^5 years) for the synthetic models with NeNa cycling (red), synthetic models without NeNa cycling (green) and the Monash models (blue) $M = 5\,M_\odot$. Note that when the red lines are invisible they are hiding under the green lines.
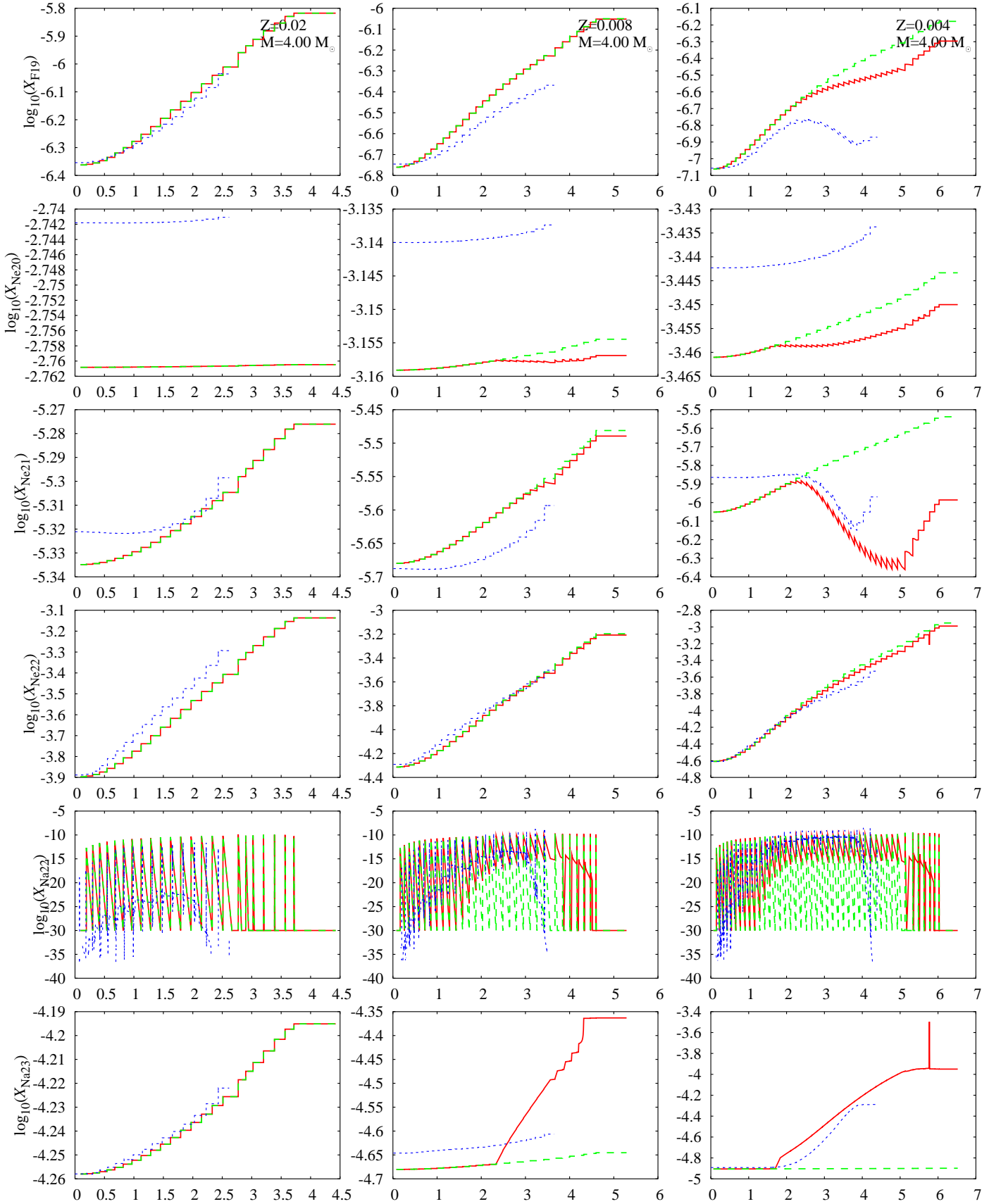
Figure 22: ^{19}F, ^{20}Ne, ^{21}Ne, ^{22}Ne, ^{22}Na and ^{23}Na vs time (in units of 10^5 years) for the synthetic models with NeNa cycling (red), synthetic models without NeNa cycling (green) and the Monash models (blue) $M = 4\,M_\odot$. Note that when the red lines are invisible they are hiding under the green lines.
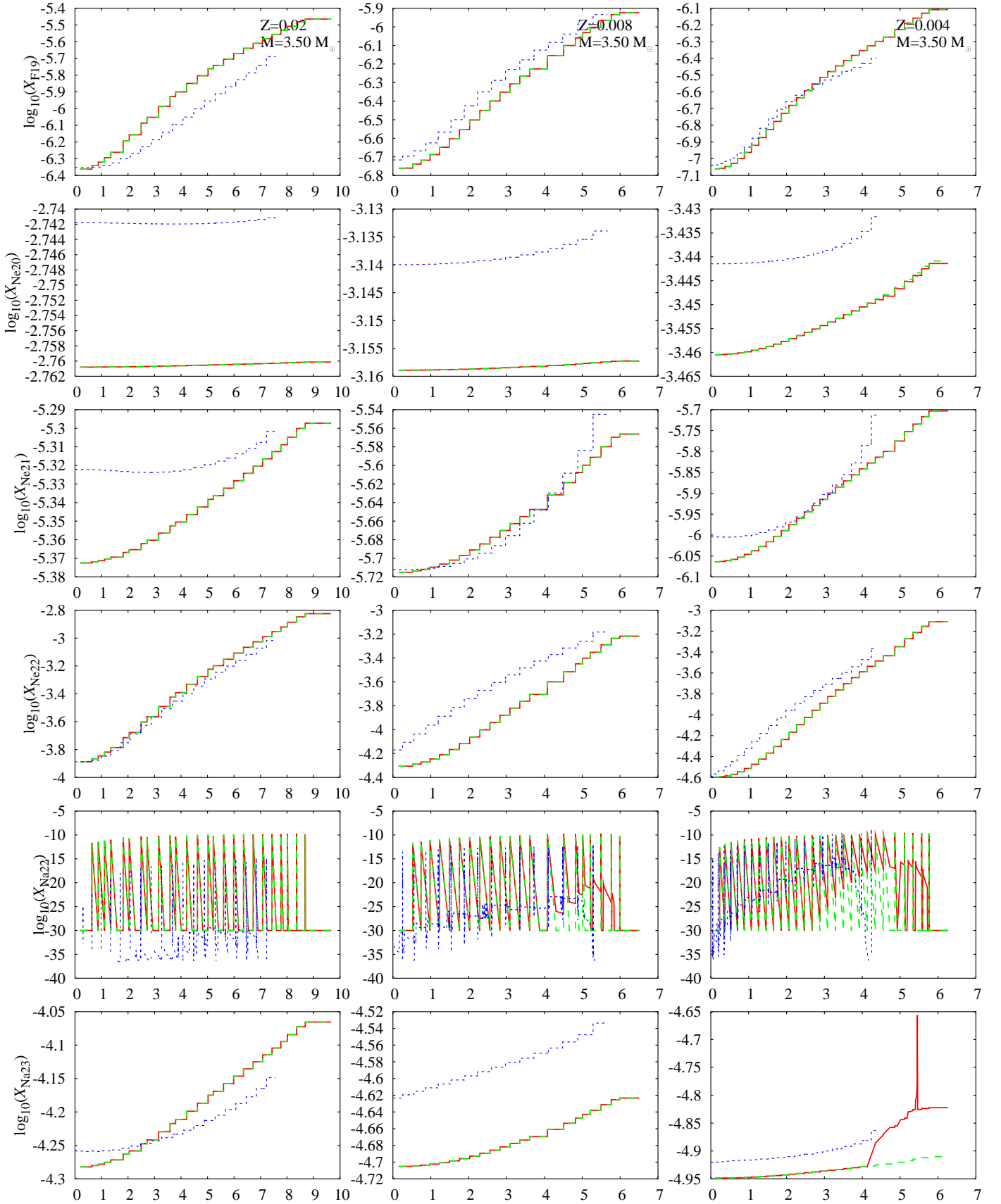
Figure 23: ^{19}F, ^{20}Ne, ^{21}Ne, ^{22}Ne, ^{22}Na and ^{23}Na vs time (in units of 10^5 years) for the synthetic models with NeNa cycling (red), synthetic models without NeNa cycling (green) and the Monash models (blue) $M = 3.5\,M_\odot$. Note that when the red lines are invisible they are hiding under the green lines.
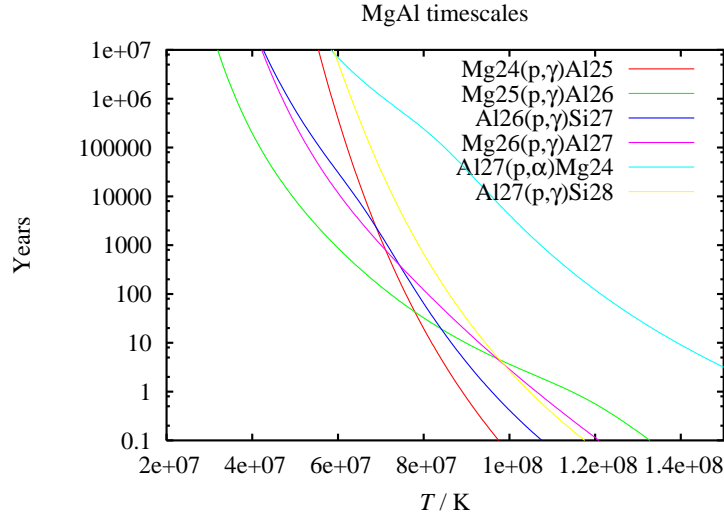
Figure 24: The timescales for the various MgAl reactions as a function of temperature.

- The beta-decays of ^{25}Al and ^{27}Si are quick enough to be considered instantaneous ($\tau = 10\,\mathrm{s}$ and $6\,\mathrm{s}$ respectively).

- The decay of ^{26}Al, with a timescale of about $7 \times 10^5\,\mathrm{yrs}$, must be included in the chain.

The differential equation set to be solved is then

$$\frac{d^{24}\mathrm{Mg}}{dt} = -\frac{^{24}\mathrm{Mg}}{\tau_{24}}\,, \tag{101}$$

$$\frac{d^{25}\mathrm{Mg}}{dt} = -\frac{^{25}\mathrm{Mg}}{\tau_{25}} + \frac{^{24}\mathrm{Mg}}{\tau_{24}}\,, \tag{102}$$

$$\frac{d^{26}\mathrm{Al}}{dt} = \frac{^{25}\mathrm{Mg}}{\tau_{25}} - \frac{^{26}\mathrm{Al}}{\tau_{\beta 26}} - \frac{^{26}\mathrm{Al}}{\tau_{26'}} = \frac{^{25}\mathrm{Mg}}{\tau_{25}} - \frac{^{26}\mathrm{Al}}{\tau_{26}'}\,, \tag{103}$$

where $\tau_{26'}^{-1} + \tau_{\beta 26}^{-1} = \tau_{26}'^{-1}$,

$$\frac{d^{26}\mathrm{Mg}}{dt} = \frac{^{26}\mathrm{Al}}{\tau_{\beta 26}} - \frac{^{26}\mathrm{Mg}}{\tau_{26}} \tag{104}$$

and

$$\frac{d^{27}\text{Al}}{dt} = \frac{^{26}\text{Mg}}{\tau_{26}} + \frac{^{26}\text{Al}}{\tau_{26'}} > 0 \tag{105}$$

where the isotopes represent number densities. The equations are each solved in turn leading to a horrendous mess of algebra. Fortunately computers do not care about such things. The method of solution is in appendix A2.

Figures 25 to 28 compare the synthetic model with and without the MgAl cycle and the Monash models. Again, when there is little burning the green lines hide the red lines. The agreement is good for most stars although again the temperature sensitivity of the cycle is evident with the $M = 6\,\text{M}_\odot$, $Z = 0.008$ star over-burning ^{24}Mg to ^{25}Mg. This does not affect the yield of a population too much because the agreement at $Z = 0.02$, $Z = 0.004$ and $M = 5\,\text{M}_\odot$ is excellent. The radioactive nucleus ^{26}Al is followed accurately and the change in ^{28}Si is negligible. This justifies the use of ^{27}Al as the terminal link in the MgAl chain.

2.11 The S-Process

The production of elements beyond iron is possible by slow neutron capture, known as the s-process. The stellar conditions responsible for this are thought to occur in the intershell region of AGB stars, where the reactions $^{13}\text{C}(\alpha, n)^{16}\text{O}$ and $^{22}\text{Ne}(\alpha, n)^{25}\text{Mg}$ provide the neutrons. The ^{13}C reaction activates at temperatures of $9 \times 10^7\,\text{K}$ but the ^{22}Ne reaction requires $T > 3 \times 10^8\,\text{K}$ which occurs only in the most massive AGB stars. For the ^{13}C source to be activated protons must be mixed from the convective envelope into the hydrogen-free intershell region. The physics of this process is still highly uncertain with suggestions that semi-convective diffusion due to carbon recombination (Iben & Renzini, 1982), gravity wave mixing (Denissenkov & Tout, 2003), convective overshooting (Herwig & Langer, 2001) or stellar rotation (Herwig, Langer & Lugaro, 2003) may be important. For the purposes of the synthetic model the details of convection zones, neutron poisons, mixing with s-process material from previous pulses and the details of the neutron source are quietly
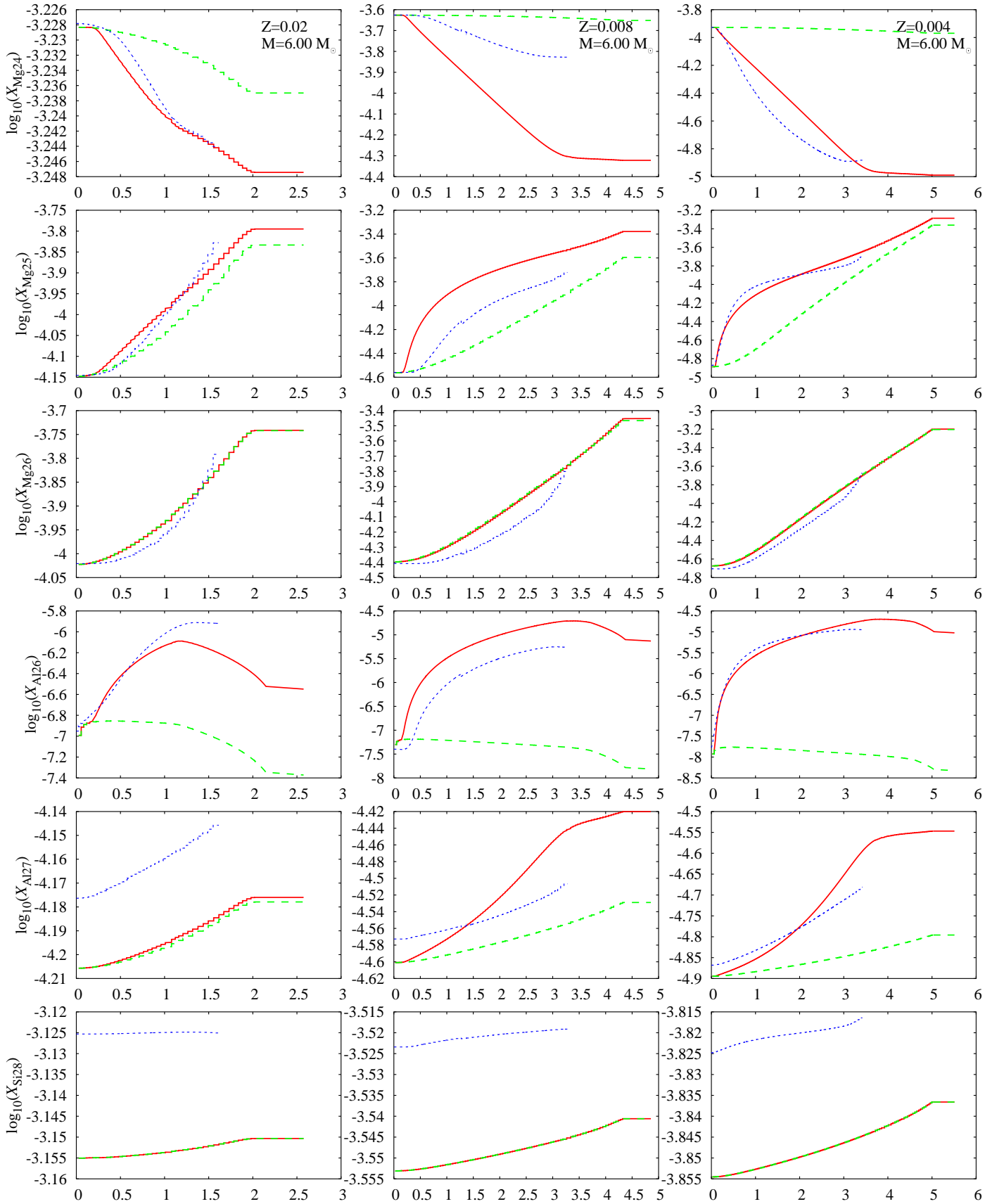
Figure 25: ^{24}Mg, ^{25}Mg, ^{26}Mg, ^{26}Al, ^{27}Al and ^{28}Si vs time for the synthetic models with MgAl chain (red), synthetic models without MgAl chain (green) and the Monash models (blue) $M = 6\,M_\odot$.
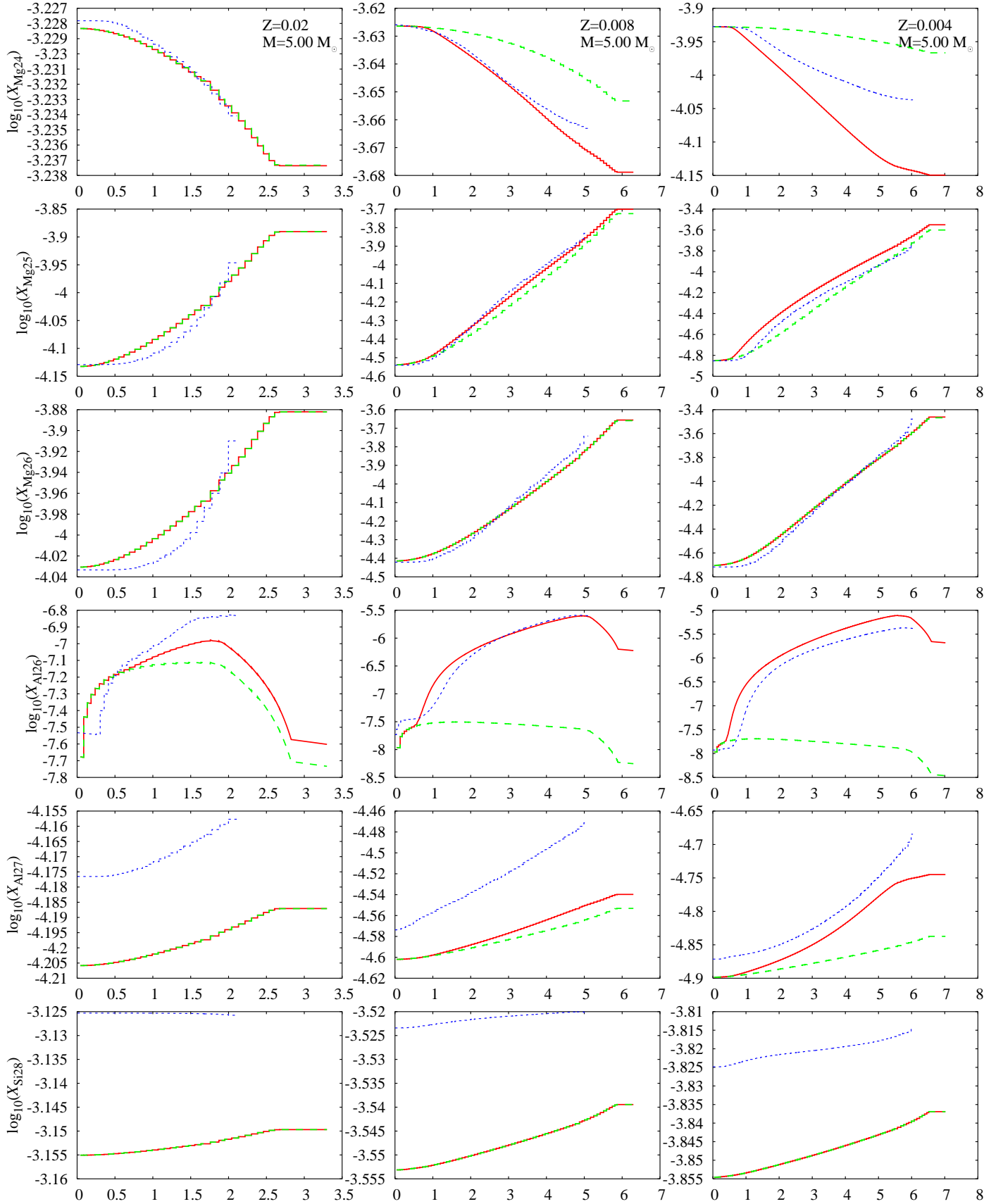
Figure 26: ^{24}Mg, ^{25}Mg, ^{26}Mg, ^{26}Al, ^{27}Al and ^{28}Si vs time for the synthetic models with MgAl chain (red), synthetic models without MgAl chain (green) and the Monash models (blue) $M = 5\,M_\odot$.
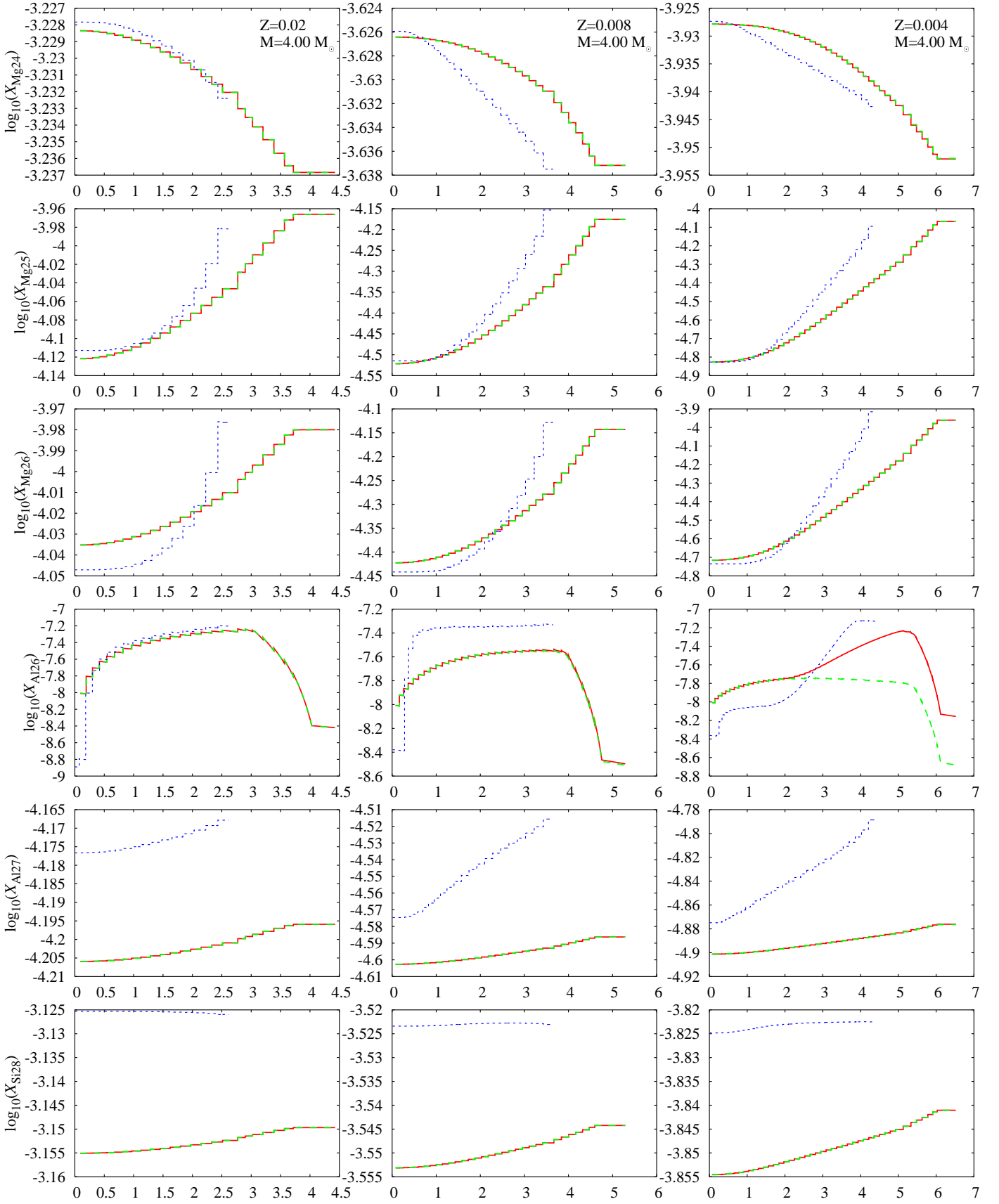
Figure 27: ^{24}Mg, ^{25}Mg, ^{26}Mg, ^{26}Al, ^{27}Al and ^{28}Si vs time (in units of 10^5 years) for the synthetic models with MgAl chain (red), synthetic models without MgAl chain (green) and the Monash models (blue) $M = 4\,M_\odot$.
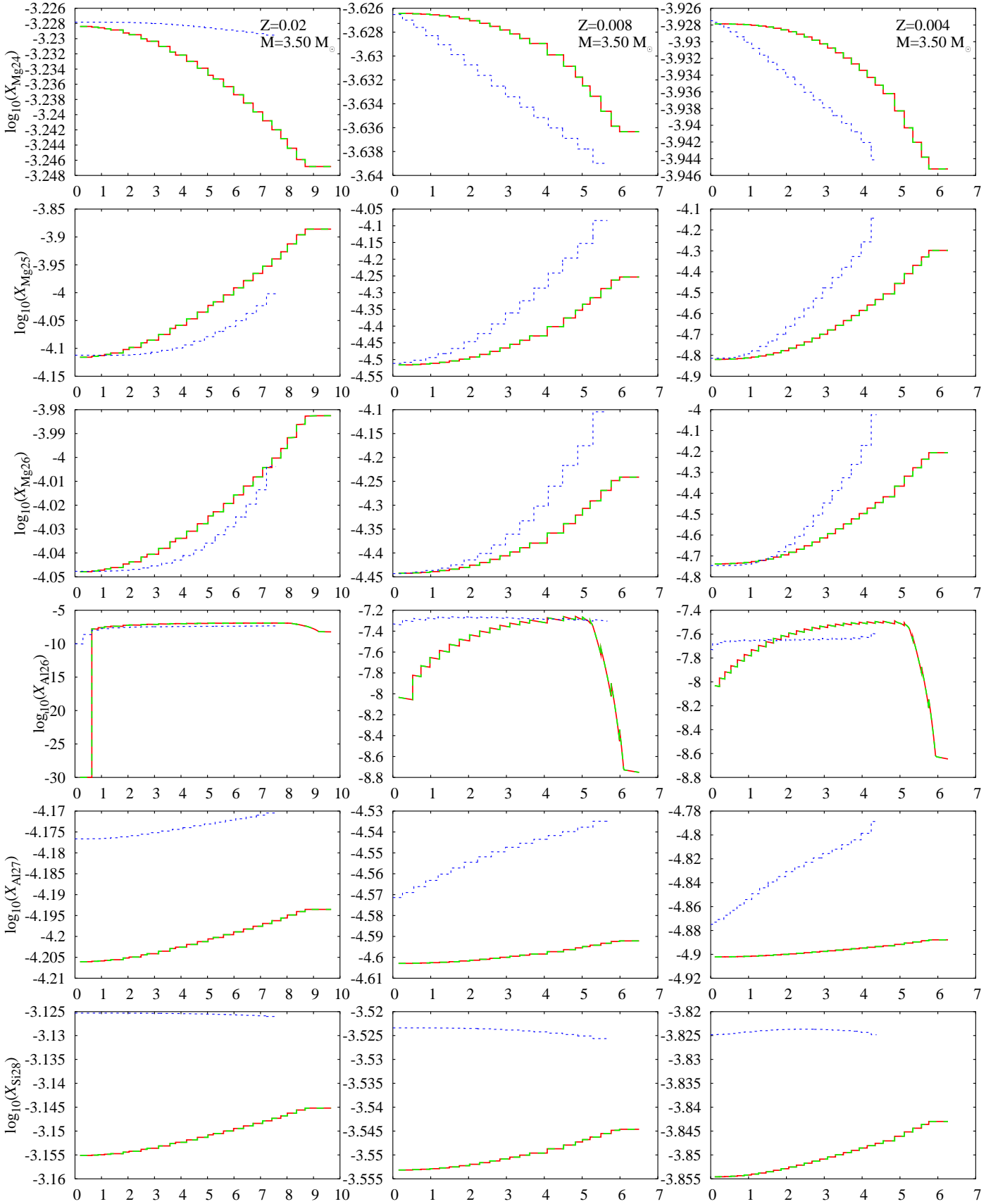
Figure 28: ^{24}Mg, ^{25}Mg, ^{26}Mg, ^{26}Al, ^{27}Al and ^{28}Si vs time (in units of 10^5 years) for the synthetic models with MgAl chain (red), synthetic models without MgAl chain (green) and the Monash models (blue) $M = 3.5\,M_\odot$.

swept under the proverbial carpet and only the composition of the *s*-process nuclei in the material dredged-up is considered. It is assumed that a ^{13}C pocket does exist and its mass (and hence the *s*-process neutron exposure) is treated as a free parameter together with stellar mass and metallicity. The models used are taken from Gallino et al. (1998) and Lugaro (private communication). Given the present uncertainties in *s*-process modelling only elemental abundances are fitted, the isotopic distributions are not reliable enough to be worth fitting.

Fortunately, the *s*-process abundances of the dredged-up material are quite simple to fit once the fits for a few key elements are established. The heavy elements Ce, Dy, Er, Eu, Gd, Hf, Hg, Lu, Nd, Os, Pr, Re, Sb, Sm, Sn, Ta, Tb, Te, Tl, W, Xe and Yb are fitted to Ba. The light elements Ag, Cd, In, Mo, Pd, Ru, Sr, Tc and Zr are fitted to Y. Rb and Kr form a separate grouping as do Bi and Pb which are the heaviest elements formed by the *s*-process. The models have masses $M = 1.5$, 3 and $5\,\mathrm{M}_\odot$ and data are taken from pulse numbers 14, 21 and 28 respectively, where the pulse is chosen to be representative of the asymptotic regime. A model of each star exists for $Z = 0.02$, 0.006, 0.002, 5×10^{-4} and 10^{-4}. The ^{13}C pocket has mass $9.3 \times 10^{-4}\,\mathrm{M}_\odot$ and is assumed to contain no ^{14}N. The ^{13}C efficiency ξ is proportional to the abundance $X_{\mathrm{C13}}^{\mathrm{p}}$ of ^{13}C in the pocket

$$\xi = X_{\mathrm{C13}}^{\mathrm{p}}/0.00382\,. \tag{106}$$

The fits for intershell Y, Ba, Kr and Pb as functions of M_{i}, Z and ξ are

$$10^5 X_{\mathrm{Y}}^{\mathrm{i}} = (a_{107}\frac{\chi^{b_{107}} + 0.1}{(\chi + c_{107})^{d_{107}} + e_{107}} - f_{107})(g_{107}\xi^2 + h_{107}\xi + i_{107}) + j_{107}M_{\mathrm{i}}^4\,, \tag{107}$$

$$10^5 X_{\mathrm{Ba}}^{\mathrm{i}} = 10^{a_{108} + \left[\frac{b_{108}\chi^{1.5} + c_{108}}{(\chi + d_{108})^3 + e_{108}}\right]} \times f_{108}(Z) \times g_{108}(\xi) + h_{108}M_{\mathrm{i}}^{4.5}\,, \tag{108}$$

$$\begin{aligned}\log_{10} \mathrm{Pb} \quad = \quad & a_{109}\chi^{b_{109}} + c_{109}\xi + d_{109}\xi^2 + e_{109}Z + f_{109} + g_{109}M_\mathrm{i} + \\ & h_{109}(\log_{10}\xi + i_{109}) \times (\log_{10}\xi + j_{109}) \times (\log_{10}\xi + k_{109}) \end{aligned} \qquad (109)$$

then

$$10^8 X_{\mathrm{Pb}}^\mathrm{i} = \mathrm{Pb} \times 10^{\max[0,(a_{110}+b_{110}M_\mathrm{i})\times(2-\log_{10}\mathrm{Pb})]} \qquad (110)$$

and

$$\log_{10} 10^8 X_{\mathrm{Kr}}^\mathrm{i} = a_{111} + b_{111}M_\mathrm{i} + c_{111}M_\mathrm{i}^2 + d_{111}\log_{10}(10^3 Z) + e_{111}\left[\log_{10}(10^3 Z)\right]^2 + f_{111}\xi + g_{111}\xi^2 \qquad (111)$$

where $\chi = 10^3 Z/\xi$. The remaining elements A are then fitted using a log-log fit

$$\log_{10} A = a_{112} \log_{10} B + b_{112} \qquad (112)$$

where B is one of Y, Ba, Pb or Kr. The fits are given in appendix B6 and comparison of the fits to the FRANEC results are shown in fig. 29.

2.12 Radioactive Decay

Some isotopes produced in the above nuclear burning algorithms are radioactively unstable, notably $^{22}\mathrm{Na}$, $^{26}\mathrm{Al}$ and Tc. These are exponentially decayed at the end of each timestep according to eq. (58) with $\boldsymbol{\alpha} = \exp(-\delta t/\tau_\mathrm{r})$ where τ_r is the radioactive lifetime and δt the timestep. Lifetimes are taken from the compilation of Tuli (2000).

2.13 Low- and Intermediate-Mass Stellar Remnants

The remnants of single low- and intermediate-mass stellar evolution are white dwarfs. These come in three flavours which are modelled as follows.
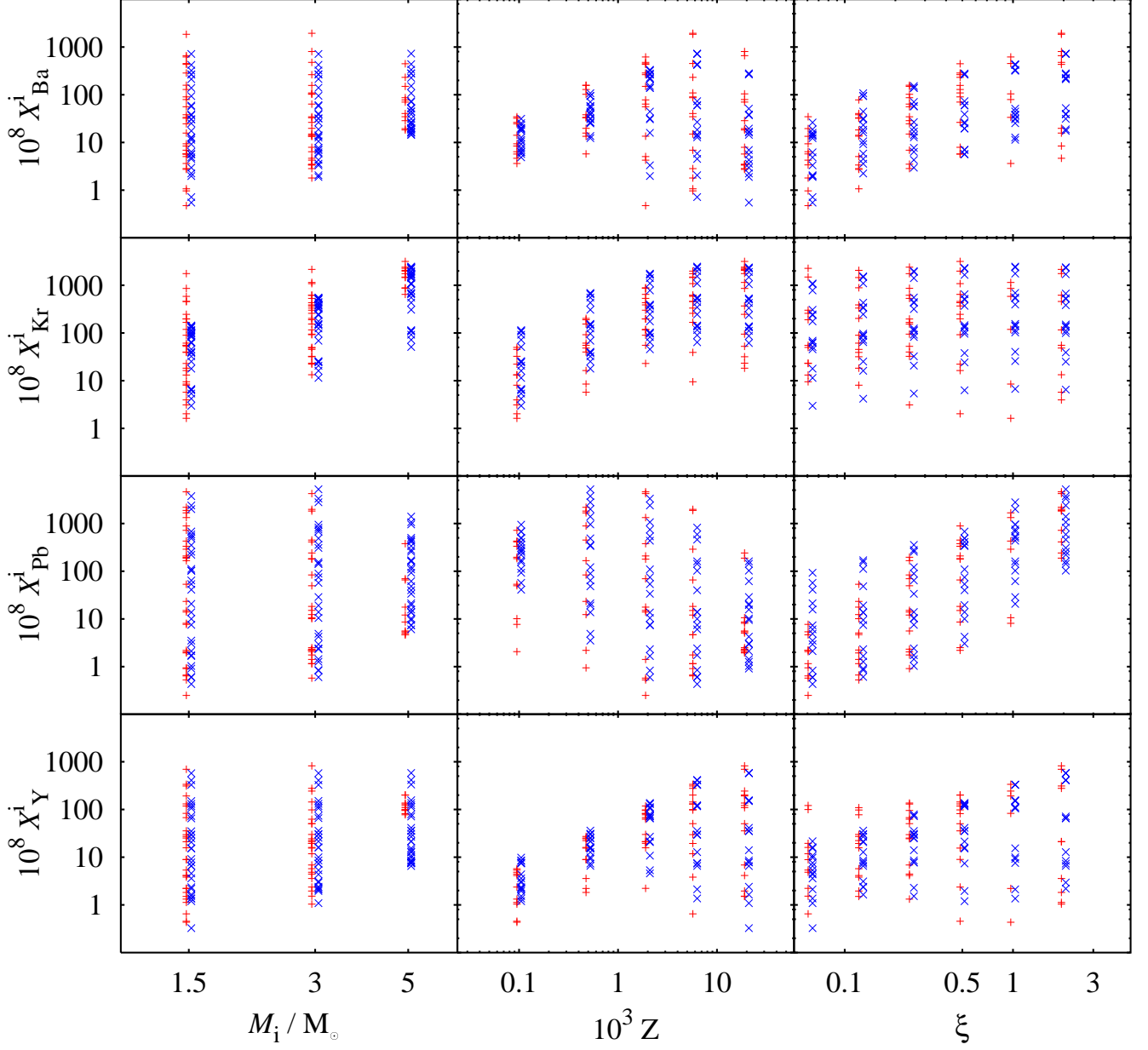
Figure 29: S-process fits (blue) vs FRANEC model data (red) for the key elements Ba, Kr, Pb and Y. The red points have been displaced slightly to the left to be visible. These are projections on M, Z and ξ.

- Helium white dwarfs (HeWDs) are the cores of giant branch stars which have lost their envelopes. All hydrogen is converted to helium so the mass fraction of helium is $1 - Z$. Helium white dwarfs are more likely to occur as a result of binary evolution.

- Carbon-oxygen white dwarfs (COWDs) are formed by helium burning. These are assumed to be, apart from metals heavier than ^{19}F which remain unchanged, 80% ^{12}C and 20% ^{16}O. The hydrogen, helium, other CNO isotopes and fluorine are set to zero abundance.

- Oxygen-neon white dwarfs (ONeWDs) form from the most massive AGB cores. The temperature in these cores is high enough that carbon ignites in semi-degenerate conditions (Pols et al., 1998). These are modelled as 80% ^{16}O and 20% ^{20}Ne, while everything heavier is unchanged and the hydrogen, helium, CNO and fluorine are zero. By definition of an intermediate-mass star these stars do not exceed a mass of M_{Ch} – if they did a supernova would occur owing to electron capture on ^{24}Mg.

No attempt is made to include detailed WD evolution or abundances in this model. This is because WDs are not directly important for nucleosynthesis, except type Ia supernovae and novae. The yields for these explosions are fitted to the results of detailed models so, while the fitted yields depend on whether the progenitor is a He-, CO- or ONe-WD, they do not depend on the stellar abundances. It is also difficult to remove matter from the surface of a WD in any other way. They are not considered to have a wind and even if they did it is likely that the surface layer of the WD is lost first. The surface layer contains hydrogen, helium and other light elements from the remnant star or a companion. Such objects require more detailed modelling than is available in a synthetic model.

2.14 Carbon Star Luminosity Functions

The Carbon Star Luminosity Function (CSLF) is defined as the number of carbon stars per unit bolometric magnitude for a particular population i.e. it is a probability density
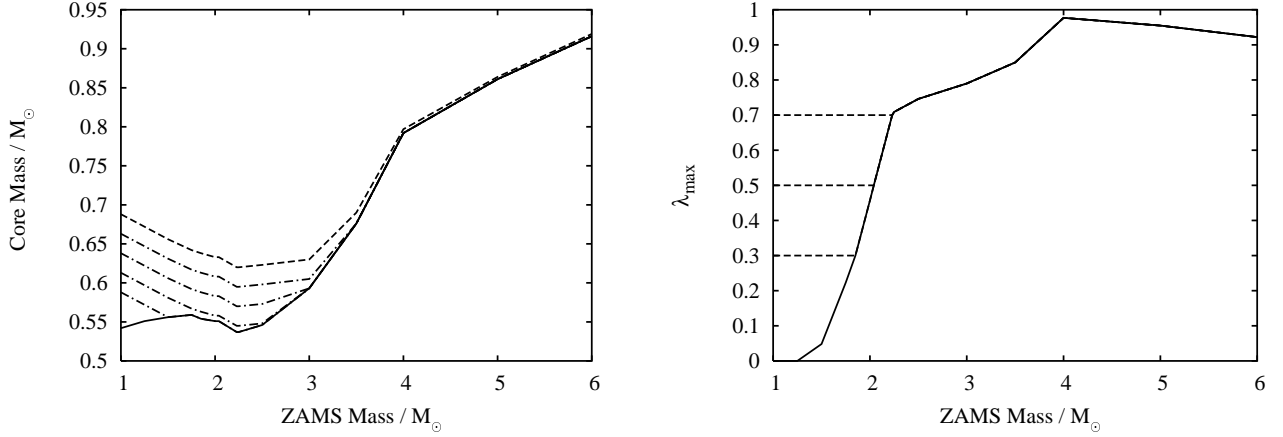
Figure 30: Left panel: the solid line is the core mass at the first thermal pulse and the dashed line is $M_c^{\min}$, both from Karakas et al. (2002) for $Z = 0.02$. The dot-dash lines, from top to bottom, are for $\Delta M_c^{\min} = 0$, -0.025, -0.05, -0.075 and -0.1. Right panel: the solid line is $\lambda_{\max}$ from Karakas et al. (2002) for $Z = 0.02$, the dashed lines are for $\lambda_{\min} = 0.3$, 0.5 and 0.7.
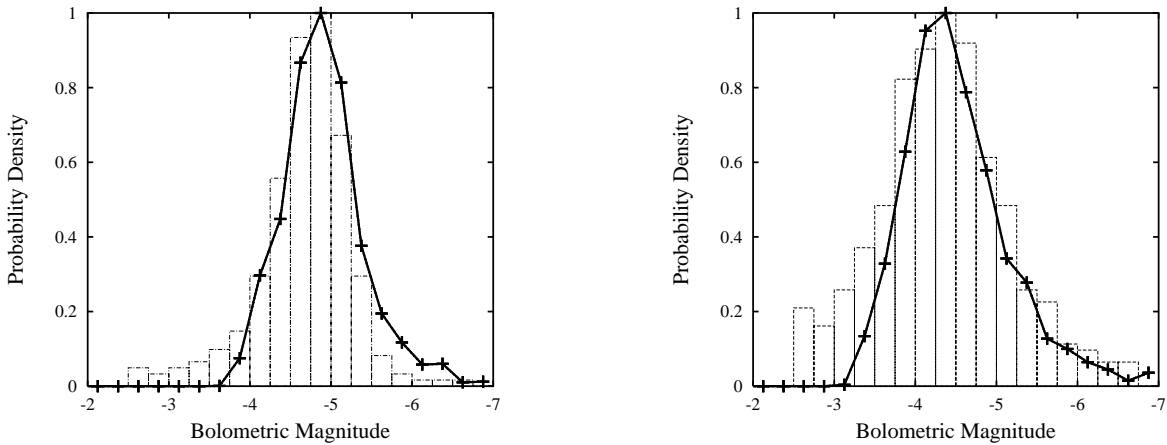
Figure 31: The best fit synthetic model carbon star luminosity functions for the LMC ($Z = 0.008$, left panel) and the SMC ($Z = 0.004$, right panel). Observations are from Groenewegen, 2002.

function. It is a common diagnostic used to check and possibly calibrate third dredge-up. Carbon star surveys of the Magellanic Clouds are thought to be complete because these stars are bright, albeit in the infra-red owing to dust, and carbon stars are easy to identify by spectrographic and photometric methods. A population of stars is modelled in the mass range $0.5 \leq M_i/M_\odot \leq 8.0$ where the probability for each star is taken from the IMF of Kroupa, Tout & Gilmore (1993, see appendix D4) and a constant star formation rate is assumed. Results are compared to the LMC ($Z = 0.008$) and SMC ($Z = 0.004$) data taken from (Groenewegen, 2002; see also Groenewegen, 1999). The theoretical distributions are binned identically to the observed data in 0.25 mag bins. All distributions are normalized such that the integrated probability is 1.0 so are independent of the star formation rate. Because the bin widths are fixed the probability density is directly proportional to the probability per bin i.e. the number of stars per bin. It is compared directly to the suitably normalized observations.

It turns out that to fit the dim carbon stars with bolometric magnitude greater than -3 a correction to the luminosity to deal with post-flash minima must be introduced. This is a factor of the form

$$f_L = 1 - 0.5 \times \min\left[1, \exp(-3\frac{\tau}{\tau_{ip}})\right], \tag{113}$$

which is activated for the first ten pulses to mimic the Monash models. After about ten pulses the luminosity dip lasts for a short time and is not of large enough magnitude to contribute to the dim CSLF tail (the maximum dip seen in the full evolution models is a factor of $0.5L$ equivalent to 0.75 mag). Extending the dip to all pulses does not significantly change the model CSLF of either the SMC or LMC. The dimmest of carbon stars with magnitude about -3 cannot be fitted at all because they are probably extrinsic carbon stars in binary systems (Izzard & Tout, 2004). Note that in order to resolve the dips the timestep is reduced to at most one tenth of the interpulse period.

The problem with the CSLF is that detailed models predict a distribution of stars that is too bright. The accepted interpretation is that dredge-up does not begin early enough on

the TPAGB or at a low enough (core) mass. The inability of stellar models to match the observed CSLFs in the Magellanic Clouds leads to the introduction of two free parameters, $\Delta M_c^{\mathrm{min}}$ and λ_{min}. The minimum core mass for third dredge-up is shifted by $\Delta M_c^{\mathrm{min}}(< 0)$ such that dredge-up occurs at lower core masses than predicted by K02 (fig. 30, left panel). The dredge up efficiency λ reaches the asymptotic value λ_{max} after a few pulses. It is adjusted so that

$$\lambda_{\mathrm{max}} = \max(\lambda_{\mathrm{min}}, \lambda_{\mathrm{max}}^{\mathrm{fit}}) \,, \tag{114}$$

where $\lambda_{\mathrm{max}}^{\mathrm{fit}}$ is the value from K02 (see figure 30, right panel). The efficiency of dredge-up in low-mass stars is increased with respect to the fit of K02 but remains suppressed for the first few pulses. The synthetic model is used to calibrate values of $\Delta M_c^{\mathrm{min}}$ and λ_{min} appropriate for the LMC ($Z = 0.008$) and SMC ($Z = 0.004$) by a least-squares minimization. The shifting of the dredge-up parameters in this way is motivated by simplicity in the face of ignorance of the physical process responsible for dredge-up in low-mass stars – a more complicated expression is not justified.

The best fit single star models (see fig. 31) have $\Delta M_c^{\mathrm{min}} = -0.07$ and $\lambda_{\mathrm{min}} = 0.5$ for the LMC and $\Delta M_c^{\mathrm{min}} = -0.07$ and $\lambda_{\mathrm{min}} = 0.65$ for the SMC. These values are similar to those of Marigo (2001) noting that $\Delta M_c^{\mathrm{min}} = -0.07$ gives $M_c^{\mathrm{min}} \approx 0.59\,\mathrm{M}_\odot$ at $M_i \approx 1.5\,\mathrm{M}_\odot$ (a typical mass for C-stars; Wallerstein & Knapp, 1998).

A simple linear fit to the above dredge-up parameters gives

$$\Delta M_c^{\mathrm{min}} = -0.07 \tag{115}$$

and

$$\lambda_{\mathrm{min}} = 0.8 - 37.5Z \tag{116}$$

which equates to 0.05 at $Z = Z_\odot$.

Comparison with figure 9 shows that a value of $\Delta M_c^{\mathrm{min}}$ nearer to $-0.09\,\mathrm{M}_\odot$ is necessary

to match Marigo's prescription although the functional form of the prescription is otherwise similar.

2.15 Single Star AGB Yields - Monash vs Synthetic

The following yields for isotopes j are defined by

$$p(j, M_{\mathrm{i}}) = \frac{1}{M_{\mathrm{i}}} \int_0^t \dot{M} \Delta X_j \, dt \tag{117}$$

where t is time (maximum evolution time is $16\,\mathrm{Gyr}$ for these calculations), M_{i} is the initial stellar mass, $\dot{M}$ the mass-loss rate and $\Delta X_j = X(t) - X(t = 0)$. An IMF-weighted form

$$\xi(M_{\mathrm{i}}) \int_0^t \dot{M} \Delta X_j dt = \xi(M_{\mathrm{i}}) M_{\mathrm{i}} p(j, M_{\mathrm{i}}) \tag{118}$$

is plotted where $\xi(M_{\mathrm{i}})$ is the KTG93 IMF as given in appendix D4. For a more detailed discussion of yield definitions see chapter 5.

The synthetic model yields should match those of the Monash models but there are some sources of difference. The synthetic models include the final few pulses in high-mass stars. These pulses occur when the effect of HBB is diminishing so contain a mixture of processed and unprocessed isotopes. Increases are seen in the yields of ^{12}C, ^{13}C, ^{14}N, ^{17}O, ^{20}Ne, ^{22}Ne, ^{25}Mg and ^{26}Mg. There is another problem with the high-mass yields of isotopes heavier than neon. The ^{20}Ne abundance is extremely sensitive to the temperature and so tiny errors on the temperature fit. For this reason it is over-produced at all metallicities for $M \geq 6\,\mathrm{M_\odot}$ although it is under-produced for $Z = 0.02$, $M = 5\,\mathrm{M_\odot}$. It proves to be extremely difficult to fix this problem. This is frustrating and an indication of how difficult yield predictions are for AGB stars. The incorrect ^{20}Ne leads to dubious ^{21}Ne, although ^{22}Ne is rather more robust to temperature changes. Na is over-produced at high mass and low metallicity. This might be attributed to the (artificial) lack of leakage to the MgAl cycle however ^{24}Mg seems correct, except at the highest mass where, at $Z = 0.008$, it is

fitted excellently while at $Z = 0.02$ and $Z = 0.004$ there is too little. Again, ^{24}Mg is very sensitive to the temperature, and hence the mass. The Monash yields decrease from -10^{-4} to -8×10^{-4}, nearly an order of magnitude, between $M = 5\,M_\odot$ and $M = 6\,M_\odot$ – that this is modeled at all by the synthetic model is a good sign. The other MgAl isotopes are reasonably well fitted but again at high masses most yields are overestimated.

In summary, the synthetic yields provide good estimates (correct to within a factor of 2 at any mass) of the AGB yields with the exception of ^{20}Ne and ^{24}Mg which can be wrong by a factor of 10 although there is no systematic variation with mass or metallicity.

2.16 Combining SSE with Nucleosynthesis and the Monash fits

Minor changes are required to make the SSE code function smoothly in conjunction with the fits to the Monash models. The core mass at the first thermal pulse is used to define the EAGB timescale and for $M \geq 7\,M_\odot$, $Z = 0.02$ the timescale is zero because the SSE $M_{\mathrm{c,1TP}}$ is quite different from the K02 fit. This affects few stars, especially when the IMF is included, and does not affect TPAGB evolution because second dredge-up is still assumed to occur at the beginning of the TPAGB. There is also a discontinuity in the luminosity and radius at the beginning of the TPAGB because the Monash model luminosities do not match those of the Eggleton-based models. This causes problems when the timestep is determined by the rate of change of the radius, so a minimum value of $0.1\tau_{\mathrm{ip}}$ is used to maintain accurate evolution and code speed. The same limit is necessary when post-pulse luminosity dips are taken into account because these dips are assumed to be instantaneous and this leads to an infinite time derivative. The nucleosynthesis code itself only[6] interacts with the stellar evolution via eq. (31) and so runs largely in parallel with the SSE code.

---

[6]Except WR mass-loss rates which may depend on surface abundance.
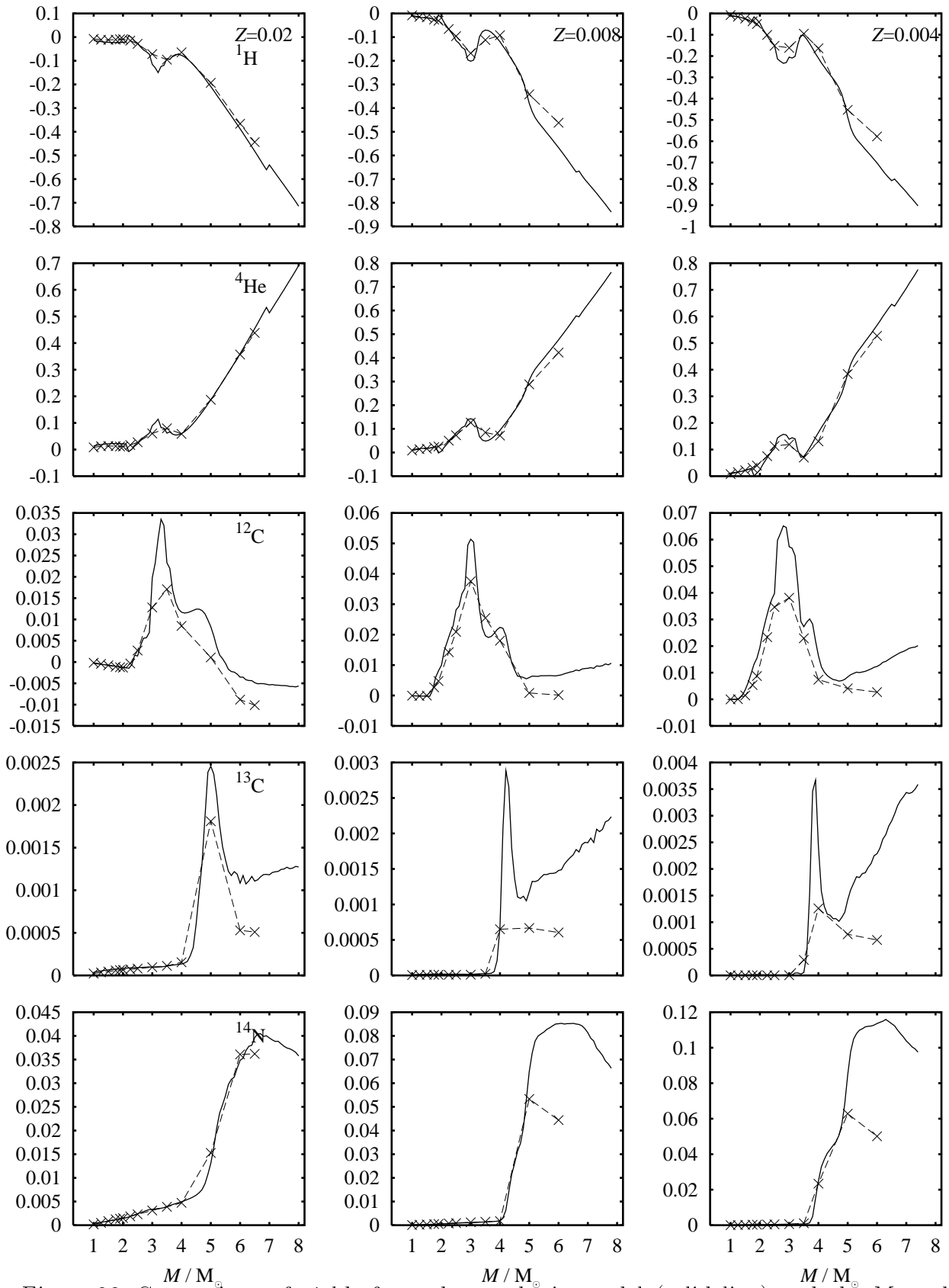
Figure 32: Comparison of yields from the synthetic model (solid line) and the Monash yields (dashed line with crosses) for $Z = 0.02$, 0.008 and 0.004, isotopes ^{1}H to ^{14}N.

Figure 33: As figure 32 but for ^{15}N to ^{21}Ne.
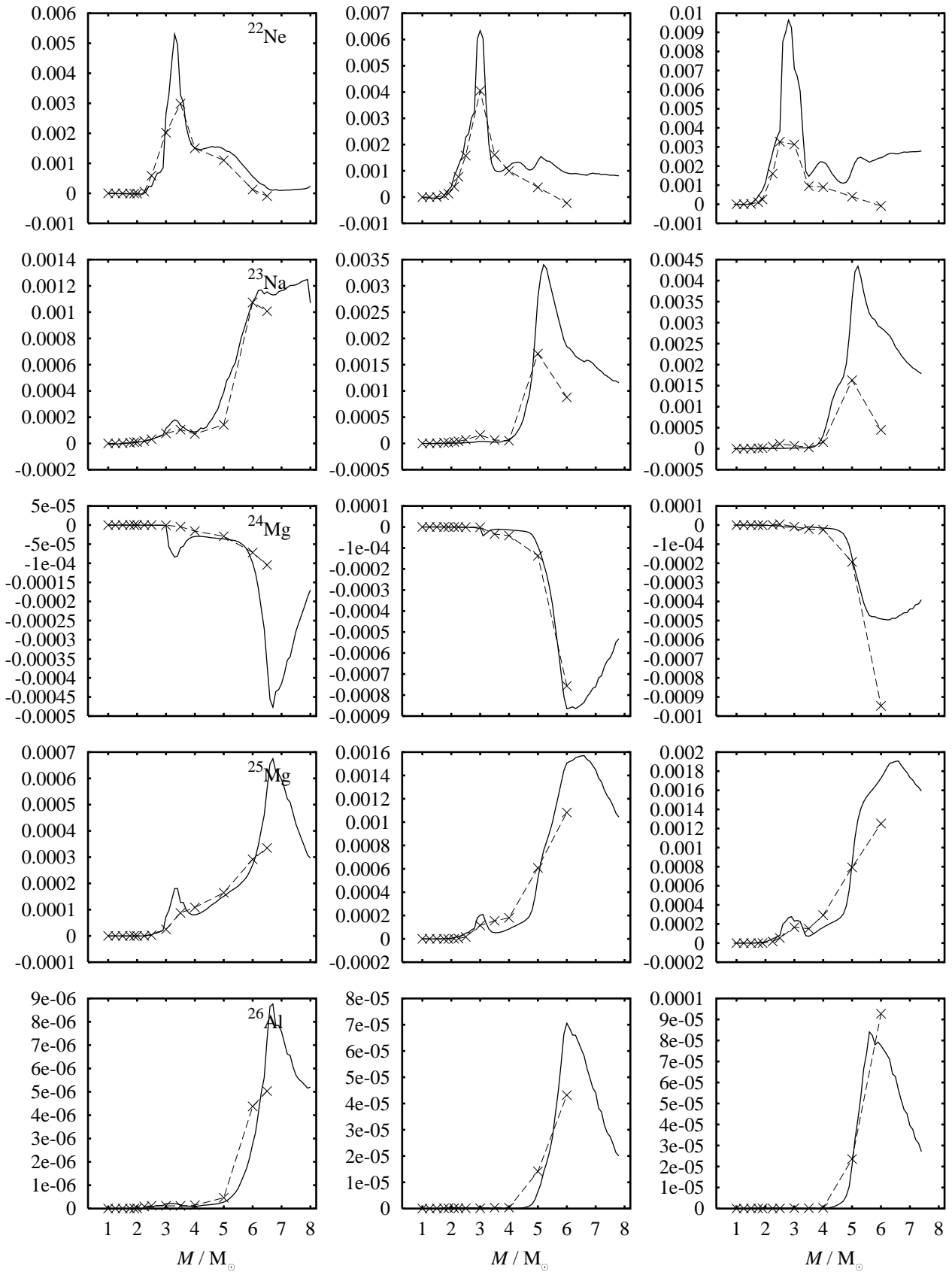
Figure 34: As figure 32 but for ^{22}Ne to ^{26}Al.

Figure 35: As figure 32 but for ^{26}Mg and ^{27}Al.

3 High-Mass Stars

Massive stars are defined as those stars which are initially massive enough to ignite carbon in their cores and progress to a nuclear runaway. This occurs in stars with a mass $M \gtrsim 7 - 8\,\mathrm{M_\odot}$. At solar metallicity the limit is $8.25\,\mathrm{M_\odot}$ according to the `SSE` model, although the choice of mass-loss prescription introduces some uncertainty. Stars in the mass range $8 \lesssim M/\mathrm{M_\odot} \lesssim 24$ evolve on to the EAGB but never make it to the TPAGB because the core grows large enough to collapse. The star explodes as a type II supernova. The hydrogen-rich envelope is ejected into the ISM together with some of the core. The remainder of the core forms a neutron star remnant with a mass $1.3 \lesssim M_{\mathrm{NS}}/\mathrm{M_\odot} \lesssim 1.7$, with the `SSE` prescription. There is some uncertainty in remnant mass and ejected mass, this is addressed in section 3.8. The abundances of mass ejected from the core cannot be modelled simply so fits to detailed models are used, see section 3.7.

For stellar masses greater than about $25\,\mathrm{M_\odot}$ the star is luminous enough that line-driven wind loss removes the hydrogen envelope to expose the helium core. Such stars are known as Wolf-Rayet stars. As the hydrogen envelope is stripped, deeper and hotter layers of the star are exposed. These layers are rich in $^{14}\mathrm{N}$ owing to CNO cycling and are called WNL stars. As the hydrogen itself is removed the star becomes a helium star, this is the WNE phase. The products of helium burning are then also exposed as mass loss continues, leading to a WC phase owing to surface carbon and a WO phase due to surface oxygen. These stars will explode as type Ib/c supernovae if the (degenerate) core mass in any post-helium-MS stage exceeds M_{Ch}.

The detailed models used for fitting are the *Dray* models. Nucleosynthesis is not as detailed as with the Monash models because a reliable interface between the version of the

Eggleton code used to construct them and Cannon's nucleosynthesis code does not yet exist (Dray, private communication). Fits to surface abundances vs ZAMS and instantaneous mass are the basis for the rapid nucleosynthesis model. It has proven extremely difficult to do any better, in the time allowed for a PhD, because the interplay between burning shells and convective regions in massive stars requires a detailed model. However, prescriptions for surface ^{1}H, ^{4}He, ^{12}C, ^{14}N, ^{16}O and ^{20}Ne have been constructed. A few minor isotopes have been introduced by comparison of the Dray models with those of Maeder & Meynet (1994, MM94).

3.1 The Models

The full evolution models of massive stars are calculated with the Eggleton code (Dray, private communication) and are published in Dray et al. (2003) and Dray & Tout (2003). The models cover the mass range $10 \leq M/\mathrm{M}_\odot \leq 150$ although only stars up to $100\,\mathrm{M}_\odot$ are used for fitting because this is the range of the SSE model. Metallicity is in the range $10^{-4} \leq Z \leq 0.03$. The SSE code was constructed with a similar code to that used to make these models so the stellar evolution should be consistent, although that does not mean it is!

The Wolf-Rayet phases are defined in a similar way to Dray et al. (2003, who took their definition from Maeder & Meynet, 1994) but without the effective temperature condition (they use $T_{\mathrm{eff}} > 4$ for WR stars) and with a lower X limit of 0.01 rather than 0. The effective temperature limit does not work well with the SSE code because the stars are often too cool to be classed as WR stars. Given the uncertainty in current WR observations this is not entirely unphysical. The X limit is for numerical convenience – the drop toward zero hydrogen is rapid so the difference between the two conditions $X = 0$ and $X = 0.01$ is small. All other massive stars are termed OB.

Surface Conditions	Phase
$X > 0.4$	OB
$0.01 < X < 0.4$	WNL
$X < 0.01$ and $(C+O)/Y < 0.03$	WNE
$X < 0.01$ and $(C+O)/Y > 0.03$	WC
$X < 0.01$ and $(C+O)/Y > 1$	WO

The full evolution models use two mass-loss rates, referred to as MM (after Maeder & Meynet, 1994) and NL (after Nugis & Lamers, 2000) details of which can be found in Dray et al. (2003) or appendix D of this dissertation.

The following synthetic fits are to the mass M, core mass M_c and initial mass M_ZAMS[1] for the $Z = 0.02$ set of models. Corrections are applied for variation in mass-loss prescription and metallicity. Stars are defined for convenience as hydrogen stars or helium stars, where helium stars are those defined by the `SSE` algorithm to be types HeMS, HeHG or HeGB and hydrogen stars are all the prior stellar evolution phases (MS, HG, GB, CHeB and EAGB).

3.2 Surface ^{1}H and ^{4}He in hydrogen stars with $M > 8\,\mathrm{M}_\odot$

Stars with $M \lesssim 38\,\mathrm{M}_\odot$ experience a sudden change in surface hydrogen abundance X_H1 when the internal convection zone reaches the surface. This is coincident with the beginning of the Hertzsprung Gap (HG) phase or the base of the RGB for $M \lesssim 14\,\mathrm{M}_\odot$[2]. The surface hydrogen abundance is fitted with a Fermi-like function of the mass lost by the star relative to the main sequence $\Delta M = M_\mathrm{ZAMS} - M$ such that

$$X_\mathrm{H1} = X_\mathrm{i,H1} - \frac{dX_1}{1 + s_1^{\Delta M - dM_1}} \,, \tag{119}$$

---

[1] M_ZAMS is the ZAMS mass in single stars, but see section 4.6 for binaries.
[2] Stars more massive than this have no RGB at solar metallicity.
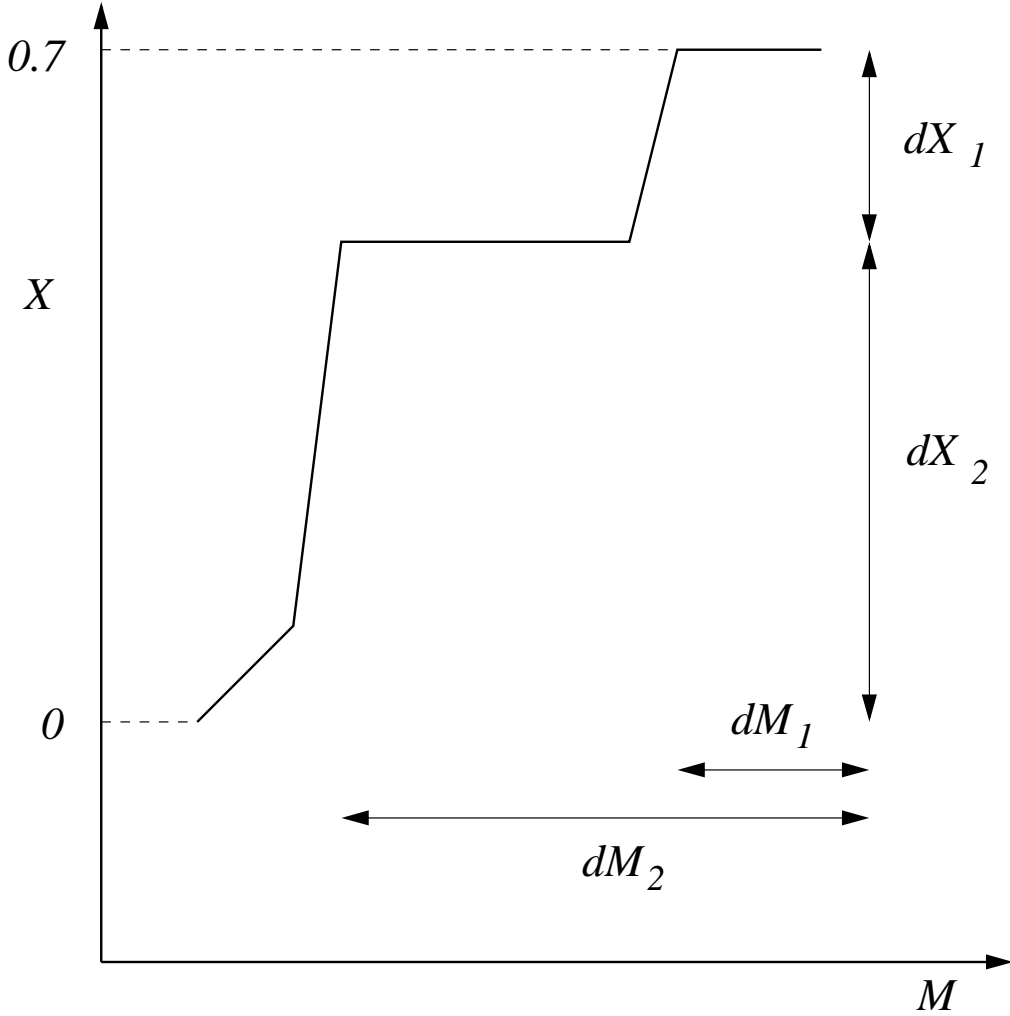
Figure 36: Schematic view of surface hydrogen abundance vs mass for $M \lesssim 40 \, \mathrm{M}_\odot$.

as shown in figure 36. The hydrogen drop of magnitude dX_1 occurs when dM_1 is lost from the star, the slope parameter s_1 models the rate of change of X_{H1} with mass lost. For $M \gtrsim 25 \, \mathrm{M}_\odot$ there is a further drop in hydrogen as the core approaches the surface. This is also modelled by a Fermi function at a mass $M_{\mathrm{ZAMS}} - dM_2$ and of magnitude dX_2 so the expression for X becomes

$$X_{\mathrm{H1}} = X_{\mathrm{i,H1}} - \frac{dX_1}{1 + s_1^{\Delta M - dm_1}} - \frac{dX_2}{1 + s_2^{\Delta M - dM_2}}. \tag{120}$$

The drop in surface hydrogen for $M \gtrsim 38 \, \mathrm{M}_\odot$ stars is not as sudden as in lower-mass

stars, so Fermi functions of $\log_{10} \Delta M$ rather than ΔM are used. Only one log-Fermi function is required for $M \gtrsim 55\,\mathrm{M}_\odot$ (see figure 37).

The two different mass-loss rates lead to different behaviour of X_{H1} but this can fitted to M_c and M_{HG} (see Appendix B7.2) where M_{HG} is the mass at which the star leaves the MS and becomes a HG star. Both the core mass and the HG mass depend on the mass loss in the SSE code because luminosity depends on mass and the mass of the core depends on the luminosity history of the star. Prior to the HG M_{HG} is approximated using a linear extrapolation based on the GB base lifetime $t_{\mathrm{BGB}} = t_{\mathrm{MS}} + t_{\mathrm{HG}}$, where t_{MS} and t_{HG} are the MS and HG lifetimes, and the stellar age t_* such that

$$M_{\mathrm{HG}} = M_{\mathrm{ZAMS}} - (M_{\mathrm{ZAMS}} - M)\frac{t_{\mathrm{BGB}}}{t_*} \tag{121}$$

and once the HG is reached M_{HG} is known.

Corrections are made for changes in metallicity. For $Z > 0.02$ there is little change but for $Z \lesssim 0.01$ the behaviour of the convection zones differs due to opacity changes such that the sudden changes in X_{H1} at $Z = 0.02$ are smoothed out. Corrections are made to the $Z = 0.02$ fits to deal with this. Appendix B7 contains the necessarily rather complicated numerical details.

Surface helium is then calculated from

$$X_{\mathrm{He4}} = 1 - X_{\mathrm{H1}} - Z_t \tag{122}$$

where Z_t is the current metallicity of the star with a correction to ensure a smooth transition to the helium star phase (see appendix B7).

3.3 Surface CNO in hydrogen stars

As hydrogen is burned by the CNO cycle the CNO isotopes other than $^{14}\mathrm{N}$ are converted to $^{14}\mathrm{N}$. It is quite simple to fit X_{C12} and X_{O16} to X_{H1} and calculate X_{N14} by conserving CNO
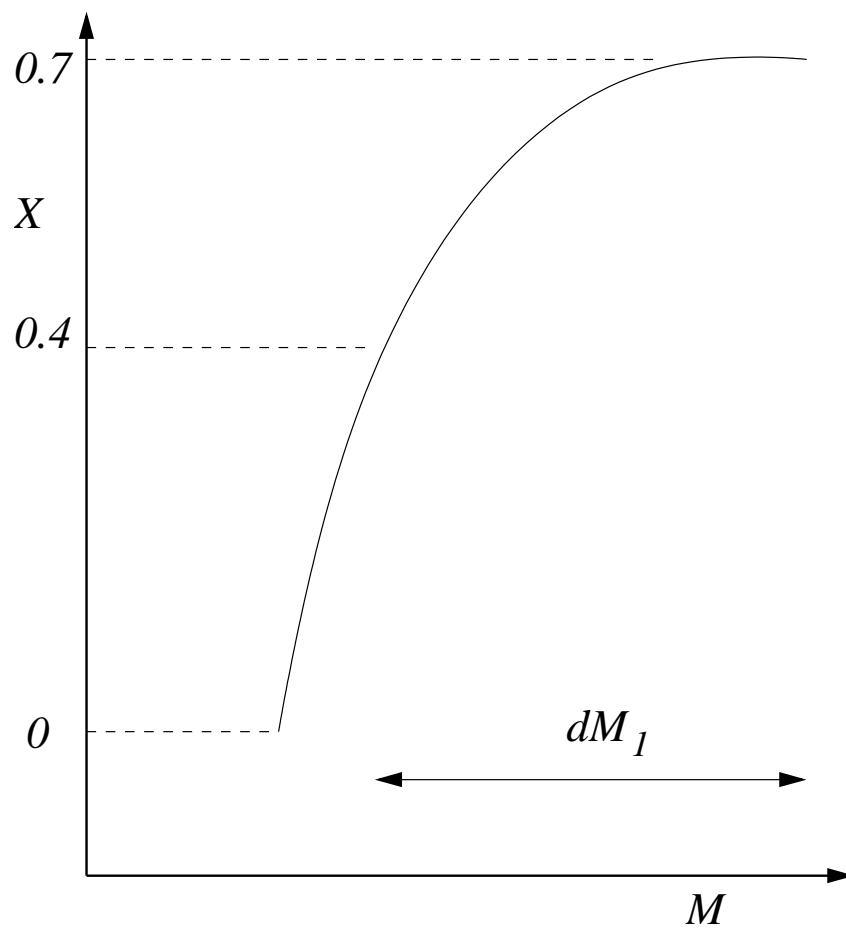
Figure 37: Schematic view of the change in surface hydrogen abundance for $M \gtrsim 55\,\mathrm{M_\odot}$.

number. First, $\psi_{\mathrm{O16}} \equiv X_{\mathrm{XO16}}/X_{\mathrm{CNO}}$ is fitted as a function of $\psi_{\mathrm{XH1}} \equiv X_{\mathrm{XH1}} \times 0.7/X_{\mathrm{i,XH1}}$ (such that $\psi_{\mathrm{XH1}} = X_{\mathrm{XH1}}$ for $Z = 0.02$ because $X_{\mathrm{i,XH1}} = 0.7$) then

$$
\begin{aligned}
\psi_{\mathrm{O16}} \;=\; \max \Big[& 0, (a_{123} + b_{123}^{c_{123}\psi_{\mathrm{XH1}}+d_{123}} + e_{123}\psi_{\mathrm{XH1}}^{f_{123}}) \times \\
& (g_{123} + h_{123}M_{\mathrm{ZAMS}} + i_{123}M_{\mathrm{ZAMS}}^2 + j_{123}M_{\mathrm{ZAMS}}^3 + \\
& k_{123}\exp(-(M_{\mathrm{ZAMS}} - 40)^2/l_{123}) \Big] \; .
\end{aligned}
\tag{123}
$$

Then $\psi_{\mathrm{C12}} \equiv X_{\mathrm{XC12}}/X_{\mathrm{CNO}}$ is fitted to ψ_{O16} as

$$
\psi_{\mathrm{C12}} = \max \big[0, a_{124} + b_{124}\psi_{\mathrm{O16}} + c_{124}\psi_{\mathrm{O16}}^2 \big] \; .
\tag{124}
$$

The change in surface $^{14}\mathrm{N}$ is then calculated from the change in surface $^{12}\mathrm{C}$ and $^{16}\mathrm{O}$ in the current timestep

$$
\Delta^{14}\mathrm{N} = 14 \left(\frac{\Delta^{12}\mathrm{C}}{12} + \frac{\Delta^{16}\mathrm{O}}{16} \right) \; .
\tag{125}
$$

The Dray models do not contain $^{13}\mathrm{C}$ however the MM94 models do so it is possible to approximate the surface abundance. The mass at which $^{12}\mathrm{C}$ and $^{14}\mathrm{N}$ are equal for the Dray models *and* the MM94 models is used as a reference and the $^{13}\mathrm{C}$ abundance taken as typical for the CNO burned layers. The change in $^{13}\mathrm{C}$ is then related to the change in $^{12}\mathrm{C}$ by

$$
d^{13}\mathrm{C} = -\gamma_{13}d^{12}\mathrm{C}
\tag{126}
$$

where γ_{13} is a function of M_{ZAMS} and X_{N14}. The maximum value of $^{13}\mathrm{C}$ is about $^{12}\mathrm{C}/4$ when the CNO cycle is in equilibrium. It turns out that about 1% of $^{13}\mathrm{C}$ is from WR stars, most is produced in AGB stars and novae so even if this approximate value is incorrect it is not important.

Similarly ^{17}O and ^{18}O are not represented in the Dray models but from the MM94 models it is clear they approximately follow ^{16}O such that

$$X_{\text{O17}} = 6 \times 10^{-4} X_{\text{O16}} \tag{127}$$

and

$$X_{\text{O18}} = 2 \times 10^{-3} X_{\text{O18}} \,. \tag{128}$$

The contribution to the total yield of ^{17}O from massive stars is small compared to that from AGB stars.

Because the CNO cycle is active in high-mass stars it is expected that the NeNa and MgAl cycles are also but modelling such nucleosynthesis is beyond the scope of this dissertation.

As the core of the star approaches the surface the abundance of CNO elements other than ^{12}C and ^{16}O, which are present because of helium burning, drops as the surface hydrogen abundance drops. Any ^{13}C, ^{17}O or ^{18}O present is converted first to ^{14}N and then all the CNO isotopes except ^{12}C and ^{16}O are converted to ^{22}Ne by double-alpha capture on ^{14}N. For $0 < M - M_{\text{c}} < 0.5$ this is approximated by

$$\Delta^{22}\text{Ne} = 22 \left(\frac{\Delta^{13}\text{C}}{13} + \frac{\Delta^{14}\text{N}}{14} + \frac{\Delta^{17}\text{O}}{17} + \frac{\Delta^{18}\text{O}}{18} \right) , \tag{129}$$

$$X_{\text{C13}} = (M - M_{\text{c}}) \frac{X_{\text{C13}}}{2.5} , \tag{130}$$

$$X_{\text{N14}} = (M - M_{\text{c}}) \frac{X_{\text{N14}}}{2.5} \tag{131}$$

and

$$X_{\text{O17}} = X_{\text{O18}} = 0 \,. \tag{132}$$

When $M_{\text{c}} = M$ the star becomes a helium star.

3.4 Helium Stars

The `SSE` code defines the helium star phase as that when $M_c = M$ where M_c is the helium core mass. The Dray models show that the surface hydrogen is zero by this stage and so is easily fitted! Helium constitutes a fraction $1 - Z_t$ of the surface abundance when the core reaches the surface however mass loss causes the surface to eat into the still burning helium core. The products of helium burning – mainly ^{12}C and ^{16}O – are seen at the surface. It proves to be extremely difficult to fit the profile of ^{12}C and ^{16}O in the interior of the star, and hence the surface evolution as mass is stripped. This is because there is a complicated interplay between the nuclear burning so the profile changes as a function of time, convective mixing of this profile and the decreasing mass and so decreasing rate of nuclear burning and exposure of deeper layers. The problem becomes even worse when both mass-loss rates are considered, then worse again when Z is varied, leading to a nightmare scenario. As Dray & Tout (2003) point out at the lowest metallicities two stars of almost identical mass follow a considerably different evolutionary path and end their evolution with different ^{12}C and ^{16}O at the surface. For this reason, and lack of brainpower of the author, a simple approach is used here. The HeMS timescale is used to fit the surface helium abundance then ^{12}C and ^{16}O are fitted to X_{He4}. The terminal abundances, just prior to model breakdown are $X_{\text{He4}} = 0.25$, $X_{\text{C12}} = 0.45$ and $X_{\text{O16}} = 0.3$.

The surface helium abundance is parameterized by

$$\gamma_{\text{He}} = \max\left[0, \min\left(\frac{t_{\text{HeMS}}}{\tau_{\text{HeMS}}}, 1\right)\right] \tag{133}$$

where t_{HeMS} is the time spent on the helium main sequence and τ_{HeMS} is the helium main sequence lifetime such that

$$X_{\text{He4}} = \max(0.25, 1 - Z_{\text{He}} - 0.7\gamma_{\text{He}}) \tag{134}$$

where Z_{He} is the surface metallicity at the start of the helium star phase before any ^{4}He is burned to ^{12}C or ^{16}O. Carbon and oxygen are fitted to

$$X_{\text{C12}} = \min\left[0.45, (0.99273 - X_{\text{He4}})/1.2811\right] \tag{135}$$

and

$$X_{\text{O16}} = 1 - Z_{\text{He}} - X_{\text{He4}} - X_{\text{C12}} \,. \tag{136}$$

All other CNO isotopes are assumed to be converted to ^{22}Ne. ^{20}Ne and ^{24}Mg do not change at the surface[3] although may in the interior (see section 3.7).

3.5 Synthetic vs Full Evolution

Figures 38, 39 and 40 show abundance vs instantaneous mass tracks for the synthetic models vs the Dray models for a selection of $Z = 0.02$ models as well as the MM94 models. The fit for ^{1}H is excellent while ^{4}He is excellent until the star becomes a helium star. The MM94 models show the same qualitative behaviour.

The rise in ^{12}C and ^{16}O during the helium star phase is clear. The mass at which the star becomes a helium star differs from full to synthetic model by a few solar masses at $M_i = 60\,\text{M}_\odot$ and the $86\,\text{M}_\odot$ MM synthetic model has no helium star phase at all (although the NL synthetic model does). The MM94 ^{13}C evolution is complicated and the initial abundance must be doubled in order to obtain a good fit. The reason for this is unclear – if pre-MS evolution is responsible for the ^{13}C abundance then the surface ^{12}C should be low, although it too is higher, which suggests MM94 used different initial surface abundances to Dray et al. (2003). Surface nitrogen is excellently fitted by the synthetic model. The approximate treatments for ^{17}O and ^{18}O are reasonable as far as they go, however the MM94 models show a peak in surface ^{18}O at the start of He-burning, the reason for this is unclear but is possibly owing to α-capture on ^{14}N. As expected surface ^{20}Ne does not change, the slight blip in the synthetic models is due to a normalization error – the

---

[3]The ^{20}Ne which changes in the Dray models is really ^{22}Ne, confirmed by the MM94 models.

magnitude of the error is 3% at most. This justifies the consideration of the Dray models' neon as ^{22}Ne, the synthetic fit for which is also good. Magnesium shows no change.

Differences between the synthetic and full evolution models are due to a number of effects. First, at low mass ($M_i \lesssim 24\,M_\odot$ for $Z = 0.02$, NL mass loss) the synthetic models' main-sequence lifetime is longer – for NL mass loss by about 1 Myr for $M_i = 20\,M_\odot$, 0.25 Myr for MM mass loss – the precise reason for this is unknown. Overshooting lengthens the main sequence lifetime but both the Dray models and the full models used to make the SSE code employ similar overshooting and both use the Eggleton code to calculate the timescales. The SSE models were made without mass loss so this is a potential reason. Helium star lifetimes are similar for all models.

Second, while the lifetimes differ by only 1 Myr, the final mass and evolutionary state is sensitive to this difference. For an initially $20\,M_\odot$ star the pre-supernova mass is $14\,M_\odot$ and $16.5\,M_\odot$ for MM and NL Dray models while for the SSE model $5\,M_\odot$ and $9\,M_\odot$. Fiddling the SSE timescales to match the Dray models is possible, although probably not justified given that changing the mass-loss rate has the same effect. For example, reduction of MS timescale by a factor of 0.91 fits the Dray and synthetic MM models well, both exploding with a pre-SN mass of $14\,M_\odot$. The same effect is achieved by a factor 3 reduction in the mass-loss rate. The net effect is that the synthetic models explode at a lower mass after becoming an EAGB star. The resulting wind yields (see below) are higher for these stars. Once SN yields are included the difference between the synthetic and full models is lessened because the SN ejects the envelope in much the same way as wind loss. The hydrogen-rich envelope is ejected either way and there is little difference total yield.

High-mass stars at high metallicity also suffer from differences in mass-loss rates. The most massive stars lose so much mass on the MS that they form a WD instead of following the standard helium star to supernova evolutionary path. As an example, the synthetic MM, $Z = 0.02$ stars explode to leave a $1.34\,M_\odot$ NS for $M_i = 81\,M_\odot$ but form a $0.9\,M_\odot$ COWD for $M_i = 82\,M_\odot$ because their cores are not massive enough to explode during the helium-star phase and mass loss on the HeGB exposes the CO core. For $M_i = 83\,M_\odot$ a $0.3\,M_\odot$ HeWD is formed as the core is exposed on the HeMS while for stars with $M_i \geq$

$84\,\mathrm{M}_\odot$ there is no helium star phase, instead they lose almost all their mass to form $\leq 0.1\,\mathrm{M}_\odot$ HeWDs. This behaviour is not seen in the Dray models at $Z = 0.02$ but is at $Z = 0.03$. The use of the NL wind also prevents such behaviour. Whether it truly occurs is unclear although it is difficult to be overly worried – the IMF renders such stars extremely rare, at least at $Z \gtrsim 0.02$. The cause of the behaviour in the synthetic models is the underestimate of the luminosity (e.g. see fig. 40) which leads to an underestimate of the core mass.

Another useful check on the synthetic models is the lifetime in a particular WR phase, as shown in table 8. The full and synthetic models are in general agreement, at least to within a factor of a few, but there are some irreconcilable problems. The synthetic MM models evolve to WR stars at $M_\mathrm{i} = 20\,\mathrm{M}_\odot$, this is due to the MS lifetime and corresponding mass-loss differences discussed above. At $M = 80\,\mathrm{M}_\odot$ the NL WNL lifetime presents the most problems however again this is disfavoured by the IMF and the $M = 40\,\mathrm{M}_\odot$ models agree well. Indeed for $M \leq 40\,\mathrm{M}_\odot$ only the WNE phase is significantly different. This is the most difficult to model because it depends on the CHeB timescale, which depends on the mass at the end of the main sequence which in turn is sensitive to the mass-loss rate. The effect on chemical yields, however, is expected to be small. The WR type vs mass plot (figure 40) shows that the amount of mass lost while the star is nitrogen rich is about the same for the detailed and synthetic models, so the enrichment is similar. The use of a reduced mass-loss rate, by a factor 0.4 (see section 3.6), leads to better agreement for the MM stars up to $30\,\mathrm{M}_\odot$ although cannot be justified on lifetime grounds alone for the NL models.

3.6 Wind Enrichment

Wind enrichment by the synthetic and full evolutionary models is compared in figure 41. The synthetic models do an excellent job of reproducing the hydrogen, helium and nitrogen yields. There are differences at low mass, again owing to MS timescale differences, and around $25\,\mathrm{M}_\odot$ due to breathing pulses in the Dray models. The effect of these breathing
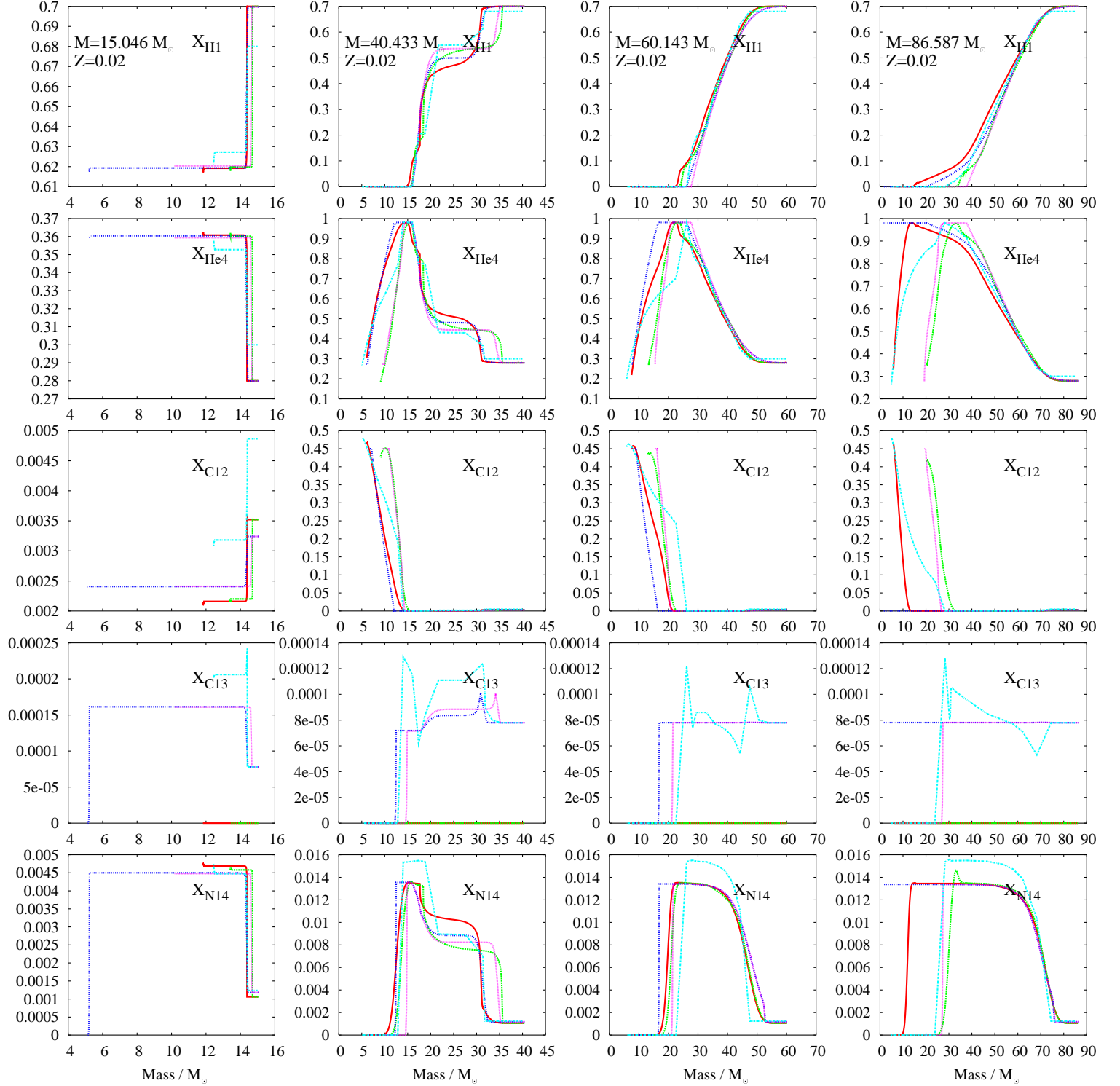
Figure 38: Comparison of surface isotopic abundances (X_{H1}, X_{He4}, X_{C12}, X_{C13} and X_{N14}) vs mass for $Z = 0.02$ and $M \approx 15, 40, 60$ and $86\,M_\odot$ ($85\,M_\odot$ for MM94) models. The number in the top panel gives the Dray/synthetic model mass, the nearest available MM94 model is used. Red and green are the Dray models with the MM and NL mass loss rates, blue and magenta are the corresponding synthetic models, cyan are the MM94 models.
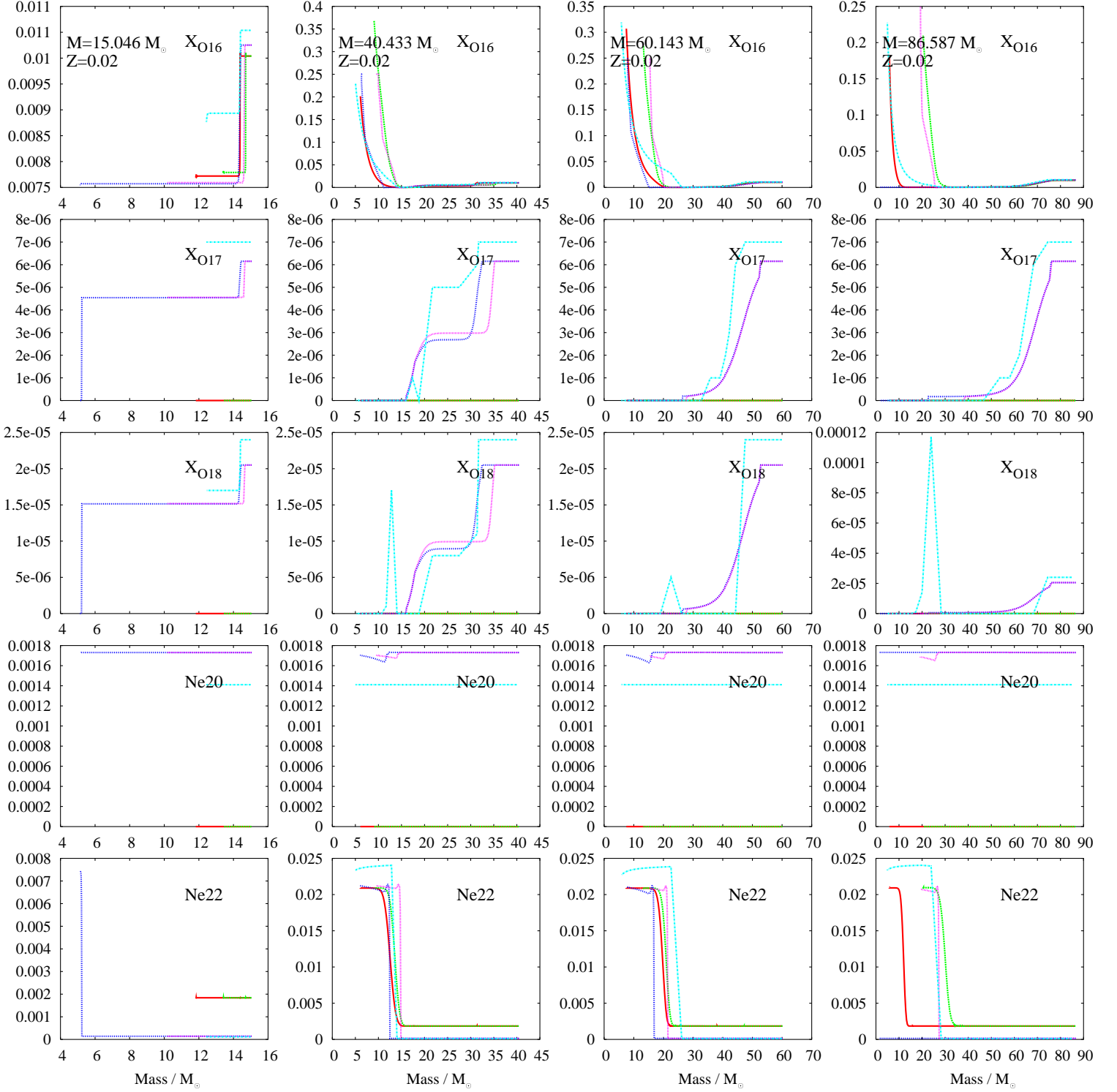
Figure 39: As figure 38 for X_{O16}, X_{O17}, X_{O18}, X_{Ne20} and X_{Ne22}. The Dray models do not separate ^{20}Ne and ^{22}Ne so all their neon is assumed to be ^{22}Ne.
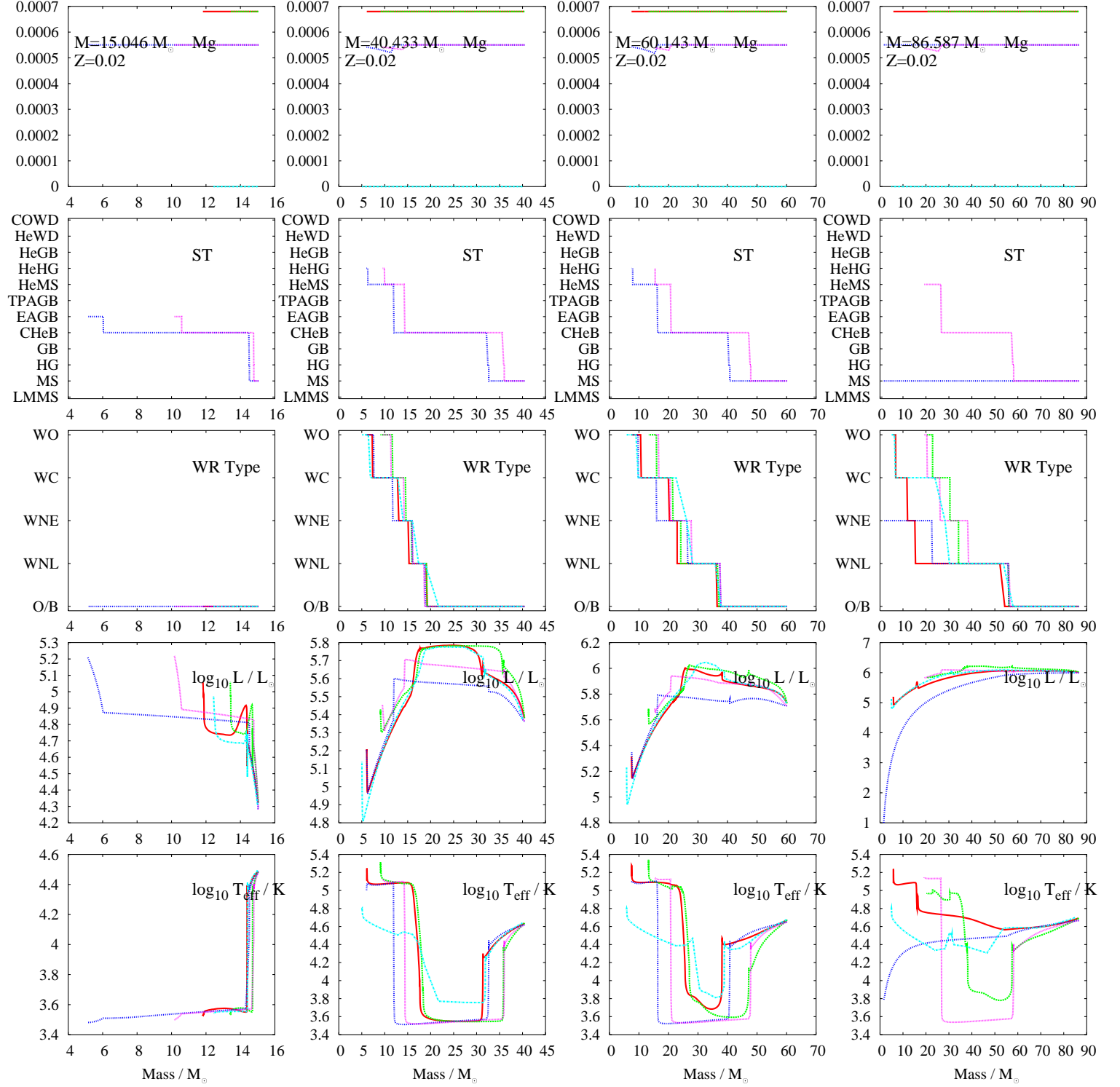
Figure 40: As figure 38 for X_{Mg24}, the stellar type (defined only for the synthetic models), the WR type, luminosity and effective temperature vs mass.

Wind Loss	Initial Mass $/ M_\odot$	$t_{\mathrm{pre\text{-}WR}}/\mathrm{yr}$	$t_{\mathrm{WNL}}/\mathrm{yr}$	$t_{\mathrm{WNE}}/\mathrm{yr}$	$t_{\mathrm{WC}}/\mathrm{yr}$	$t_{\mathrm{WO}}/\mathrm{yr}$
MM	10	2.6×10^7	0	0	0	0
MM×0.4		2.6×10^7	0	0	0	0
MM Dray		2.5×10^7	0	0	0	0
NL	10	2.6×10^7	0	0	0	0
NL×0.4		2.6×10^7	0	0	0	0
NL		2.5×10^7	0	0	0	0
MM	20	9.3×10^6	0	4.7×10^4	1.1×10^5	1.6×10^5
MM×0.4		9.3×10^6	0	0	0	0
MM Dray		9.5×10^6	0	0	0	0
NL	20	9.4×10^6	0	0	0	0
NL×0.4		9.3×10^6	0	0	0	0
NL Dray		8.6×10^6	0	0	0	0
MM	30	6×10^6	2.4×10^4	1.0×10^5	2.2×10^5	2.4×10^5
MM×0.4		6.1×10^6	6.1×10^4	3.7×10^4	4.7×10^4	5.6×10^4
		5.9×10^6	2.1×10^4	8.9×10^3	2.5×10^5	1.9×10^5
NL	30	6×10^6	1.1×10^5	4.0×10^4	6.1×10^4	7.6×10^4
NL×0.4		6.2×10^6	0	0	0	0
		6×10^6	1×10^5	1.3×10^4	9.3×10^4	2.9×10^4
MM	40	4.9×10^6	3.2×10^4	1.0×10^5	2.5×10^5	2.2×10^5
		4.5×10^6	3.3×10^4	4.3×10^4	3.2×10^5	1.9×10^5
NL	40	4.8×10^6	9.9×10^4	4.1×10^4	1.3×10^5	1×10^5
		4.5×10^6	9.0×10^4	5.2×10^4	1.5×10^5	1.5×10^5
MM	60	4×10^6	1.4×10^5	9.4×10^4	1.9×10^5	1.7×10^5
		3.5×10^6	4.5×10^4	3.1×10^4	1.9×10^5	2.3×10^5
NL	60	3.9×10^6	1.8×10^5	6.8×10^4	1.0×10^5	6.7×10^4
		3.5×10^6	4.3×10^4	4.1×10^4	1.7×10^5	1.5×10^5
MM	80	3.4×10^6	3.8×10^5	4.5×10^5	2.9×10^5	2.7×10^5
		2.7×10^6	3.9×10^5	5.1×10^4	2.9×10^5	2.1×10^5
NL	80	3.5×10^6	1.8×10^5	5.3×10^4	1.1×10^5	6.4×10^4
		3×10^6	3.3×10^4	3×10^3	1.9×10^5	1.3×10^5

Table 8: Single star WR phase lifetimes ($Z = 0.02$) for various initial masses. Black text (above) is the synthetic model, red text (below) is from the Dray models. The blue text is a reduced mass-loss rate synthetic model.

pulses is small and over a narrow mass range so is ignored and indeed may only be a numerical artifact.

The qualitative behaviour of the synthetic and full models for ^{12}C and ^{16}O is similar, with the high-mass drop off evident for MM rates, however the synthetic model does a poor job of reproducing the yields above $30\,\mathrm{M_\odot}$ for the MM mass-loss rates. This is because of the longer CHeB lifetime of the synthetic models which leads to HeMS entry at a lower mass than in the full evolutionary models and a shorter HeMS lifetime. This in turn leads to lower helium-burning product yields by up to a factor of 1.8 (a difference of $2\,\mathrm{M_\odot}$) at $M \approx 70\,\mathrm{M_\odot}$. An artificial increase in the HeMS lifetime by a factor of 3 (or corresponding decrease in $\dot{M}$) fits the MM yields but raises the NL yields so they are discrepant.

However, this problem becomes small when the IMF is folded into the yields. Far more important is the over-production by wind loss for stars with mass below $25\,\mathrm{M_\odot}$. Figure 42 (right panels) shows the problem clearly as an over-production of *everything* at low mass. Applying a factor 0.4 reduction (MM and NL) to $\dot{M}$ for $M \leq 25\,\mathrm{M_\odot}$ enables far better fitting of all the isotopes. Once the $\dot{M}$ correction is applied the problem with C and O above $30\,\mathrm{M_\odot}$ again dominates, but is a minor effect on the integrated yield, as are the breathing pulses. It is perhaps also fortunate that C and O yields are dominated by supernovae, so the errors on the wind loss become irrelevant.

3.7 Core Collapse Supernovae

The usual fate of massive single stars is to die in a supernova explosion. As nuclear fuel runs out the core becomes more and more degenerate. Eventually it reaches the Chandrasekhar mass and collapses. Neutrinos from electron capture reactions on protons are thought to yield the energy required, up to 10^{53} ergs, to power the ejecta. The remaining matter forms either a neutron star or black hole. The abundance of the ejected material is impossible to predict with a synthetic model so a set of previously calculated yields must be used. The most complete set to date is that of Woosley & Weaver (1995, hereafter WW95) which covers a mass range $10 \leq M_\mathrm{i}/\mathrm{M_\odot} \leq 40$, metallicity range $0 \leq Z \leq 0.02$ (the A models) and
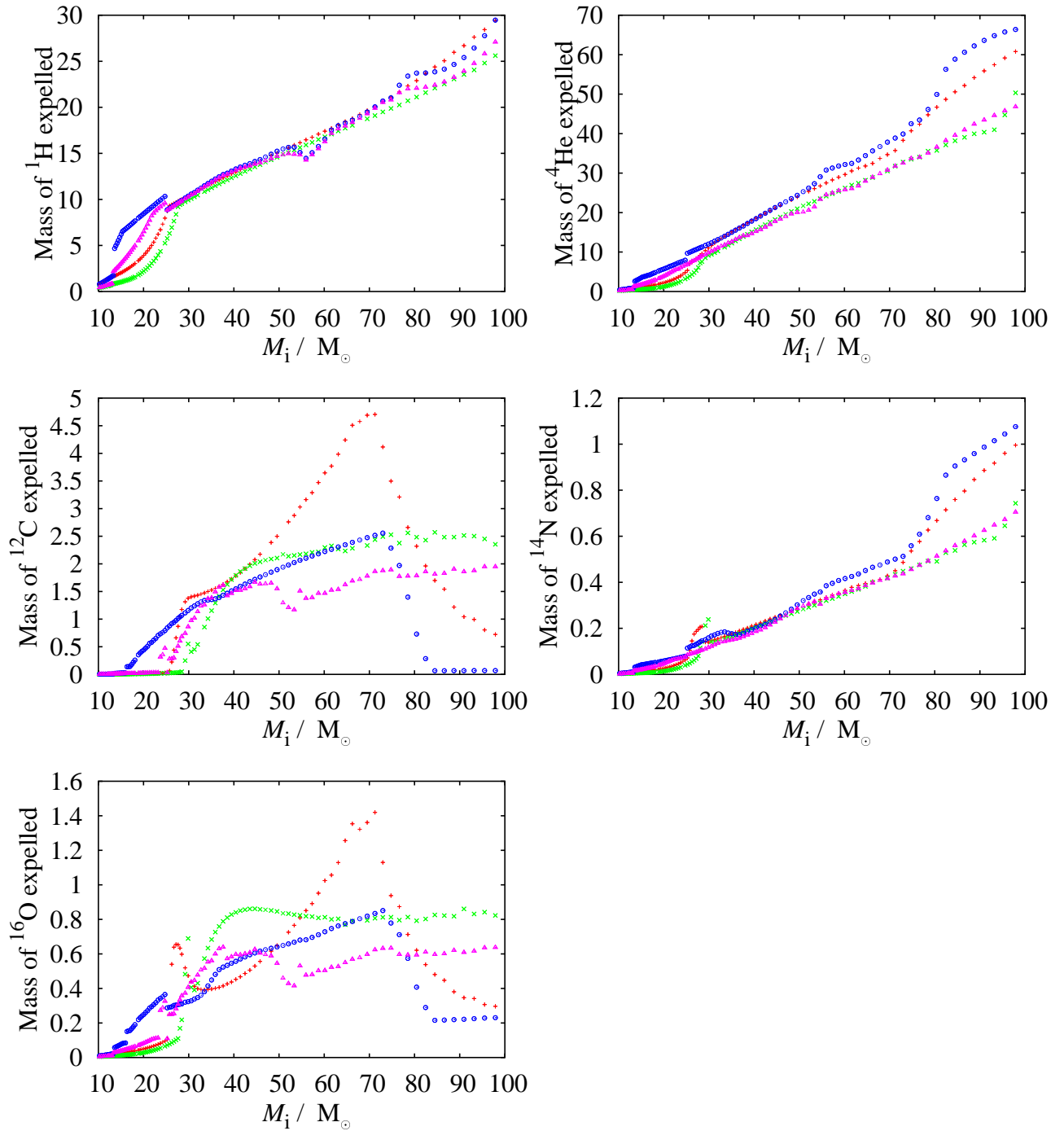
Figure 41: Dray model vs synthetic model wind enrichment vs initial mass ($Z = 0.02$). Red and green are the Dray models for MM and NL mass loss respectively, blue and magenta are the corresponding synthetic models.
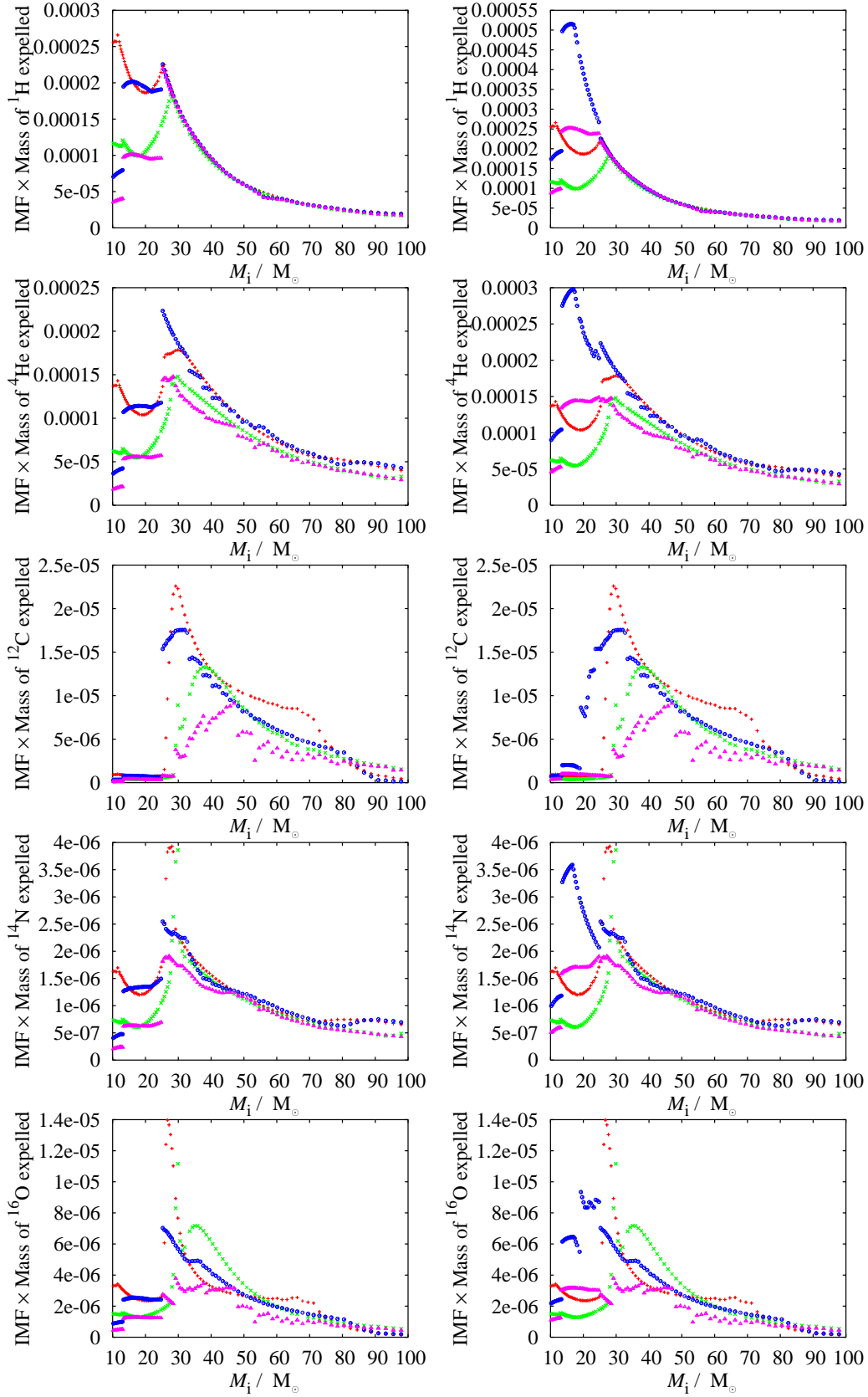
Figure 42: Synthetic model massive star wind enrichment modulated by the KTG93 IMF. The left panels show the case for a reduced wind-loss rate ($\times 0.4$ for $M \leq 25\,\mathrm{M}_\odot$) while the right panels show the standard case. Colours are as in figure 41.

isotopes less massive than ^{71}Ge. Only the $Z = 0.02$, 0.002 and 2×10^{-4} models are used for fitting (the others lie outside the `SSE` metallicity range). The mass range corresponds to a final CO core mass range of $2 \leq M_{\mathrm{CO}}/M_{\odot} \leq 15$. The WW95 models are evolved without mass loss so there is some degree of faith required to link CO cores of the same mass between the WW95 models and the `SSE` code, although it is currently not possible to do any better. There is also the question of remnant mass (see section 3.8) which determines the amount of mass ejected and is also subject to much uncertainty.

For each WW95 star the yields quoted represent everything outside the remnant, including the hydrogen-rich envelope. The method of Portinari, Chiosi & Bressan (1998) is used to remove the envelope and obtain the enrichment from the CO core alone (see appendix A3). The enrichment from the CO core is converted to a mass fraction in the ejecta $X_j^{\mathrm{ej,CO}}$ which is then fitted to M_{CO} and Z. The final supernova yields are given by

$$
X_j^{\mathrm{ej}} = \frac{X_j^{\mathrm{ej,CO}} \times \max\left(0, M_{\mathrm{CO}} - M_{\mathrm{NS/BH}}\right) + X_j' \times \left(M_{\mathrm{pre\text{-}SN}} - \max\left[M_{\mathrm{NS/BH}}, M_{\mathrm{CO}}\right]\right)}{M_{\mathrm{pre\text{-}SN}} - M_{\mathrm{NS/BH}}},
$$
(137)

where the first term results from matter ejected from the CO core and the second term is due to the ejected envelope, $M_{\mathrm{pre\text{-}SN}}$ is the mass of the star just prior to the SN and $M_{\mathrm{NS/BH}}$ is the remnant mass. If $M_{\mathrm{NS/BH}}$ is greater than the CO core mass then the first term is zero and only the envelope contributes. The abundance X_j' is set to the envelope abundance X_j for hydrogen stars. The star is a post-MS star so the envelope is probably convectively mixed or is mixed shortly before the SN. The surface abundance is a good approximation to the envelope abundance. If the star is a helium star a correction must be applied because the envelope is heterogeneous. According to the only available Dray model ($56\,\mathrm{M}_{\odot}$, $Z = 0.02$) shown in figure 43 (Dray, private communication), between the surface (at $7.2\,\mathrm{M}_{\odot}$) and $1.5\,\mathrm{M}_{\odot}$ outside the CO core (at $6.2\,\mathrm{M}_{\odot}$) the ^{4}He,^{12}C, ^{16}O and ^{20}Ne mass fractions change approximately linearly (magenta region). Inside $M_{\mathrm{CO}} + 1.5\,\mathrm{M}_{\odot}$ the core is homogeneous (red region) with mass fractions $X_{\mathrm{CO}}^{\mathrm{hom}}$ given by ^{4}He $= 0.06$, ^{12}C $= 0.3$, ^{16}O $= 0.6$ and ^{20}Ne $= 0.03$. The other mass and metallicity models behave similarly (Dray,

private communication) although a proper fit would require details of all the models and is beyond the scope of this work. The envelope abundances are then given by averaged values

$$X'_j = \frac{\delta M}{2}(X_j + X_{\mathrm{CO}}^{\mathrm{hom}}) + (M_{\mathrm{env}} - \delta M)X_{\mathrm{CO}}^{\mathrm{hom}}\,, \tag{138}$$

where $\delta M = \max(0, M_{\mathrm{env}} - 1.5\,\mathrm{M_\odot})$. The abundance changes near the centre of the star are within the remnant so do not require such treatment. The NS/BH remnant mass depends on prescription (see below) and it is assumed that there is no dependence of X_j^{ej} on this mass. The fits for $X_j^{\mathrm{ej,CO}}$ to the models of WW95 are in appendix B8.

The difference between SN and wind yields for the `SSE` standard mass-loss rates and `SSE` BH prescription are shown in figure 44. Any worries over differences between the Dray C/O yields and the synthetic C/O yields are unfounded because the C/O yields are dominated by SNe over most of the mass range. The break in ^{12}C yields at $25\,\mathrm{M_\odot}$ corresponds to the formation of helium stars (i.e. WR stars), below this mass the star explodes as an EAGB star shortly after the end of core helium burning. All hydrogen, helium and nitrogen contributions to supernovae are due to removal of the EAGB star convective envelope, hence the justification of the homogeneous envelope assumption.

Note that core collapse SN yields for r-process isotopes are not included because no yield sets have been published.

3.8 SN Remnants and Their Masses

The `SSE` model defines the remnant neutron star or black hole baryonic mass as a linear function of the core mass

$$M_{\mathrm{NS/\,BH}} = 1.17 + 0.09 M_{\mathrm{CO}} \tag{139}$$

with BH formation for $M_{\mathrm{CO}} > 7\,\mathrm{M_\odot}$. This gives a minimum BH baryonic mass, and corresponding maximum NS baryonic mass, of $1.8\,\mathrm{M_\odot}$ and a BH baryonic mass of $3\,\mathrm{M_\odot}$
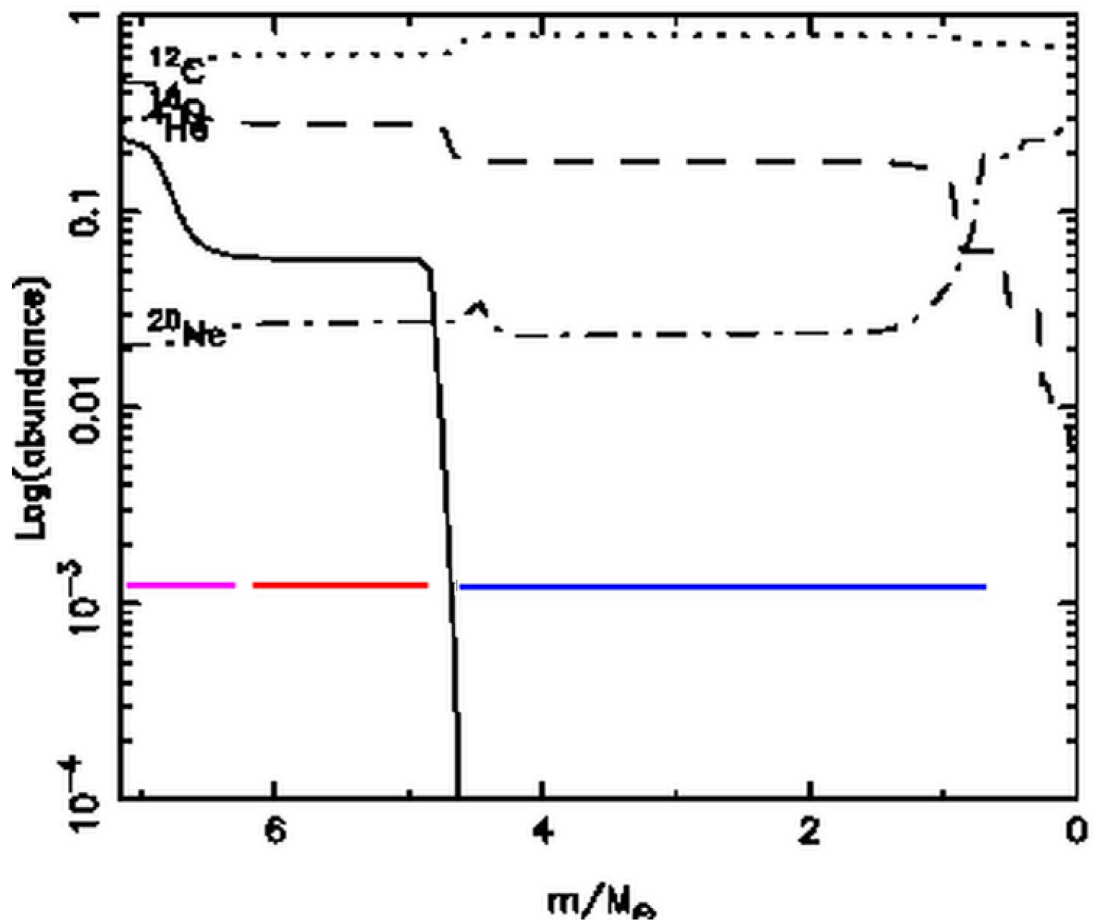
Figure 43: Abundance profile just prior to SN in the Dray $56\,M_\odot$, $Z = 0.02$ model. The blue region shows the mass in the CO core, the red region the homogeneous envelope and the magenta region the heterogeneous envelope. The solid line is ^{4}He, dashes ^{12}C, dots ^{16}O and dot-dash ^{20}Ne.
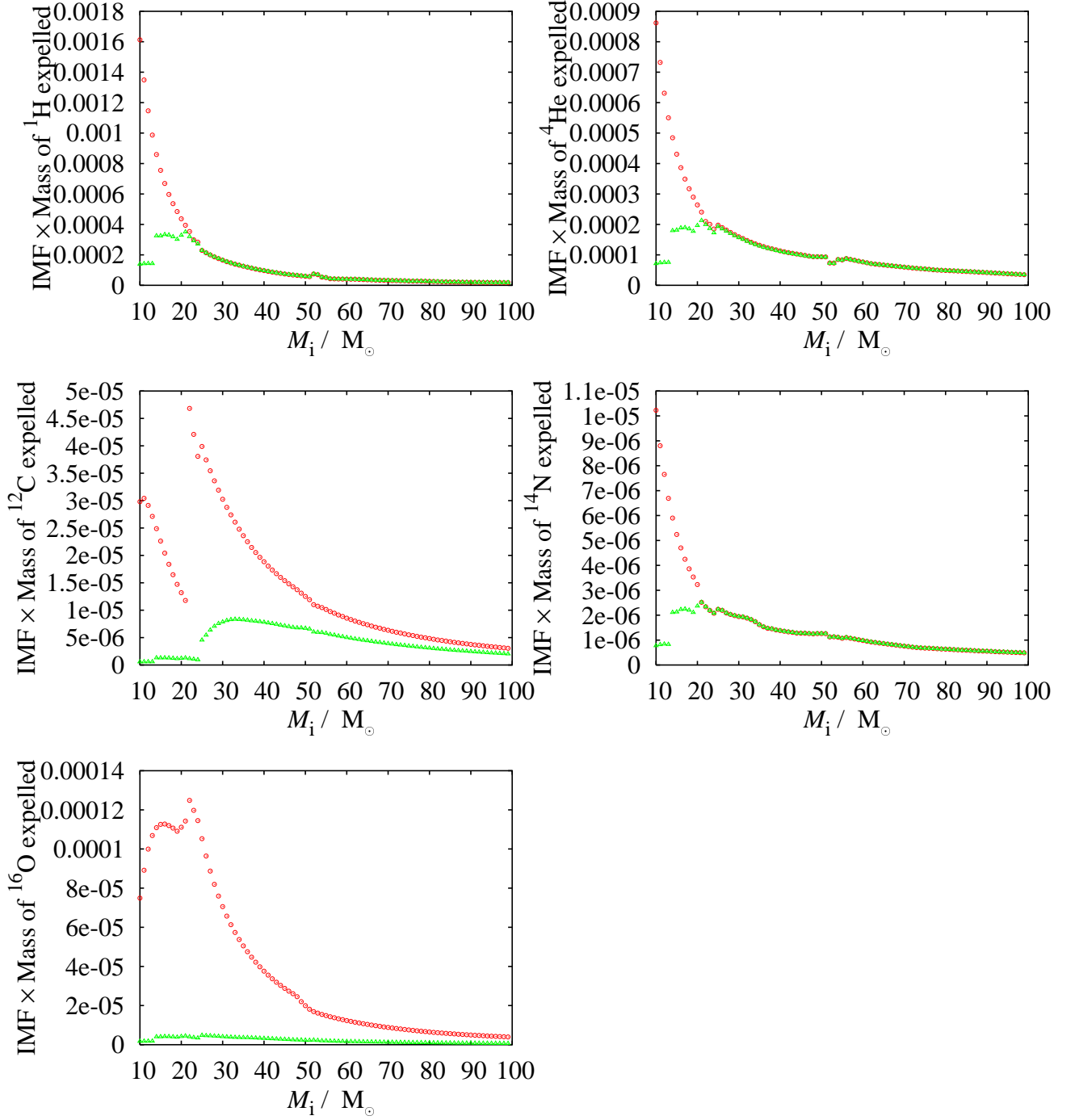
Figure 44: Wind and wind+supernova yields vs initial mass for the $Z = 0.02$ synthetic model (standard `SSE` black hole and mass loss prescription, KTG93 IMF weight included). Red is for wind and supernovae, green is wind alone.

for a $20\,M_\odot$ CO core. Observations of BHs in X-ray binaries (Orosz, 2003) suggest far higher masses, perhaps up to $18\,M_\odot$, although it is unclear whether these black holes are due to binary accretion or a high mass at birth. Using high-mass remnants Fryer & Kalogera (2001) claim to reproduce the then available BH binary mass distribution. The BH mass prescription of Belczynski, Kalogera & Bulik (2002) is added to the `SSE` code (see appendix B9) to provide an option for high-mass single star BHs. Figure 45 shows the remnant masses for the `SSE` or Belczynski et al. BH mass prescription for the `SSE`, MM or NL mass-loss rates at $Z = 0.02$. The mass-loss prescription has some effect on the remnant mass but in order to obtain any remnants more massive than $3\,M_\odot$ in single stars the Belczynski et al. formula must be used. Note that for $M_c \geq 7\,M_\odot$ according to the Belczynski et al. prescription the entire stellar mass is swallowed into a BH, corresponding to an upper initial mass for SN of $70\,M_\odot$ for the `SSE` wind prescription, $85\,M_\odot$ for MM and $45\,M_\odot$ for NL.

For nucleosynthesis the surface of a NS or BH is considered to be made up entirely of neutrons

$$X_n = 1 \tag{140}$$

although this is mainly to balance the accounts – the matter cannot escape (in this model NS-NS mergers are assumed to yield nothing) so cannot contribute to stellar yields.
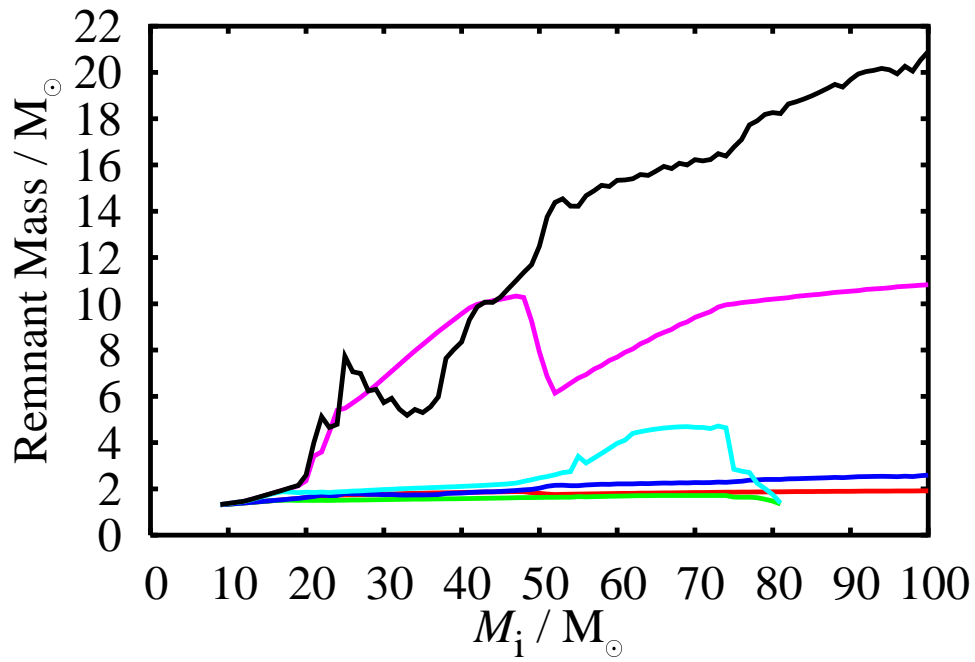
Figure 45: Remnant masses from single stars. Red, green and blue are for the `SSE` NS/BH mass prescription with `SSE`, MM and NL wind loss prescriptions respectively. Magenta, cyan and black are the same but with the Belczynski et al. (2002) NS/BH prescription.

4 Binary Stars

The nucleosynthesis prescriptions described in the previous chapters are now applied to binary stars. The `BSE` algorithm already deals with the dynamics of binary evolution, including orbital motion, tidal interaction, wind loss and accretion, common envelopes, mergers, novae and type Ia supernovae. It remains to again link these mechanisms with a synthetic nucleosynthesis model which runs in parallel with `BSE`. This proves to be "more complicated than I thought" (Tout, private communication), which is something of an understatement! Wind accretion, by the Bondi-Hoyle mechanism, is complicated by colliding winds and the question arises: what is the abundance of the accreting material? Tidal interaction is ignored as far as nucleosynthesis is concerned except for Roche lobe overflow which may pollute a secondary or cause an explosion. Common envelopes are dealt with in a simple way by completely mixing the stellar envelopes on the assumption they are uniform – such stars are usually convective so this is not a bad assumption. Mergers are similarly modelled by complete mixing. Nova and type Ia supernova yields are fitted to detailed explosion models. A nucleosynthesis-specific problem is that of thermohaline mixing where a material from an evolved star accretes on to an unevolved star. Does it sink or does it swim? An approximate, but fast, treatment is presented. Other less important binary-specific effects are also considered such as binary-enhanced wind loss. Finally a few example systems are presented.

4.1 Wind Accretion

As in Hurley et al. (2002) wind accretion is assumed to be by a Bondi-Hoyle mechanism (Bondi & Hoyle, 1944) averaged over a binary period (because wind loss typically occurs for many orbits) which leads to an accretion rate on star 2 from star 1 of

$$\left\langle \dot{M}_{2\mathrm{A}} \right\rangle = \min\left(0.8\left| \dot{M}_{1\mathrm{W}} \right|, \frac{-1}{\sqrt{1-e^2}} \left[\frac{GM_2}{v_{1\mathrm{W}}^2} \right]^2 \frac{\alpha_{\mathrm{B\text{-}H}}}{2a^2} \frac{1}{(1+v^2)^{3/2}} \dot{M}_{1\mathrm{W}} \right) \tag{141}$$

where $\alpha_{\mathrm{B\text{-}H}}$ is the accretion efficiency (typically $\alpha_{\mathrm{B\text{-}H}} = 3/2$), a is the semi-major axis of the orbit,

$$v^2 = \frac{v_{\mathrm{orb}}^2}{v_{1\mathrm{W}}^2}, \tag{142}$$

where the (RMS) binary orbital velocity is given by

$$v_{\mathrm{orb}} = \sqrt{\langle v_{\mathrm{orb}}^2 \rangle} = \sqrt{\frac{G(M_1 + M_2)}{a}} \tag{143}$$

and the wind velocity $v_{1\mathrm{W}}$ is assumed to be proportional to the escape velocity from the donor star

$$v_{1\mathrm{W}} = 2\beta \sqrt{\frac{GM_1}{R_1}}, \tag{144}$$

where $\beta = 0.125$ is the default `BSE` value. The limitation to $0.8\dot{M}_{1\mathrm{W}}$ is to ensure more mass is not accreted by star 2 than is lost by star 1.

If both stars have stellar winds then the original `BSE` model ignores any interaction between the two winds and eq. (141) is used for each star separately. Because, for nucleosynthesis, the composition of the accreted matter must be followed this approximation is no longer applicable.

Consider the fate of one star, here called the accretor, although it both gains and loses mass. In one timestep δt it loses mass

$$\delta M_{\mathrm{r}} = \dot{M}_{\mathrm{W}} \delta t \tag{145}$$

where $\dot{M}_{\mathrm{W}}$ is its mass-loss rate and gains mass δM_{t} from the donor (its companion star)

$$\delta M_{\mathrm{t}} = \dot{M}_{\mathrm{A}} \delta t \tag{146}$$

where the accretion rate $\dot{M}_{\mathrm{A}}$ is calculated with eq. (141). The mass lost has the abundance of the surface of the accreting star $X_{j,\mathrm{accretor}}$ while the mass gained has the abundance of the donor surface $X_{j,\mathrm{donor}}$. With the assumption that the winds do not interact the situation is as in figure 46 and it is obvious that all the accreted material has the abundance of the donor.

Now consider that the winds mix such that a fraction f_{mix} of the accreted material, originally from the donor, mixes with the accretor's own wind. Such mixing could be due to a number of physical instabilities, e.g. Kelvin-Helmholtz or turbulence, or perhaps shocks forming between the winds leading to direct exposure of the donor to its own wind material. The situation is shown in figure 47. There is no mixing of previously expelled wind which might be in the space surrounding the binary system, such material is assumed to be lost to the ISM forever.

The abundance $X_{j,\mathrm{gain}}$ of species j in the material gained by the accretor is given by

$$\delta m_{\mathrm{t}} X_{j,\mathrm{gain}} = \delta m_{\mathrm{t}} X_{j,\mathrm{donor}} - \delta m_{\mathrm{t}} f_{\mathrm{mix}} X_{j,\mathrm{donor}} + \delta m_{\mathrm{t}} f_{\mathrm{mix}} X_{j,\mathrm{accretor}} \tag{147}$$

i.e.

$$X_{j,\mathrm{gain}} = (1 - f_{\mathrm{mix}}) X_{j,\mathrm{donor}} + f_{\mathrm{mix}} X_{j,\mathrm{accretor}} \,. \tag{148}$$

Conservation of mass leads to an expression for the abundance of the mass lost $X_{j,\mathrm{lost}}$

$$\delta m_{\mathrm{r}} X_{j,\mathrm{lost}} = \delta m_{\mathrm{r}} X_{j,\mathrm{accretor}} - \delta m_{\mathrm{t}} f_{\mathrm{mix}} X_{j,\mathrm{accretor}} + \delta m_{\mathrm{t}} f_{\mathrm{mix}} X_{j,\mathrm{donor}} \tag{149}$$
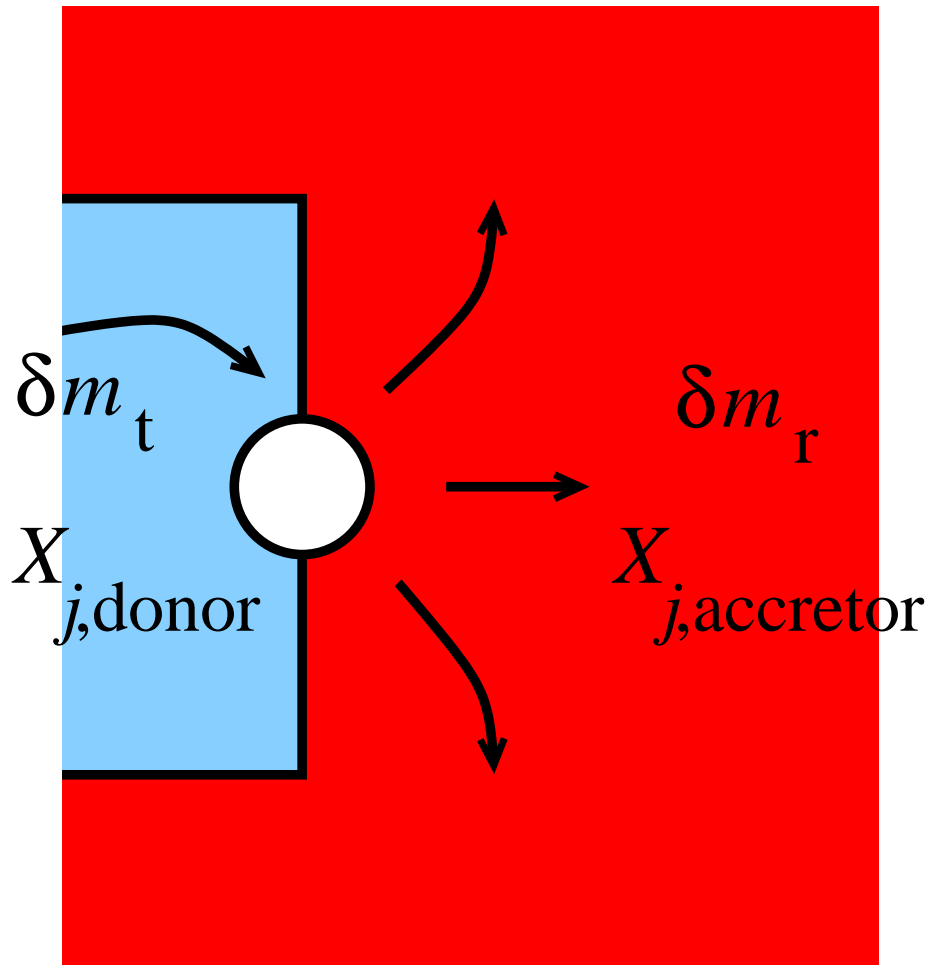
Figure 46: Accretion without interacting winds. Blue represents material from the donor star (not shown) of abundance $X_{j,\mathrm{donor}}$, red is material from the accreting star of abundance $X_{j,\mathrm{accretor}}$.
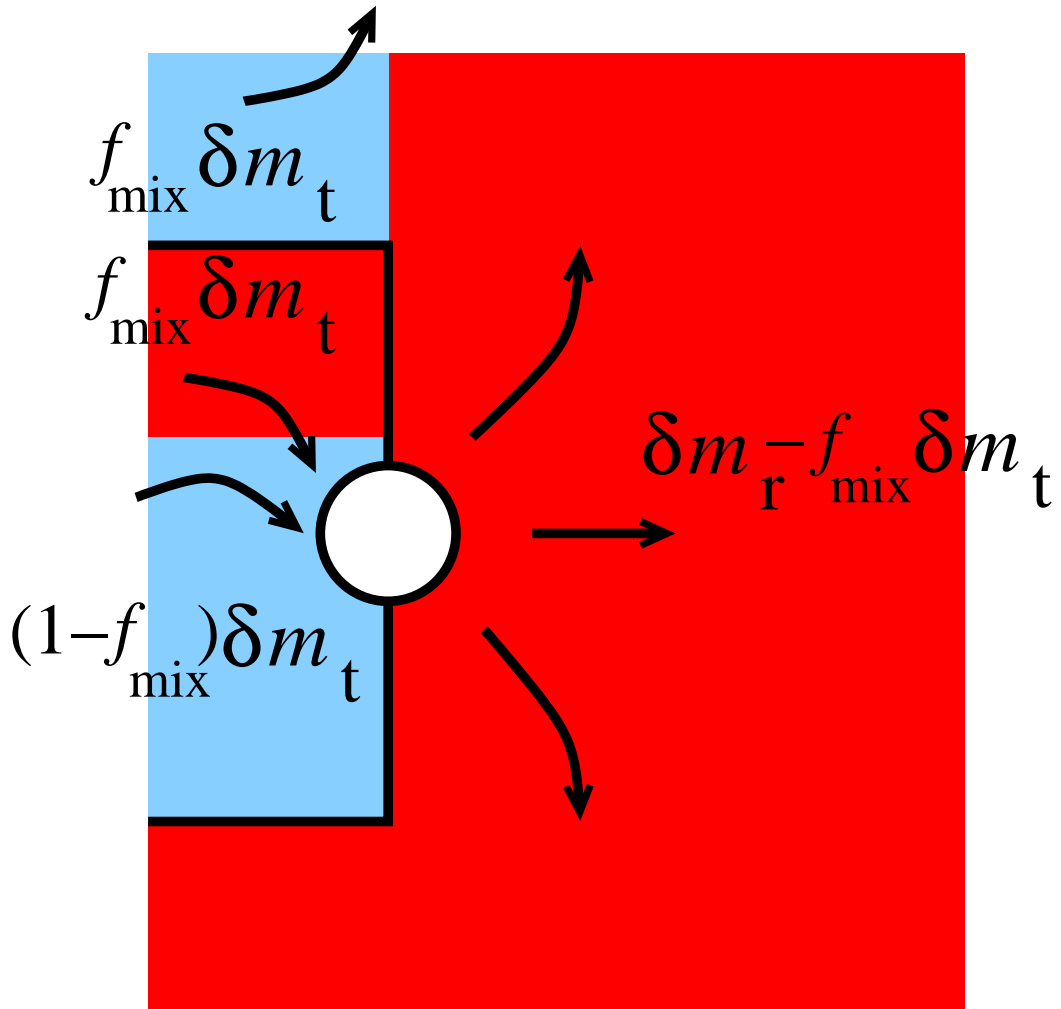
Figure 47: As Fig. 46 with interacting winds. A fraction f_{mix} of the donor's material (blue) mixes with the wind (red) prior to accretion.

i.e.

$$X_{j,\text{lost}} = X_{j,\text{accretor}} \left(1 - f_{\text{mix}} \frac{\delta m_\text{t}}{\delta m_\text{r}}\right) + f_{\text{mix}} \frac{\delta m_\text{t}}{\delta m_\text{r}} X_{j,\text{donor}} \,. \tag{150}$$

There are two limiting cases. First the case of no accretion such that $\delta m_\text{t} = 0$ and $\delta m_\text{r} \neq 0$. From eq. (150) $X_{j,\text{lost}} = X_{j,\text{accretor}}$, as expected because all material lost comes from the accretor's surface, and $X_{j,\text{gain}}$ is undefined but this does not matter because no mass is accreted. The second limit is no wind loss such that $\delta m_\text{t} \neq 0$ and $\delta m_\text{r} = 0$. Eq. (150) diverges but again this does not matter because no mass is lost, $f_{\text{mix}} = 0$ because there is nothing to mix into so $X_{j,\text{gain}} = X_{j,\text{donor}}$ as expected.

It remains to determine f_{mix}. It cannot be negative or greater than one because negative mass has not been discovered and it is impossible to mix more mass than is actually there so $0 \leq f_{\text{mix}} \leq 1$. RLOF and/or accretion without an opposing wind leads to $f_{\text{mix}} = 0$ so this is definitely possible. When the accreting star's own wind is strong the incoming material is shocked and never reaches the accreting star so $f_{\text{mix}} = 1$ (see fig. 48). However, if the accretor's wind is weak f_{mix} has an upper limit of $f_{\text{mix}} \delta m_\text{t} \leq \delta m_\text{r}$ because there is a maximum mass δm_r to mix into. As fig. 49 shows this leads to the accretion of the accretor's own wind and some of the donor material, while the material expelled to the ISM comes directly from the donor.

It follows that the limits on f_{mix} are

$$0 \leq f_{\text{mix}} \leq \min\left(1, \frac{\delta m_\text{r}}{\delta m_\text{t}}\right) \,. \tag{151}$$

Still f_{mix} remains unknown but it is possible to model the collision of the two winds using a momentum flux argument similar to that of Huang & Weigert (1982). The momentum flux at a distance r from each star is

$$J = \frac{\dot{M} v_\text{w}}{4\pi r^2} \tag{152}$$
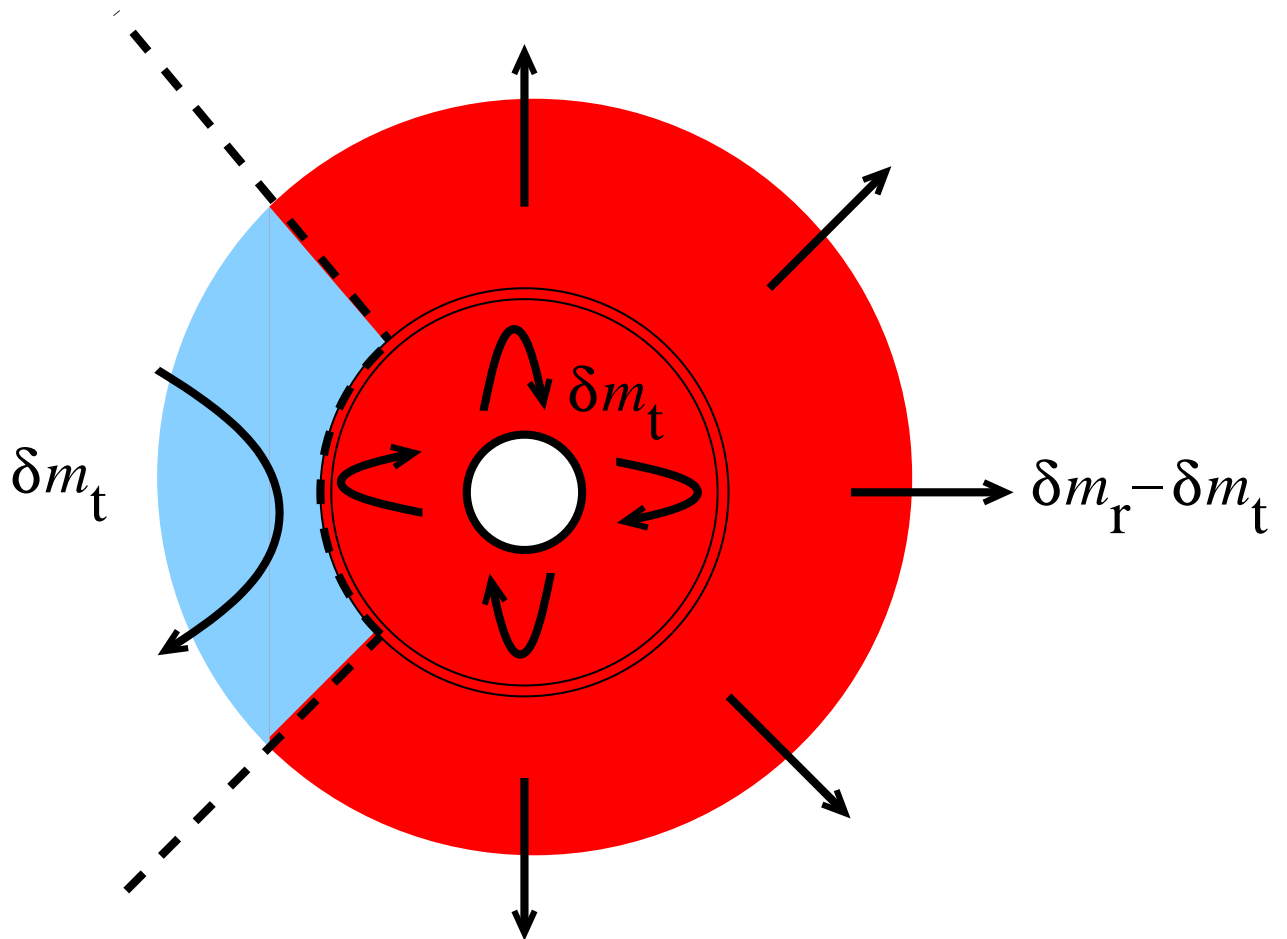
Figure 48: As Fig. 47 with a strong wind and $f_{\mathrm{mix}} = 1$. Mass δm_{t} from the donor (blue) is pushed back into space by the accreting star's strong wind. The accreting star still accretes δm_{t} but of its own matter so the surface abundance remains unchanged. The dashed line shows the shock position, not to scale!
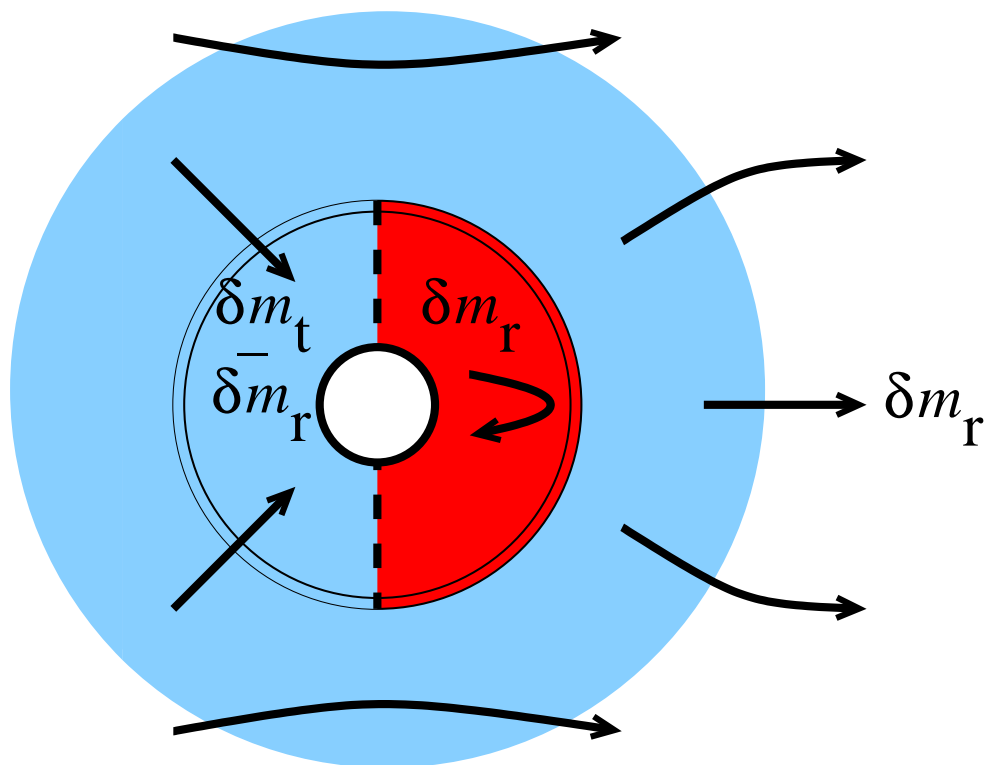
Figure 49: As Fig. 48 with a weak wind and $f_{\mathrm{mix}} \leq \delta m_{\mathrm{r}}/\delta m_{\mathrm{t}}$. The accreting star accretes a mixture of material from itself and the donor star. Mass δm_{r} is still lost to the ISM but it is all from the donor.
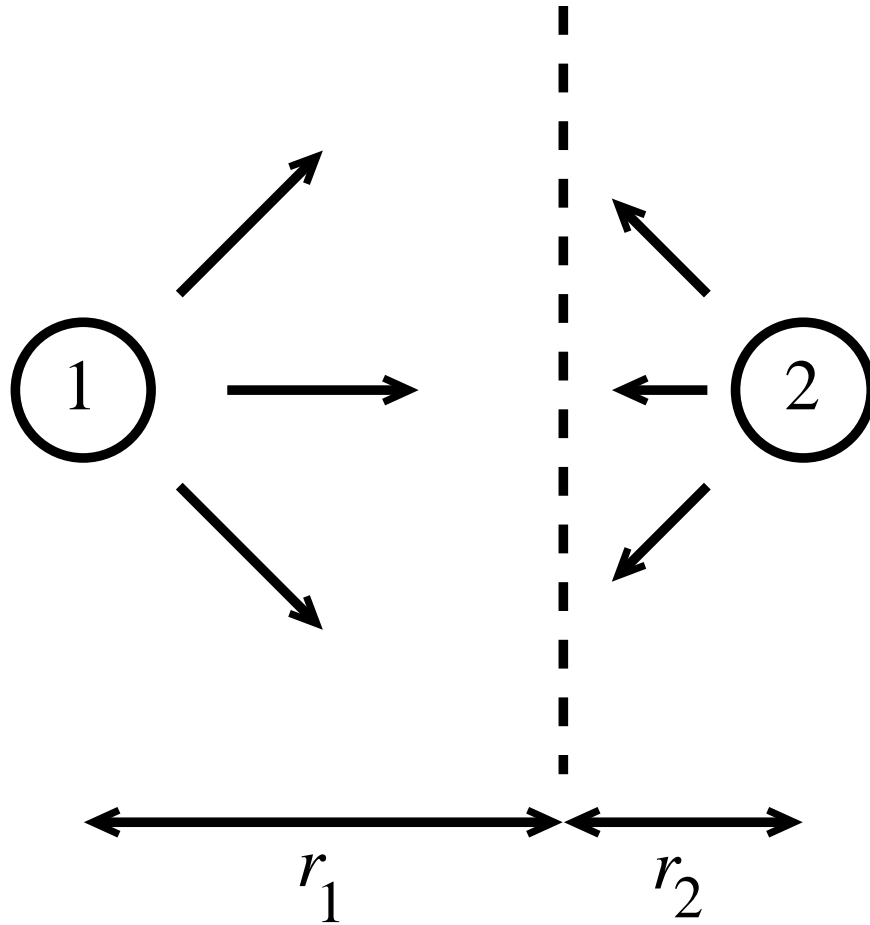
Figure 50: Geometry of the simple interacting wind model. The stronger wind from star 1 shocks with that of star 2 at a distance r_1 from star 1 (or r_2 from star 2).

where v_{w} is the velocity of the wind and $\dot{M}$ the mass-loss rate. The momentum flux of both stars is equal at the point where they interact and shock

$$J_1 = J_2 \tag{153}$$

such that (fig. 50)

$$r_1 = r_2 \sqrt{\frac{\dot{M}_1 v_1}{\dot{M}_2 v_2}} = r_2 f_v \tag{154}$$

where the $\dot{M}v$ terms are factored into f_v. The stars are a distance a apart (the orbit is assumed circular) so $r_1 + r_2 = a$ which gives

$$r_1/a = \frac{f_v}{1 + f_v} \tag{155}$$

and

$$r_2/a = \frac{1}{1 + f_v} \tag{156}$$

so r_1 and r_2 are solved in terms of the known variables a, $\dot{M}$ and v. For each star r_i is compared to the stellar radius R_i. If $r_i > R_i$ the shock is outside the star and none of the donor material makes it to the surface - this is the case $f_{\text{mix}} = 1$. If $r_i \leq R_i$ the shock is inside, or rather on the surface of, the star and all the accreted material is from the donor, hence $f_{\text{mix}} = 0$. In reality there is likely to be a smooth continuum between 0 and 1 but quite how f_{mix} varies is unknown and depends on details of hydrodynamics around the star – approximations used here, such as spherical symmetry, are likely to be invalid.

The above treatment is applicable to fast winds, such as OB/WR stars, when the binary motion is negligible. In other cases such as giant branch winds, which are slow, or symbiotic stars the situation is complicated by turbulent instabilities (Walder & Folini, 2000). Hydrodynamical simulations have been performed (e.g. the series of papers by Ruffert, 1994; Foglizzo & Ruffert, 1999) but only for specific cases and not the large parameter space needed to cover all binary stars. Disk formation is also neglected here. Given the uncertainties it seems an impossible situation but really it is not so bad. The chance of winds interacting is small – most wind accretion is on to a main sequence star with a low mass-loss rate.

4.2 Thermohaline Mixing and the Accretion Process

The fate of material accreted on to the surface of a star is unclear. It is possible that the material either remains on the surface or that it sinks and mixes, and then it is unclear to

what depth such mixing occurs. To deal with this problem accreted material is assumed to form an accretion layer on the surface of the star or, if one already exists, the accreted material is mixed into it. In this way the number of sets of abundances that has to be followed is reduced to two – the accretion layer and the stellar envelope – compared to the many hundreds in full stellar evolution models. While this is required to keep the code from being too slow it is at the expense of the consideration of abundance gradients in the accreted material. Such consideration is rarely required. The layer usually has a higher molecular weight than the envelope because it comes from a star with significant wind loss, which occurs during the latter stages of stellar evolution. In this case the layer mixes instantaneously with the envelope by a thermohaline instability (Kippenhahn, Ruschenplatt & Thomas, 1980; Proffitt, 1989).

When an amount of mass δm_{t} with abundance $X_{j,\text{gain}}$ is accreted the accretion layer increases in mass from δm_{acc} to $\delta m'_{\text{acc}} = \delta m_{\text{acc}} + \delta m_{\text{t}}$ and has a new abundance

$$X'_{j,\text{layer}} = \frac{1}{\delta m'_{\text{acc}}}(\delta m_{\text{acc}} X_{j,\text{layer}} + \delta m_{\text{t}} X_{j,\text{gain}}). \tag{157}$$

For stars with convective envelopes the layer is instantly mixed with the envelope to give a new surface abundance

$$X_{j,\text{env}} = \frac{1}{\delta m'_{\text{acc}} + M_{\text{env}}}(\delta m'_{\text{acc}} X'_{j,\text{layer}} + M_{\text{env}} X_{\text{env}}) \tag{158}$$

where X_{env} is the composition of the envelope which has a mass M_{env}. The accretion layer mass is then set to zero. The accreted material is assumed not to mix into the star's core except for MS stars which do not have a well defined core and can mix completely.

Stars with radiative envelopes are more complicated. The molecular weight of the accretion layer μ_{acc} and the envelope μ_{env} are calculated from

$$\frac{1}{\mu} = \sum_j X_j \frac{(Z_j + 1)}{m_j} \tag{159}$$

where Z_j is the atomic number of species j and m_j its mass number. Two limiting cases are considered:

- $\mu_{\mathrm{env}} > \mu_{\mathrm{acc}}$ – the envelope is heavier than the accreted material so no mixing occurs. The surface abundance is given by $X'_{j,\mathrm{layer}}$. Any subsequent wind loss removes the accretion layer before removing mass from the envelope.

- $\mu_{\mathrm{env}} \leq \mu_{\mathrm{acc}}$ – the accretion layer is heavier than the envelope. The accretion layer and envelope are completely and instantly mixed by a thermohaline instability and the situation is identical to the convective case. When $\mu_{\mathrm{env}} = \mu_{\mathrm{acc}}$ mixing is assumed to occur due to instabilities introduced during the accretion process. This situation is extremely unlikely to occur unless the stars have an identical surface composition, e.g. two low-mass main-sequence stars, in which case the whole process is irrelevant anyway. Mixing does not extend into the core because dilution within the envelope reduces the molecular weight and in addition it is unlikely that mixing can occur across burning shells.

Degenerate material is assumed to have a high molecular weight $\mu = 10$ such that degenerate material always mixes with other degenerate material and non-degenerate material always floats on the surface of white dwarfs. The study of envelopes on WDs is complicated and beyond the scope of this work.

4.3 RLOF and Common Envelopes

The prescription used in the BSE code for RLOF is described in detail in Hurley et al. (2002). There are several consequences for nucleosynthesis. The first is the truncation of phases of stellar evolution of the primary when the radius is large such as the GB and AGB. This means there are relatively fewer giants in binaries and the nucleosynthesis associated with dredge-up in giants does not take place, to a greater or lesser extent depending on the initial binary distributions. The BSE algorithm deals with this already, it is just a matter of not calling the appropriate sections of code.

The other effect of RLOF is due to accretion on to the secondary star. RLOF need not be conservative so matter can be lost to the ISM directly. Rapid accretion can also lead to a common envelope forming around the stars which may be expelled into the ISM. The cores of the stars may merge in the envelope forming a new star. If there is no common envelope, the stars may completely merge (section 4.4) or relatively slow accretion can lead to explosive events such as novae (section 4.5.1) or type Ia supernovae (section 4.5) or the acquisition of a new stellar envelope and rejuvenation of the star. The situation is complex and far from fully understood so while the Hurley et al. (2002) prescription is used to follow the accreted matter there is always an element of doubt about the outcome.

Non-conservative RLOF is the dominant mass-loss mechanism in low-mass binaries. This is because the primaries are deeply convective low-mass ($M \lesssim 0.7\,\mathrm{M_\odot}$) MS stars so mass transfer occurs on a dynamical timescale. The stellar radius expands more quickly than the Roche lobe as mass is lost and the secondary, most likely also a MS star, has a long thermal timescale so cannot adapt quickly to the accretion and the mass is lost from the system. Dynamical mass transfer may also lead to the secondary filling its Roche lobe as the orbit shrinks and the stars merge - this is dealt with below (section 4.4).

When a giant transfers mass on a dynamical timescale to a companion with a long thermal timescale, such as a MS star, a common envelope forms if contact is avoided. The giant fills the Roche lobes of both stars so that its compact core and the companion star are contained in the envelope. As the envelope expands it slows relative to the orbital motion and by a magical (i.e. uncertain) mechanism energy is transferred from the orbit to the envelope. This energy may be enough to completely drive off the envelope, leaving the compact objects and yielding its contents to the ISM, or the cores merge and stellar evolution continues. Thus common envelopes provide a mechanism for the creation of close double-degenerate binaries and cataclysmic variable stars. The prescription of common-envelope evolution from H02 is used. It contains two free parameters, first λ_{CE} which affects the initial envelope binding energy

$$E_{\text{bind},i} = -\frac{G}{\lambda_{\text{CE}}} \left[\frac{M_1 M_{\text{env1}}}{R_1} + \frac{M_2 M_{\text{env2}}}{R_2} \right] , \tag{160}$$

where λ_{CE} is calculated according to the prescription in appendix E. The initial orbital energy of the cores is

$$E_{\text{orb},i} = -\frac{1}{2} \frac{G M_{\text{c1}} M_{\text{c2}}}{a_i} , \tag{161}$$

where a_i is the initial semi-major axis at the onset of the common-envelope phase. The spiral-in of the cores and orbital energy transfer to the envelope is parameterized by α_{CE} such that if the envelope is completely removed

$$E_{\text{bind},i} = \alpha_{\text{CE}}(E_{\text{orb},f} - E_{\text{orb},i}) , \tag{162}$$

where $\alpha_{\text{CE}} \approx 1$ and

$$E_{\text{orb},f} = -\frac{1}{2} \frac{G M_{\text{c1}} M_{\text{c2}}}{a_f} , \tag{163}$$

where a_f is the final separation. This can be solved to give a_f, the final separation, and the entire envelope escapes to contribute directly to the (binary) stellar yield.

However, it is also possible that RLOF occurs for either core as the spiral-in process occurs, in which case the cores merge and some of the envelope remains. The binding energy remaining in the envelope is then given by

$$E_{\text{bind},f} - E_{\text{bind},i} = \alpha_{\text{CE}} \left(\frac{1}{2} \frac{G M_{\text{c1}} M_{\text{c2}}}{a_{\text{L}}} + E_{\text{orb},i} \right) , \tag{164}$$

where a_{L} is the separation at which RLOF occurs. A new giant star forms with a core composed of the merged progenitor cores. The mass of the new star is calculated using a Newton-Raphson iteration (see H02 for the gory details) and if any mass is lost it contributes to the stellar yield.

It is assumed that common-envelope evolution occurs quickly relative to the nuclear

burning timescales at the surface of the spiralling cores so there is no nuclear processing. This is partly for simplicity and partly because the process is already uncertain. Detailed and reliable hydrodynamical models of common envelopes are lacking. Hurley et al. (2002) suggest that a value $\alpha_{CE} \approx 3$ is possible if other energy sources such as nuclear burning shells, magnetic fields or recombination of ionization zones[1] in giants are included. For this reason α is treated as a free parameter. It is also assumed that no matter accretes from the common envelope on to either star (Hjellming & Taam, 1991).

4.4 Stellar Mergers

The treatment of stellar mergers in H02 deals with each of the 15x15 possibilities involved, there being 15 stellar types. Symmetry reduces this to half but still there are more than 100 possibilities. Fortunately, for nucleosynthesis, all that is required is knowledge of where the material goes. Rarely does a stellar merger contribute to the stellar yield and then usually via a supernova which is dealt with separately. This approach assumes there is no additional nucleosynthesis during the merging process. The new stellar envelope is formed by one of the following routes:

1. Star 2 is compact compared to the envelope of star 1 so star 2 merges with the core of star 1 to form a new core. The new envelope composition is the same as that of star 1 prior to the merger. This happens when a helium star or WD merges with a giant. It is also possible to form a new envelope from the whole of star 1 if star 1 is a MS star accreting on to e.g. a helium star. The MS star is less compact so the new core is formed from the helium star and the envelope from the MS star. Again, all of the envelope comes from star 1.

2. As above with 1 and 2 interchanged.

3. Both cores are compact compared to their envelopes so the new envelope is a mixture of the existing envelopes and both cores sink. White dwarfs, MS and HeMS stars

---

[1]At least one of the authors claims he does not believe this!

		Primary Stellar Type													
		0	1	2	3	4	5	6	7	8	9	10	11	12	13	14
Secondary Stellar Type	0	3	3	3	3	3	3	3	2	2	2	2	2	2	4	4
	1	3	3	3	3	3	3	3	2	2	2	2	2	2	4	4
	2	3	3	3	3	3	3	3	2	2	2	2	2	2	4	4
	3	3	3	3	3	3	3	3	2	2	2	2	2	2	4	4
	4	3	3	3	3	3	3	3	2	2	2	2	2	2	4	4
	5	3	3	3	3	3	3	3	2	2	2	2	2	2	4	4
	6	3	3	3	3	3	3	3	2	2	2	2	2	2	4	4
	7	1	1	1	1	1	1	1	3	3	3	3	2	2	4	4
	8	1	1	1	1	1	1	1	3	3	3	3	2	2	4	4
	9	1	1	1	1	1	1	1	3	3	3	3	2	2	4	4
	10	1	1	1	1	1	1	1	3	3	3	3	2	2	4	4
	11	1	1	1	1	1	1	1	1	1	1	1	3	3	4	4
	12	1	1	1	1	1	1	1	1	1	1	1	3	3	4	4
	13	4	4	4	4	4	4	4	4	4	4	4	4	4	4	4
	14	4	4	4	4	4	4	4	4	4	4	4	4	4	4	4

Table 9: Collision matrix. See text for details.

are treated as having no core, so are composed purely of an envelope because if they are dense enough to sink through the other star's envelope they will be caught by conditions 1 or 2 above.

4. A Thorne-Żytkow object is formed by the merger of a NS/BH with a star of stellar type ≤ 9. The envelope is removed instantaneously without any extra nucleosynthesis. WDs and other NS/BHs collide with a NS/BH to form a heavier NS/BH (BH if $M > 1.8\,\mathrm{M_\odot}$) again without any nucleosynthesis.

The route taken by each type of merger is shown in table 9. Note that collision of two HeWDs may lead to an explosion (see below).

4.5 Type Ia Supernovae and AICs

Three types of type Ia supernovae are considered here. Edge-lit detonations are thought to occur when $0.15\,\mathrm{M_\odot}$ of helium-rich matter is accreted on a dynamical timescale on to

a sub-M_{Ch} COWD. This was modelled in 2D by Livne & Arnett (1995) who made eight models with CO core mass $0.55 \leq M_{\mathrm{CO}}/\mathrm{M}_\odot \leq 0.9$ and helium layer mass M_{He} between 0.1 and $0.2\,\mathrm{M}_\odot$. The yields are fitted to functions of the form

$$\Delta M(a_{165} + b_{165}M_{\mathrm{CO}} + c_{165}M_{\mathrm{CO}}^2) \times (1 + d_{165}M_{\mathrm{He}}) \tag{165}$$

where ΔM is the amount of mass ejected in the explosion and the coefficients are given in table B20. COWDs that accrete hydrogen-rich matter are treated in the same way, with the hydrogen steadily burnt to helium then CO on the COWD surface prior to the explosion.

COWDs that accrete enough mass by steady accretion of hydrogen or helium-rich material, which is burned to CO, accretion of CO from another COWD or owing to a COWD-COWD merger, to reach the Chandrasekhar mass are blown up with the yields of Iwamoto et al.'s (1999) model DD2. They claim this model best fits observed spectra and lightcurves. The DD2 model is preferred to the more commonly used W7 model of Nomoto, Thielemann & Yokoi (1984) because W7 predicts significantly higher $^{58}\mathrm{Ni}/^{56}\mathrm{Fe}$ ratios than solar. Yields are listed in table B22.

Helium white dwarfs which accrete helium-rich matter until the total mass exceeds $0.7\,\mathrm{M}_\odot$ explode with the yields of Woosley, Taam & Weaver (1986) as shown in table B21, scaled to the ejected mass ΔM by a factor $\Delta M/0.664\mathrm{M}_\odot$. Strictly these yields are applicable only for the accretion of helium on to the helium WD but are used in the absence of any other models for the merger of two HeWDs. Such events are probably too common to represent SNeIa but may be responsible for some low-luminosity explosions.

Accretion-induced collapse to a NS owing to accretion of material on to an ONeWD, which is not really a SNIa but only occurs in binaries, produces zero yield according to Nomoto & Kondo (1991). This has recently been challenged by Qian & Wasserburg (2003) who speculate that there may be some r-processing in a wind leaving the nascent NS. The situation is unclear and in any case there are no published yields to include in the synthetic model so the yield is set to zero.

4.5.1 Novae

Accretion of hydrogen-rich material on to a WD at a rate $\dot{M}/(\mathrm{M_\odot\,yr^{-1}}) < 1.03 \times 10^{-7}$ (Warner, 1995) leads to unstable nuclear burning in explosive events called novae. During the explosion hydrogen is converted to helium and the temperature is high enough to activate the CNO, NeNa and MgAl cycles. Novae are thought to contribute a significant fraction of the Galactic content of ^{13}C, ^{15}N and ^{17}O. The most complete set of yields yet published is that of José & Hernanz (1998) who evolve 14 sequences spanning a CO/ONeWD mass range of $0.8 - 1.35\,\mathrm{M_\odot}$. Mixing of accreted material with the surface layer of the WD is essential to the explosion and mixing fractions of $25-75\%$ are considered with the mixing fraction f_{nov} a free parameter with a default value of 50%. Models CO1-6 and ONe1-7 are used for fitting to CO and ONe novae respectively, model CO7 is ignored (it uses different opacities to the other models). The fits are listed in appendix B11. The fraction of accreted matter retained after the explosion ϵ_{nov} is set to 10^{-3} although this is also a free parameter. The small value of ϵ_{nov} means these systems are unlikely to grow significantly in mass and explode as SNeIa.

Accretion of hydrogen by a HeWD was assumed to give similar novae in the original `BSE` model, however there is nothing published in the literature which relates to this probably quite common situation. It is now assumed that accretion of $0.01\,\mathrm{M_\odot}$ of hydrogen reignites helium and turns the star into a low-mass HeMS star, although there is no evidence in the form of detailed models to support this hypothesis. It burns its helium and becomes a COWD, resuming nova explosions in a similar way to the original `BSE`, albeit a few Myr later and at a slightly higher mass.

4.6 Other Binary-specific Effects

Observations of RS CVn binaries led Tout & Eggleton (1988) to introduce extra mass loss from cool giants owing to the effect of tides produced by a close companion. They give an expression

$$\dot{M} = \dot{M}_{\mathrm{R}} \left[1 + B \max \left(\frac{1}{2}, \frac{R}{R_{\mathrm{L}}} \right)^6 \right],$$ (166)

where R_{L} is the Roche-lobe radius, $\dot{M}_{\mathrm{R}}$ is the Reimers mass-loss rate and $B \approx 10^4$. As pointed out by H02 it is unclear whether this should be applied to all stars so B is a free parameter, usually set to zero.

The impact of a supernova on the companion star is not included in `BSE`, other than its effect on the orbital dynamics. Matter from the SN explosion can either be accreted by a companion or can strip the companion of matter. The latter is more likely (Wheeler, Lecar & McKee, 1975; Marietta, Burrows & Fryxell, 2000) and the companion star probably survives the stripping (Taam & Fryxell, 1984). Accretion may occur from a weak supernova such as an AIC and such a process may explain stars which are simultaneously r-process and s-process rich (Qian & Wasserburg, 2003). Given these uncertainties mass accretion and stripping from SNe are not currently included in the synthetic model.

The nucleosynthesis model used for low- and intermediate-mass stars (chapter 2) contains functions of either the instantaneous mass M (for first and second dredge-up) or the mass at the start of the TPAGB (for third dredge-up and HBB) so is not affected by mass transfer in binaries. The massive star nucleosynthesis model (chapter 3) is different because it necessarily uses M_{ZAMS} as a fitting parameter. This is a problem during binary evolution because it is likely, in binaries where both stars are of high mass, that a star accretes significant amounts material from its companion. The accreted material is dealt with in section 4.2 above. It probably mixes by a thermohaline instability with the stellar envelope. In itself this is an approximation because the star is processed internally so should not be mixed through its entire depth. However this is a problem that cannot be addressed without full evolution models which include composition gradients. The real problem occurs when the star evolves further because its surface abundances evolve according to a prescription based on M_{ZAMS} rather than the larger M. For this reason M_{ZAMS} is set to M when matter is accreted on to a MS star. The ZAMS surface abundances are also changed to the abundances after the accretion. The star then behaves as a MS star more massive than it

originally was and which has different initial abundances.

Accretion on to a post-MS star is not treated in the same way. This would lead to inconsistencies but for several important effects. First, mass loss is strongest in post-MS stars, so there is unlikely to be any mass accretion because the winds shock. Second, if both stars have evolved off the main sequence then both will have large radii and a common-envelope phase is likely. As an example, for a solar metallicity, circular binary with primary mass $M_1 = 30.000\,\mathrm{M_\odot}$ and period $P = 100\,\mathrm{d}$, the secondary must have a mass $M_2 > 29.968\,\mathrm{M_\odot}$ in order to evolve off the main sequence before mass transfer occurs and if this is the case common-envelope evolution follows with the loss of 2/3 of the mass of the system. The region of parameter space in which there are problems is very small indeed and is not resolved in the grids of stars used in chapters 5-7.

There is also the problem of stellar phases not modelled by any of the full stellar evolution codes. A good example is the low-mass helium star formed by stripping off a RG's envelope before core helium burning has finished. In this case the same fitting formulae are used as deal with helium stars (see section 3.4). Most of these systems then go on to form COWDs so the excess C and O given by the helium star fits is a reflection of their true behaviour. Of course, there is no way to test whether the fits are correct without investigation using detailed models beyond the scope of this dissertation.

Supernova kicks are included in exactly the same way as in Hurley et al. (2002) with a kick imparted to the companion according to a Maxwellian velocity distribution with dispersion σ_{SN}. Typically $\sigma_{\mathrm{SN}} = 190\,\mathrm{km\,s^{-1}}$ (Hansen & Phinney, 1997).

The Eddington limit may be applied to accreting neutron stars and black holes (Cameron & Mock, 1967),

$$\dot{M}_{\mathrm{Edd}} = f_{\mathrm{EDD}} \frac{2.08 \times 10^{-3}}{X_{\mathrm{H1}}^{\mathrm{ZAMS}}} (R_{\mathrm{NS/BH}}/\,\mathrm{R_\odot})\,\mathrm{M_\odot\,yr^{-1}} \qquad (167)$$

which sets a maximum value to the mass-accretion rate. The free parameter f_{EDD} is typically either 1.0 or 10^6, i.e. there is either a limit or not.

4.7 Example Systems

Figures 51 and 52 show the evolution of a binary with initial parameters $M_1 = 30\,\mathrm{M_\odot}$, $M_2 = 20\,\mathrm{M_\odot}$, $P = 1000\,\mathrm{d}$, $e = 0$ and $Z = 0.02$ with the MM mass-loss prescription. Mass transfer owing to RLOF from star 1 to star 2 occurs at about $6\,\mathrm{Myr}$ while star 1 is in the HG and star 2 is on the MS. Star 2 accretes $15\,\mathrm{M_\odot}$ of hydrogen-poor, helium and nitrogen-rich material raising its mass to $35\,\mathrm{M_\odot}$ and altering its surface abundances. Star 2 then evolves like a $35\,\mathrm{M_\odot}$ ZAMS star with excess helium and nitrogen in the envelope and less hydrogen, carbon and oxygen. It is also clear that most carbon and oxygen production is during the helium star phase.

Another interesting example is $M_1 = 6\,\mathrm{M_\odot}$, $M_2 = 3\,\mathrm{M_\odot}$ and $P = 40\,\mathrm{d}$ (see figure 53). The initial separation, about $100\,\mathrm{R_\odot}$, is small enough that the primary overflows its Roche lobe while on the late-HG and red-giant branch (at $68.2\,\mathrm{Myr}$), so a common envelope forms. The envelope is lost leaving a $1.1\,\mathrm{M_\odot}$ helium star and the slightly polluted secondary. The helium star evolves on the HeMS to form a HeHG and again expands, overflows its Roche lobe and transfers $0.24\,\mathrm{M_\odot}$ of material to the secondary. The important point is that this material is of very different composition to the original star – $^{12}\mathrm{C} \approx 0.4$, $^{14}\mathrm{N} \approx 0$ and $^{16}\mathrm{O} \approx 0.2$. The primary becomes a $0.82\,\mathrm{M_\odot}$ COWD. The secondary is a $3.28\,\mathrm{M_\odot}$ MS carbon star: $^{12}\mathrm{C} = 0.036$, $^{16}\mathrm{O} = 0.027$ so $\mathrm{C/O} \approx 1.8$ by number. At $320\,\mathrm{Myr}$, while in the its HG phase, the secondary overflows its Roche lobe and a common envelope forms. There is not enough energy in the orbit to drive off the envelope, even though $\alpha_{\mathrm{CE}} = 3$, so the cores merge and a new CO core, with surrounding helium-burning shell, is formed. The now single star is an EAGB star of mass $3.44\,\mathrm{M_\odot}$ with a $0.82\,\mathrm{M_\odot}$ CO core which goes on to evolve on the TPAGB – but note it is *already* a carbon star! The star has a peculiarly high core mass for its total mass so its high luminosity drives the envelope off rapidly. The few thermal pulses that occur add little extra carbon to the envelope and it is not massive enough to undergo HBB. It loses its envelope in 10^5 years and forms a $0.85\,\mathrm{M_\odot}$ COWD remnant. Such carbon-rich EAGB stars, known as *extrinsic* carbon stars, are one explanation of the mysterious dim carbon stars (Izzard & Tout, 2004).
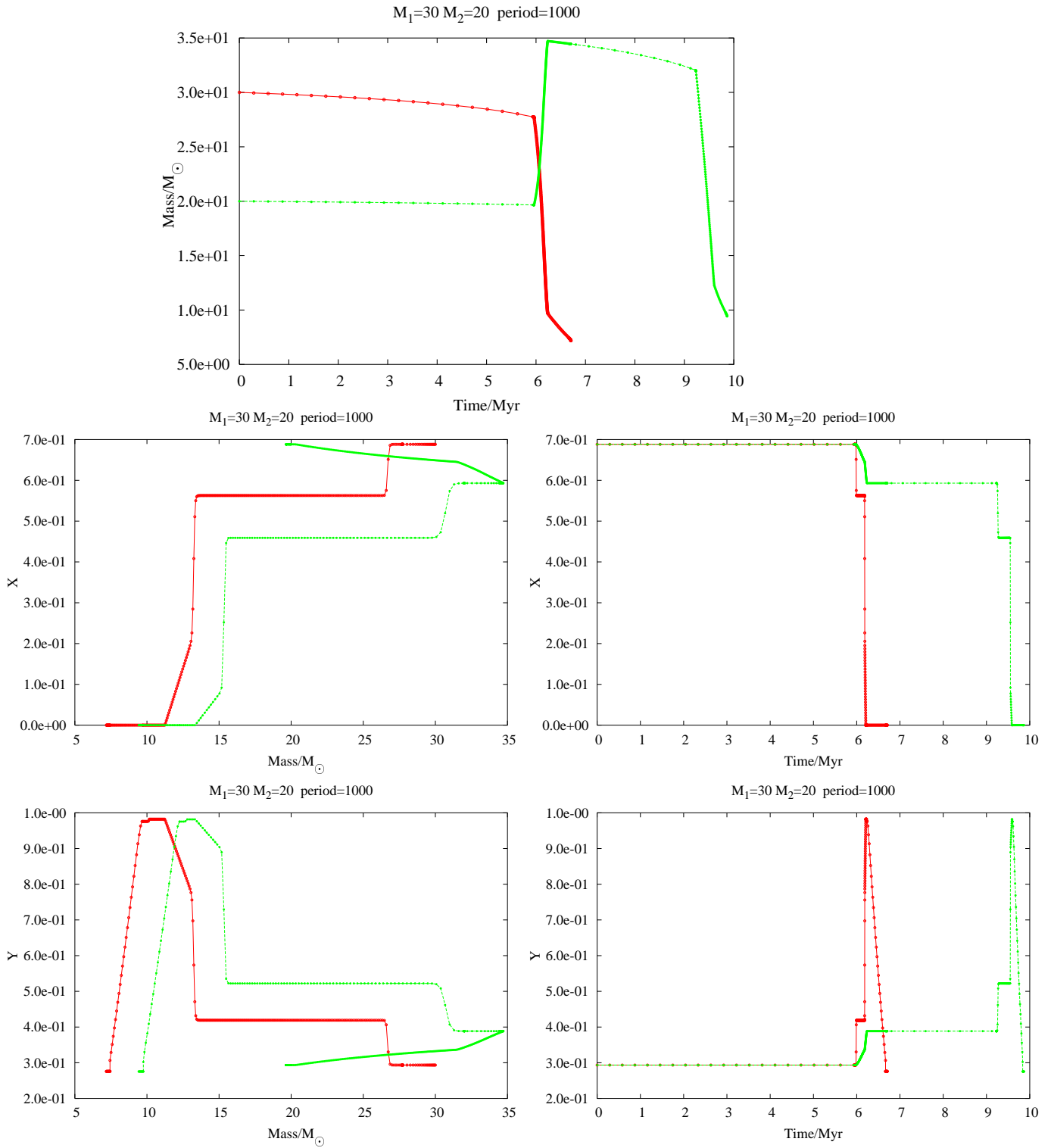
Figure 51: Stellar mass vs time, surface abundances X_{H1}, X_{He4} vs instantaneous mass and vs time for a binary with initial parameters $M_1 = 30\,M_\odot$, $M_2 = 20\,M_\odot$ and $P = 1000\,d$ (MM wind loss). Star 1 is red, star 2 is green.
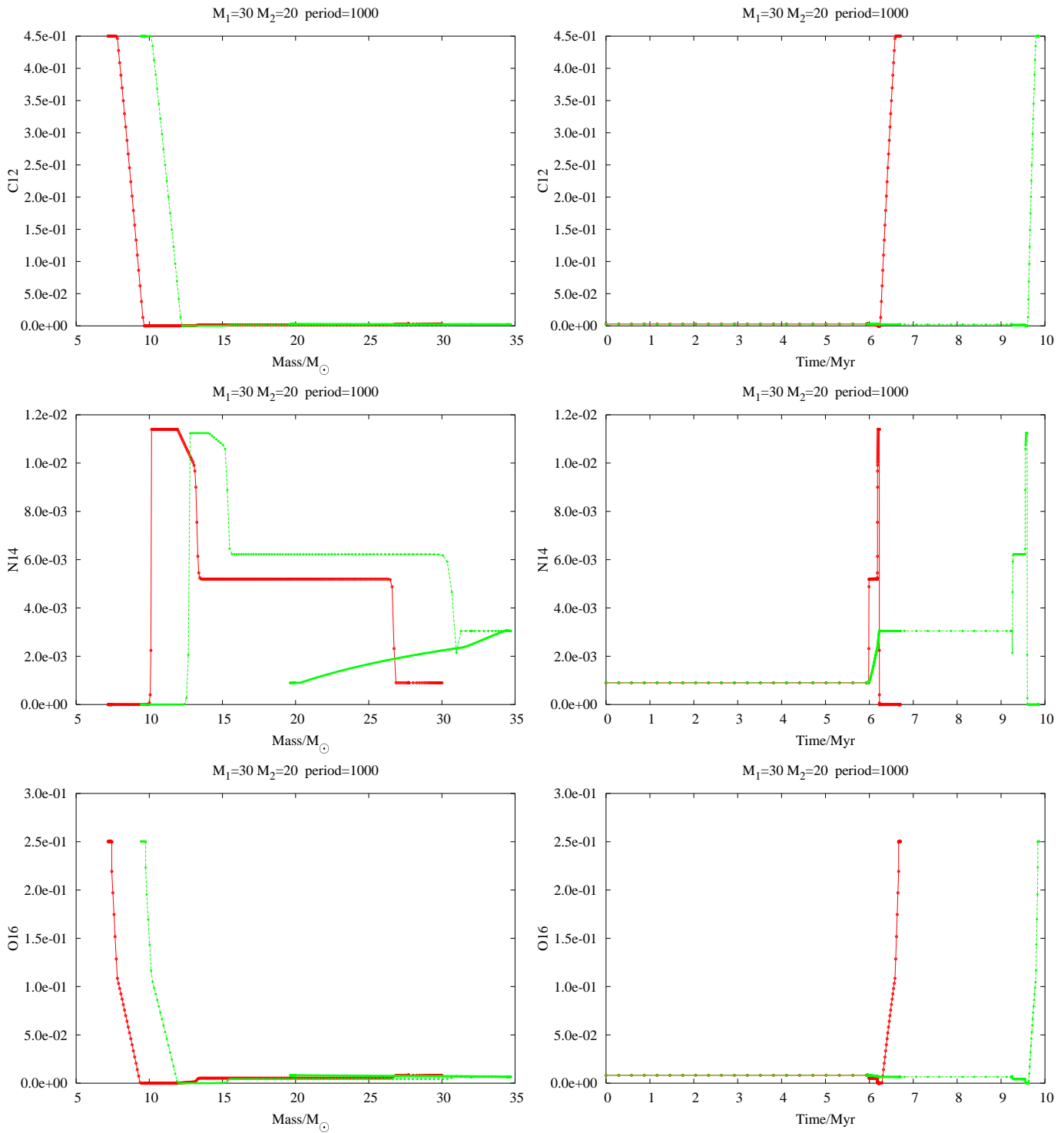
Figure 52: As Fig. 51 for X_{C12}, X_{N14} and X_{O16}.
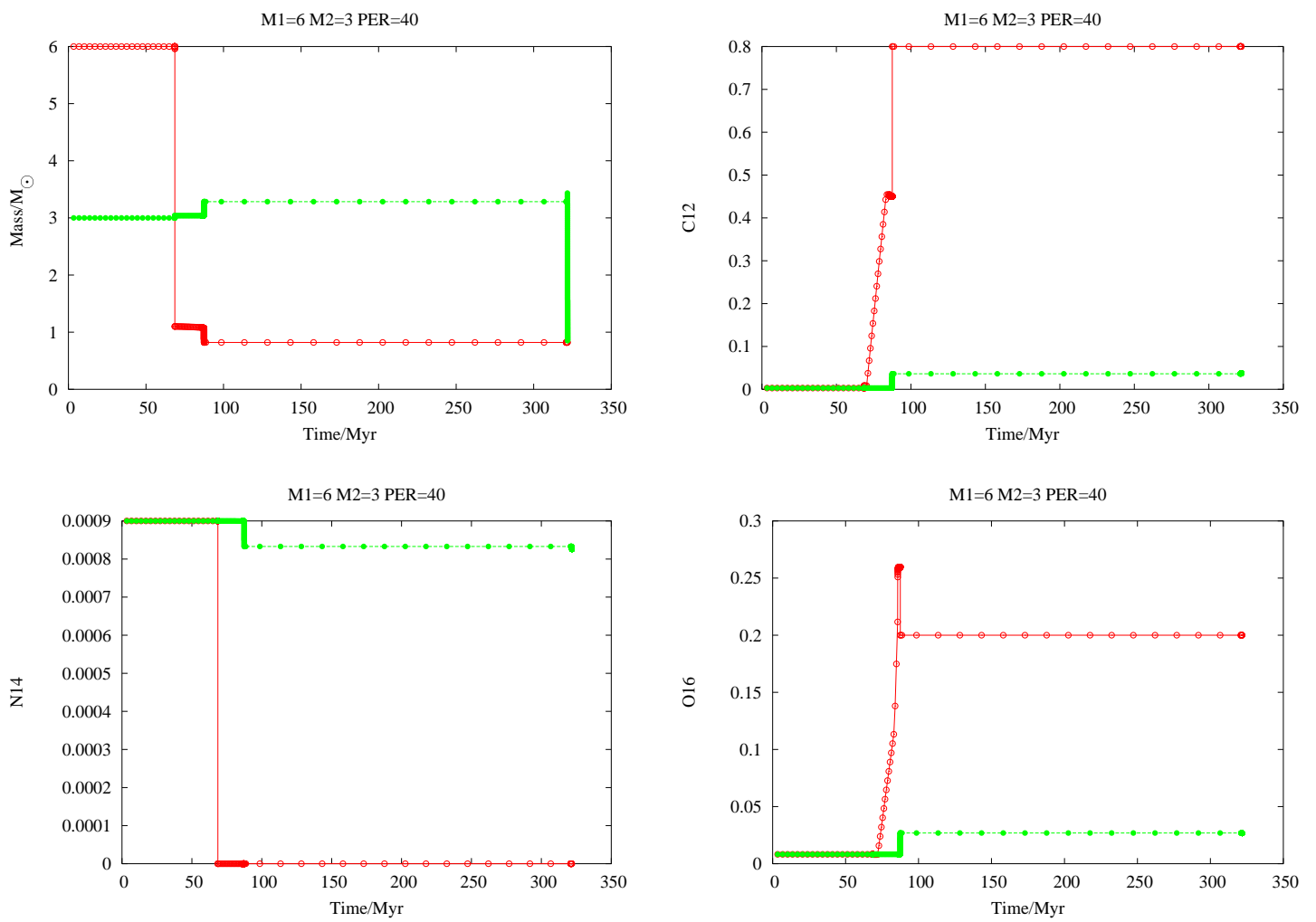
Figure 53: Extrinsic carbon star formation from a dwarf carbon star. See text for details.
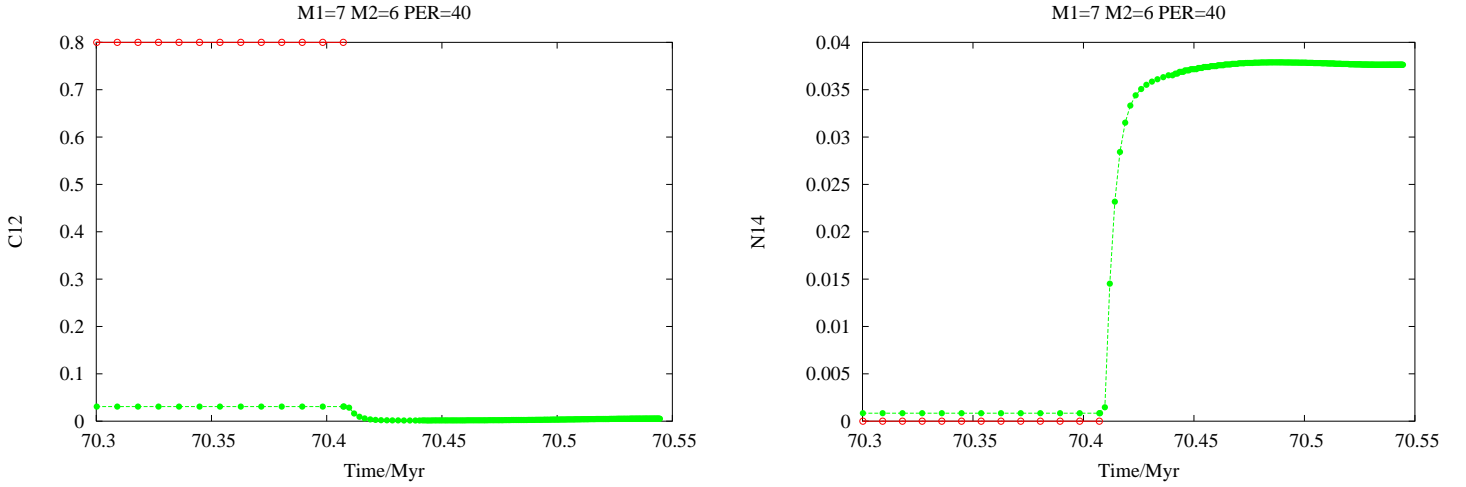
Figure 54: Formation of a nitrogen-rich giant from a dwarf carbon star. See text for details.

As a final example, a system like the above but with $M_1 = 7\,M_\odot$, $M_2 = 6\,M_\odot$ and $P = 4\,$days undergoes a similar dynamic evolution. Again the primary transfers mass during its HG and HeHG phases to the secondary which becomes a dwarf carbon star with ^{12}C $= 0.031$ and ^{16}O $= 0.024$ (C/O $= 1.72$). At this stage the secondary surface ^{14}N ($= 0.0008$) is low because the primary star has nearly zero nitrogen surface abundance. However, when the second common-envelope phase occurs the resulting single star is massive enough, at around $6.8\,M_\odot$, for HBB to be effective. Within 5×10^4 years most of the envelope ^{12}C is converted to ^{14}N (figure 54) giving terminal abundances of ^{12}C $= 0.005$, ^{16}O $= 0.022$ and ^{14}N $= 0.038$. This star is not a carbon star, rather a peculiar oxygen- and nitrogen-rich giant.

5 Stellar Yields: Fast Parameters

The previous three chapters presented a synthetic model for stellar nucleosynthesis. It now remains to answer the question of whether binaries are important in the calculation of stellar yields and how the yields vary with changes in free parameters.

5.1 Introduction

In order to calculate the yield of any isotope from a population of stars initial distributions must be chosen. Single star masses M are distributed according to the Initial Mass Function (IMF). In the case of binaries, initial distributions of primary masses M_1, secondary masses M_2, or the mass ratios $q = M_2/M_1$, and separations a, must be chosen. These distributions are not well constrained by observations. Accurate observations of initial q or a, or more likely the period P, are constrained to a few hundred nearby binaries (Popova, Tutukov & Yungelson, 1982; Abt, 1983; Goldberg, Mazeh & Latham, 2003). Star formation theory and modelling, even with present-day SPH simulations, is some way from a prediction of how, and how many, single or binary stars form. However various choices can be made based on the observations. In what follows populations of single or binary stars are considered rather than a mixture of the two.

Given a chosen set of these distributions a logarithmic grid is set up in one-dimensional M space for single stars or 3D M_1–M_2–a space for binary stars. The grid is split into n stars per dimension such that each star represents the centre of a logarithmic grid-cell of size δV where

$$\delta V = \begin{cases} \delta \ln M & \text{single stars} \\ \delta \ln M_1 \, \delta \ln M_2 \, \delta \ln a & \text{binary stars} \end{cases} \tag{168}$$

and

$$\delta \ln x = \frac{\ln x_{\max} - \ln x_{\min}}{n}, \tag{169}$$

where x represents M, M_1, M_2 or a and $x_{\max}$ and $x_{\min}$ are the grid limits. The total number of stars is denoted by N such that $N = n$ for single stars and $N = n^3$ for binary stars.

The probability of existence of star i is given by

$$\delta p_i = \Psi \delta V_i = \Psi \delta V, \tag{170}$$

because δV is a constant. Here

$$\Psi = \begin{cases} \psi(\ln M_i) & \text{single stars} \\ \psi(\ln M_{1i}) \, \phi(\ln M_{2i}) \, \chi(\ln a_i) & \text{binary stars} \end{cases} \tag{171}$$

is the probability density function for each set of stars. The single star IMF is denoted by $\psi(\ln M_i)$. In the case of binaries the primary star IMF is given by $\psi(\ln M_{1i})$, the secondary star IMF by $\phi(\ln M_{2i})$ and the initial separation distribution by $\chi(\ln a_i)$. Note that $\phi(\ln M_{2i})$ can be calculated via $\phi(q_i)$ where $q_i = M_{2i}/M_{1i}$ is the initial mass ratio.

For any output value, such as mass ejected of a given isotope, ζ_i of the star representing the grid cell δV_i a weighting factor δp_i must be applied so that the sum of the ζ_i represents the value for the whole population of stars

$$\zeta = \sum_i \delta p_i \, \zeta_i. \tag{172}$$

In the above expression δp_i represents the set of *fast parameters* which can be changed without having to rerun the stellar models. Once a whole set of ζ_i have been constructed it is a relatively quick process to sum over them for a given Ψ.

The construction of many sets of ζ_i represents changes in the set of *slow parameters* which depend on the choice of input physics. The construction of many datasets takes longer than a change in the distributions Ψ given the ζ_i, hence the name of this parameter set. This chapter deals exclusively with the fast parameters, chapter 6 deals with the slow parameters.

The usual condition on any probability distribution

$$\sum_i \delta p_i = 1 \tag{173}$$

means Ψ must be suitably normalized.

5.2 Default Model Sets

In order to construct a set of chemical yields a default set of slow parameters must be chosen upon which the fast parameters are varied. These are values thought to be typical in the literature or as were used in previous studies made with the `BSE` code (Hurley et al., 2002).

- Maximum stellar evolution time $t_{max} = 13.7\,\mathrm{Gyr}$ – the WMAP result ($\pm 0.2\,\mathrm{Gyr}$; Bennett et al., 2003) for the age of the Universe. It turns out (see section 61) that yields are not too sensitive to variation of t_{max}.

- $Z = 0.02$ – solar metallicity. The models are most likely to be as correct as possible at this metallicity, especially the phenomenological WR models which are fitted to $Z = 0.02$ models.

- Initial abundances are taken from Anders & Grevesse (1989).

- Eccentricity $e = 0$. This is for simplicity. Most interacting binary systems are expected to be circular owing to tidal circularization of the orbit. Some systems may exchange mass by winds rather than RLOF in which case non-zero eccentricity may be

important but this is neglected here in favour of a reduction in the parameter space by one dimension (and a corresponding reduction in grid runtime by a factor $n \approx 100$). Some consideration of a change in initial eccentricity is given in section 6.2.9.

- The mass-loss prescription of Hurley et al. (2002) is used for all stellar evolution phases except the TPAGB when the prescription of Karakas et al. (2002) is used. This is because the synthetic TPAGB model is calibrated with their mass-loss prescription.

- Common-envelope parameter $\alpha_{\mathrm{CE}} = 3$. Hurley et al. (2002) found $\alpha_{\mathrm{CE}} = 3$ is required to reproduce the observed number of double-degenerate binary systems.

- No Eddington limit for accretion ($f_{\mathrm{EDD}} = 10^6$).

- s-process ^{13}C pocket mass factor $\xi = 1.0$.

- SN kick velocity dispersion $\sigma_{\mathrm{SN}} = 190\,\mathrm{km\,s^{-1}}$ (Hansen & Phinney, 1997).

- No enhanced binary wind loss ($B = 0$).

- Bondi-Hoyle accretion factor $\alpha_{\mathrm{B\text{-}H}} = 3/2$.

- The fraction of matter retained in a nova explosion $f_{\mathrm{nova}} = 10^{-3}$ (Hurley et al., 2002).

- The Hurley et al. (2002) black hole mass prescription.

- The calibration of third dredge-up found by comparison to SMC and LMC carbon star luminosity distributions: $\Delta M_{\mathrm{c,min}} = -0.07$ and $\lambda_{\mathrm{min}} = 0.8 - 37.5Z = 0.05$.

It is necessary to make a selection of isotopes for study because the synthetic model currently predicts 126 isotopes. Some isotopes closely follow the behaviour of others such as the s-process groups, the α elements from type Ia supernovae etc. and so are represented by just a few isotopes. Table 10 lists the isotopes chosen.

^{1}H, ^{4}He	hydrogen, helium
^{12}C, ^{13}C, ^{14}N, ^{15}N, ^{16}O, ^{17}O	CNO
^{20}Ne, ^{21}Ne, ^{22}Ne, ^{23}Na	NeNa
^{24}Mg, ^{25}Mg, ^{26}Mg, ^{26}Al, ^{27}Al	MgAl
^{32}S, ^{36}Ar, ^{40}Ca, ^{44}Ca, ^{48}Ti, ^{52}Cr, ^{56}Fe	SNIa and HeWD-HeWD mergers
^{65}Cu	SNII
Ba, Pb, Y, Kr	s-process

Table 10: Isotopes used in fast parameter comparisons.

5.3 Definition of the yield

There are many ways to define the yield of a particular isotope j from a generation of stars. The integrated mass lost from star i as isotope j during its lifetime $t_{\max}$ is

$$\delta Y_{ij} = \delta p_i \int_0^{t_{\max}} \dot{M}(t)\, X_j(t)\, dt \tag{174}$$

where $\dot{M}(t)$ is the rate of mass loss from the system, $X_j(t)$ is the surface abundance of j and δp_i is the probability of the star's existence. The total mass lost from a population of stars as isotope j is then

$$Y_j = \sum_i \delta Y_{ij}\,. \tag{175}$$

More useful is y_j defined as the mass lost as isotope j per unit mass input to stars

$$y_j = \begin{cases} Y_j / \sum_i \left[M_i \delta p_i \right] & \text{single stars} \\ Y_j / \sum_i \left[(M_{1i} + M_{2i}) \delta p_i \right] & \text{binary stars} \end{cases} \tag{176}$$

or y_j' the mass lost as j per unit mass lost – i.e. the mass fraction of j in the ejecta

$$y_j' = \frac{Y_j}{\sum_i \delta p_i \int \dot{M}(t)\, dt}\,. \tag{177}$$

There is also p_M defined in terms of the enhancement of isotope j during the lifetime of the star relative to the initial abundance and normalized to the initial mass of the star[1]

$$\delta p_{Mij}(i, j, M_i) = \frac{\delta p_i}{M_i} \int_0^{t_{\max}} \dot{M}_i \Delta X_{ij} \, dt \,, \tag{178}$$

where M_i is the initial mass of the (single) star and $\Delta X_{ij} = X_{ij}(t) - X_{ij}(0)$ is the change in surface abundance of isotope j between its birth and time t. For binaries the idea is the same but the expression slightly different

$$\delta p_{Mij}(i, j, M_1, M_2) = \frac{\delta p_i}{(M_{1i} + M_{2i})} \int_0^{t_{\max}} \left(\dot{M}_{1i} \Delta X_{1ij} + \dot{M}_{2i} \Delta X_{2ij} \right) dt \,, \tag{179}$$

where the ΔX now refer to each star.

The population enhancement of isotope j is then

$$p_{Mj} = \sum_i \delta p_{Mij} \,. \tag{180}$$

Note p_{Mj} can be negative if an isotope is consumed rather than created.

In what follows the simpler form y_j is used because it is always positive.

5.4 Numerical Resolution

The number of stars N required to obtain an accurate sum of the yield relative to mass input y (eq. 176) is constrained by considerations of accuracy and CPU time. Figure 55 shows $y(N)$ relative to the default dataset for single (red) and binary stars (blue) for a selection of important isotopes. For single stars the default value is $N = 10^4$ and all the yields converge to within 0.5% of their default values for $N \geq 5 \times 10^3$.

Binary stars are more unpredictable owing to the increased number of grid dimensions and the plethora of interaction mechanisms involved. Supernova kick velocities are modelled by a Monte-Carlo process so slight differences in yields are also because of this. The

---

[1]This is the form used in section 2.15.

Isotope	Resolution Error/%	Timestep Error/%	Isotope	Resolution Error/%	Timestep Error/%
^{1}H	1.0	0.02	^{24}Mg	0.3	0.25
^{12}C	1.4	0.2	^{44}Ca	0.03	0.15
^{14}N	0.9	1.8	^{56}Fe	0.04	0.22
^{16}O	0.6	0.3	^{65}Cu	0.1	0.02
^{22}Ne	1.7	0.2	Ba	0.5	0.1

Table 11: Maximum errors on the integrated binary star yields y due to resolution and variable timestep effects.

default value $n = 100$ corresponds to a 3D grid of $N = n^3 = 10^6$ points. This is chosen because 10^6 models take approximately 14 hours to run on a 1.4GHz Athlon PC. Figure 55 has high-resolution, $n \geq 100$, binary data points at $n = 100, 105, 152$ and 200. The maximum error on the yield for each isotope when using an $n = 100$ data set can be approximated by the maximum difference between the $n = 100$ set and any of the $n > 100$ sets. Table 11 shows that the errors (marked *Resolution Error*) are smaller than 1.7%.

Table 55 also lists the errors induced when the timestep during the TPAGB phase is modulated by a constant factor less than 1 (columns marked *Timestep Error*). The timestep is multiplied by a factor 0.1 and 0.5 and the maximum difference between the results and the standard timestep tabulated. Only ^{14}N is affected by more than 0.5%. It is produced copiously by HBB so small changes in the burning time change the yield by 1.8%. It will be shown below that such errors are negligible compared to other sources of uncertainty.
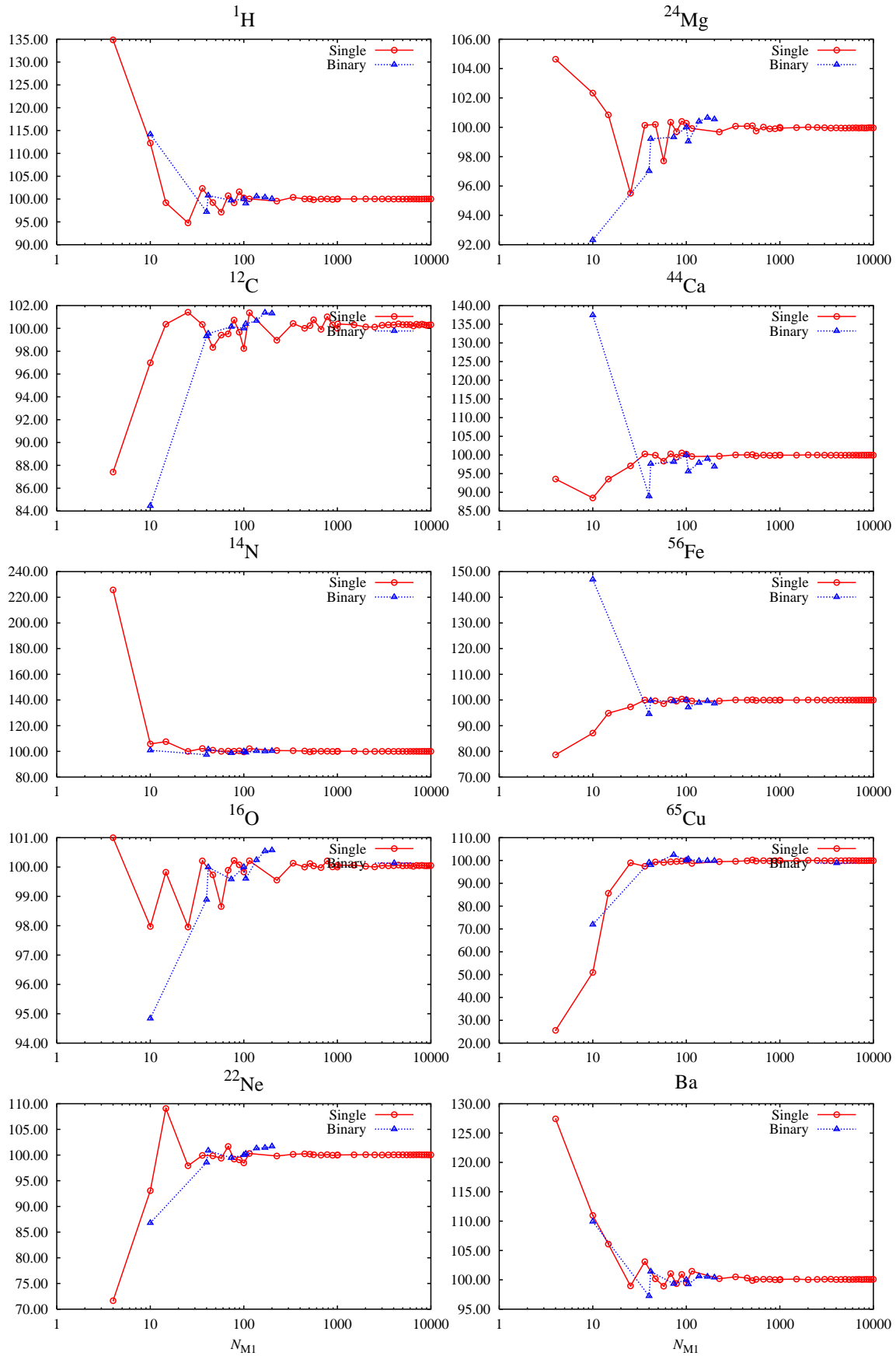
Figure 55: Variation in yield relative to $n = 10^4$ (single stars) or $n = 100$ (binary stars) for various isotopes.

5.5 Single/Primary Star Mass Distribution

The distribution of single stars, the Initial Mass Function (IMF), has long been known to approximate a power law (Salpeter, 1955), at least for stars of mass greater than about $1 \, \mathrm{M_\odot}$. Below this mass the power law flattens off and at high mass there is some uncertainty (Kroupa, 2002). The default IMF used here is that of Kroupa et al. (1993, KTG93). This, the Salpeter IMF and the one of Chabrier (2003) are compared.

The IMF is defined as a probability density function of initial stellar mass M

$$\psi(M) = \frac{dp}{dM} \tag{181}$$

such that $dp = \psi(M) \, dM$ is the probability of a star's existence between masses M and $M + dM$. It is assumed that all stars form in the mass interval $m_0 \leq M/\mathrm{M_\odot} \leq 80.0$ where m_0 is usually 0.1.

Note that

$$\frac{dp}{d \ln M} = \psi(\ln M) = M\psi(M) \tag{182}$$

is used in the grid described above.

The Salpeter IMF is a single power law in M

$$\psi(M) = AM^\alpha \tag{183}$$

with $\alpha = -2.35$ over the assumed mass range $0.1 \leq M/\mathrm{M_\odot} \leq 80$ and A normalized such that

$$\int_{0.1}^{80} \psi(M)dM = 1 \tag{184}$$

which gives

$$A = \frac{1 + \alpha}{80^{1+\alpha} - 0.1^{1+\alpha}} = 0.06031 \,. \tag{185}$$

5 Stellar Yields: Fast Parameters

The KTG93 IMF is a three part power law

$$
\psi(M) = \begin{cases}
0 & M/\mathrm{M}_\odot \leq m_0 \\
a_1(M/\mathrm{M}_\odot)^{p_1} & m_0 < M/\mathrm{M}_\odot \leq m_1 \\
a_2(M/\mathrm{M}_\odot)^{p_2} & m_1 < M/\mathrm{M}_\odot \leq m_2 \\
a_3(M/\mathrm{M}_\odot)^{p_3} & m_2 < M/\mathrm{M}_\odot \leq m_{\max} \\
0 & m > m_{\max}
\end{cases}
\tag{186}
$$

where $p_1 = -1.3$, $p_2 = -2.2$, $p_3 = -2.7$, $m_0 = 0.1$, $m_1 = 0.5$, $m_2 = 1.0$ and $m_{\max} = 80.0$. The normalization condition

$$
\int_{m_0}^{m_{\max}} \psi(M)dM = 1
\tag{187}
$$

together with continuity at m_1 and m_2 leads to

$$
\begin{aligned}
a_2^{-1} &= \frac{m_1^{p_2-p_1}}{1+p_1}\left(m_1^{1+p_1} - m_0^{1+p_1}\right) + \left(m_2^{1+p_2} - m_1^{1+p_2}\right)\frac{1}{1+p_2} \\
&\quad + \frac{m_2^{p_2-p_3}}{1+p_3}\left(m_{\max}^{1+p_3} - m_2^{1+p_3}\right),
\end{aligned}
\tag{188}
$$

$$
a_1 = a_2 m_1^{p_2-p_1}
\tag{189}
$$

and

$$
a_3 = a_2 m_2^{p_2-p_3}.
\tag{190}
$$

A recent alternative IMF is that of Chabrier (2003)

$$
\psi(\log_{10} M) = \begin{cases}
A_0 A_1 \exp\left[-(\log_{10} M/\mathrm{M}_\odot - \log_{10} M_\mathrm{C})/2\sigma^2\right] & M < 1\,\mathrm{M}_\odot \\
A_0 A_2 (M/\mathrm{M}_\odot)^{-x} & M \geq 1\,\mathrm{M}_\odot
\end{cases}
\tag{191}
$$

where $A_1 = 0.158$, $A_2 = 4.43 \times 10^{-2}$, $M_\mathrm{C} = 0.079$, $\sigma = 0.69$, $x = 1.3$ and $A_0 = 0.12024$ is

a constant which has to be introduced because Chabrier's IMF is not suitably normalized over the entire mass range. This is related to $\psi(M)$ by

$$\psi(M) = \frac{\psi(\log_{10} M)}{M \ln(10)} \tag{192}$$

so at high mass $\psi(M)$ is a power law with slope $\alpha = -2.3$ (compared to KTG93's -2.7).

Figure 56 compares the above IMFs. The Salpeter IMF reduces the number of intermediate-mass stars relative to the KTG93 IMF and compensates for this with an increase in low- and high-mass stars. Low-mass stars with $M \lesssim 0.95 \, \mathrm{M_\odot}$ do not leave the main sequence in 13.7 Gyr and so do not contribute to the stellar yield. However, the mass function is normalized over the entire mass range so these stars and the lower-mass limit m_0 are still important. The Chabrier IMF is similar to KTG93 for $M < 2 \, \mathrm{M_\odot}$ but over-produces intermediate- and high-mass stars by up to a factor 10 at $M = 80 \, \mathrm{M_\odot}$ relative to KTG93. This is indicative of the present-day uncertainty in mass determinations of high-mass stars.

Table 12 shows the yield y relative to mass input to stars for the KTG93, Salpeter and Chabrier IMFs. The default data set is KTG93, the other sets are shown as percentage fractions of the default so an under-production relative to KTG93 is denoted by a figure less than 100% and over-production by a figure greater than 100%. The rightmost column shows the limits between which the yield varies for the data sets in the table.

The Salpeter IMF over-produces everything relative to KTG93 owing to the excess of high-mass stars. The increase in s-process elements and $^{13}\mathrm{C}$ is small because these are mainly produced in intermediate-mass stars. Typically y increases to about twice the KTG93 value for isotopes heavier than helium (153% for $^{14}\mathrm{N}$, 241% for $^{16}\mathrm{O}$). The SNIa isotopes, except $^{56}\mathrm{Fe}$ from SNeII/Ib/c, are produced in tiny amounts due to the lack of a production mechanism in single stars so any yield is due to the presence of the isotope at $t = 0$. These isotopic yields increase with the Salpeter IMF owing to the increased number of massive stars and associated wind loss. The yield of the SnII isotope $^{65}\mathrm{Cu}$ also doubles due to the excess number of massive stars and core-collapse supernovae.

The Chabrier IMF shows a similar pattern to the Salpeter IMF but is even more extreme.

IMF	KTG93	Salpeter $\alpha = -2.2$	Chabrier	
Isotope	y	Relative Yields %	%	Limits
^{1}H	1.857×10^{-1}	116	200	$(1.86 < 1.86 < 3.72) \times 10^{-01}$
^{4}He	1.044×10^{-1}	137	227	$(1.04 < 1.04 < 2.37) \times 10^{-01}$
^{12}C	4.589×10^{-3}	209	320	$(4.59 < 4.59 < 14.70) \times 10^{-03}$
^{13}C	3.609×10^{-5}	124	213	$(3.61 < 3.61 < 7.67) \times 10^{-05}$
^{14}N	9.562×10^{-4}	153	250	$(9.56 < 9.56 < 23.95) \times 10^{-04}$
^{15}N	1.185×10^{-6}	188	295	$(1.18 < 1.18 < 3.50) \times 10^{-06}$
^{16}O	8.372×10^{-3}	241	364	$(8.37 < 8.37 < 30.44) \times 10^{-03}$
^{17}O	3.398×10^{-6}	103	186	$(3.40 < 3.40 < 6.31) \times 10^{-06}$
^{20}Ne	1.178×10^{-3}	202	313	$(1.18 < 1.18 < 3.69) \times 10^{-03}$
^{21}Ne	3.882×10^{-6}	194	305	$(3.88 < 3.88 < 11.83) \times 10^{-06}$
^{22}Ne	3.776×10^{-4}	189	295	$(3.78 < 3.78 < 11.14) \times 10^{-04}$
^{23}Na	4.457×10^{-5}	177	283	$(4.46 < 4.46 < 12.61) \times 10^{-05}$
^{24}Mg	3.715×10^{-4}	208	321	$(3.71 < 3.71 < 11.91) \times 10^{-04}$
^{25}Mg	7.992×10^{-5}	201	313	$(7.99 < 7.99 < 25.05) \times 10^{-05}$
^{26}Al	4.698×10^{-7}	219	339	$(4.70 < 4.70 < 15.93) \times 10^{-07}$
^{26}Mg	8.353×10^{-5}	211	326	$(8.35 < 8.35 < 27.19) \times 10^{-05}$
^{27}Al	6.130×10^{-5}	225	343	$(6.13 < 6.13 < 21.03) \times 10^{-05}$
^{32}S	4.278×10^{-4}	210	326	$(4.28 < 4.28 < 13.93) \times 10^{-04}$
^{36}Ar	8.542×10^{-5}	216	334	$(8.54 < 8.54 < 28.52) \times 10^{-05}$
^{40}Ca	5.265×10^{-5}	207	321	$(5.26 < 5.26 < 16.90) \times 10^{-05}$
^{44}Ca	9.134×10^{-7}	185	292	$(9.13 < 9.13 < 26.69) \times 10^{-07}$
^{48}Ti	1.704×10^{-6}	189	298	$(1.70 < 1.70 < 5.08) \times 10^{-06}$
^{52}Cr	5.687×10^{-6}	147	241	$(5.69 < 5.69 < 13.69) \times 10^{-06}$
^{56}Fe	1.018×10^{-3}	190	300	$(1.02 < 1.02 < 3.05) \times 10^{-03}$
^{65}Cu	9.997×10^{-6}	205	324	$(10.00 < 10.00 < 32.35) \times 10^{-06}$
Ba	8.060×10^{-9}	116	201	$(8.06 < 8.06 < 16.23) \times 10^{-09}$
Kr	9.696×10^{-8}	119	208	$(9.70 < 9.70 < 20.21) \times 10^{-08}$
Pb	7.660×10^{-9}	118	204	$(7.66 < 7.66 < 15.66) \times 10^{-09}$
Y	1.496×10^{-8}	104	187	$(1.50 < 1.50 < 2.80) \times 10^{-08}$

Table 12: Single star yields relative to mass input y with variation of the single star IMF. The leftmost column gives the isotope, the second column the default yield y of the isotope and the next two columns the yield relative to the default with the Salpeter or Chabrier IMF. The final column shows the limits between which y varies, the central value is the default value.
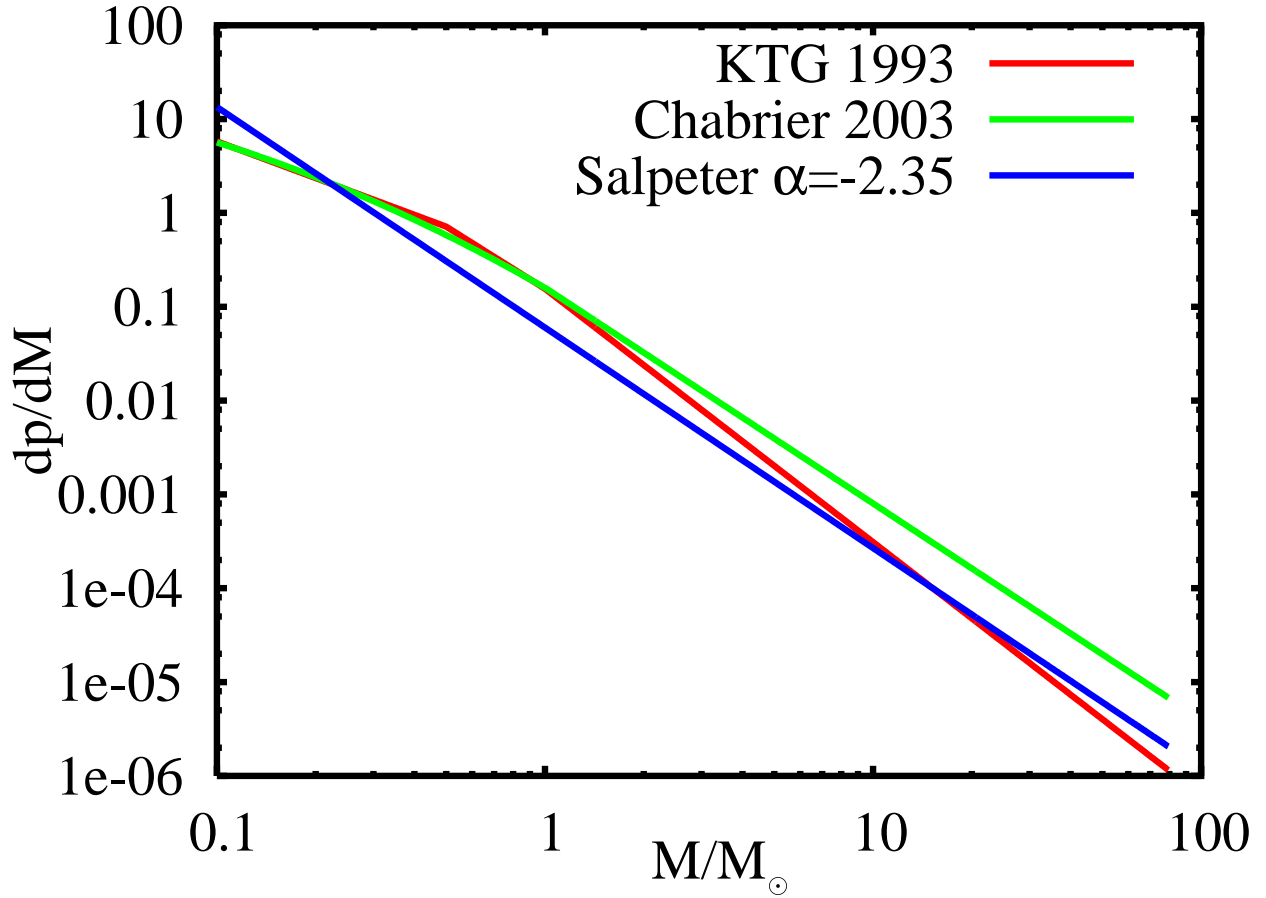
Figure 56: Single star IMFs.

Both intermediate- and high-mass stars are over-produced with respect to the KTG93 IMF, so the yields of all the isotopes increase to between 186 and 364% of the KTG93 values. The s-process elements increase by about 200%, the SNIa and SNIb/c/II isotopes by about 300%, ^{14}N, produced by intermediate-mass AGB stars and high-mass WR stars, by 250%, while ^{12}C and ^{16}O increase by 320% and 364% respectively owing to an increased number of WR stars and core-collapse supernovae. Because total probability must equal 1 some stars must be removed to make way for these excess intermediate- and high-mass stars. In this case these stars are around $0.7 \, \mathrm{M}_\odot$, see figure 56 where the green line drops below the red line, and so make no contribution to the stellar yield and so there is no associated drop in the yield.

The minimum possible stellar mass m_0 is 0.1 for the KTG93 IMF. As explained above,

IMF	KTG93	KTG93 $m_0 = 0.8$	KTG93 $m_0 = 1.2$	KTG93 $m_0 = 8.0$	
Isotope	y	Relative Yields %	%	%	Limits
^{1}H	1.857×10^{-1}	202	241	230	$(1.86 < 1.86 < 4.47) \times 10^{-01}$
^{4}He	1.044×10^{-1}	202	245	315	$(1.04 < 1.04 < 3.29) \times 10^{-01}$
^{12}C	4.589×10^{-3}	202	266	643	$(4.59 < 4.59 < 29.49) \times 10^{-03}$
^{13}C	3.609×10^{-5}	202	250	239	$(3.61 < 3.61 < 9.02) \times 10^{-05}$
^{14}N	9.562×10^{-4}	202	257	345	$(9.56 < 9.56 < 32.97) \times 10^{-04}$
^{15}N	1.185×10^{-6}	202	249	780	$(1.18 < 1.18 < 9.24) \times 10^{-06}$
^{16}O	8.372×10^{-3}	202	262	951	$(8.37 < 8.37 < 79.65) \times 10^{-03}$
^{17}O	3.398×10^{-6}	202	260	82	$(2.78 < 3.40 < 8.83) \times 10^{-06}$
^{20}Ne	1.178×10^{-3}	202	257	770	$(1.18 < 1.18 < 9.07) \times 10^{-03}$
^{21}Ne	3.882×10^{-6}	202	260	890	$(3.88 < 3.88 < 34.56) \times 10^{-06}$
^{22}Ne	3.776×10^{-4}	202	267	519	$(3.78 < 3.78 < 19.59) \times 10^{-04}$
^{23}Na	4.457×10^{-5}	202	263	608	$(4.46 < 4.46 < 27.11) \times 10^{-05}$
^{24}Mg	3.715×10^{-4}	202	257	769	$(3.71 < 3.71 < 28.57) \times 10^{-04}$
^{25}Mg	7.992×10^{-5}	202	262	744	$(7.99 < 7.99 < 59.45) \times 10^{-05}$
^{26}Al	4.698×10^{-7}	202	270	831	$(4.70 < 4.70 < 39.06) \times 10^{-07}$
^{26}Mg	8.353×10^{-5}	202	261	795	$(8.35 < 8.35 < 66.40) \times 10^{-05}$
^{27}Al	6.130×10^{-5}	202	261	893	$(6.13 < 6.13 < 54.76) \times 10^{-05}$
^{32}S	4.278×10^{-4}	202	261	915	$(4.28 < 4.28 < 39.14) \times 10^{-04}$
^{36}Ar	8.542×10^{-5}	202	262	941	$(8.54 < 8.54 < 80.40) \times 10^{-05}$
^{40}Ca	5.265×10^{-5}	202	260	874	$(5.26 < 5.26 < 46.00) \times 10^{-05}$
^{44}Ca	9.134×10^{-7}	202	256	753	$(9.13 < 9.13 < 68.75) \times 10^{-07}$
^{48}Ti	1.704×10^{-6}	202	259	838	$(1.70 < 1.70 < 14.28) \times 10^{-06}$
^{52}Cr	5.687×10^{-6}	202	247	443	$(5.69 < 5.69 < 25.21) \times 10^{-06}$
^{56}Fe	1.018×10^{-3}	202	259	837	$(1.02 < 1.02 < 8.52) \times 10^{-03}$
^{65}Cu	9.997×10^{-6}	202	270	1197	$(10.00 < 10.00 < 119.70) \times 10^{-06}$
Ba	8.060×10^{-9}	202	253	169	$(8.06 < 8.06 < 20.39) \times 10^{-09}$
Kr	9.696×10^{-8}	202	261	112	$(9.70 < 9.70 < 25.33) \times 10^{-08}$
Pb	7.660×10^{-9}	202	251	185	$(7.66 < 7.66 < 19.24) \times 10^{-09}$
Y	1.496×10^{-8}	202	264	63	$(0.94 < 1.50 < 3.95) \times 10^{-08}$

Table 13: As table 12 but for variation of the KTG93 parameter m_0.

IMF1 IMF2 Sepdist	KTG93 Flat-Q Flat ln(a)	Salpeter $\alpha = -2.2$ Flat-Q Flat ln(a)	Chabrier Flat-Q Flat ln(a)	
Isotope	y	Relative Yields %	%	Limits
^{1}H	1.898×10^{-1}	109	190	$(1.90 < 1.90 < 3.61) \times 10^{-01}$
^{4}He	1.019×10^{-1}	126	215	$(1.02 < 1.02 < 2.19) \times 10^{-01}$
^{12}C	5.735×10^{-3}	200	320	$(5.74 < 5.74 < 18.34) \times 10^{-03}$
^{13}C	6.111×10^{-5}	113	203	$(6.11 < 6.11 < 12.39) \times 10^{-05}$
^{14}N	8.111×10^{-4}	136	232	$(8.11 < 8.11 < 18.80) \times 10^{-04}$
^{15}N	9.950×10^{-6}	147	253	$(9.95 < 9.95 < 25.22) \times 10^{-06}$
^{16}O	9.561×10^{-3}	211	334	$(9.56 < 9.56 < 31.93) \times 10^{-03}$
^{17}O	6.256×10^{-6}	124	221	$(6.26 < 6.26 < 13.81) \times 10^{-06}$
^{20}Ne	1.186×10^{-3}	185	297	$(1.19 < 1.19 < 3.52) \times 10^{-03}$
^{21}Ne	3.719×10^{-6}	179	292	$(3.72 < 3.72 < 10.87) \times 10^{-06}$
^{22}Ne	2.842×10^{-4}	197	314	$(2.84 < 2.84 < 8.92) \times 10^{-04}$
^{23}Na	3.707×10^{-5}	171	281	$(3.71 < 3.71 < 10.43) \times 10^{-05}$
^{24}Mg	4.228×10^{-4}	177	287	$(4.23 < 4.23 < 12.12) \times 10^{-04}$
^{25}Mg	7.309×10^{-5}	189	305	$(7.31 < 7.31 < 22.30) \times 10^{-05}$
^{26}Al	3.985×10^{-7}	213	341	$(3.98 < 3.98 < 13.57) \times 10^{-07}$
^{26}Mg	7.733×10^{-5}	198	316	$(7.73 < 7.73 < 24.40) \times 10^{-05}$
^{27}Al	5.920×10^{-5}	207	328	$(5.92 < 5.92 < 19.41) \times 10^{-05}$
^{32}S	6.028×10^{-4}	166	274	$(6.03 < 6.03 < 16.54) \times 10^{-04}$
^{36}Ar	1.251×10^{-4}	167	276	$(1.25 < 1.25 < 3.46) \times 10^{-04}$
^{40}Ca	9.848×10^{-5}	148	251	$(9.85 < 9.85 < 24.72) \times 10^{-05}$
^{44}Ca	3.602×10^{-5}	85	164	$(3.06 < 3.60 < 5.89) \times 10^{-05}$
^{48}Ti	3.267×10^{-5}	86	165	$(2.81 < 3.27 < 5.40) \times 10^{-05}$
^{52}Cr	7.949×10^{-5}	91	173	$(7.27 < 7.95 < 13.75) \times 10^{-05}$
^{56}Fe	2.485×10^{-3}	125	218	$(2.49 < 2.49 < 5.43) \times 10^{-03}$
^{65}Cu	8.835×10^{-6}	192	314	$(8.83 < 8.83 < 27.74) \times 10^{-06}$
Ba	6.505×10^{-9}	112	197	$(6.50 < 6.50 < 12.80) \times 10^{-09}$
Kr	6.366×10^{-8}	113	202	$(6.37 < 6.37 < 12.85) \times 10^{-08}$
Pb	6.453×10^{-9}	113	198	$(6.45 < 6.45 < 12.80) \times 10^{-09}$
Y	8.861×10^{-9}	102	186	$(8.86 < 8.86 < 16.48) \times 10^{-09}$

Table 14: Binary star yields relative to mass input y with variation primary star mass distribution.

raising m_0 does not matter because the stars around $M \lesssim 0.95\,M_\odot$ have zero yield in 13.7 Gyr (at solar metallicity) *but* the IMF must still be suitably normalized. As shown in table 13 when m_0 is raised to $0.8\,M_\odot$ (as was done for the primary mass distribution in Hurley et al., 2002) all the y yields are doubled because more mass goes into massive stars. A change of m_0 also affects the secondary star q distribution (see section 5.6). Further increase of m_0, which is not justified by observations e.g. Goldberg et al. (2003), causes further increase in the yields although the effect is not uniform because m_0 rises above the $0.95\,M_\odot$ limit.

Primary star masses are thought to be distributed according to the single star IMF (Popova et al., 1982). Binary yields for various primary mass distributions show trends similar to the single-star yields for a varying IMF, as shown in table 14.

In conclusion, while the Salpeter IMF is based on limited data and old models, two newer IMFs (KTG93 and Chabrier) still lead to quite different yields. This is due to the different slope at intermediate and high mass (-2.7 for KTG93, -2.3 for Chabrier) which is the hardest mass range to measure. The minimum stellar mass is important for normalization of the IMF and variation in a reasonable range alters all single-star yields by up to a factor of two.

5.6 Secondary Star Mass Distribution

Binary stars are distributed on a 3D grid of the primary mass M_1, assumed to be KTG93, secondary mass M_2 and separation a, assumed to be flat in $\ln a$ between 3 and $10^4\,\mathrm{R_\odot}$ (see section 5.7). The secondary mass is then distributed according to a distribution $\phi(M_2)$ in the range $0.1 \leq M_2/\mathrm{M_\odot} \leq 80$. It is conventional to use $\phi(q)$ where $q = M_2/M_1$ is the mass ratio. For insertion into eq. (171) $\phi(q)$ must be related to $\phi(\ln M_2)$. For a given M_1,

$$\frac{dp}{dq} = \phi(q) \tag{193}$$

then

$$dq = \frac{dM_2}{M_1} = \frac{M_2\, d\ln M_2}{M_1} = q\, d\ln M_2 \tag{194}$$

so

$$q\phi(q) = q\frac{dp}{dq} = \frac{dp}{d\ln M_2} = \phi(\ln M_2) \tag{195}$$

and only an extra factor of q is required.

The default distribution is a flat distribution in q for $q \leq 1$ and zero otherwise. However this is not as simple as it seems! For a given M_1 there is a minimum value of q given by

$$q_{\min} = \frac{0.1\,\mathrm{M_\odot}}{M_1}, \tag{196}$$

so the distribution is only flat in q in the range $q_{\min} \leq q \leq 1$. Because $q_{\min}$ is a function of M_1 the probability density function for the population as a whole, which is what must be used to compare with observations, is *not* flat in q! However, as the minimum observable primary star mass m_0 is increased the simulated population approaches a true flat-q distribution. To illustrate this, figure 57 shows $d\Psi/dq$ vs q for a stellar population[2] for two values of m_0, $0.1\,\mathrm{M_\odot}$ and $0.5\,\mathrm{M_\odot}$, in 20 uniformly-spaced bins. Recent observations of spectroscopic binaries of Goldberg et al. (2003) are also plotted. The simulated flat-q

---

[2]The population consists of 10^7 stars, 100×100 in $M_1 \times a$ space, 1000 stars in M_2
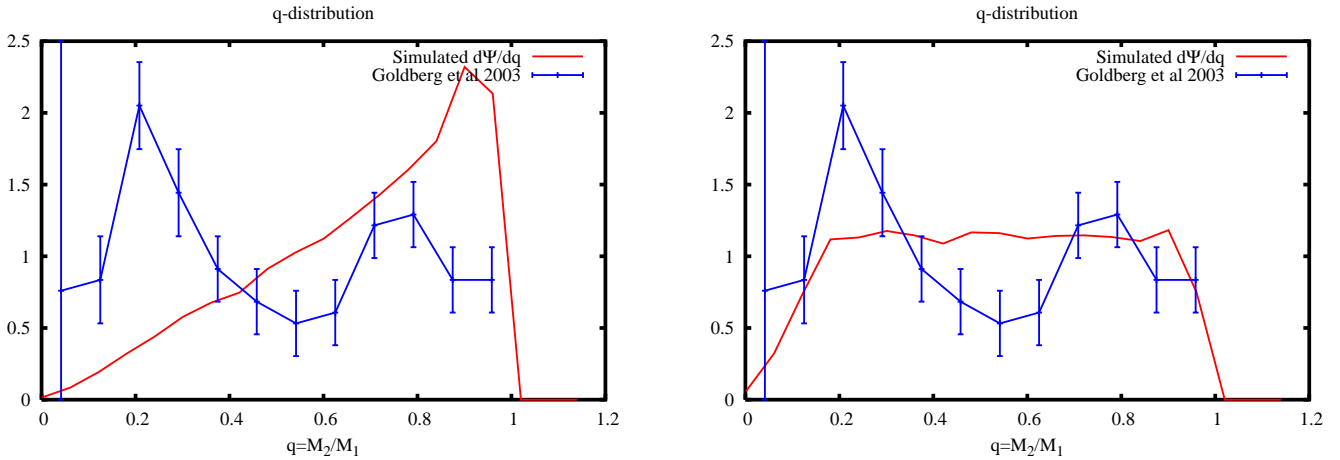
Figure 57: $d\Psi(M_1, q, a)/dq$ vs q (red lines) for a flat-q distribution. The left panel is for $m_0 = 0.1$, the right panel for $m_0 = 0.5$. Also shown (in blue) is the observed spectroscopic binary q-distribution (Goldberg et al., 2003).

distribution with $m_0 = 0.1\,\mathrm{M}_\odot$ peaks at $q = 1$ while with $m_0 = 0.5\,\mathrm{M}_\odot$ the simulated distribution is truly flat above $q = 0.2$. However, it is difficult to observe binaries with low-mass primaries so observed distributions prefer a higher m_0 (e.g. $0.5\,\mathrm{M}_\odot$) even if the true value is lower (e.g. $0.1\,\mathrm{M}_\odot$).

For single stars the only effect on stellar yields of choosing m_0 higher than 0.1, provided $m_0 \lesssim 0.9$, is to change the normalization of the IMF because the yield of low-mass stars is negligible in 13.7 Gyr. The change in yields owing to variation of m_0 in binaries is shown in table 15. As with the single stars the effect is to alter the normalization of the distribution provided $m_0 \leq 1\,\mathrm{M}_\odot$. This seems reasonable given that Goldberg et al. (2003) measure primary masses down to $0.4\,\mathrm{M}_\odot$ and secondaries down to $0.1\,\mathrm{M}_\odot$.

Other forms of $\psi(q)$ have been suggested in the literature. As extreme examples Garmany, Conti & Massey (1980) suggest $\phi(q) \propto q^{0.5}$ from a survey of O-stars and as a complete, and unjustified, contrast $\phi(q) \propto q^{-1.5}$ is also considered. It is perhaps also reasonable to assume the secondary star is taken at random from the primary IMF (Duquennoy & Mayor, 1991) so $\phi(M_2) = \psi(M_1)$ with $q \leq 1$. These distributions are shown in figure 58 which facilitate comparison of the simulated $d\Psi/dq$ with the most recent observations (Goldberg et al., 2003). It is impossible to distinguish between the flat-q distribution and

IMF1 IMF2 Sepdist	KTG93 Flat-Q Flat ln(a)	KTG93 $m_0 = 0.1$ Flat-Q Flat ln(a)	KTG93 $m_0 = 0.5$ Flat-Q Flat ln(a)	KTG93 $m_0 = 1.0$ Flat-Q Flat ln(a)	KTG93 $m_0 = 8.0$ Flat-Q Flat ln(a)	
Isotope	y	Relative Yields %	%	%	%	Limits
^{1}H	$1.898{\times}10^{-1}$	100	156	229	207	$(1.90 < 1.90 < 4.35){\times}10^{-01}$
^{4}He	$1.019{\times}10^{-1}$	100	156	232	302	$(1.02 < 1.02 < 3.08){\times}10^{-01}$
^{12}C	$5.735{\times}10^{-3}$	100	158	241	794	$(5.74 < 5.74 < 45.53){\times}10^{-03}$
^{13}C	$6.111{\times}10^{-5}$	100	158	240	138	$(6.11 < 6.11 < 14.64){\times}10^{-05}$
^{14}N	$8.111{\times}10^{-4}$	100	157	238	305	$(8.11 < 8.11 < 24.77){\times}10^{-04}$
^{15}N	$9.950{\times}10^{-6}$	100	158	241	178	$(9.95 < 9.95 < 24.02){\times}10^{-06}$
^{16}O	$9.561{\times}10^{-3}$	100	158	240	910	$(9.56 < 9.56 < 87.05){\times}10^{-03}$
^{17}O	$6.256{\times}10^{-6}$	100	158	240	141	$(6.26 < 6.26 < 15.03){\times}10^{-06}$
^{20}Ne	$1.186{\times}10^{-3}$	100	157	237	746	$(1.19 < 1.19 < 8.85){\times}10^{-03}$
^{21}Ne	$3.719{\times}10^{-6}$	100	157	238	787	$(3.72 < 3.72 < 29.27){\times}10^{-06}$
^{22}Ne	$2.842{\times}10^{-4}$	100	158	241	714	$(2.84 < 2.84 < 20.29){\times}10^{-04}$
^{23}Na	$3.707{\times}10^{-5}$	100	157	239	646	$(3.71 < 3.71 < 23.93){\times}10^{-05}$
^{24}Mg	$4.228{\times}10^{-4}$	100	157	238	654	$(4.23 < 4.23 < 27.66){\times}10^{-04}$
^{25}Mg	$7.309{\times}10^{-5}$	100	157	239	760	$(7.31 < 7.31 < 55.56){\times}10^{-05}$
^{26}Al	$3.985{\times}10^{-7}$	100	158	243	967	$(3.98 < 3.98 < 38.52){\times}10^{-07}$
^{26}Mg	$7.733{\times}10^{-5}$	100	157	239	819	$(7.73 < 7.73 < 63.35){\times}10^{-05}$
^{27}Al	$5.920{\times}10^{-5}$	100	157	239	889	$(5.92 < 5.92 < 52.61){\times}10^{-05}$
^{32}S	$6.028{\times}10^{-4}$	100	158	240	620	$(6.03 < 6.03 < 37.39){\times}10^{-04}$
^{36}Ar	$1.251{\times}10^{-4}$	100	158	240	620	$(1.25 < 1.25 < 7.76){\times}10^{-04}$
^{40}Ca	$9.848{\times}10^{-5}$	100	158	240	442	$(9.85 < 9.85 < 43.50){\times}10^{-05}$
^{44}Ca	$3.602{\times}10^{-5}$	100	158	243	19	$(0.69 < 3.60 < 8.74){\times}10^{-05}$
^{48}Ti	$3.267{\times}10^{-5}$	100	158	243	39	$(1.28 < 3.27 < 7.93){\times}10^{-05}$
^{52}Cr	$7.949{\times}10^{-5}$	100	158	242	32	$(2.58 < 7.95 < 19.25){\times}10^{-05}$
^{56}Fe	$2.485{\times}10^{-3}$	100	158	241	289	$(2.49 < 2.49 < 7.19){\times}10^{-03}$
^{65}Cu	$8.835{\times}10^{-6}$	100	158	243	929	$(8.83 < 8.83 < 82.07){\times}10^{-06}$
Ba	$6.505{\times}10^{-9}$	100	156	233	201	$(6.50 < 6.50 < 15.17){\times}10^{-09}$
Kr	$6.366{\times}10^{-8}$	100	157	237	157	$(6.37 < 6.37 < 15.08){\times}10^{-08}$
Pb	$6.453{\times}10^{-9}$	100	156	233	211	$(6.45 < 6.45 < 15.02){\times}10^{-09}$
Y	$8.861{\times}10^{-9}$	100	157	238	109	$(8.86 < 8.86 < 21.10){\times}10^{-09}$

Table 15: Binary yields relative to mass input y with variation of the minimum primary mass m_0.
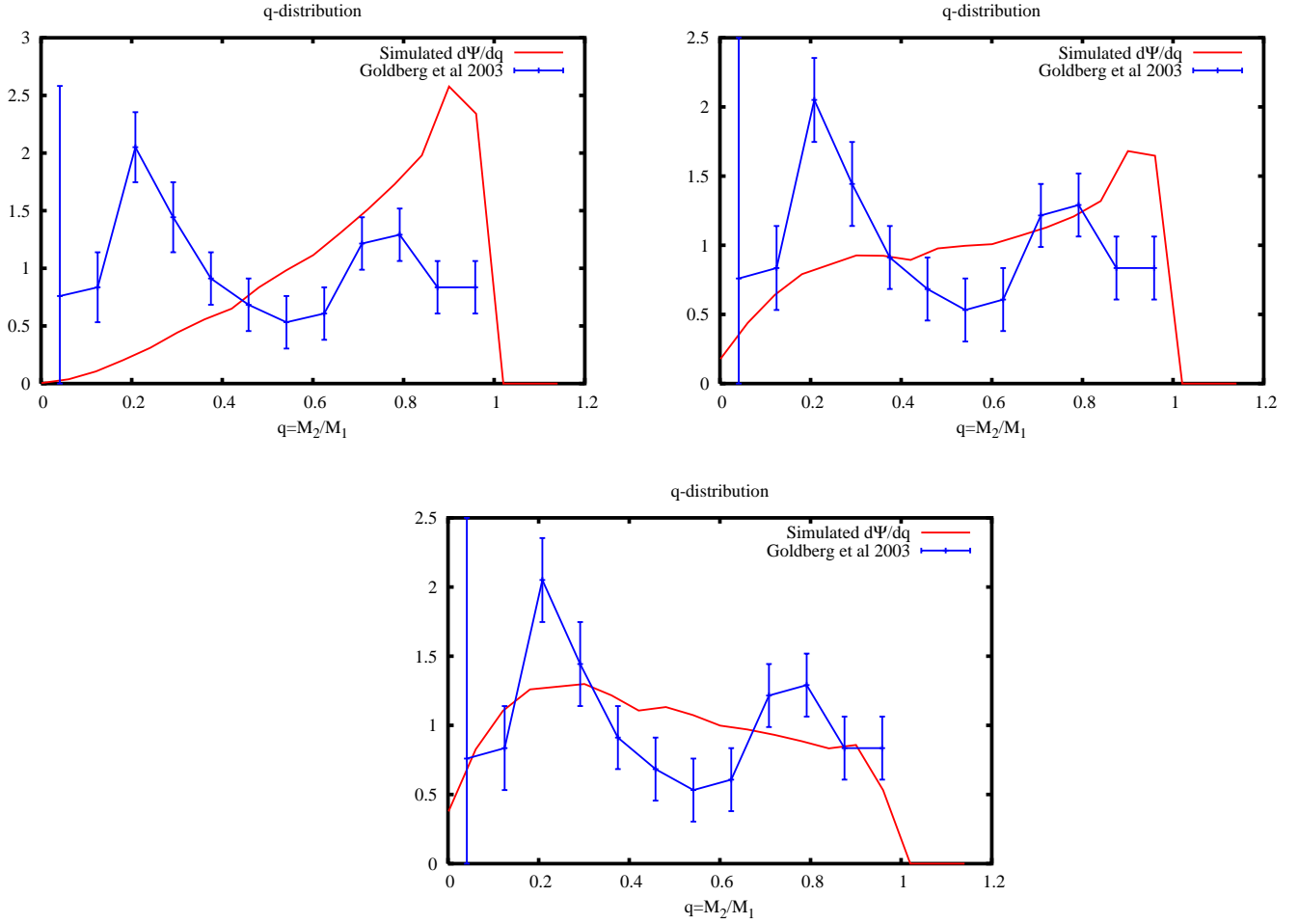
Figure 58: $d\Psi/dq$ vs q (red lines) for $\phi(q) \propto q^{0.5}$ (upper left), $\phi(q) \propto q^{-1.5}$ (upper right) and $\psi(M_2) = \psi(M_1)$ with $q \leq 1$ (lower panel). The minimum primary mass $m_0 = 0.1$.

the choice of both stars from the IMF, with $M_2 \leq M_1$, on observational grounds alone, especially given low-q selection effects. The observed peak at $q \approx 0.2$ is hinted at by the synthetic distribution when both stars are chosen from the IMF. No attempt is made to model selection effects except by increasing m_0 – and this tends to flatten the distribution and does not produce the peak.

The effect on stellar yields y due to a variation of the secondary mass distribution is shown in table 16. The default data set has a KTG93 primary mass distribution (with $m_0 = 0.1$), flat-q secondary mass distribution and flat in $\ln a$ separation distribution.

Choosing M_2 from the primary star IMF has the effect of boosting the number of low- and intermediate-mass secondary stars at the expense of high-mass secondaries. This distribution increases the s-process and HBB yields: ^{14}N increases to 119% of the default yield, Ba increases to 121%, as well as the nova yields, ^{13}C increases to 129%, ^{15}N to 296%, ^{17}O to 326%. The number of type Ia supernovae is reduced so ^{44}Ca, ^{48}Ti and ^{52}Cr yields drop to a fifth of the default value and ^{56}Fe to 59%. The reduction in high-mass companions leads to a drop in ^{65}Cu which is not surprising because there are fewer core collapse supernovae compared to the flat-q distribution.

The power law forms do not significantly change most yields compared to the flat-q case except for the explosive binary process yields. Nova yields (as measured by ^{13}C or ^{15}N) drop for $q^{0.5}$ but rise for $q^{-1.5}$, core-collapse SN yields (^{65}Cu) rise slightly for $q^{0.5}$ and drop by up to 20% with $q^{-1.5}$ while SNIa yields rise by up to 14% for $q^{0.5}$ and drop by 65% for $q^{-1.5}$.

In conclusion the binary explosive process yields depend strongly on the secondary mass distribution. SNIa yields vary from 30% to 114% of the flat-q model, while ^{15}N and ^{17}O are boosted by a factor of three if the secondary is chosen from the IMF. The changes in any of the non-explosive isotope yields are usually less than 20% – far less than the 200% changes due to uncertainty in the single/primary star mass distribution.

IMF1 IMF2 Sepdist	KTG93 Flat-Q Flat ln(a)	KTG93 IMF1 $q \leq 1$ Flat ln(a)	KTG93 $q^{0.5}$ Flat ln(a)	KTG93 $q^{-1.5}$ Flat ln(a)	
Isotope	y	Relative Yields %	%	%	Limits
^{1}H	1.898×10^{-1}	116	102	91	$(1.73 < 1.90 < 2.24) \times 10^{-01}$
^{4}He	1.019×10^{-1}	115	103	90	$(0.91 < 1.02 < 1.18) \times 10^{-01}$
^{12}C	5.735×10^{-3}	81	107	66	$(3.76 < 5.74 < 6.14) \times 10^{-03}$
^{13}C	6.111×10^{-5}	128	92	101	$(5.60 < 6.11 < 7.91) \times 10^{-05}$
^{14}N	8.111×10^{-4}	121	101	93	$(7.55 < 8.11 < 9.83) \times 10^{-04}$
^{15}N	9.950×10^{-6}	291	84	200	$(8.41 < 9.95 < 29.43) \times 10^{-06}$
^{16}O	9.561×10^{-3}	96	105	76	$(7.22 < 9.56 < 10.04) \times 10^{-03}$
^{17}O	6.256×10^{-6}	321	81	216	$(5.07 < 6.26 < 20.38) \times 10^{-06}$
^{20}Ne	1.186×10^{-3}	106	104	83	$(0.98 < 1.19 < 1.28) \times 10^{-03}$
^{21}Ne	3.719×10^{-6}	107	104	83	$(3.09 < 3.72 < 4.04) \times 10^{-06}$
^{22}Ne	2.842×10^{-4}	111	104	85	$(2.41 < 2.84 < 3.15) \times 10^{-04}$
^{23}Na	3.707×10^{-5}	114	103	87	$(3.23 < 3.71 < 4.29) \times 10^{-05}$
^{24}Mg	4.228×10^{-4}	96	105	76	$(3.22 < 4.23 < 4.44) \times 10^{-04}$
^{25}Mg	7.309×10^{-5}	107	104	83	$(6.04 < 7.31 < 7.93) \times 10^{-05}$
^{26}Al	3.985×10^{-7}	108	102	84	$(3.35 < 3.98 < 4.38) \times 10^{-07}$
^{26}Mg	7.733×10^{-5}	108	104	83	$(6.45 < 7.73 < 8.48) \times 10^{-05}$
^{27}Al	5.920×10^{-5}	107	104	83	$(4.90 < 5.92 < 6.42) \times 10^{-05}$
^{32}S	6.028×10^{-4}	78	106	65	$(3.94 < 6.03 < 6.39) \times 10^{-04}$
^{36}Ar	1.251×10^{-4}	76	106	64	$(0.80 < 1.25 < 1.33) \times 10^{-04}$
^{40}Ca	9.848×10^{-5}	65	107	57	$(5.62 < 9.85 < 10.51) \times 10^{-05}$
^{44}Ca	3.602×10^{-5}	30	114	33	$(1.07 < 3.60 < 4.11) \times 10^{-05}$
^{48}Ti	3.267×10^{-5}	34	114	35	$(1.09 < 3.27 < 3.72) \times 10^{-05}$
^{52}Cr	7.949×10^{-5}	34	112	36	$(2.65 < 7.95 < 8.93) \times 10^{-05}$
^{56}Fe	2.485×10^{-3}	59	108	52	$(1.30 < 2.49 < 2.69) \times 10^{-03}$
^{65}Cu	8.835×10^{-6}	103	105	80	$(7.03 < 8.83 < 9.24) \times 10^{-06}$
Ba	6.505×10^{-9}	119	102	92	$(5.99 < 6.50 < 7.84) \times 10^{-09}$
Kr	6.366×10^{-8}	125	103	95	$(6.04 < 6.37 < 8.04) \times 10^{-08}$
Pb	6.453×10^{-9}	118	102	92	$(5.92 < 6.45 < 7.73) \times 10^{-09}$
Y	8.861×10^{-9}	126	102	96	$(8.50 < 8.86 < 11.31) \times 10^{-09}$

Table 16: Binary star yields relative to mass input y with variation of the secondary mass distribution.

5.7 Separation Distribution

The default distribution of the initial binary separation a is a flat distribution in $\ln a$ in the range $3 \leq a/\mathrm{R}_\odot \leq 10^4$ (as in Hurley et al., 2002)

$$\chi(\ln a) = \mathrm{constant}\,. \tag{197}$$

The upper limit is chosen because, while stars at higher separations may be gravitationally bound, they do not interact significantly enough to alter their evolution. The lower limit is somewhat arbitrary and it should be noted that stars born in an equal mass binary with $M_1 = M_2 \geq 2.1\,\mathrm{M}_\odot$ and $a = 3\,\mathrm{R}_\odot$ merge within 10^5 years. Although this is not very physical there are not many of these stars.

It is difficult to compare this distribution with observed separation distributions because these rely on well known distances to binaries and that the stars are optically distinguishable. Periods are easier to observe e.g. by spectroscopic methods. An initial period distribution can be constructed from $\chi(a)$ by use of Kepler's law

$$P^2 = \left(\frac{4\pi^2}{G}\right)\frac{a^3}{(M_1 + M_2)} \tag{198}$$

which for the Sun/Earth system with a measured in AU (1 AU being the Sun-Earth distance), period P in years and M_1 and M_2 measured in $\mathrm{M}_\odot$ becomes

$$1 = \frac{4\pi^2}{G} \tag{199}$$

because[3] $M_1 + M_2 \approx M_1$ and $a = P = M_1 = 1$. Thus for any system measured in these units,

$$P = \left(\frac{a^3}{M_1 + M_2}\right)^{1/2} \text{ years} \tag{200}$$

which, with a converted to $\mathrm{R}_\odot$ and periods in days, leads to

---

[3]The mass of the Earth, M_2, is negligible compared to the mass of the Sun, $M_1 = \mathrm{M}_\odot$.

$$P = 365.24 \left(\frac{R_\odot}{1\,\text{AU}} \right)^{3/2} \frac{a^{3/2}}{(M_1 + M_2)^{1/2}} \text{ days} \tag{201}$$

where $R_\odot/1\,\text{AU} = 1/214.95$.

The distributions of separation and period obtained from the flat $\ln a$ distribution with M_1 distributed by the KTG93 IMF and M_2 by the flat-q distribution are shown in figure 59. The flat distribution obtained between $P = 1\,\text{d}$ and $164\,\text{yr}$ agrees reasonably well with the range in observations of Popova et al. (1982) and Abt (1983) although there is definitely room for improvement. The linear period distribution fit from Goldberg et al. (2003, based on spectroscopic binaries) is also plotted and it should be noted that this is anything but flat in $\ln P$! While the synthetic binary separation distribution reproduces the observed range of binary periods it does not reproduce Goldberg et al. (2003)'s peak at periods of about $10\,\text{yrs}$. The shortest period binaries are probably not observed because they merge quickly while both stars are on the MS so will be seen as single stars. The highest period synthetic binaries, e.g. $\ln P \approx 11$ so $P \approx 164\,\text{yrs}$, would suffer from observational selection effects – most stars have not been observed continuously for 160 years.

A more accurate match to the Goldberg et al. (2003) data can be made with a negative-exponent power law $\psi(a) \propto a^{-0.7}$ (so $\psi(\ln a) \propto a^{0.3}$) in the range $10 \leq a/R_\odot \leq 1.3 \times 10^3$. The lower separation limit agrees better with the observations of Popova et al. (1982). This is considered along with a positive-exponent power law $\psi(a) \propto a^{1.0}$ and a more extreme negative-exponent power law $\psi(a) \propto a^{-2.0}$. There is no observational justification for these latter exponents but it is interesting to see if they have any effect on the integrated yields.

The effect on yields y of these various distributions is shown in table 17. The difference between the default separation distribution (flat in $\ln a$) and the better fit to the observations (power law $a^{-0.7}$) is a small drop for all isotopes except the SnIa isotopes which drop by half. Nova yields, if measured by ^{15}N or ^{17}O, rise by 147% or 122% respectively while the yield of ^{13}C actually drops. The reason for this is uncertain – novae and TPAGB stars are the main producers of ^{13}C and there is no drop in the s-process or ^{14}N yields, so there should be no drop in ^{13}C. However, if most ^{13}C is produced by novae (see chapter 7),
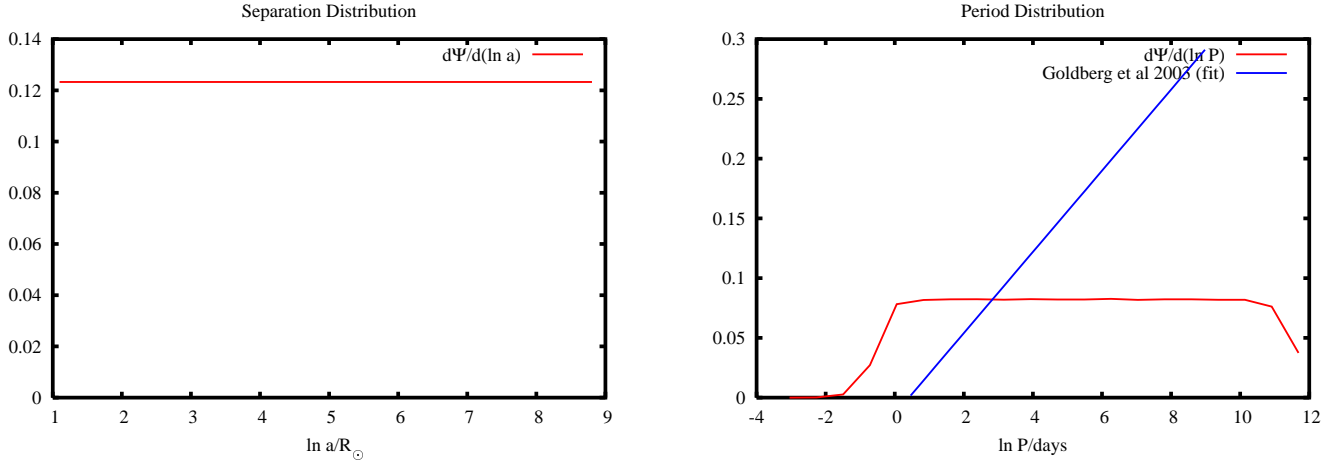
Figure 59: $d\Psi/d\ln a$ and $d\Psi/d\ln P$ generated from a flat-$\ln a$ separation distribution. The blue line is the fit from Goldberg et al. (2003) for the orbital period of spectroscopic binaries.
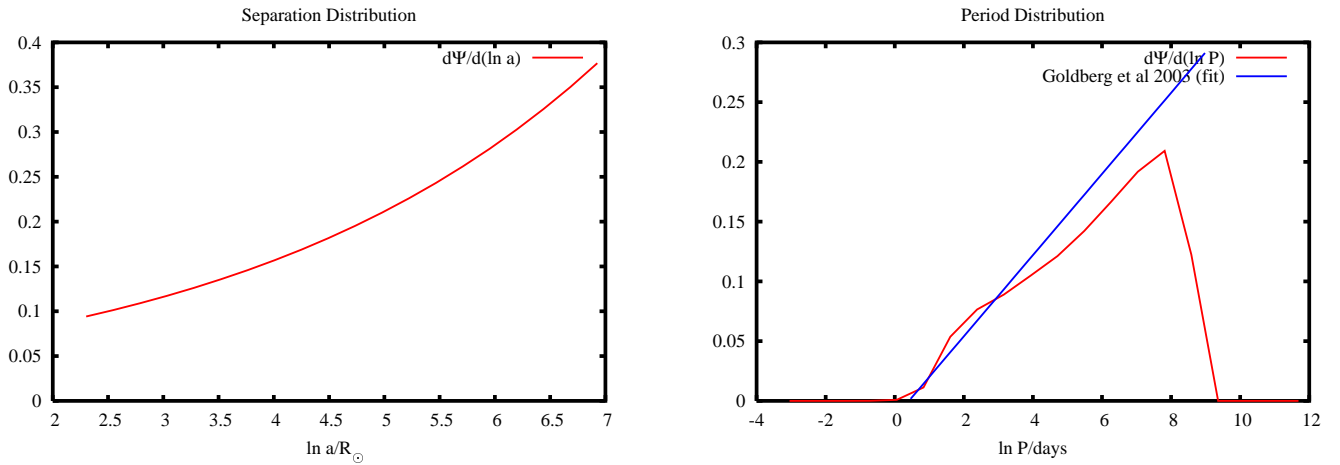
Figure 60: As figure 59 for a power-law separation distribution $\psi(a) \propto a^{-0.7}$ in the range $10 \le a/R_\odot \le 1.3 \times 10^3$.

167

IMF1 IMF2 Sepdist	KTG93 Flat-Q Flat ln(a)	KTG93 Flat-Q $a^{-0.7}$ $10 \le a/\mathrm{R}_\odot \le 1.3e3$	KTG93 Flat-Q $a^{1.0}$	KTG93 Flat-Q $a^{-2.0}$	
Isotope	y	Relative Yields %	%	%	Limits
^{1}H	1.898×10^{-1}	90	83	137	$(1.57 < 1.90 < 2.60) \times 10^{-01}$
^{4}He	1.019×10^{-1}	93	88	129	$(0.90 < 1.02 < 1.31) \times 10^{-01}$
^{12}C	5.735×10^{-3}	90	71	109	$(4.04 < 5.74 < 6.28) \times 10^{-03}$
^{13}C	6.111×10^{-5}	82	51	77	$(3.12 < 6.11 < 6.11) \times 10^{-05}$
^{14}N	8.111×10^{-4}	97	100	117	$(7.88 < 8.11 < 9.47) \times 10^{-04}$
^{15}N	9.950×10^{-6}	147	62	19	$(1.89 < 9.95 < 14.61) \times 10^{-06}$
^{16}O	9.561×10^{-3}	89	74	120	$(7.11 < 9.56 < 11.47) \times 10^{-03}$
^{17}O	6.256×10^{-6}	122	64	62	$(3.87 < 6.26 < 7.63) \times 10^{-06}$
^{20}Ne	1.186×10^{-3}	91	84	129	$(1.00 < 1.19 < 1.53) \times 10^{-03}$
^{21}Ne	3.719×10^{-6}	92	88	133	$(3.29 < 3.72 < 4.94) \times 10^{-06}$
^{22}Ne	2.842×10^{-4}	101	111	125	$(2.84 < 2.84 < 3.54) \times 10^{-04}$
^{23}Na	3.707×10^{-5}	95	103	143	$(3.51 < 3.71 < 5.30) \times 10^{-05}$
^{24}Mg	4.228×10^{-4}	88	75	124	$(3.16 < 4.23 < 5.26) \times 10^{-04}$
^{25}Mg	7.309×10^{-5}	95	96	133	$(6.98 < 7.31 < 9.74) \times 10^{-05}$
^{26}Al	3.985×10^{-7}	94	99	138	$(3.75 < 3.98 < 5.49) \times 10^{-07}$
^{26}Mg	7.733×10^{-5}	92	92	135	$(7.08 < 7.73 < 10.41) \times 10^{-05}$
^{27}Al	5.920×10^{-5}	92	88	132	$(5.19 < 5.92 < 7.80) \times 10^{-05}$
^{32}S	6.028×10^{-4}	84	60	111	$(3.62 < 6.03 < 6.68) \times 10^{-04}$
^{36}Ar	1.251×10^{-4}	83	58	111	$(0.72 < 1.25 < 1.39) \times 10^{-04}$
^{40}Ca	9.848×10^{-5}	76	45	112	$(4.47 < 9.85 < 11.04) \times 10^{-05}$
^{44}Ca	3.602×10^{-5}	56	3	139	$(0.09 < 3.60 < 5.02) \times 10^{-05}$
^{48}Ti	3.267×10^{-5}	55	5	150	$(0.16 < 3.27 < 4.91) \times 10^{-05}$
^{52}Cr	7.949×10^{-5}	57	6	135	$(0.51 < 7.95 < 10.75) \times 10^{-05}$
^{56}Fe	2.485×10^{-3}	70	35	138	$(0.87 < 2.49 < 3.42) \times 10^{-03}$
^{65}Cu	8.835×10^{-6}	91	96	140	$(8.03 < 8.83 < 12.41) \times 10^{-06}$
Ba	6.505×10^{-9}	96	106	144	$(6.24 < 6.50 < 9.39) \times 10^{-09}$
Kr	6.366×10^{-8}	100	130	162	$(6.34 < 6.37 < 10.31) \times 10^{-08}$
Pb	6.453×10^{-9}	95	101	142	$(6.11 < 6.45 < 9.18) \times 10^{-09}$
Y	8.861×10^{-9}	105	144	165	$(8.86 < 8.86 < 14.59) \times 10^{-09}$

Table 17: The variation in yield y for different separation distributions.

and if these novae are predominantly high-mass COWDs ($M \geq 1.15\,\mathrm{M_\odot}$) or ONeWDs the results of José & Hernanz (1998) show that ^{13}C is anti-correlated with both ^{15}N and ^{17}O. Perhaps highly separated systems are more likely to lead to nova-like accretion rates for long periods of time without the possibility of common-envelope evolution, whereas closer binaries lead to higher accretion rates, common-envelope evolution and possible SNeIa.

The positive-exponent power law $a^{1.0}$ severely reduces the SnIa yields to almost nothing and reduces the nova yields. For other isotopes there is up to 25% reduction. The reason for this is that large-separation binaries are favoured so interaction leading to novae or type Ia supernovae are unlikely. There is an increase in the s-process yields corresponding to the survival of more TPAGB systems in wide binaries.

The $a^{-2.0}$ power law reduces SnIa and nova yields but increases everything else. This separation distribution leads to a peak in the initial period distribution at 1 day. For most initial masses the stars merge while both are on the MS so effectively the population behaves as a single star population boosted to higher mass. This increase in stellar mass, and increase in single star fraction, leads to an increase in yields from single star processes such as TPAGB/WR wind loss (and associated ^{14}N yield) and core-collapse SNe (as ^{65}Cu) and a drop in the yield from novae. It is interesting to note that the SNeIa yields increase – probably owing to an increased number of close binaries leading to common-envelope evolution – while the nova yields decrease; exactly the opposite of the $a^{-0.7}$ distribution.

5.8 Conclusions

Yields relative to mass input, y, increase by up to a factor of 3 due to reasonable uncertainties in the single/primary star mass distribution compared to the KTG93 IMF, $\pm 20\%$ owing to q distributions different from the flat-q distribution and a similar amount due to separation distributions which differ from the flat-$\ln a$ distribution.

The low-mass cutoff m_0 alters normalization of the single/primary star mass distribution or q distribution and because most stars lie in the range $m_0 \leq M/\mathrm{M}_\odot \leq m_1$ raising m_0 by a small amount significantly boosts the yields.

Type Ia supernova and nova isotopes are dominated by changes in the q and separation distributions – SnIa isotope production drops by about 70% if the secondary star is chosen from the primary star IMF even though this distribution is favoured by spectroscopic binary observations. An extreme separation distribution ($a^{1.0}$) effectively stops type Ia supernovae from occurring, but a more realistic distribution ($a^{-0.7}$) which agrees better with observations is different to the default flat-$\ln a$ distribution by at most 50%.

In comparison to these uncertainties, errors in yields owing to numerical resolution, which are less than 2%, are negligible for $N = 10^4$ single stars or $N = 100^3$ binary stars.

6 Stellar Yields: Slow Parameters

6.1 Introduction

The slow parameters correspond to changes in the input physics and there are many such parameters. It is impossible to analyse the parameter space covered by all of them so the default model (see section 5.2) is used with one parameter varied at a time. The total yield ζ_j of isotope j can then be expanded as a Taylor series

$$\zeta_j \approx \zeta_{j0} + \frac{d\zeta_j}{dx_i}(x_i - x_{i0}) = \zeta_{j0}\left(1 + T_{ij}\frac{\delta x_i}{\Delta x_i}\right) \qquad (202)$$

where x_i are the slow parameters, x_{i0} are the default values, $\delta x_i = x_i - x_{i0}$ and x varies from $x_{\min}$ to $x_{\min} + \Delta x_i$. A fitting routine is used to evaluate

$$\frac{d(\zeta_j/\zeta_{j0})}{d(x_i/\Delta x_i)} = T_{ij} \qquad (203)$$

from the data. Because the derivative terms T_{ij} are normalized to both the x range and the default yield they provide a relatively unbiased comparison of the effect of the slow parameters x_i. The Taylor series does *not* contain cross terms between the x_i so the effect of varying two slow parameters at the same time remains unknown although the series will provide a first-order estimate. Note that this is a linear approximation only, in some cases, such as variation with Z, higher order expansions may be necessary for inclusion of yields into GCE models. The yield relative to mass input is used $\zeta_j = y_j$.

The parameters which are varied are:

- Maximum stellar evolution time $1\,\mathrm{Myr} \leq t_{\max} \leq 13.7\,\mathrm{Gyr}$.

- Metallicity $0.0001 \leq Z \leq 0.02$. Note that initial abundances are taken from a quadratic fit to the initial abundances of Anders & Grevesse (1989, $Z = 0.02$) and Russell & Dopita (1992, LMC $Z = 0.008$ and SMC $Z = 0.004$) for $Z \geq 0.004$ when the isotopic abundance is available. Lower metallicities and isotopes which are not considered by Russell & Dopita (1992) are scaled to solar abundances of Anders & Grevesse (1989).

- Eccentricity $0 \leq e \leq 1$.

- GB wind Reimers factor $0.25 \leq \eta \leq 0.75$.

- AGB $\dot{M}$ of H02, K02 or a Reimers wind with $\eta = 3$.

- WR wind of H02, MM or NL.

- WR wind enhancement factor $0.1 \leq f_{\mathrm{WR}} \leq 10$.

- Common-envelope parameter $0.1 \leq \alpha_{\mathrm{CE}} \leq 5$.

- Eddington limit for accretion, $f_{\mathrm{EDD}} = 1$, or no limit for accretion, $f_{\mathrm{EDD}} = 10^6$.

- s-process $^{13}\mathrm{C}$ pocket mass factor $0.01 \leq \xi \leq 2.0$.

- SN kick velocity dispersion $0 \leq \sigma_{\mathrm{SN}}/\mathrm{km\,s^{-1}} \leq 400$.

- Enhanced binary wind loss $0 \leq B \leq 10^4$.

- BH masses given by the prescription of H02, which leads to low masses, or Belczynski et al. (2002), which gives higher BH masses (see e.g. Izzard, Ramirez-Ruiz & Tout 2004 or section 3.8).

- Dredge-up parameters $-0.1 \leq \Delta M_{\mathrm{c,min}} \leq 0$ and $0 \leq \lambda_{\min} \leq 1$.

The above parameters are varied on a grid of 1000 single stars and 10^6 binary stars. Given the large number of slow parameters and the number of isotopes it is possible to consider (currently 126), a selection of isotopes must be made which is more restrictive than that used during the slow parameter analysis, these are ^{1}H, ^{12}C, ^{14}N, ^{15}N, ^{16}O, ^{22}Ne, ^{44}Ca, ^{56}Fe, ^{65}Cu and Ba.

6.2 Isotopic Comparison

6.2.1 Maximum Stellar Evolution Time

The time when a particular isotope is released, relative to stellar birth, plays a critical role in GCE models. In single stars the accepted picture is a prompt release of WR-star processed material, N in the WN phase, ^{4}He, ^{12}C and ^{16}O in the WC/WO phases, and core-collapse supernova isotopes such as ^{12}C, ^{16}O, some ^{56}Fe and ^{65}Cu, after about $4 - 100$ Myr. The longer lived stars explode as EAGB stars. This is followed by the release of ^{14}N after about $100 - 200$ Myr owing to hot bottom burning TPAGB stars in the mass range $4 \lesssim M/M_\odot \lesssim 8$. Then there is further release of ^{12}C and Ba by TPAGB stars which undergo third dredge-up, significant s-processing and no HBB $(1.5 \lesssim M/M_\odot \lesssim 4) L_\odot$ on timescales of billions of years. There is little production of ^{15}N or ^{44}Ca in single stars – any yield is due to ejection of material present at stellar birth. This is illustrated by figure 61.

For binary stars the picture is more complicated. Mass transfer leads to more WR stars, some massive merged stars and (probably[1]) fewer AGB stars. More WR and massive stars means more SNeIb/c and more ^{12}C. The second peak in production owing to AGB stars, while still evident, is vastly reduced and replaced by a more continuous yield of ^{12}C to the ISM. There is a drop in the ^{65}Cu production in binaries, probably because core-collapse supernovae are more likely to be of type Ib/c in binaries but type II in single stars. Binary mass transfer acts to strip the stars of their envelopes prior to the explosion. This also leads to smaller cores in SNeIb/c and the WW95 fits have ^{65}Cu decreasing with decreasing CO core mass.

AGB stars are destroyed by mass transfer so the yields of ^{14}N, ^{22}Ne and Ba drop compared to single stars. Similarly ^{22}Ne yields drop at times later than about 1 Gyr and Ba at times later than 100 Myr. Note that ^{16}O yields are similar between single and binary stars. The excess beyond about 100 Myr is due to some extra WR stars, a small yield from SNeIa and fewer AGB stars[2].

There are also binary-only explosive processes at work. These lead to the over-production of ^{15}N from novae and ^{44}Ca and ^{56}Fe from SNeIa and HeWD mergers at times later than about 1 Gyr.

---

[1]There may be a large population of post-common-envelope AGB stars. This depends on the free parameter α_{CE}.

[2]The ^{16}O intershell abundance is low enough in these stars that it leads to a slight *depletion* of ^{16}O in the stellar envelope because at $Z = 0.02$ the envelope abundance of ^{16}O can be as high as 0.01.
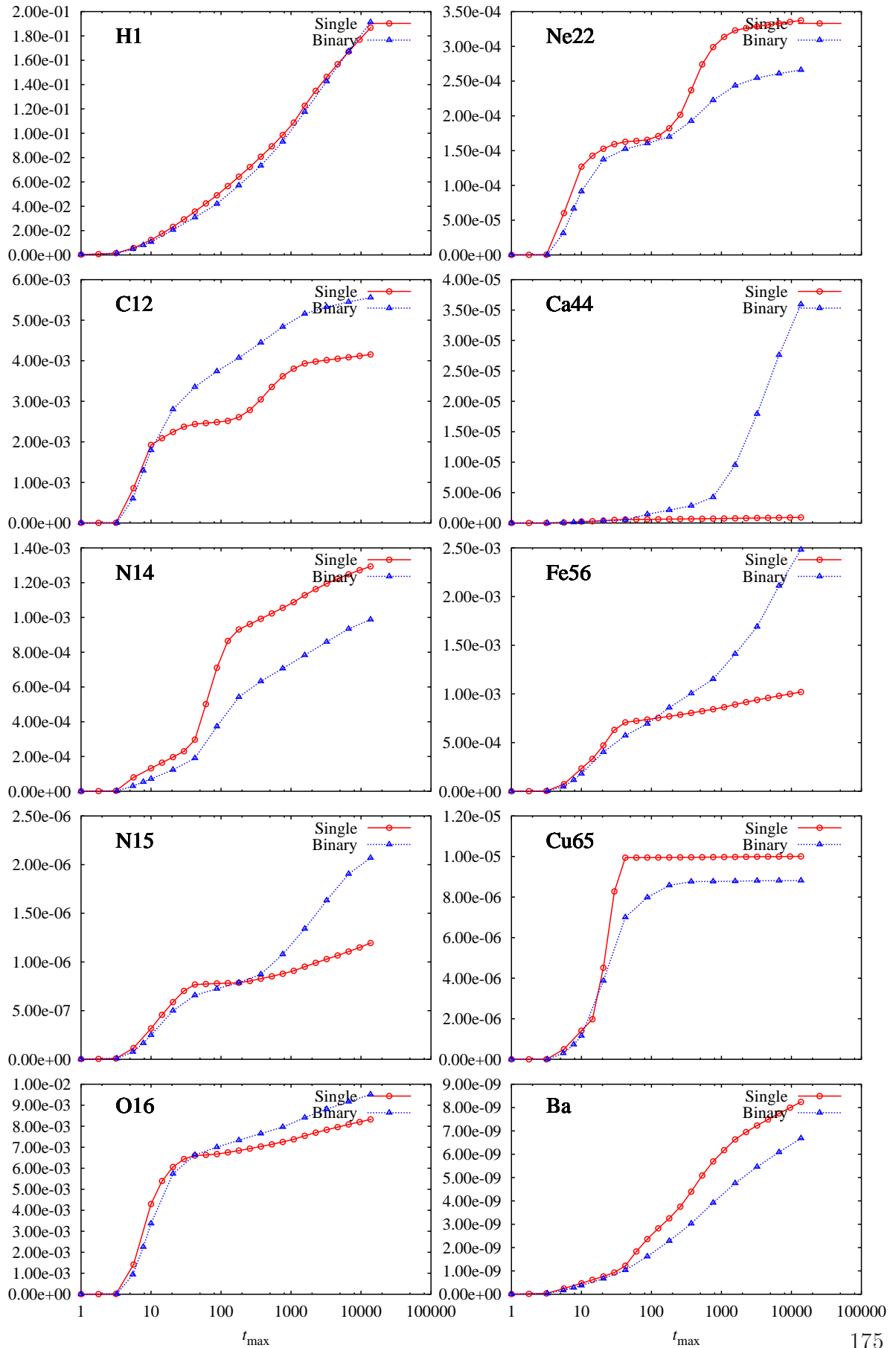
Figure 61: Yield relative to mass input y vs time.

6.2.2 Metallicity

The effect of varying the metallicity varies greatly from isotope to isotope (see fig. 62). At metallicities greater than 0.01 there is a tendency for material present in the star at birth to dominate the yield as it is lost in stellar winds, this is true for ^{12}C, ^{15}N, ^{16}O and ^{22}Ne, and ^{14}N because it is produced from ^{12}C. However there is no such tendency for the SNIa, nova or s-process isotopes - mainly because their initial abundances are so small. If isotopes heavier than ^{4}He are truly dependent only on the initial stellar abundance they should have zero yield as $Z \to 0$. This is not seen in any of the models, indeed the opposite is usually true.

At low metallicity the yield of ^{12}C relative to the mass input to stars is almost identical for single and binary stars, compared to a significant increase owing to binary stars at $Z = 0.02$. This is because dredge-up is more efficient at low metallicity so the TPAGB stars that do form make more ^{12}C which cancels out the increase in SN yields from binaries. This is purely a coincidence! At solar metallicity dredge-up is less efficient but SNe are not so the single star ^{12}C yield drops relative to the binary yield. There is no such SN compensation for ^{14}N which has its yields reduced in all binaries although the lower metallicity stars produce more ^{14}N by virtue of their hotter HBB.

Below $Z = 0.01$ ^{16}O is over-produced a little in binaries because of the higher number of SNeII/Ib/c. Above $Z = 0.01$ the yield is dominated by stellar wind losses. The yield of ^{22}Ne drops in the binaries because its major source is usually TPAGB star dredge-up. Barium likewise, the abundance of the dredged-up material is a strong function of Z, and the yields reflect this, but the single-star yields are always about twice the binary yields.

Nova-produced ^{15}N is always greater in binaries, by up to a factor of 4 at $Z = 0.0001$. Production of ^{44}Ca increases as Z decreases, perhaps due to the increased mass of sub-M_{Ch} SNIa progenitors (there is less mass loss as metallicity decreases). ^{56}Fe follows ^{44}Ca and while at $Z = 0.02$ only 60% of ^{56}Fe is made in binaries, at $Z = 0.0001$ it is nearly 80% which reflects the greater amount of mass ejected by SNeIa at low Z. The ^{65}Cu yield is again dominated by type II supernovae rather than Ib/c and the yield from single stars is up to 30% greater than the yield from binaries.
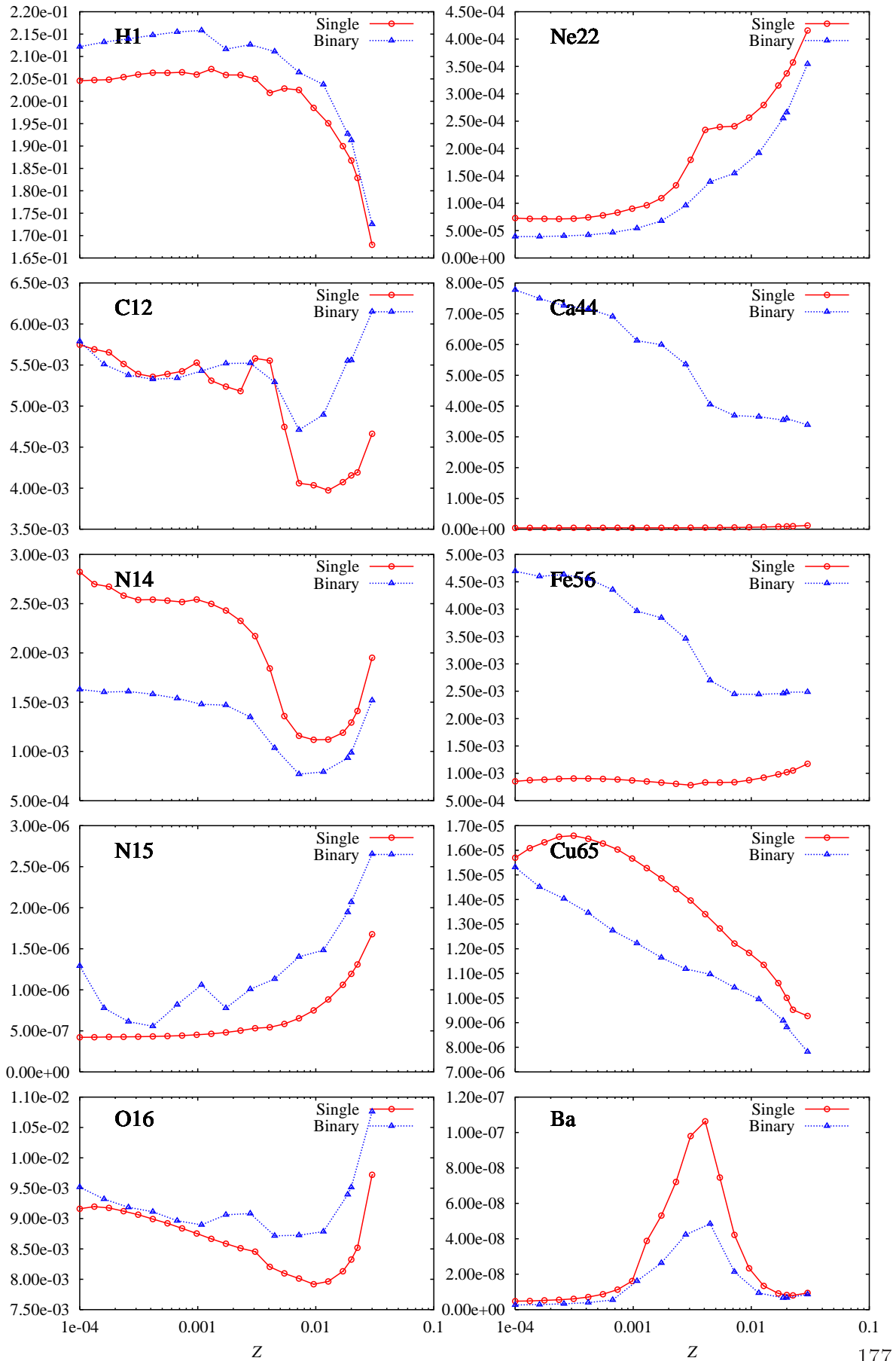
Figure 62: Yield relative to mass input y vs metallicity.

6.2.3 GB Wind Prescription

Figure 63 shows the effect of varying η_{GB} on the yields. It is expected that an increase of η_{GB} leads to a decreased stellar mass at the beginning of the TPAGB. This leads to a decrease in both third dredge-up and HBB so the yields of HBB/3DUP isotopes (^{12}C, ^{14}N, ^{22}Ne and Ba) decrease slightly – the effect on ^{15}N is in the opposite direction because it is destroyed in TPAGB stars. The hydrogen yield rises with η_{GB} because material ejected on the GB is less likely to be CNO processed (or polluted by a companion) than material ejected at a later stage of evolution. Compared to the difference between the single and binary star yields changing η_{GB} has a small effect.
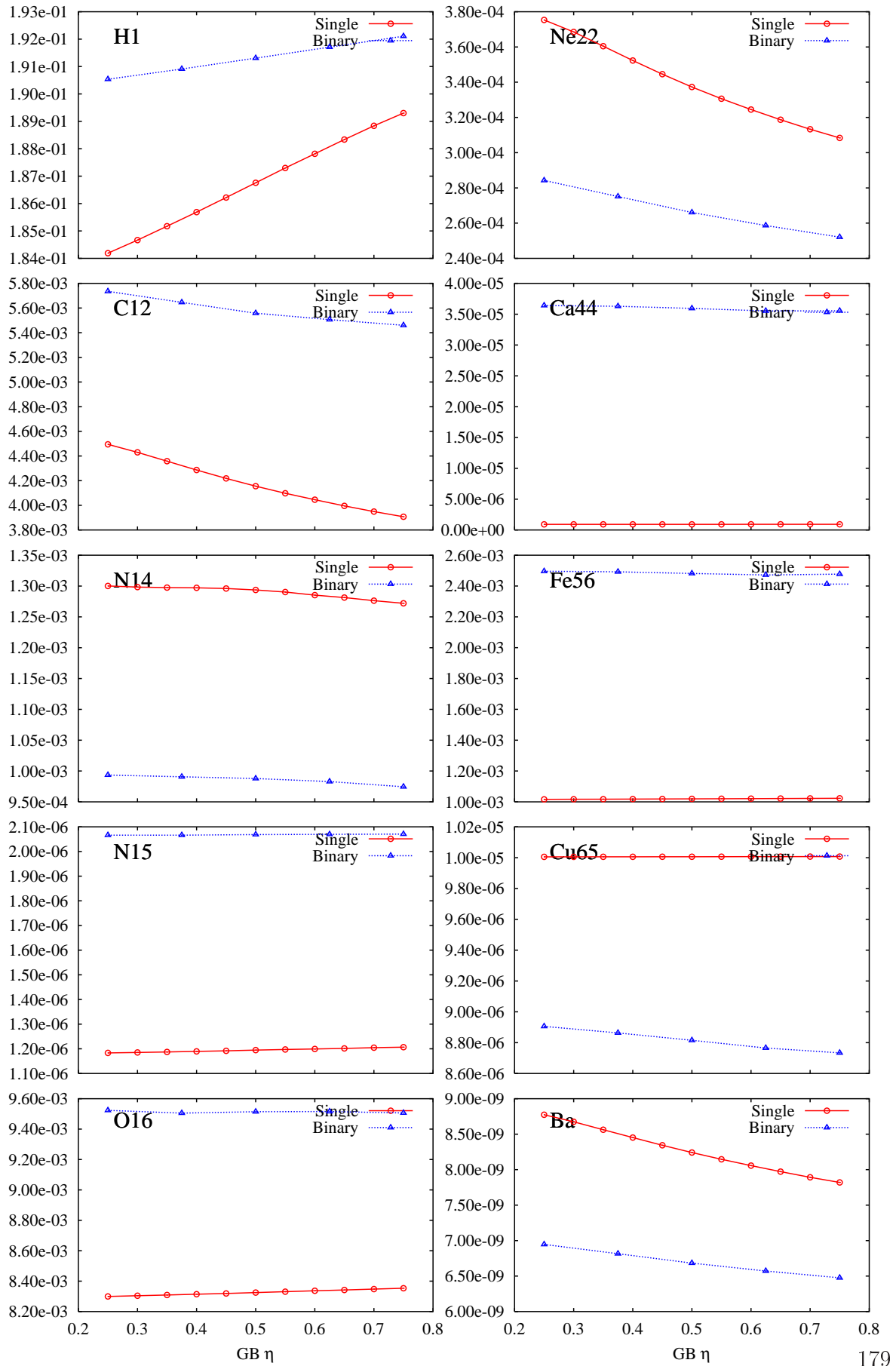
Figure 63: Yield relative to mass input y vs GB wind factor η.

6.2.4 AGB Wind Prescription

Figure 64 shows the effect of varying the AGB wind-loss prescription using the prescriptions of H02, K02 and a Reimers $\eta = 3$ mass-loss rate. The effect on most isotopes is smaller than the difference between single and binary stars with the exception of ^{14}N and Ba. The Reimers mass-loss rate leads to a slow erosion of the stellar envelope, rather than the strong superwind of the H02 and K02 wind-loss prescriptions (both are based on VW93). This means that HBB and third dredge-up can proceed for longer so more ^{12}C is converted to ^{14}N and more Ba is dredged-up. The uncertainty in ^{14}N yield is particularly troublesome – binaries with a Reimers mass-loss rate produce more nitrogen than single stars with a H02 mass-loss rate and a similar amount to binaries with the K02 prescription. The under-production owing to duplicity ranges from about 20% (H02) to 40% (Reimers).
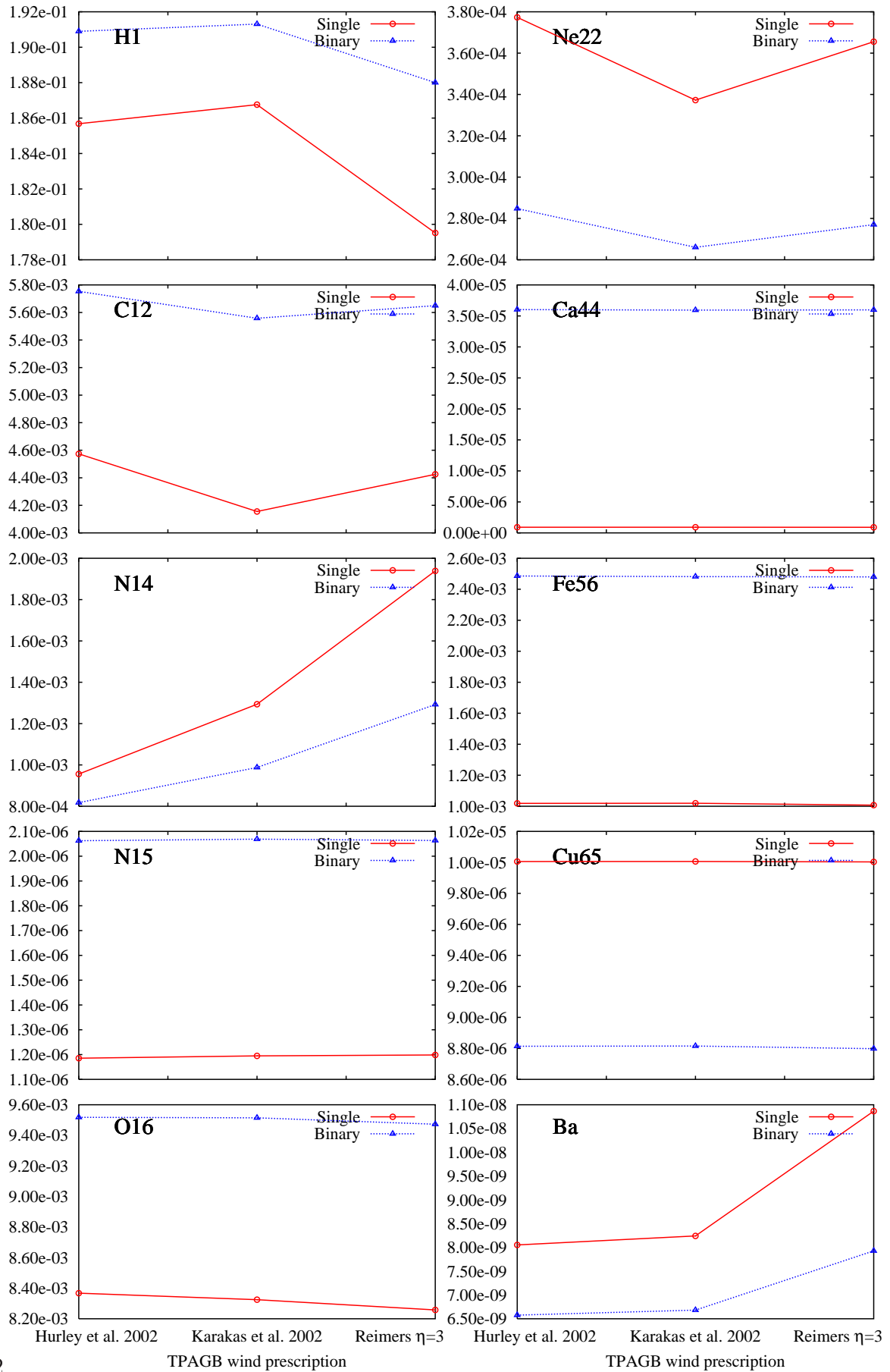
Figure 64: Yield relative to mass input y vs AGB wind prescription.

6.2.5 WR Wind Prescription and Enhancement Factor

The effect of varying the WR wind-loss prescription is shown in fig. 65. The effect on most isotopes is less than the effect of duplicity with the exception of ^{12}C and ^{16}O. Oxygen yields are up to 30% lower with the MM mass loss than the NL or H02, while carbon is increased for NL relative to MM and H02. The different mass-loss rates lead to different pre-SN CO core masses and these give different yields. The MM mass-loss rates are generally higher, so while more ^{16}O is lost during the WR phase the final core mass is lower, corresponding to a lower ^{16}O mass fraction (and higher ^{12}C) in the SN ejecta. The default (H02) mass-loss rate is then modulated by a parameter f_{WR} to reflect current uncertainty in mass-loss rate (see fig. 66). This has a similar effect to the use of the MM mass-loss rates. That is less ^{16}O and more ^{12}C.
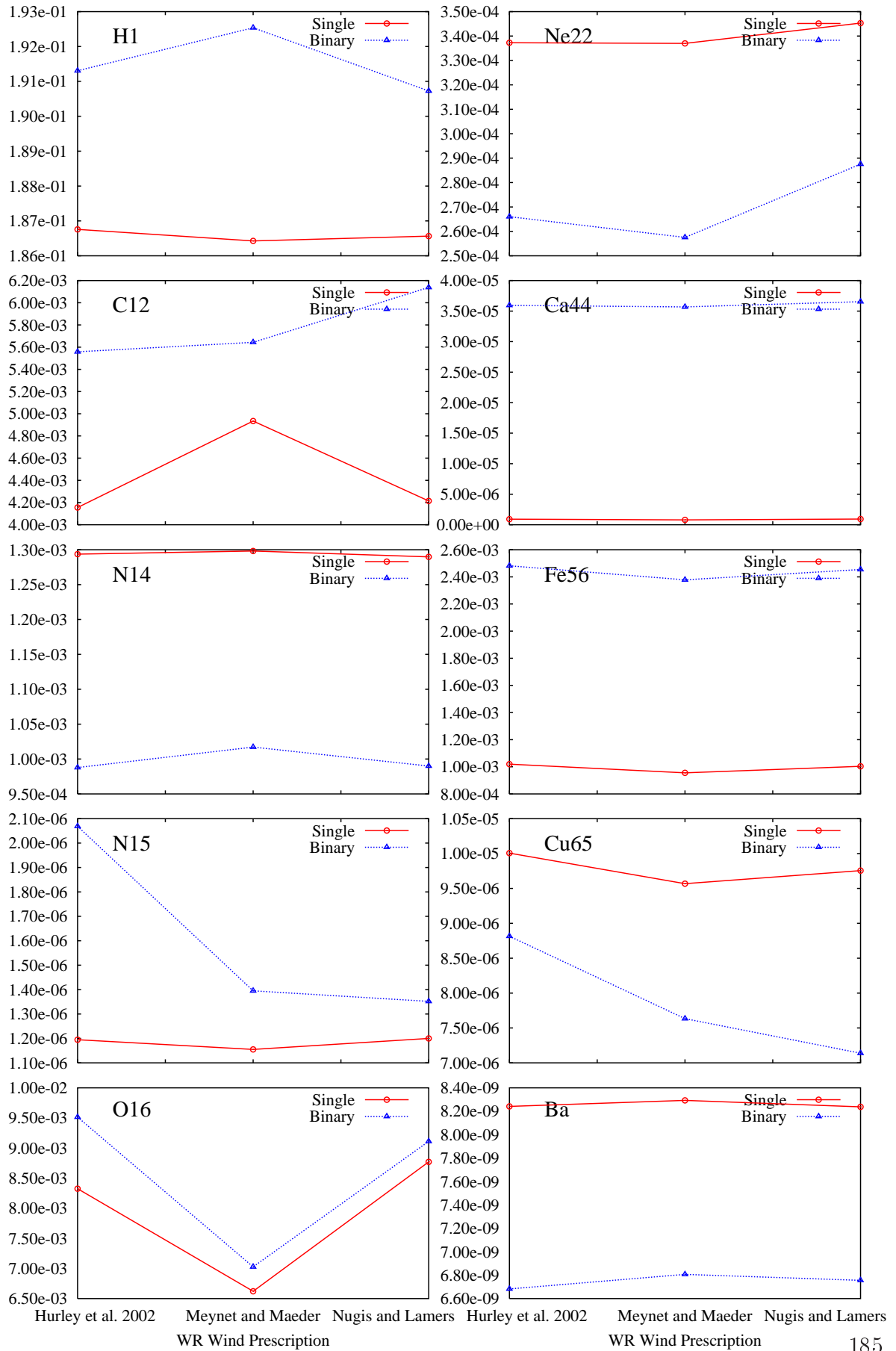
Figure 65: Yield relative to mass input y vs WR wind prescription.
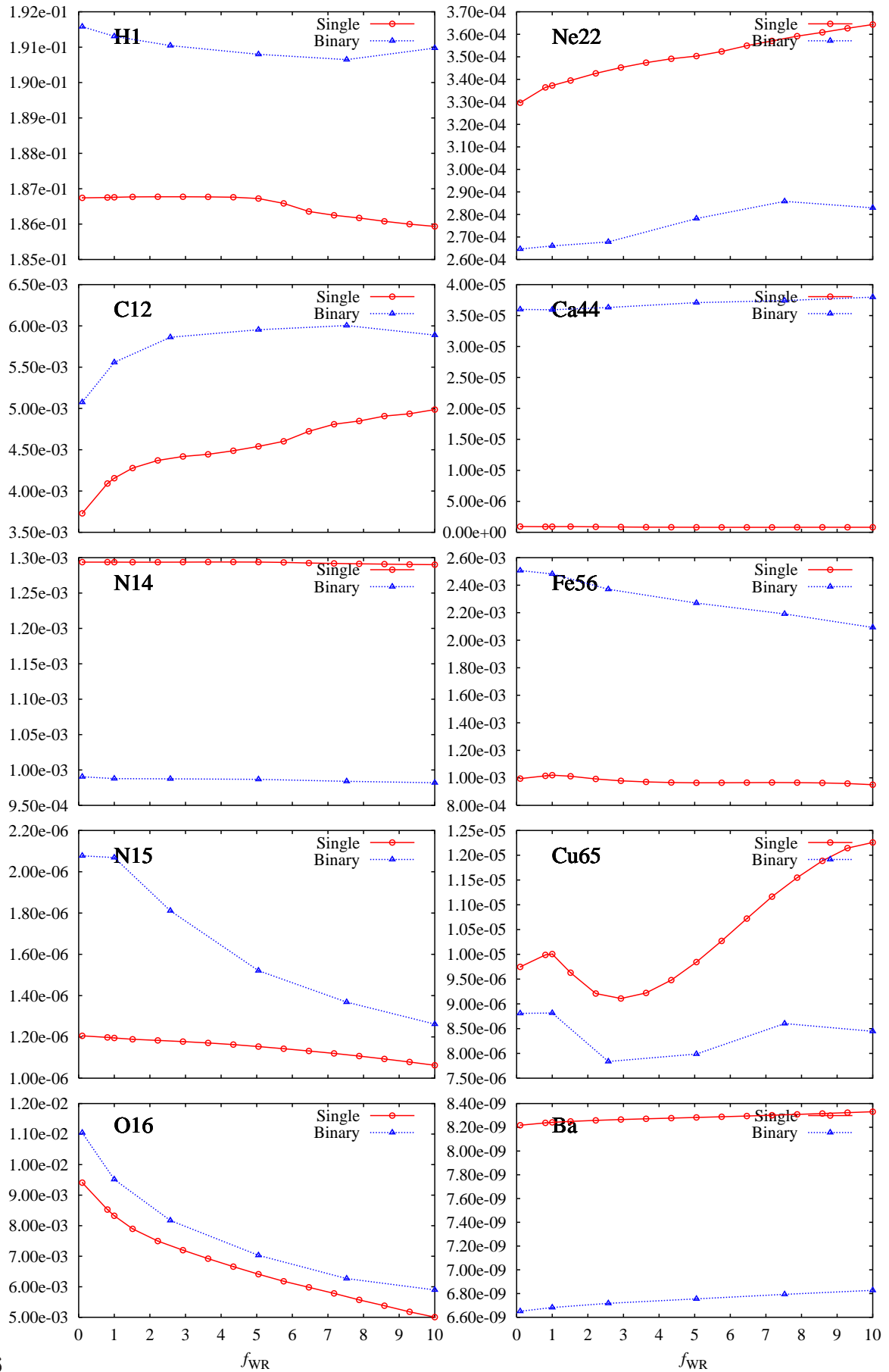
Figure 66: Yield relative to mass input y vs WR wind enhancement factor.

6.2.6 S-process Pocket Efficiency

The amount of ^{13}C present in the intershell region of TPAGB stars is poorly constrained and at present is treated as a free parameter. It should not, and as shown in fig. 67, does not affect any isotopes except Ba apart from negligible numerical errors. For $\xi \lesssim 0.8$ the barium yield is constant – this is indicative of negligible production in the intershell, all yield is due to material present at the birth of the star. For $\xi \gtrsim 1.0$ there is some Ba production, mainly in single stars because the binaries are more likely to have their AGB phases truncated. Barium production is a strong function of metallicity and a complete description of its yields requires analysis of the $\xi - Z$ plane (beyond the scope of this work). The effect of duplicity is to reduce the yield by about 40% for $\xi \gtrsim 1.0$.
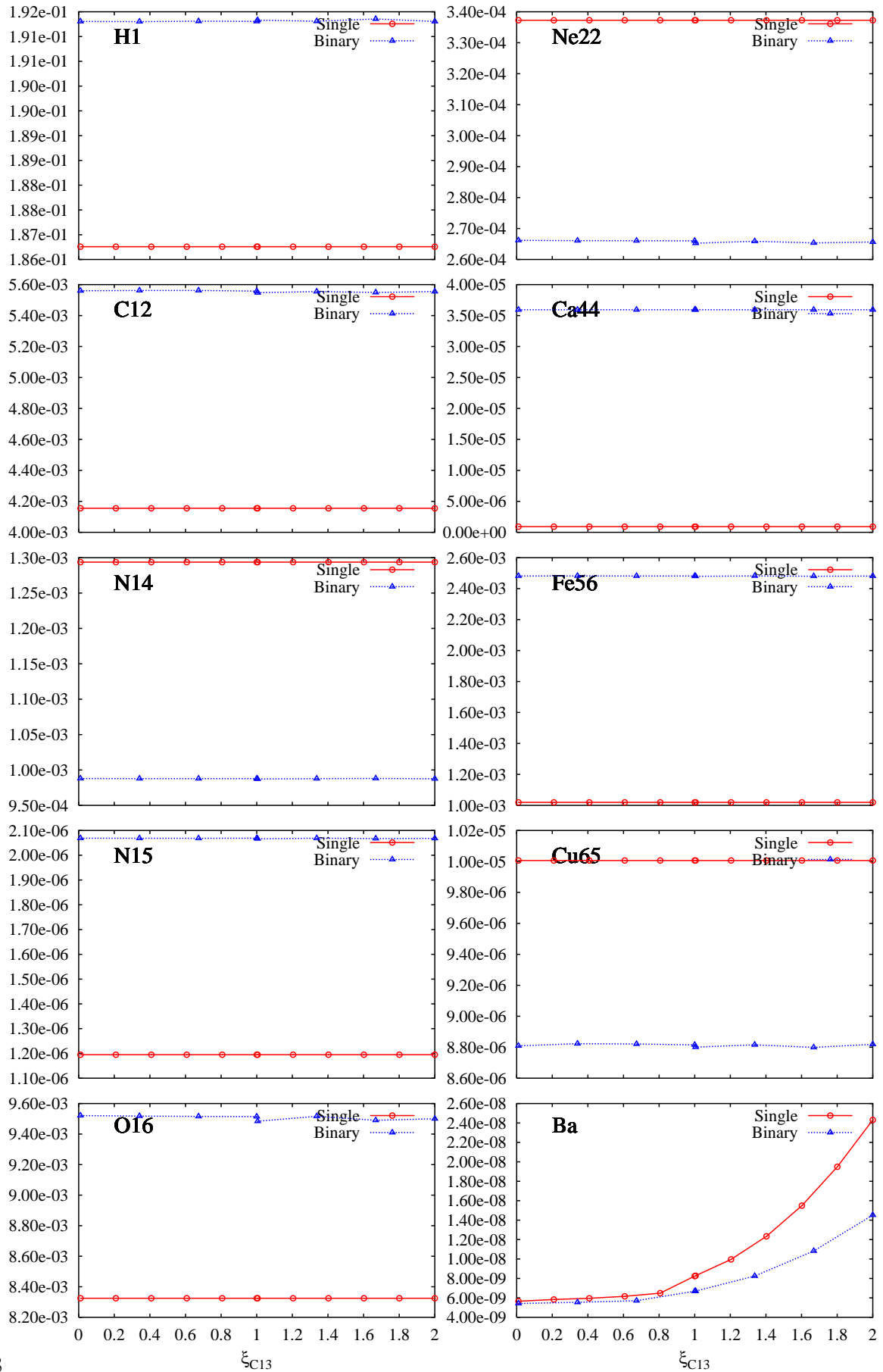
Figure 67: Yield relative to mass input y vs s-process pocket efficiency.

6.2.7 BH Mass Prescription

Figure 68 shows the variation in yields with BH mass prescription. The H02 prescription leads to lower-mass black holes than the Belczynski prescription. This means that more matter escapes to the ISM and the corresponding yield is higher. The true BH mass that results from a given stellar progenitor remains a hotly debated topic within the IoA stellar evolution group! The difference between single and binary yields for a given isotope is approximately constant. This suggests the BH prescription has most of its nucleosynthetic effect by its influence on the mass ejected from the supernova explosion (eq. 137) rather than on the subsequent evolution of the binary system after the supernova. This may also be because it is unlikely that a system survives a supernova so it is unlikely the secondary interacts with the BH.
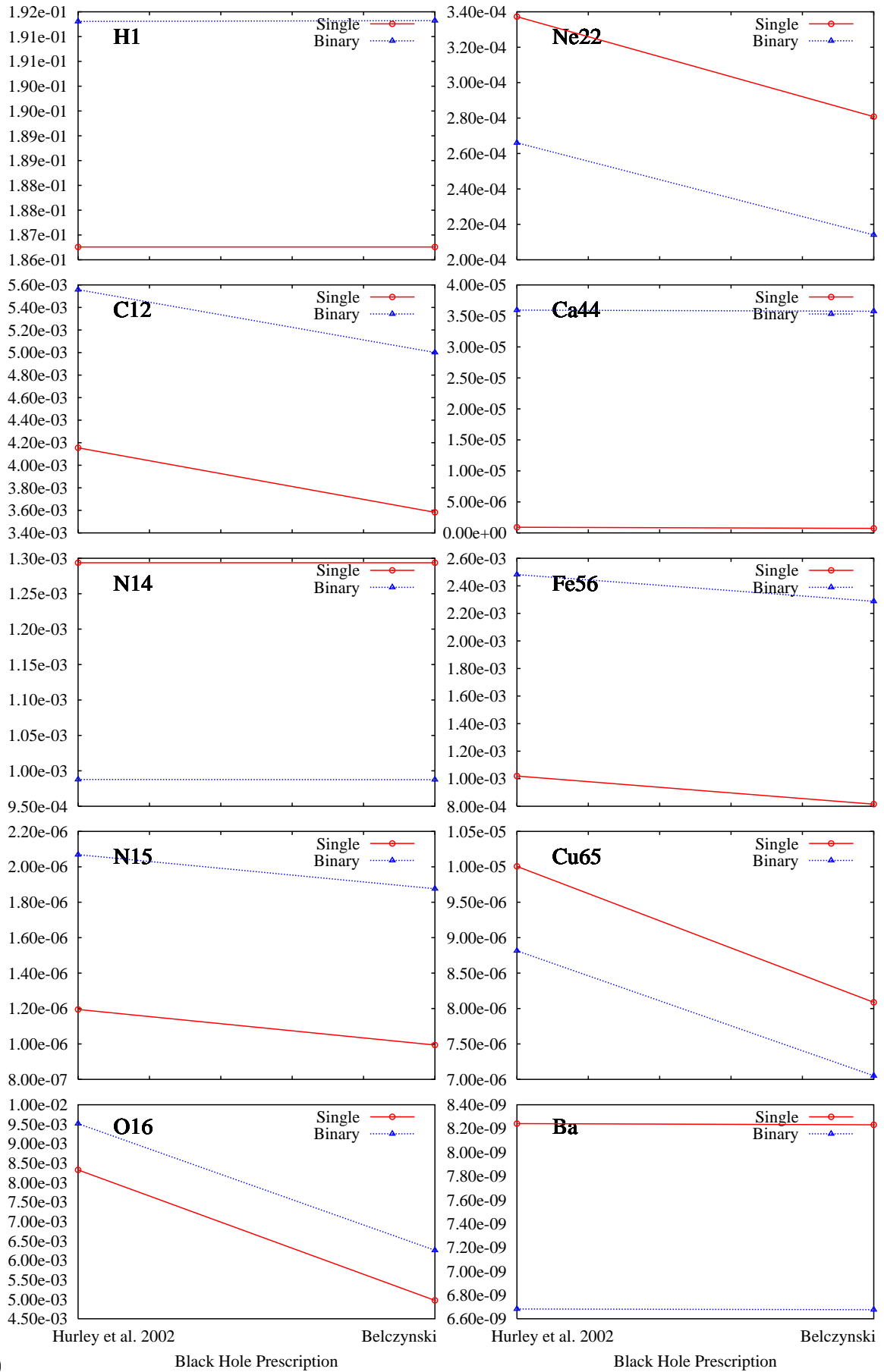
Figure 68: Yield relative to mass input y vs black hole mass prescription.

6.2.8 Dredge-up Parameters

The two free parameters introduced to solve the problem of the over-luminous carbon stars can also be considered as free parameters given the current fragile constraint on their values. They are only calibrated for the SMC and LMC.

Decreasing $\Delta M_{c,min}$ leads to more and earlier dredge-up in lower-mass stars than predicted by calibration to the Monash models. Consequently more helium is brought to the surface at the expense of hydrogen and the yields of helium burning products, ^{12}C, ^{22}Ne and Ba from the *s*-process pocket, increase. The effect of $\Delta M_{c,min}$ on the yields is always smaller than the effect of duplicity.

Provided $\lambda_{min} \leq 0.8$ the effect on stellar yields is less than about 10% (fig. 70), certainly less than the effect of duplicity. If $\lambda_{min} = 1.0$ the yields from intershell isotopes are almost doubled – certainly comparable to duplicity effects although currently ruled out by LMC/SMC observations.
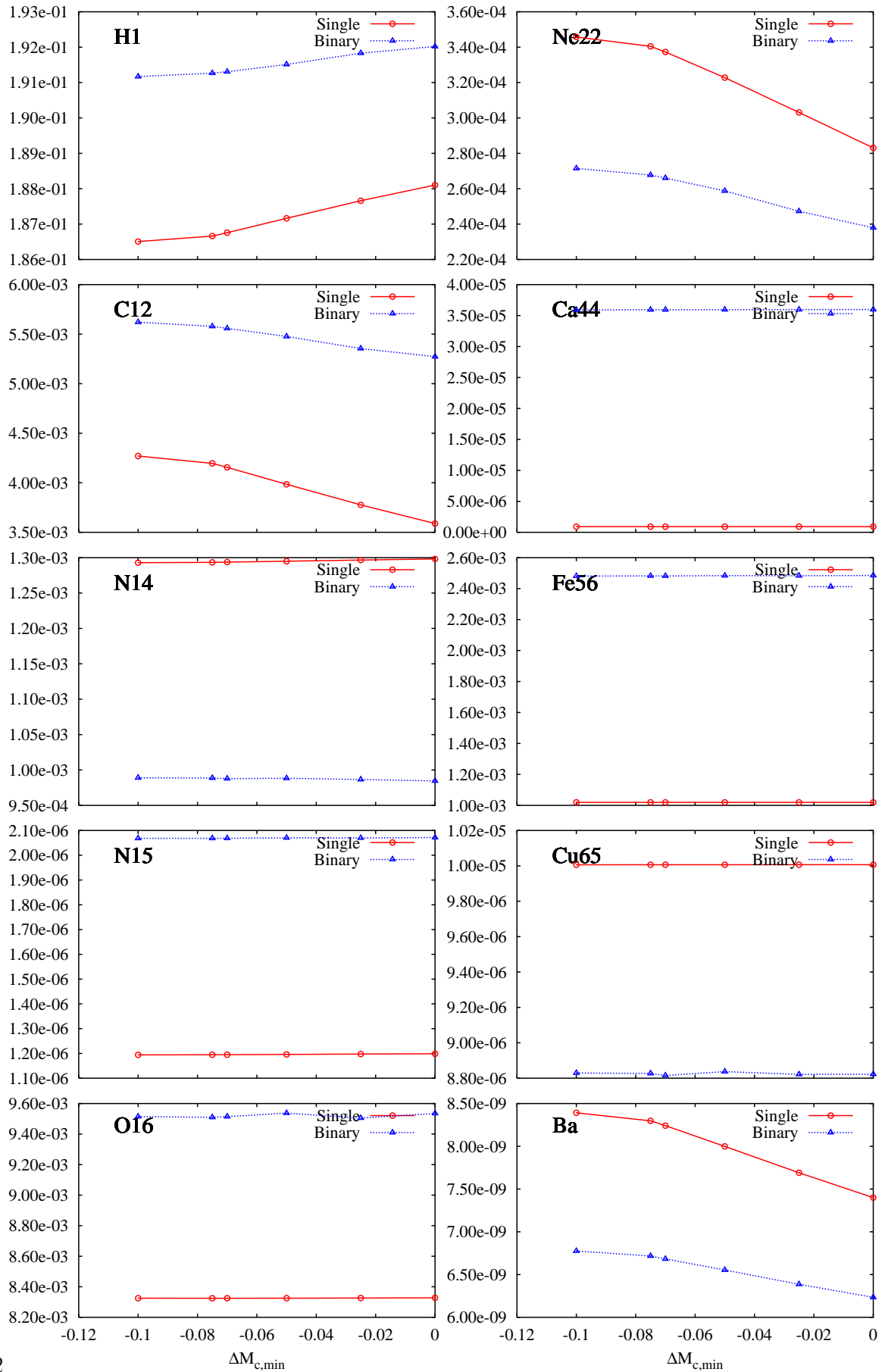
Figure 69: Yield relative to mass input y vs $\Delta M_{c,min}$.
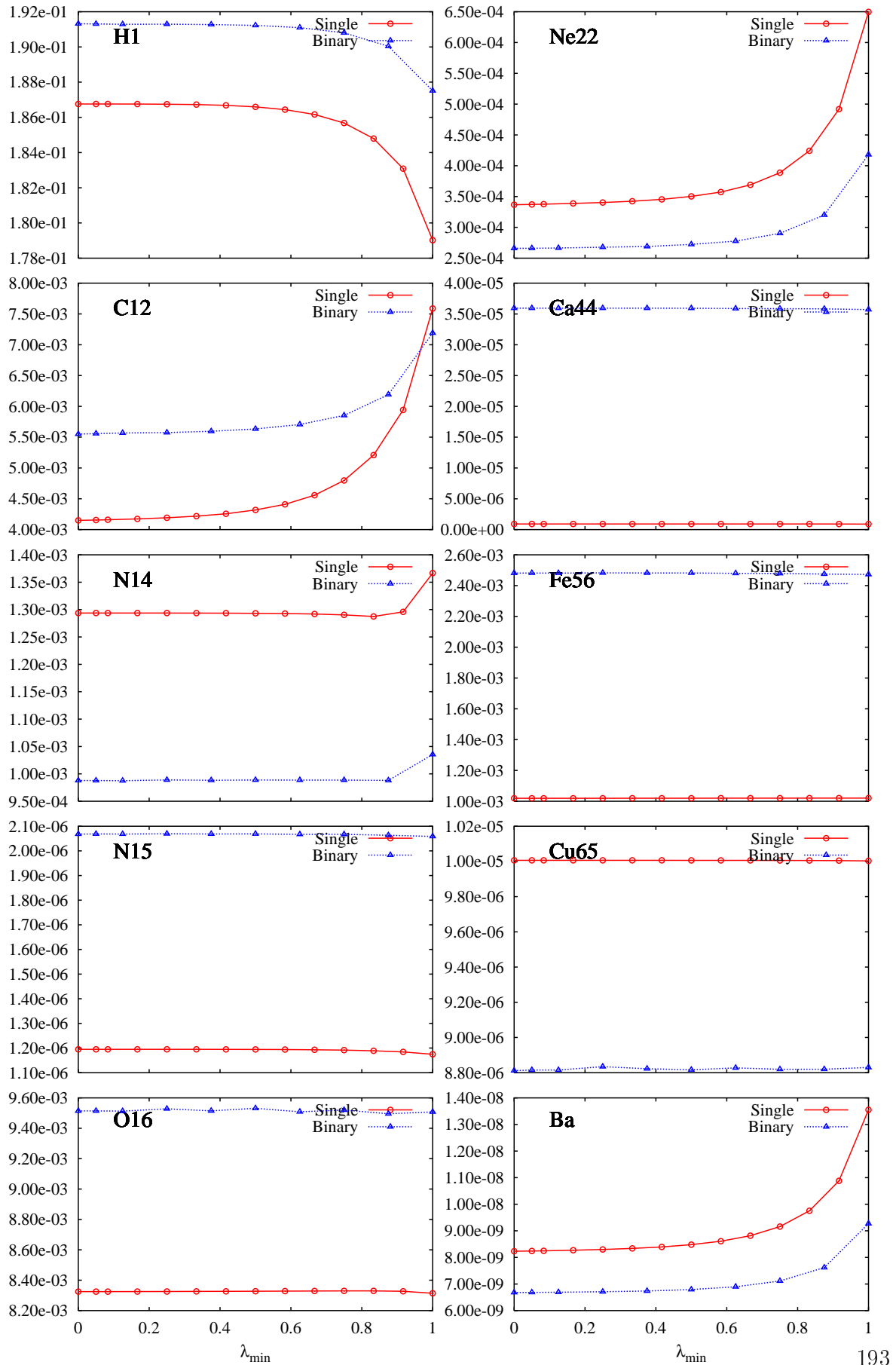
Figure 70: Yield relative to mass input y vs $\lambda_{\min}$.

6.2.9 Eccentricity

The remaining free parameters relate only to binary star processes.

The eccentricity is set to zero in section 5.2 for two reasons. The first is to reduce the dimension of the parameter space by one and therefore increase the speed of a grid run by a factor of 100. The second is because interacting binary systems are thought to circularize their orbits during mass transfer. Figure 71 shows the effect of varying the initial eccentricity of the entire population. In a real population of stars the eccentricity would be distributed in some way but the yields do not vary enough with e to warrant introduction of such a distribution and the factor of 100 in the grid runtime.

A value $e = 1$ is clearly unrealistic, these are like single stars. Most yields vary by less than 10% for $e < 0.8$. The copper yield increases at $e = 0.8$ owing to an increase in the SNII/SNIb/c ratio, probably resulting from mergers of systems at periastron which would not merge if $e = 0$. The barium yield is increased a small amount by a combination of non-conservative RLOF in low-mass stars.
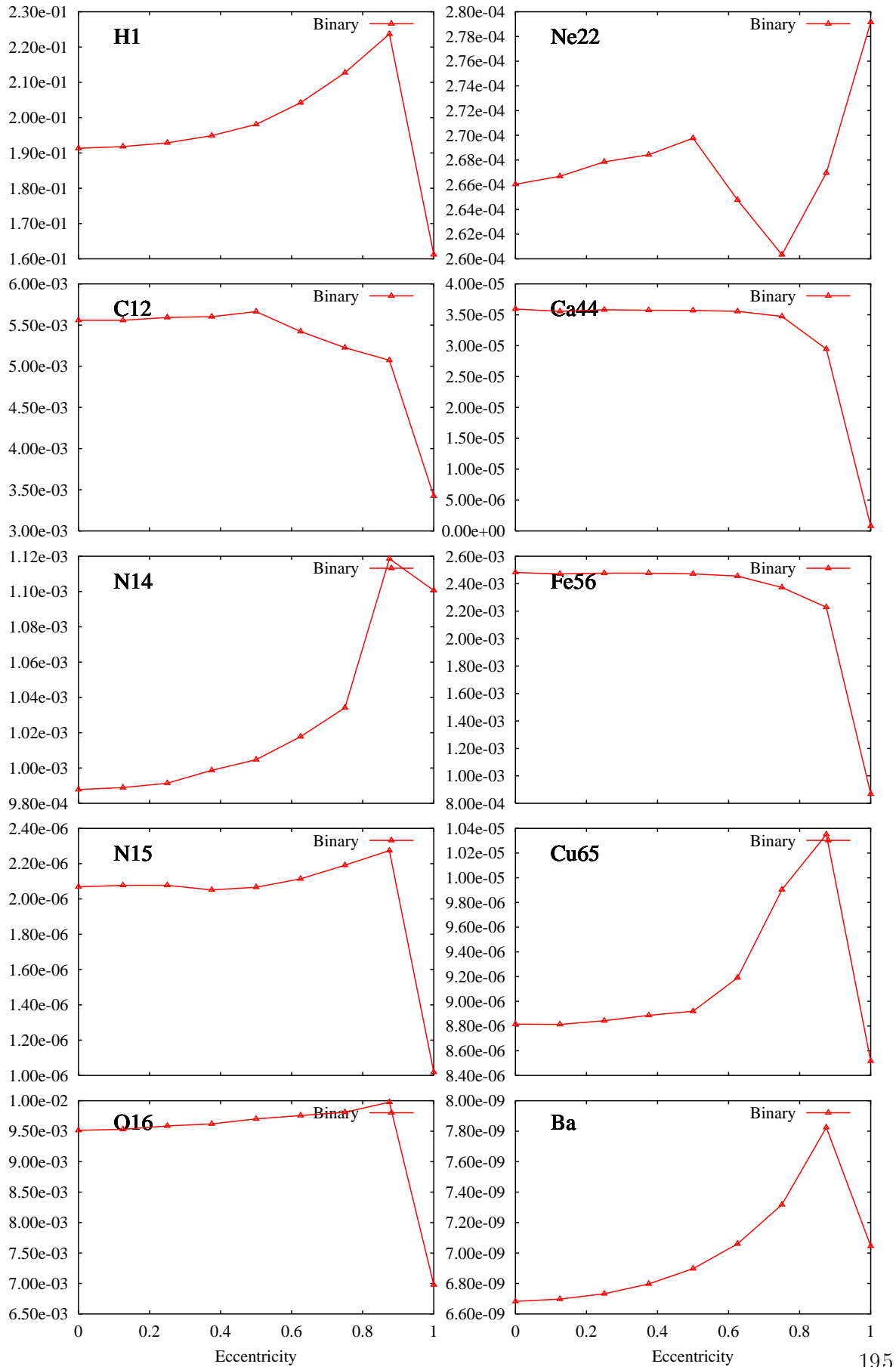
Figure 71: Yield relative to mass input y vs eccentricity.

6.2.10 Common-Envelope Parameter α_{CE}

The effect of varying the common-envelope parameter α_{CE} on the yields is shown in fig. 72. An increase in α_{CE} means the common envelope is ejected more easily. One possible post-common-envelope object is a new TPAGB star which forms if the cores merge to form a new CO core and the envelope is not lost. An increase in α_{CE} leads to a slight decrease in yields of ^{14}N and barium, although yields of ^{12}C rise because this is less likely to be processed to ^{14}N. A low value of α_{CE} is also more likely to lead to a massive star remnant and correspondingly the ^{65}Cu yield increases owing to an increase in the SNII/SNIb/c ratio. Quite surprisingly, for $\alpha_{\mathrm{CE}} \gtrsim 1.0$ the SNIa yields are quite constant. At $\alpha \approx 0.5$ the SNIa yields are halved.
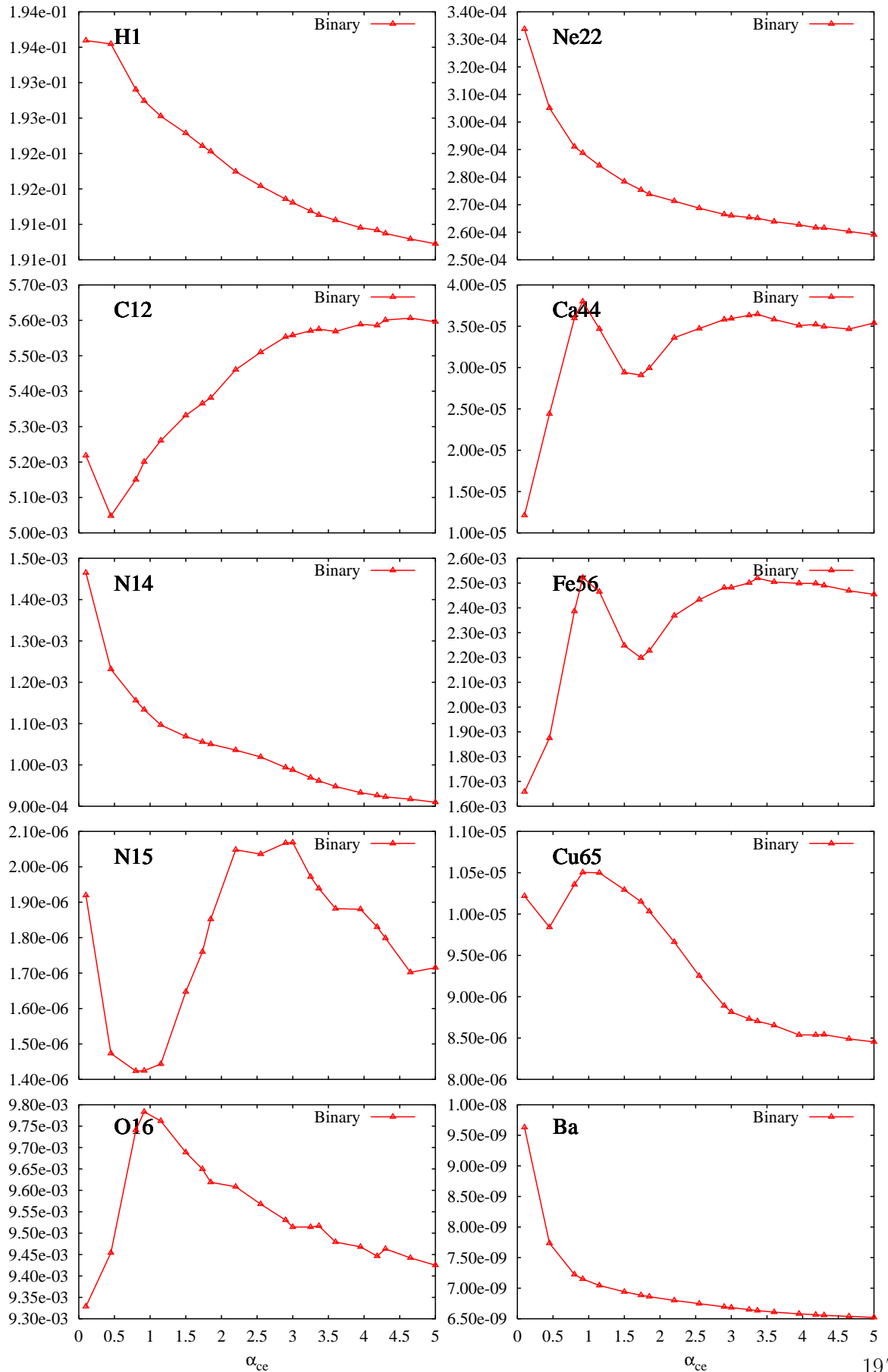
Figure 72: Yield relative to mass input y vs α_{CE}.

6.2.11 Eddington Limit

Figure 73 shows that the only noticeable effect of imposing the Eddington limit on chemical yields is on the ^{56}Fe yield and even that is negligible compared to the variation of other slow parameters.
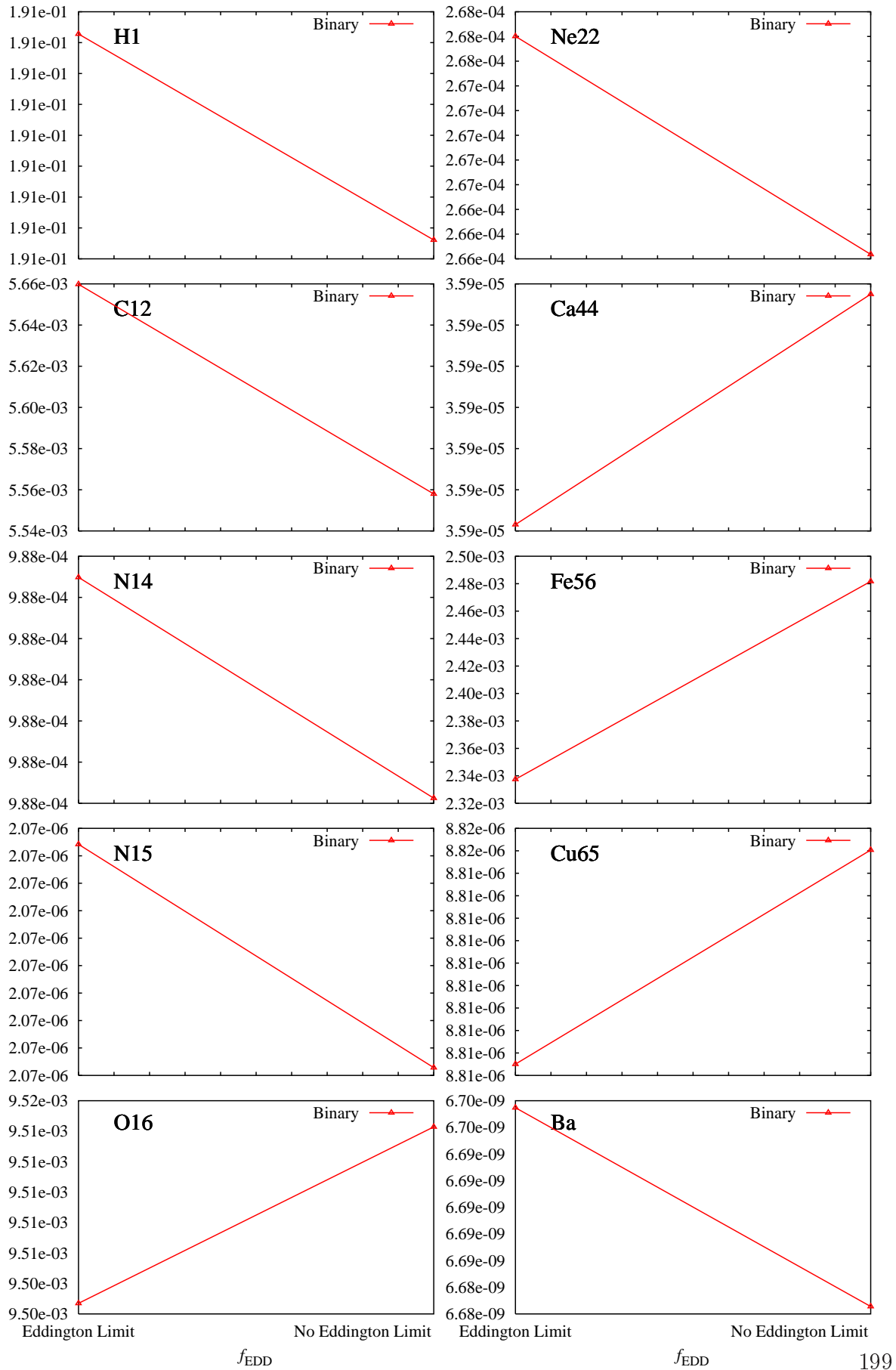
Figure 73: Yield relative to mass input *y* vs Eddington limit.

6.2.12 SN-Kick Velocity Dispersion

The supernova-kick velocity dispersion could be important because a low kick dispersion leads to more binaries surviving a SN. This would lead to more mergers with NSs or BHs and a reduced yield. This effect is shown in fig. 74 – the yield of everything drops as $\sigma_{\mathrm{SN}} \to 0$ (except hydrogen, which rises slightly).
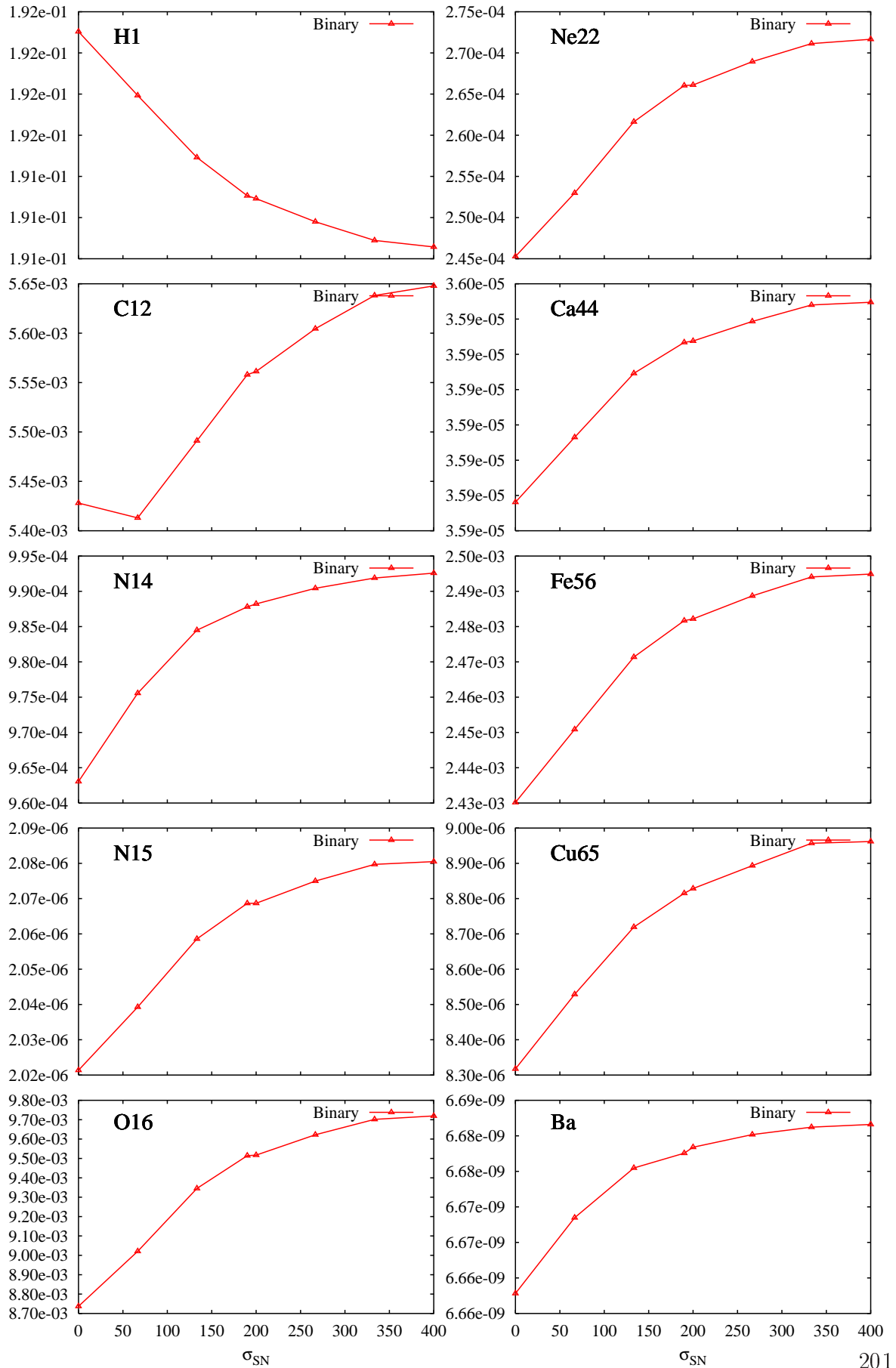
Figure 74: Yield relative to mass input y vs σ_{SN}.

6.2.13 Binary-Enhanced Wind Loss

Figure 75 shows the effect of varying the enhanced binary wind loss factor B between 0 and 10^4. The effect is to increase the yield of most isotopes at the expense of hydrogen when there is no extra wind loss. This is to be expected as the stars with lower B are more massive. The difference between $B = 0$ and $B = 10^4$ is up to 40% for ^{44}Ca although most other isotopes vary by only 10-20%.
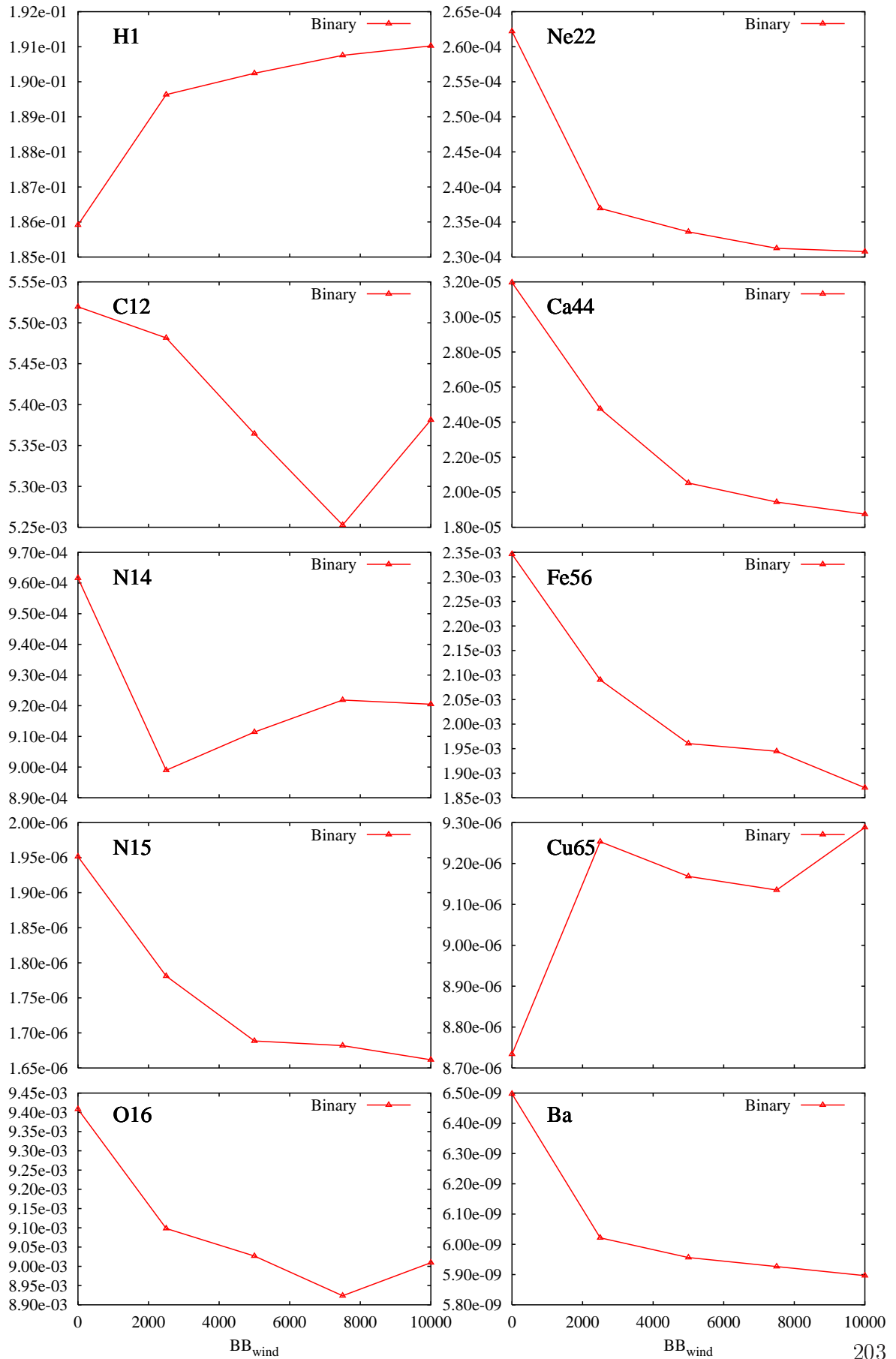
Figure 75: Yield relative to mass input y vs the enhanced binary wind loss factor B.

6.3 Taylor Series Coefficients

The calculated T_{ij} are listed in table 18. The leftmost column shows the isotope corresponding to each row, the second column is the default yield of the isotope relative to mass input to stars, the remaining columns are the T_{ij}. The first row of the table lists the free parameters, the second row the default parameters and the third row the range Δx_i. T_{ij} with a higher magnitude are the important parameters that vary greatly with their variable x_i – those with magnitude greater than 0.1 are marked in red.

The value for Z is approximate owing to the non-linear behaviour of most yields with Z (e.g. $T_{Z\,\text{Ba}} \approx 0$) – in these cases a higher order fit is required.

Isotope	Single	ξ_{C13}	f_{WR}	$\Delta M_{\text{c,min}}$	η_{GB}	λ_{min}	Z
	Default	1	1	$-7^{(-2)}$	$5^{(-1)}$	$5^{(-2)}$	$2^{(-2)}$
-	Δx	1.99	9.90	$1^{(-1)}$	$5^{(-1)}$	1	$2.99^{(-2)}$
^{1}H	$1.87^{(-1)}$	0	$-3.99^{(-3)}$	$9.80^{(-3)}$	$2.78^{(-2)}$	$-1.85^{(-2)}$	$-1.64^{(-1)}$
^{12}C	$4.16^{(-3)}$	0	$2.37^{(-1)}$	$-1.86^{(-1)}$	$-1.43^{(-1)}$	$4.08^{(-1)}$	$-4.42^{(-1)}$
^{14}N	$1.29^{(-3)}$	0	$-2.27^{(-3)}$	$4.72^{(-3)}$	$-2.15^{(-2)}$	$1.23^{(-2)}$	-1.25
^{15}N	$1.19^{(-6)}$	0	$-1.07^{(-1)}$	$4.48^{(-3)}$	$1.99^{(-2)}$	$-7.99^{(-3)}$	$9.90^{(-1)}$
^{16}O	$8.32^{(-3)}$	0	$-4.85^{(-1)}$	$3.37^{(-4)}$	$6.59^{(-3)}$	$1.73^{(-4)}$	$-6.95^{(-2)}$
^{22}Ne	$3.37^{(-4)}$	0	$9.31^{(-2)}$	$-2.12^{(-1)}$	$-2.02^{(-1)}$	$4.39^{(-1)}$	1.06
^{44}Ca	$9.16^{(-7)}$	0	$-1.74^{(-1)}$	$4.48^{(-3)}$	$1.25^{(-2)}$	$-8.45^{(-3)}$	$8.07^{(-1)}$
^{56}Fe	$1.02^{(-3)}$	0	$-8.65^{(-2)}$	$-7.67^{(-5)}$	$6.96^{(-3)}$	$1.20^{(-3)}$	$2.59^{(-1)}$
^{65}Cu	$1^{(-5)}$	0	$1.74^{(-1)}$	$7.65^{(-5)}$	$2.14^{(-4)}$	$-1.44^{(-4)}$	$-8.39^{(-1)}$
Ba	$8.24^{(-9)}$	2.13	$1.21^{(-2)}$	$-1.37^{(-1)}$	$-1.18^{(-1)}$	$3.09^{(-1)}$	-4.56

Isotope	Binary	ξ_{C13}	f_{WR}	α_{CE}	$\Delta M_{\text{c,min}}$	e	f_{EDD}	η_{GB}	λ_{min}	σ_{SN}	Z
	Default	1	1	3	$-7^{(-2)}$	0	$1^{(6)}$	$5^{(-1)}$	$5^{(-2)}$	$1.90^{(2)}$	$2^{(-2)}$
-	Δx	1.99	9.90	4.90	$1^{(-1)}$	1	$1^{(6)}$	$5^{(-1)}$	1	$4^{(2)}$	$2.99^{(-2)}$
^{1}H	$1.91^{(-1)}$	$1.21^{(-4)}$	$-3.61^{(-3)}$	$-1.63^{(-2)}$	$5.19^{(-3)}$	$4.52^{(-2)}$	$-3.49^{(-4)}$	$8.23^{(-3)}$	$-9.81^{(-3)}$	$-5.27^{(-3)}$	$-1.88^{(-1)}$
^{12}C	$5.56^{(-3)}$	$-1.83^{(-3)}$	$1.04^{(-1)}$	$1.11^{(-1)}$	$-7.14^{(-2)}$	$-1.59^{(-1)}$	$-1.83^{(-2)}$	$-4.96^{(-2)}$	$1.58^{(-1)}$	$4.62^{(-2)}$	$5.99^{(-2)}$
^{14}N	$9.88^{(-4)}$	$-1.26^{(-4)}$	$-5.93^{(-3)}$	$-4.13^{(-1)}$	$-3.84^{(-3)}$	$9.35^{(-2)}$	$-2.71^{(-5)}$	$-1.85^{(-2)}$	$1.74^{(-2)}$	$2.65^{(-2)}$	$-6.46^{(-1)}$
^{15}N	$2.07^{(-6)}$	$-5.15^{(-4)}$	$-4.83^{(-1)}$	$2.57^{(-1)}$	$1.70^{(-3)}$	$-1.14^{(-1)}$	$-1.97^{(-4)}$	$2.35^{(-3)}$	$-2.75^{(-3)}$	$2.74^{(-2)}$	$9.02^{(-1)}$
^{16}O	$9.51^{(-3)}$	$-2.63^{(-3)}$	$-4.89^{(-1)}$	$-2.29^{(-2)}$	$1.95^{(-3)}$	$-5.29^{(-2)}$	$1.22^{(-3)}$	$-1.02^{(-3)}$	$-3.97^{(-4)}$	$9.96^{(-2)}$	$8.75^{(-2)}$
^{22}Ne	$2.66^{(-4)}$	$-2.67^{(-3)}$	$8.68^{(-2)}$	$-2.12^{(-1)}$	$-1.43^{(-1)}$	$1.43^{(-2)}$	$-6.64^{(-3)}$	$-1.22^{(-1)}$	$2.95^{(-1)}$	$9.54^{(-2)}$	1.21
^{44}Ca	$3.59^{(-5)}$	$-2.91^{(-5)}$	$6.40^{(-2)}$	$3.60^{(-1)}$	$1.73^{(-3)}$	$-3.69^{(-1)}$	$7.78^{(-5)}$	$-2.75^{(-2)}$	$-3.87^{(-3)}$	$1.49^{(-3)}$	-1.19
^{56}Fe	$2.48^{(-3)}$	$-3.86^{(-4)}$	$-1.80^{(-1)}$	$2.30^{(-1)}$	$1.81^{(-3)}$	$-2.46^{(-1)}$	$5.81^{(-2)}$	$-9.28^{(-3)}$	$-2.48^{(-3)}$	$2.48^{(-2)}$	$-9.55^{(-1)}$
^{65}Cu	$8.82^{(-6)}$	$-5.84^{(-4)}$	$-7.52^{(-2)}$	$-3.13^{(-1)}$	$1.02^{(-3)}$	$7.76^{(-2)}$	$1.08^{(-3)}$	$-2^{(-2)}$	$1.44^{(-3)}$	$6.98^{(-2)}$	$-7.20^{(-1)}$
Ba	$6.68^{(-9)}$	1.30	$2.48^{(-2)}$	$-2.63^{(-1)}$	$-9.13^{(-2)}$	$1.05^{(-1)}$	$-2.23^{(-3)}$	$-7.09^{(-2)}$	$2.02^{(-1)}$	$3.14^{(-3)}$	-2.16

Table 18: Taylor series coefficients T_{ij} – see text for details, especially eq. 202. The format $x^{(y)}$ represents $x \times 10^{y}$.

6.4 Conclusions

It is immediately obvious from table 18 that some slow parameters are important for calculation of chemical yields.

In single stars ^{12}C is sensitive to all the slow parameters except ξ_{C13}. ^{14}N is sensitive only to Z while ^{15}N yields are also sensitive to massive star mass-loss rates. The WR mass-loss rate also affects the ^{16}O yield, which is otherwise robust. For all the free parameters except f_{WR} the ^{44}Ca yields are very small compared to the binary population. ^{56}Fe and ^{65}Cu are only really sensitive to Z. Barium is sensitive to all parameters except f_{WR} but mostly to ξ_{C13} and Z.

For binary populations the trend is for the same dependency as with single stars, although the magnitude of the variation tends to drop at the expense of more free parameters. For example, $T_{f_{WR}^{12}C} = 0.237$ for single stars but only 0.104 for binary stars. However, in binaries, there is the uncertain α_{CE} for which $T_{\alpha_{CE}^{12}C} = 0.111$ so the total uncertainty in the yield is about the same.

Some parameters are irrelevant for calculation of yields: f_{EDD} and σ_{SN}. The s-process factor ξ_{C13} affects only the s-process yields. $\Delta M_{c,min}$ affects only ^{22}Ne in a serious way. λ_{min} only affects ^{12}C, ^{22}Ne and Ba because these are isotopes involved in third dredge-up. Again the magnitude of the λ_{min} dependence is smaller in binary stars.

7 Conclusions – Yields from Single and Binary Stars

The considerations of the previous two chapters aside, the aim of this work is to determine the effect of a binary companion on the stellar yield. Figures 76 to 82 show this for a $Z = 0.02$ default population (see chapter 5). The yield per unit mass input to stars, normalized to the KTG93 IMF and multiplied by the mass M, is plotted against $\ln M$. For single stars this is

$$f_j = \frac{dy_j}{d \ln M} = \frac{M \, dy_j}{dM} = \frac{M \, \psi(M) \int_0^t \dot{M}(t) \, X_j(t) \, dt}{\int M \, \psi(M) \, dM}, \qquad (204)$$

while for binary stars the M_2 and a distributions (flat-q and flat-a, the defaults) are integrated over to give

$$
\begin{aligned}
f_j = \frac{dy_j}{d \ln M_1} &= \frac{M_1 \, dy_j}{dM_1} \\
&= \frac{M_1 \psi(M) \int_0^t \int_a \int_{M_2} \phi(M_2)\chi(a)\dot{M}(t)X_j(t) \, dM_2 \, da \, dt}{\int_{M_1} \int_{M_2} (M_1 + M_2)\psi(M)\phi(M_2) \, dM_2 \, dM_1} ,
\end{aligned}
\qquad (205)
$$

where

$$y_j = \frac{\text{MASS OUT AS } j \text{ FROM ALL STARS}}{\text{MASS INTO ALL STARS}} = \frac{\int_{\text{all stars}} \int_0^t \Psi_i \dot{M}_i(t) X_j(t) \, dt \, di}{\int_{\text{all stars}} M_i \Psi_i \, di} \qquad (206)$$

as previously.

The figures show the yield $M_1 f = M_1 dy/d \ln M_1$ from various sources, Thorne-Żytkow objects (TZ), giant-branch winds (GB), AGB winds (AGB), WR winds (WR), novae, SNeIa, SNeIb/c, SNeII, common-envelope evolution (Comenv), non-conservative Roche Lobe Overflow (RLOF) and wind loss from other stellar types (Wind). The corresponding colours are shown in the key in the top-right corner of each plot. Between each source name and the colour are two numbers. These are the y for the source and the fraction of the total yield due to this source. The total yield is the number in the top left corner of the plot. Single stars are shown in the left plots, binary stars on the right.

These plots answer the question *what is the effect of binary stars on chemical yields?* For many isotopes there is little change between single and binary stars[1]. This is not to say the source of yield is the same between single and binary stars.

Take hydrogen as an example. The single-star yield is 0.1868, the binary yield 0.1913, a small difference. However, *where the hydrogen comes from* is quite different. In going from single to binary stars the AGB yield is cut by more than half, the same applies to SNeII. These effects are compensated by common envelope and non-conservative RLOF losses. Similar arguments apply to helium but also the WR and SNIb/c yields are doubled. Is this change in stellar source important? Perhaps, because some sources present more uncertainty than others. Models of massive stars are relatively robust compared to models of common envelope evolution. The possibility of a burning-shell on the core(s), some mixing into the core(s) or an incorrect α_{CE} cannot be excluded and might have a major effect.

All isotopes which are produced on the TPAGB have their yields diminished in binaries, relative to single stars, quite consistently by a factor of two (see ^{12}C, ^{13}C, ^{14}N, ^{22}Ne). Type II supernovae give way to type Ib/c, which with smaller cores have different patterns of yields (more carbon and less oxygen according to WW95).

In most cases there is some binary process which compensates the loss of AGB and SNII yields. The ^{12}C yields are boosted by a doubling of SNIb/c and WR yields as well as

---

[1]This is true because the yields are normalized to *mass input* − this seems the most sensible definition of the yield.

significant common envelope output. Presumably the latter is carbon present at the stars' birth although it could be from extreme HeGB stars. Massive star output of carbon, from SNII/Ib/c and WR stars, accounts for about 60% of the total carbon yield, assuming a 50% binary fraction (by input mass).

Novae are important contributors to ^{13}C yields but, interestingly, TPAGB stars are more so. If a 50% binary fraction is assumed then AGB ^{13}C outweighs novae by two to one. However, given the uncertainties involved in AGB and nova modelling, it is unwise to say novae are not important. Most ^{15}N comes from novae but most ^{17}O comes from single AGB stars. The majority of ^{14}N comes from single AGB stars – the massive star contribution is only a few per cent. Common-envelope output boosts the ^{16}O yield from binaries a little but it is still quite similar to the single-star yield.

The NeNa-isotope yields all drop in binaries with the exception of ^{20}Ne. This is because there is less NeNa cycling on the AGB and the ^{20}Ne is more likely to escape the binary unprocessed in a common envelope ejection. The usual rearrangement of SNII to SNIb/c has little effect on the combined yield.

The MgAl yields are more interesting because there is some contribution to ^{24}Mg from SNeIa leading to a 20% boost in binaries. There is also the usual drop in yields associated with fewer TPAGB stars in binaries.

The heavier α-isotopes, ^{32}S, ^{36}Ar, ^{40}Ca, ^{44}Ca, ^{48}Ti, ^{52}Cr and ^{56}Fe, are all associated with SNeIa and single-star yields are small for most of them. Iron is also produced in core-collapse supernovae, though if a 50% binary fraction is assumed then 57% of the iron yield is from SNeIa.

The r-process-only isotope ^{65}Cu is produced in roughly equal amounts from single and binary stars, but 86% of its single-star yield is from SNeII compared to only 54% in binaries. Again SNIb/c make up the difference. The s-process yields drop by 20-40% in binaries due to a smaller number of TPAGB stars.

So are the binary yields *significantly* different from single-star yields? That all depends on how accurate the GCE model is desired to be. But it is now possible to at least *quantify* the difference between single and binary star yields over a wide parameter space. If a factor
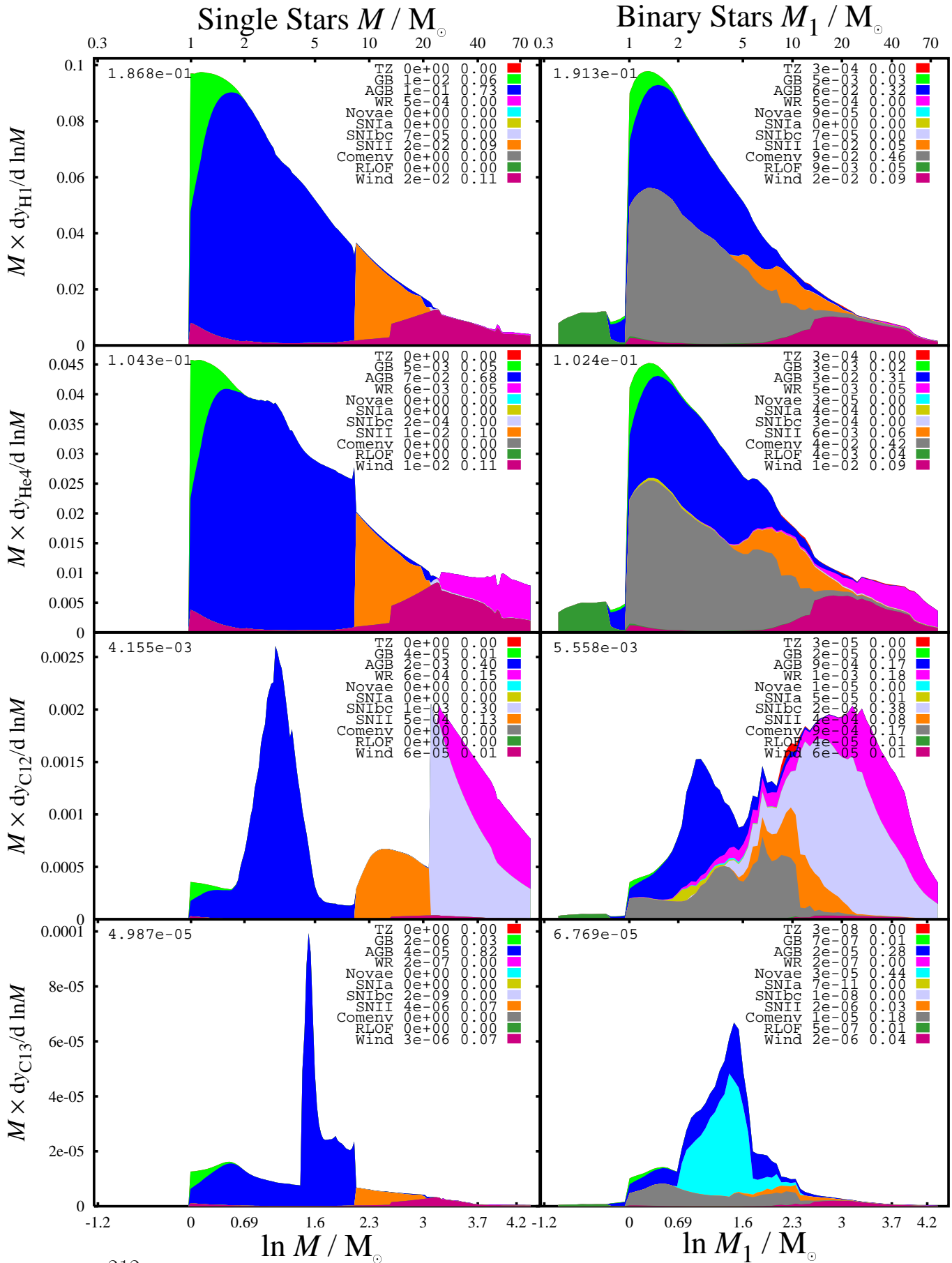
Figure 76: Yield per unit mass input to stars y for ^{1}H, ^{4}He, ^{12}C and ^{13}C. See text for details.
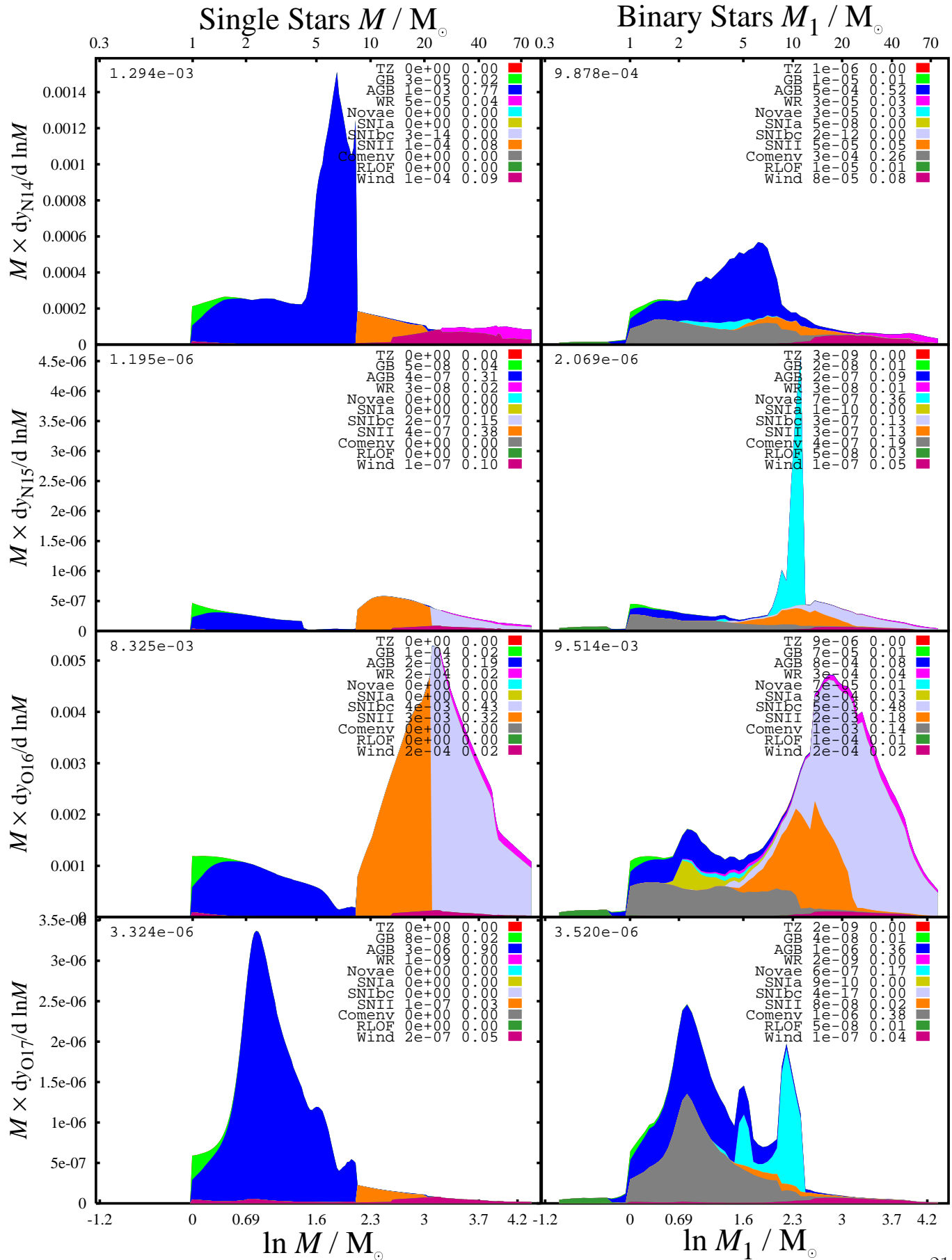
Figure 77: Yield per unit mass input to stars for ^{14}N, ^{15}N, ^{16}O and ^{17}O.

213
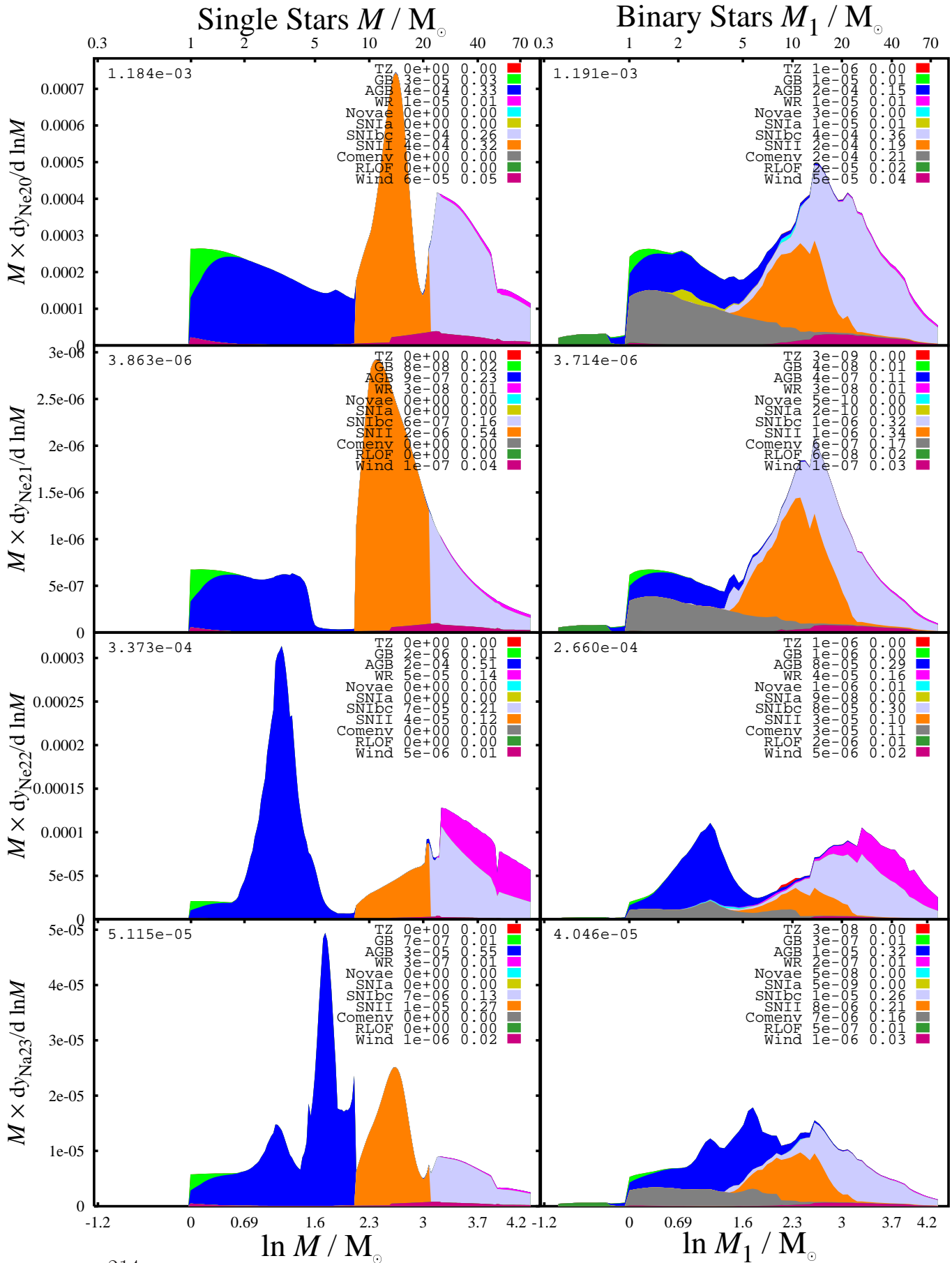
Figure 78: Yield per unit mass input to stars for ^{20}Ne, ^{21}Ne, ^{22}Ne and ^{23}Na.

Single Stars M / M$_\odot$

TZ	0e+00	0.00
GB	1e-05	0.03
AGB	1e-04	0.32
WR	4e-06	0.01
Novae	0e+00	0.00
SNIa	0e+00	0.00
SNIbc	1e-04	0.30
SNII	1e-04	0.29
Comenv	0e+00	0.00
RLOF	0e+00	0.00
Wind	2e-05	0.05

3.675e-04

Binary Stars M_1 / M$_\odot$

TZ	4e-07	0.00
GB	5e-06	0.01
AGB	5e-05	0.12
WR	4e-06	0.01
Novae	3e-08	0.00
SNIa	6e-05	0.14
SNIbc	1e-04	0.32
SNII	6e-05	0.15
Comenv	8e-05	0.19
RLOF	8e-06	0.02
Wind	2e-05	0.04

4.209e-04
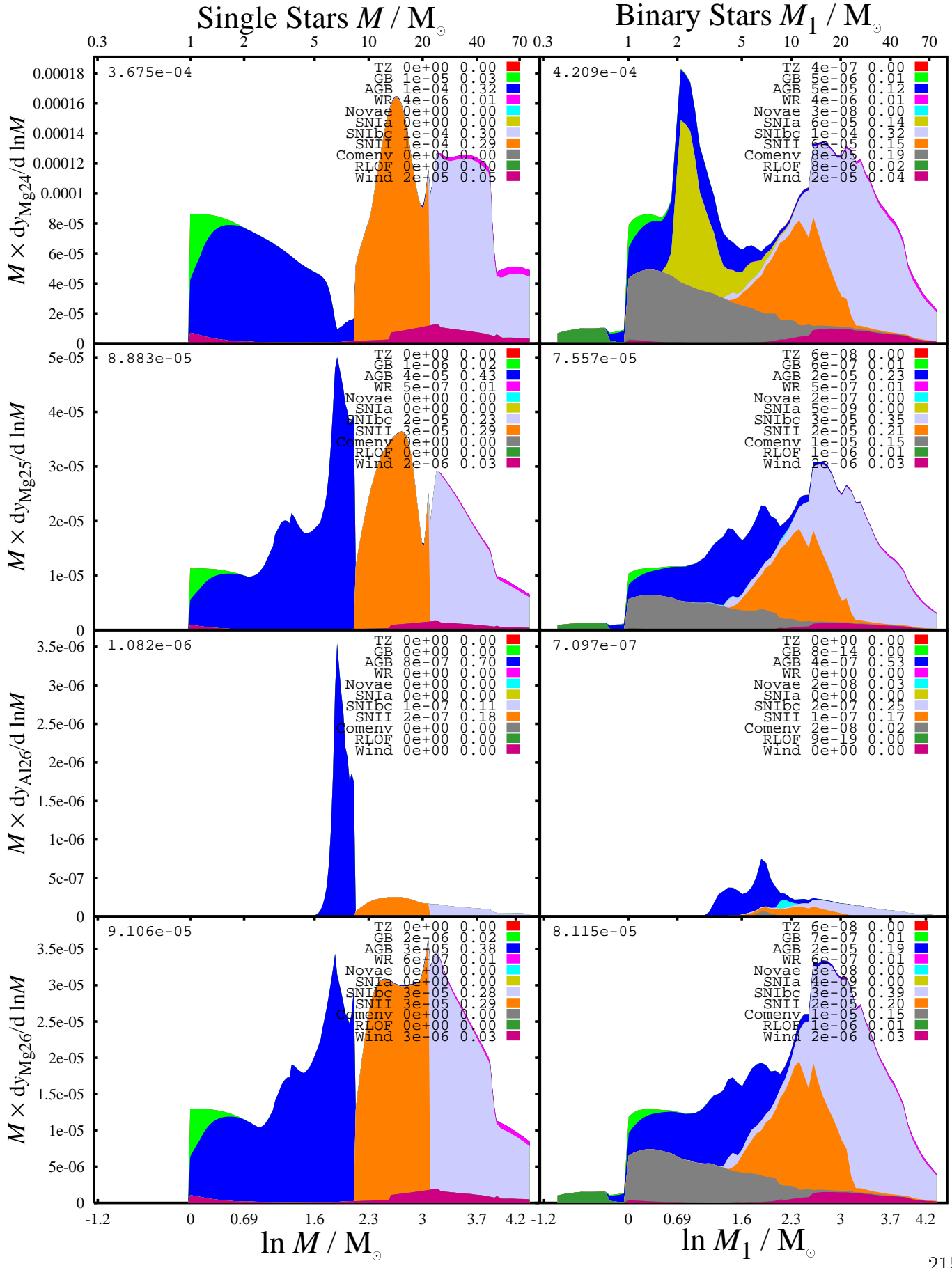
Figure 79: Yield per unit mass input to stars for ^{24}Mg, ^{25}Mg, ^{26}Al and ^{26}Mg.

215
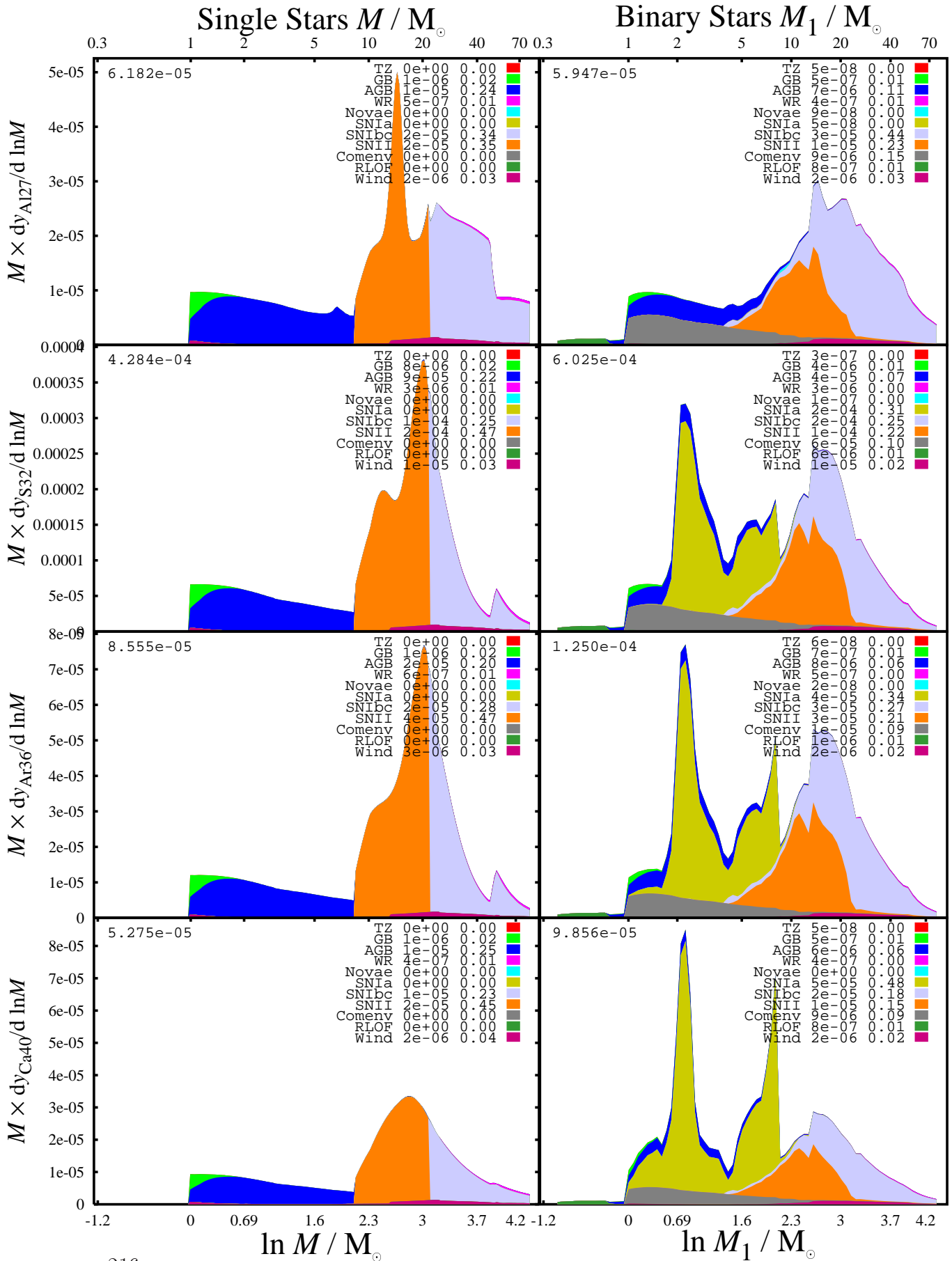
Figure 80: Yield per unit mass input to stars for ^{27}Al, ^{32}S, ^{36}Ar and ^{40}Ca.
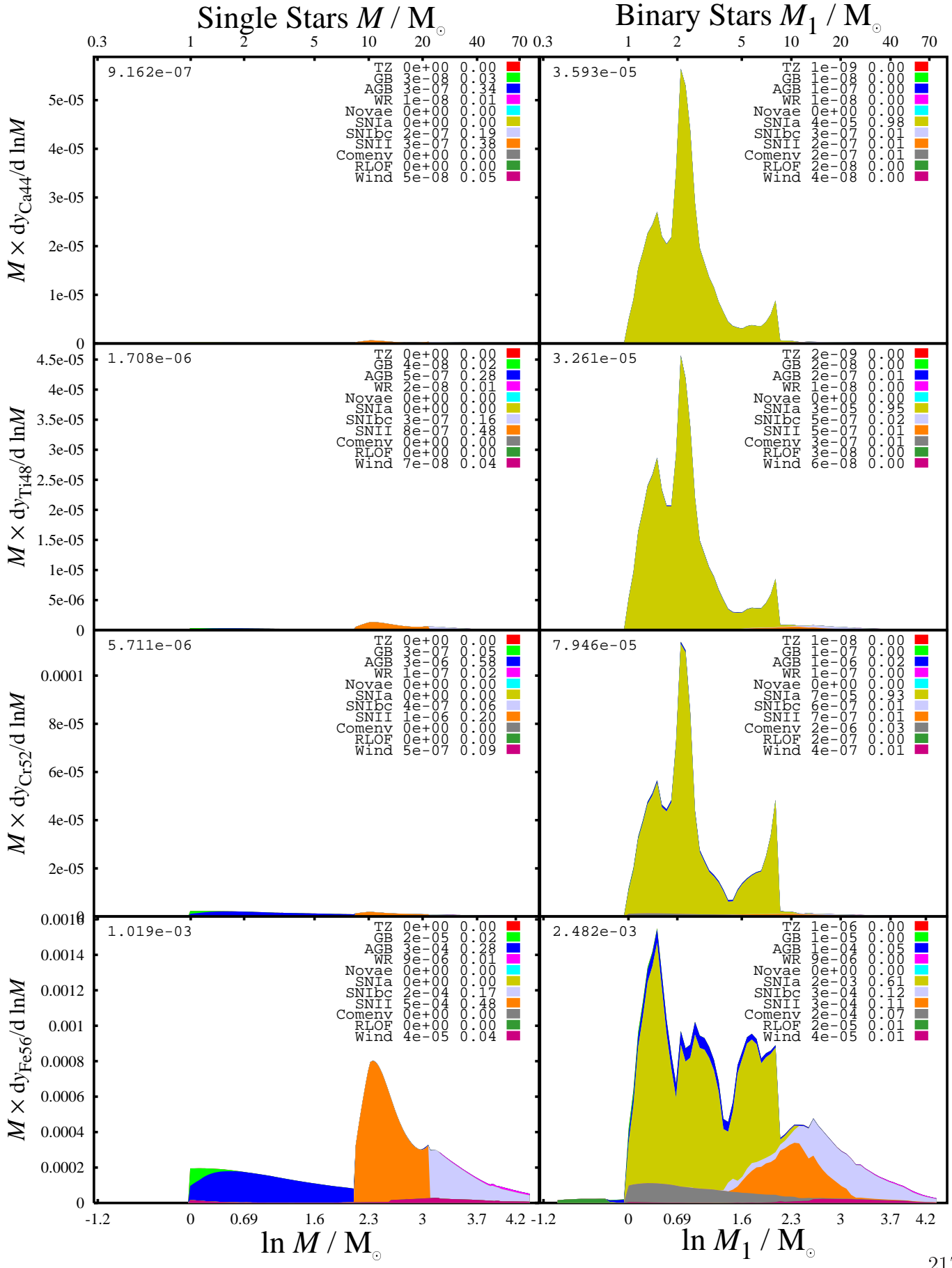
Figure 81: Yield per unit mass input to stars for ^{44}Ca, ^{48}Ti, ^{52}Cr and ^{56}Fe.
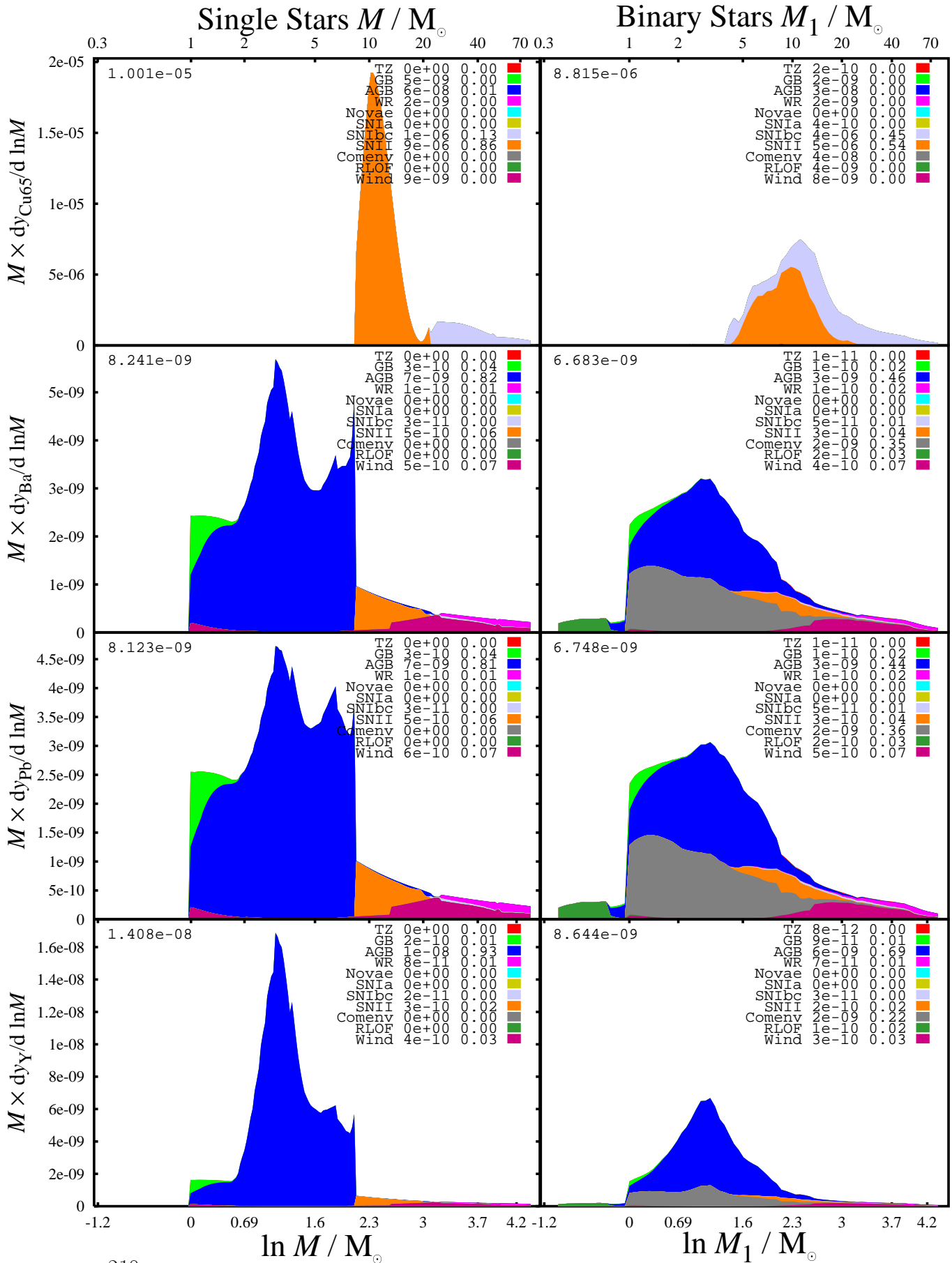
Figure 82: Yield per unit mass input to stars for ^{65}Cu, Ba, Pb and Y.

of two is important to GCE modellers then they should seriously think about including binary yields. This becomes especially true if the GCE model is sophisticated enough to include yields as a function of both time and metallicity. If a factor of 10 (or worse) is all that is required then they can live with their old, probably false, assumptions, but that's not a good way to make progress in science.

7.1 Future Prospects

Chapters 5, 6 and 7 answer the primary question: are binary yields important for Galactic chemical evolution?

However, there are a number of aspects of `binary_c/nucsyn` which can be improved in order to constrain some of the uncertain processes at work in binary stars. A speculative list is as follows:

- The abundances in dredged-up material are currently treated approximately. This will be looked at soon (Karakas, private communication), with fits to M, Z and perhaps N_{TP} for a all the isotopes available, up to and including silicon.

- More intermediate-mass full stellar evolution models are needed, especially for $M > 6\,\mathrm{M_\odot}$ and $10^{-4} < Z < 0.004$. Perhaps some stars with a different mixing-length parameter would be useful, perhaps TPAGB stars evolved with a different code.

- Detailed massive star surface abundances include only ^{1}H, ^{4}He, ^{12}C, ^{14}N, ^{16}O and Ne. It will be necessary to tie the massive-star evolution models to the post-processing nucleosynthesis code to do any better. Perhaps this is worth doing. This is not planned at present although Richard Stancliffe is developing a similar nucleosynthesis code which may be up to the task. It would be better to extend the rapid shell-burning routines presented here to include massive stars – this was attempted for this thesis but did not work. . .

- Diffusion of elements in stellar envelopes.

- r-process yields – it would be good if even crude theoretical estimates of these yields were published.

- Accretion and/or stripping of stars due to supernovae (and perhaps novae).

- Pre-MS or MS CNO cycling in the stellar interior. This is *very* difficult.

- WD surface layers and low-mass helium stars could be treated properly. Detailed evolution models are required for this.

- A GCE model to test all the above should be developed.

- Incorporation of this model into Hurley and Aarseth's `NBODY` code (the gas will be tricky. . .).

- An easily accessible database of stellar surface abundances with which to compare the strange stars made by the model. This is a *big* project but is ultimately necessary.

There is, as always, plenty to get on with. But I am going for a pint or maybe that bottle of Gigondas that Chris promised me. . . Carolina suggests a crate!

Bibliography

Abt H. A., 1983, Annual review of Astronomy and Astrophysics, 21, 343

Abt H. A., Levy S. G., 1976, The Astrophysical Journal Supplement Series, 30, 273

Anders E., Grevesse N., 1989, Geochimica et Cosmochimica Acta, 53, 197

Angulo C., Arnould M., Rayet M., Descouvemont P. e. a., 1999, Nuclear Physics A

Batten A. H., 1995, Reports on Progress in Physics, 58, 885

Belczynski K., Kalogera V., Bulik T., 2002, The Astrophysical Journal, 572, 407

Bennett C., Halpern M., Hinshaw G., Jarosik N., Kogut A., Limon M., Meyer S., Page L.,
    Spergel and others 2003, The Astrophysical Journal Supplement Series, 148, 1

Blöcker T., Schönberner D., 1991, Astronomy and Astrophysics, 244, L43

Bondi H., Hoyle F., 1944, MNRAS, 104, 273

Boothroyd A. I., Sackmann I.-J., 1988, The Astrophysical Journal, 328, 632

Busso M., Gallino R., Lambert D. L., Travaglio C., Smith V. V., 2001, The Astrophysical
    Journal, 557, 802

Cameron A. G. W., Mock M., 1967, Nature, 215

Cannon R., 1993, MNRAS, 263, 817

Bibliography

Chabrier G., 2003, PASP, 115, 763

Clayton D. D., 1983, Principles of Stellar Evolution and Nucleosynthesis. Chicago

Conti P. S., Underhill A. B., Jordan S., Thomas R., 1988, O stars and Wolf-Rayet stars. Bernan Assoc

De Donder E., Vanbeveren D., 2002, New Astronomy, 7, 55

de Jager C., Nieuwenhuijzen H., van der Hucht K. A., 1988, Astronomy & Astrophysics Supplement Series, 72, 259

Denissenkov P. A., Tout C. A., 2003, MNRAS, 340, 722

Dewi J. D. M., Tauris T. M., 2000, Astronomy and Astrophysics, 360, 1043

Dray L. M., Tout C. A., 2003, MNRAS, 341, 299

Dray L. M., Tout C. A., Karakas A. I., Lattanzio J. C., 2003, MNRAS, 338, 973

Duquennoy A., Mayor M., 1991, Astronomy and Astrophysics, 248, 485

Foglizzo T., Ruffert M., 1999, Astronomy and Astrophysics, 347, 901

Forestini M., Charbonnel C., 1997, Astronomy & Astrophysics Supplement Series, 123, 241

Frankland E., Lockyer J. N., 1868, Royal Society of London Proceedings Series I, 17, 453

Frost C. A., 1997, PhD thesis, Monash University

Frost C. A., Lattanzio J. C., Wood P. R., 1998, The Astrophysical Journal, 500, 355

Fryer C. L., Kalogera V., 2001, The Astrophysical Journal, 554, 548

Gallino R., Arlandini C., Busso M., Lugaro M., Travaglio C., Straniero O., Chieffi A., Limongi M., 1998, The Astrophysical Journal, 497, 388

Garmany C. D., Conti P. S., Massey P., 1980, The Astrophysical Journal, 242, 1063

Girardi L., Bressan A., Bertelli G., Chiosi C., 2000, Astronomy & Astrophysics Supplement Series, 141, 371

Goldberg D., Mazeh T., Latham D. W., 2003, The Astrophysical Journal, 591, 397

Groenewegen M. A. T., 1999, in IAU Symp. 191: Asymptotic Giant Branch Stars Vol. 191, Carbon stars in populations of different metallicity. p. 535

Groenewegen M. A. T., 2002, Carbon stars in the Local Group, astro-ph/0208449

Groenewegen M. A. T., de Jong T., 1993, Astronomy and Astrophysics, 267, 410

Hansen B. M. S., Phinney E. S., 1997, MNRAS, 291, 569+

Herwig F., 2000, Astronomy and Astrophysics, 360, 952

Herwig F., Langer N., 2001, Memorie della Societa Astronomica Italiana, 72, 277

Herwig F., Langer N., Lugaro M., 2003, The Astrophysical Journal, 593, 1056

Hjellming M. S., Taam R. E., 1991, The Astrophysical Journal, 370, 709

Huang R. Q., Weigert A., 1982, Astronomy and Astrophysics, 112, 281

Humphreys R. M., Davidson K., 1994, PASP, 106, 1025

Hurley J. R., Pols O. R., Tout C. A., 2000, MNRAS, 315, 543

Hurley J. R., Tout C. A., Aarseth S. J., Pols O. R., 2001, MNRAS, 323, 630+

Hurley J. R., Tout C. A., Pols O. R., 2002, MNRAS, 329, 897

Iben I., Renzini A., 1982, The Astrophysical Journal Letters, 263, L23

Iben I., Truran J. W., 1978, The Astrophysical Journal, 220, 980

Iwamoto K., Brachwitz F., Nomoto K., Kishimoto N., Umeda H., Hix W. R., Thielemann F. K., 1999, The Astrophysical Journal Supplement Series, 125, 439

Bibliography

Izzard R. G., Ramirez-Ruiz E., Tout C. A., 2004, Formation Rates of Core Collapse SNe and GRBs, Accepted for publication by MNRAS

Izzard R. G., Tout C. A., 2003, Publications of the Astronomical Society of Australia, 20, 345

Izzard R. G., Tout C. A., 2004, A Binary Origin for Low-Luminosity Carbon Stars, Accepted for publication in MNRAS

Izzard R. G., Tout C. A., Karakas A. I., Pols O. R., 2004, A New Synthetic Model for AGB Stars, Accepted for publication by MNRAS

José J., Hernanz M., 1998, The Astrophysical Journal, 494, 680

Karakas A. I., Lattanzio J. C., Pols O. R., 2002, PASA, 19, 515

Kippenhahn R., Ruschenplatt G., Thomas H.-C., 1980, Astronomy and Astrophysics, 91, 175

Kippenhahn R., Weigert A., 1994, Stellar Structure and Evolution. Stellar Structure and Evolution, XVI, 468 pp. 192 figs.. Springer-Verlag Berlin Heidelberg New York. Also Astronomy and Astrophysics Library

Kroupa P., 2002, Science, 295, 82

Kroupa P., Tout C., Gilmore G., 1993, MNRAS, 262, 545

Kudritzki R., Reimers D., 1978, Astronomy and Astrophysics, 70, 227

Langer N., 1989, Astronomy and Astrophysics, 220, 135

Livne E., Arnett D., 1995, The Astrophysical Journal, 452, 62

Maeder A., Meynet G., 1994, Astronomy and Astrophysics, 287, 803

Marietta E., Burrows A., Fryxell B., 2000, The Astrophysical Journal Supplement Series, 128, 615

Marigo P., 1999, in IAU Symp. 191: Asymptotic Giant Branch Stars Vol. 191, Improved synthetic TP-AGB models. p. 53

Marigo P., 2001, Astronomy and Astrophysics, 370, 194

Marigo P., Bernard-Salas J., Pottasch S. R., Tielens A. G. G. M., Wesselius P. R., 2003, Astronomy and Astrophysics, 409, 619

Marigo P., Bressan A., Chiosi C., 1998, Astronomy and Astrophysics, 331, 564

Marigo P., Girardi L., Bressan A., 1999, Astronomy and Astrophysics, 344, 123

Marigo P., Girardi L., Weiss A., Groenewegen M. A. T., 1999, Astronomy and Astrophysics, 351, 161

Nieuwenhuijzen H., de Jager C., 1990, Astronomy and Astrophysics, 231, 134

Nomoto K., Kondo Y., 1991, The Astrophysical Journal Letters, 367, L19

Nomoto K., Thielemann F.-K., Yokoi K., 1984, The Astrophysical Journal, 286, 644

Nugis T., Lamers H. J. G. L. M., 2000, Astronomy and Astrophysics, 360, 227

Orosz J. A., 2003, in IAU Symposium Inventory of black hole binaries. pp 365–+

Paczynski B., 1970, Acta Astronomica, 20, 47

Pols O. R., Schröder K. P., Hurley J. R., Tout C. A., Eggleton P. P., 1998, MNRAS, 298, 525

Popova E. I., Tutukov A. V., Yungelson L. R., 1982, APSS, 88, 55

Portinari L., Chiosi C., Bressan A., 1998, Astronomy and Astrophysics, 334, 505

Prialnik D., 2000, An Introduction to the Theory of Stellar Structure and Evolution. Cambridge University Press

Proffitt C. R., 1989, The Astrophysical Journal, 338, 990

Bibliography

Qian Y.-Z., Wasserburg G. J., 2003, The Astrophysical Journal, 588, 1099

Ramsay W., Collie J. N., Travers M., 1895, Journal of the Chemical Society, 68, 684

Renzini A., Voli M., 1981, Astronomy and Astrophysics, 94, 175

Ruffert M., 1994, The Astrophysical Journal, 427, 342

Russell S. C., Dopita M. A., 1992, The Astrophysical Journal, 384, 508

Salpeter E. E., 1955, The Astrophysical Journal, 121, 161

Schwarzschild M., Härm R., 1965, The Astrophysical Journal, 142, 855

Taam R. E., Fryxell B. A., 1984, The Astrophysical Journal, 279, 166

Tout C. A., Eggleton P. P., 1988, MNRAS, 231, 823

Tout C. A., Pols O. R., Eggleton P. P., Han Z., 1996, MNRAS, 281, 257

Tuli J., 2000, Nuclear Wallet Cards (Brookhaven Natl. Lab.)

van den Hoek L. B., Groenewegen M. A. T., 1997, Astronomy & Astrophysics Supplement Series, 123, 305

Vassiliadis E., Wood P. R., 1993, The Astrophysical Journal, 413, 641

Wagenhuber J., Groenewegen M. A. T., 1998, Astronomy and Astrophysics, 340, 183

Walder R., Folini D., 2000, in ASP Conf. Ser. 204: Thermal and Ionization Aspects of Flows from Hot Stars Complex Wind Dynamics and Ionization Structure in Symbiotic Binaries. p. 331

Wallerstein G., Knapp G. R., 1998, Annual review of Astronomy and Astrophysics, 36, 369

Warner B., 1995, Cataclysmic variable stars. Cambridge Astrophysics Series, Cambridge, New York: Cambridge University Press, 1995

Wheeler J. C., Lecar M., McKee C. F., 1975, The Astrophysical Journal, 200, 145

Wood P. R., Cahn J. H., 1977, The Astrophysical Journal, 211, 499

Wood P. R., Zarro D. M., 1981, The Astrophysical Journal, 247, 247

Woosley S. E., Taam R. E., Weaver T. A., 1986, The Astrophysical Journal, 301, 601

Woosley S. E., Weaver T. A., 1995, The Astrophysical Journal Supplement Series, 101, 181

Glossary

For Carolina.

AIC Accretion induced collapse. An ONeMg WD accretes material until it is so massive it collapses to a NS. Possibly a source of r-process nucleosynthesis (Qian & Wasserburg, 2003) or possibly not (Nomoto & Kondo, 1991).

Asymptotic Giant Branch (AGB) See EAGB and TPAGB.

Barium star A star with a very strong BaII 4554 line.

binary_c As BSE but written in C, not the evil Fortran.

binary_c/nucsyn The combination of binary_c and the nucsyn library.

Binary Star A star born with a nearby companion star.

BSE The *rapid Binary Star Evolution* code of Hurley et al. (2002). Similar to SSE but for binary stars.

Carbon Star Red giant with surface abundance ratio $N_C/N_O \geq 1.0$.

Carbon-Oxygen White Dwarf (COWD) See white dwarf.

Core-Helium Burning (CHeB) The stellar evolution phase between the GB and EAGB in which the star burns helium steadily in its core.

Glossary

Dray Lynnette, or a reference to her massive star models.

Dwarf Carbon Star A carbon star which is not a giant, formed by accretion of carbon-rich material.

Early Asymptotic Giant Branch (EAGB) A shell helium-burning giant star with a large, cool, convective envelope.

Eggleton Stellar evolutionist (Peter) or a reference the code he wrote or the models made with this code for SSE/BSE.

First Dredge Up The mixing of hydrogen-burned material which occurs as the star ascends the giant branch.

Giant Branch (GB) A hydrogen shell-burning star which has a very large convective envelope. Because the envelope is large it is cool so these are often termed *Red Giants*.

Helium Star A star which has a high surface abundance of helium and very little hydrogen, up to $1 - Z$ (in the Dray models).

Helium Main Sequence (HeMS) A star which burns helium in its core and has no hydrogen envelope.

Helium Giant Branch (HeGB) Similar to the GB but with shell helium burning instead of shell hydrogen burning.

Helium Hertzsprung Gap (HeHG) A phase of stellar evolution between the HeMS and HeGB associated with relatively rapid core contraction.

Helium White Dwarf (HeWD) See white dwarf.

Hertzsprung Gap (HG) A phase of stellar evolution between the MS and GB associated with relatively rapid core contraction.

Hertzsprung-Russell Diagram (HRD) A plot of $\log L$ vs $\log T_{\text{eff}}$ often used to help explain stellar evolution.

Karakas Amanda, or a reference to her models.

Main Sequence (MS) The phase of core hydrogen burning that all stars experience.

MSSSP John Lattanzio's version of the Mount Stromlo stellar evolution code.

Novae Thermonuclear explosions caused by accretion and ignition of hydrogen-rich material on to a white dwarf.

nucsyn The synthetic nucleosynthesis code presented in this dissertation. See also Izzard et al. (2004); Izzard & Tout (2003, 2004).

Nucleosynthesis The cosmic formation of atoms more complex then the hydrogen atom (OED).

Oxygen-Neon-Magnesium White Dwarf (ONeWD) See white dwarf.

*r***-process** Rapid neutron capture which leads to the production of heavy metals, thought to occur in supernovae, perhaps in neutron star mergers or AIC explosions.

Roche-Lobe Overflow (RLOF) Mass transfer which occurs when a star becomes so large (or so close to its companion) that its surface material is transferred to the companion.

Second Dredge Up The mixing of hydrogen-burned material into the stellar envelope which occurs as the convective envelope develops on the EAGB.

Single Star A star born alone in space. See also *binary star*.

SSE The *rapid Single Star Evolution* code of Hurley et al. (2000). This code mimics a detailed stellar evolution code for L, M, M_c, R etc. by the use of analytic formulae. The resulting model runs in fractions of a second rather than hours or days.

*s***-process** Slow neutron capture which leads to the production of heavy metals, thought to occur in TPAGB stars (see Clayton, 1983; Busso et al., 2001).

Supernova (SN, plural SNe) An explosion resulting from either stellar core-collapse (type II/Ib/Ic) or thermonuclear explosion of a white dwarf (type Ia).

Thermally Pulsing Asymptotic Giant Branch (TPAGB) A twin shell-burning (hydrogen and helium) giant star with a large, convective envelope.

Third Dredge Up The mixing of helium (and some hydrogen) burned material into the stellar envelope caused by thermal pulses (see TPAGB).

Tout Everything (French) or an r-less fish. According to the OED also "*A thieves' scout or watchman*" which sounds about right!

WC, WN, WO See Wolf-Rayet.

White Dwarf (WD) The final stage in intermediate- and low-mass stellar evolution – the degenerate remains of the stellar core. Three subclasses exist, helium white dwarfs (HeWDs), carbon-oxygen white dwarfs (COWDs) and oxygen-neon white dwarfs (ONeWDs), all with different progenitors.

Wolf-Rayet (WR) A star with a spectrum of broad emission lines (due to enormous mass-loss rates) similar to an O or B star but dominated by carbon (WC subclass), oxygen (WO subclass) or nitrogen lines (WN subclass).

Zero-Age Main Sequence (ZAMS) The time at which hydrogen burning begins in the stellar core, conventionally $t = 0$ in stellar evolution.

A Algorithms

A1 NeNa

With α, β, γ and δ as before (section 2.9) and number densities of ^{20}Ne...^{23}Na as w, x, y and z the eigenvalue equation is

$$\begin{bmatrix} -\alpha & 0 & 0 & \delta \\ \alpha & -\beta & 0 & 0 \\ 0 & \beta & -\gamma & 0 \\ 0 & 0 & \gamma & -\delta \end{bmatrix} \begin{bmatrix} w \\ x \\ y \\ z \end{bmatrix} = \lambda_i \begin{bmatrix} w \\ x \\ y \\ z \end{bmatrix} . \tag{A1}$$

As is typical in this sort of problem there is no unique solution to this set of equations however one variable (x in this case) can be set to 1 and the other variables w, y and z evaluated as functions of x. The eigenvector is then normalized according to the initial conditions by fixing up the A_i in eq. (99). Note that when $\alpha = 0$ there is a problem because the determinant is zero, so the solution is ignored on timesteps where this happens and recovers nicely for the next timestep with only a minor glitch in the surface abundances. Writing out the equations in full

$$-\alpha w + \delta z = \lambda_i w \,, \tag{A2}$$

$$\alpha w - \beta x = \lambda_i x \,, \tag{A3}$$

$$\beta x - \gamma y = \lambda_i y \tag{A4}$$

A Algorithms

and

$$\gamma y - \delta z = \lambda z\,. \tag{A5}$$

The first two can be combined to give

$$w = \left(\frac{\lambda_i + \beta}{\alpha}\right) x \tag{A6}$$

and

$$z = \frac{(\lambda_i + \alpha)(\lambda_i + \beta)}{\alpha\delta} x \tag{A7}$$

while the third is easily converted to

$$y = \left(\frac{\beta}{\lambda_i + \gamma}\right) x\,. \tag{A8}$$

Then

$$\mathbf{U}_i = \begin{bmatrix} \left(\frac{\lambda_i+\beta}{\alpha}\right) \\ 1 \\ \left(\frac{\beta}{\lambda_i+\gamma}\right) \\ \frac{(\lambda_i+\alpha)(\lambda_i+\beta)}{\alpha\delta} \end{bmatrix} \tag{A9}$$

or in terms of the τ's

$$\mathbf{U}_i = \begin{bmatrix} \tau_{20}(\lambda_i + \frac{1}{\tau_{21}}) \\ 1 \\ \frac{1}{\tau_{21}(\lambda_i+\frac{1}{\tau_{22}})} \\ \tau_{20}\tau_{23}(\lambda_i + \frac{1}{\tau_{21}})(\lambda_i + \frac{1}{\tau_{20}}) \end{bmatrix} \tag{A10}$$

which can be calculated easily because τ_i and λ_i are known.

Normalization is the obtained from the full equation

234

$$\mathbf{U}(t) = N_{\mathrm{NeNa}}\mathbf{U}_0 + \sum_{i=1,2,3} A_i e^{\lambda_i t}\mathbf{U}_i \tag{A11}$$

at time $t = 0$ and where $N_{\mathrm{NeNa}}\mathbf{U}_0 = \mathbf{U}_e$ is the equilibrium solution. Everything is known including the abundances $\mathbf{U}(t = 0)$ (subscript 0 on the number densities) from the previous timestep, except the A_i. The exponential terms are unity at $t = 0$ and $A_0\mathbf{U}_0$ is the equilibrium solution so

$$\mathbf{U}(t = 0) = \begin{bmatrix} {}^{20}\mathrm{Ne}_0 \\ {}^{21}\mathrm{Ne}_0 \\ {}^{22}\mathrm{Ne}_0 \\ {}^{23}\mathrm{Na}_0 \end{bmatrix} = \begin{bmatrix} {}^{20}\mathrm{Ne}_e \\ {}^{21}\mathrm{Ne}_e \\ {}^{22}\mathrm{Ne}_e \\ {}^{23}\mathrm{Na}_e \end{bmatrix} + \sum_{i=1,2,3} A_i \begin{bmatrix} \tau_{20}(\lambda_i + \frac{1}{\tau_{21}}) \\ 1 \\ \frac{1}{\tau_{21}(\lambda_i + \frac{1}{\tau_{22}})} \\ \tau_{20}\tau_{23}(\lambda_i + \frac{1}{\tau_{21}})(\lambda_i + \frac{1}{\tau_{20}}) \end{bmatrix}. \tag{A12}$$

The deviations from equilibrium at $t = 0$ are then

$$\Delta^{20}\mathrm{Ne} = {}^{20}\mathrm{Ne}_0 - {}^{20}\mathrm{Ne}_e = A_1\tau_{20}(\lambda_1 + \frac{1}{\tau_{21}}) + A_2\tau_{20}(\lambda_2 + \frac{1}{\tau_{21}}) + A_3\tau_{20}(\lambda_3 + \frac{1}{\tau_{21}}), \tag{A13}$$

$$\Delta^{21}\mathrm{Ne} = {}^{21}\mathrm{Ne}_0 - {}^{21}\mathrm{Ne}_e = A_1 + A_2 + A_3 \tag{A14}$$

and

$$\Delta^{22}\mathrm{Ne} = {}^{22}\mathrm{Ne}_0 - {}^{22}\mathrm{Ne}_e = A_1\frac{1}{\tau_{21}(\lambda_1 + \frac{1}{\tau_{22}})} + A_2\frac{1}{\tau_{21}(\lambda_2 + \frac{1}{\tau_{22}})} + A_3\frac{1}{\tau_{21}(\lambda_3 + \frac{1}{\tau_{22}})}. \tag{A15}$$

These can be rewritten as

$$\Delta^{20}\mathrm{Ne} = A_1 a + A_2 b + A_3 c, \tag{A16}$$

$$\Delta^{21}\mathrm{Ne} = A_1 + A_2 + A_3 \tag{A17}$$

and

$$\Delta^{22}\text{Ne} = A_1 d + A_2 e + A_3 f \tag{A18}$$

so solve for A_i to find

$$A_3 = \frac{\Delta^{22}\text{Ne-}\Delta^{21}\text{Ne} \ - \left(\frac{e-d}{b-1}\right)\left(\Delta^{20}\text{Ne} - \Delta^{21}\text{Ne}\right)}{\left(\frac{e-d}{b-1}\right)(1-c) + (f-d)}, \tag{A19}$$

$$A_2 = \frac{\Delta^{20}\text{Ne -}\Delta^{21}\text{Ne} - A_3(c-1)}{(b-1)} \tag{A20}$$

and

$$A_1 = \Delta^{21}\text{Ne} - A_2 - A_3 \,. \tag{A21}$$

Substitute $a = \lambda_1 + \frac{1}{\tau_{21}}$, $b = \lambda_2 + \frac{1}{\tau_{21}}$, $c = \lambda_3 + \frac{1}{\tau_{21}}$, $d = \frac{1}{\tau_{21}(\lambda_1 + \frac{1}{\tau_{22}})}$, $e = \frac{1}{\tau_{21}(\lambda_2 + \frac{1}{\tau_{22}})}$ and $f = \frac{1}{\tau_{21}(\lambda_3 + \frac{1}{\tau_{22}})}$ to give the constants A_i and hence the solution (phew!).

A2 MgAl

The following is the general solution to the MgAl cycle assuming ^{27}Al acts as a sink – more correctly this is the solution to the MgAl chain. The solution used in section 2.10 assumes the rate of input to the cycle, I, is zero, an assumption which works well when compared with the Monash models. A useful result is the solution to the differential equation

$$\dot{y} + \lambda y = \alpha + \sum_i \beta_i e^{-\gamma_i t} \tag{A22}$$

which is

$$y = \frac{\alpha}{\lambda} + \sum_i \left(\frac{\beta_i}{\lambda - \gamma_i}\right) e^{-\gamma_i t} + \left(y_0 - \frac{\alpha}{\lambda} - \sum_i \frac{\beta_i}{\lambda - \gamma_i}\right) e^{-\lambda t} \,. \tag{A23}$$

The first equation of the chain can be rearranged as

$$\frac{d^{24}\mathrm{Mg}}{dt} = I - \frac{^{24}\mathrm{Mg}}{\tau_{24}}, \tag{A24}$$

the solution to which is

$$^{24}\mathrm{Mg} = a_{24} + b_{24}e^{-t/\tau_{24}} \tag{A25}$$

where $a_{24} = \tau_{24}I$ and $b_{24} = {}^{24}\mathrm{Mg}_0 - a_{24}$. The $^{25}\mathrm{Mg}$ equation can be arranged as

$$\begin{aligned}
\frac{d^{25}\mathrm{Mg}}{dt} + \frac{^{25}\mathrm{Mg}}{\tau_{25}} &= \frac{^{24}\mathrm{Mg}}{\tau_{24}} = \frac{a_{24}}{\tau_{24}} + \frac{b_{24}}{\tau_{24}}e^{-t/\tau_{24}} \\
&= a'_{24} + b'_{24}e^{-t/\tau_{24}}
\end{aligned} \tag{A26}$$

which has the solution

$$^{25}\mathrm{Mg} = a_{25} + b_{25}e^{-t/\tau_{24}} + c_{25}e^{-t/\tau_{25}} \tag{A27}$$

where $a_{25} = \tau_{25}a'_{24}$, $b_{25} = b'_{24}/(\frac{1}{\tau_{25}} - \frac{1}{\tau_{24}})$ and $c_{25} = {}^{25}\mathrm{Mg}_0 - b_{25} - a_{25}$. The $^{26}\mathrm{Al}$ equation is

$$\begin{aligned}
\frac{d^{26}\mathrm{Al}}{dt} + \frac{^{26}\mathrm{Al}}{\tau'_{26}} &= \frac{^{25}\mathrm{Mg}}{\tau_{25}} \\
&= a'_{25} + b'_{25}e^{-t/\tau_{24}} + c'_{25}e^{-t/\tau_{25}}
\end{aligned} \tag{A28}$$

where

$$\frac{1}{\tau'_{26}} = \frac{1}{\tau_{26'}} + \frac{1}{\tau_{\beta 26}} \tag{A29}$$

and $a'_{25} = a_{25}/\tau_{25}$, $b'_{25} = b_{25}/\tau_{25}$ and $c'_{25} = c_{25}/\tau_{25}$. The solution is

$$^{26}\mathrm{Al} = a_{26} + b_{26}e^{-t/\tau_{24}} + c_{26}e^{-t/\tau_{25}} + d_{26}e^{-t/\tau'} \tag{A30}$$

where $a_{26} = \tau'a'_{25}$, $b_{26} = b'_{25}/(\frac{1}{\tau'} - \frac{1}{\tau_{24}})$, $c_{26} = c'_{25}/(\frac{1}{\tau'} - \frac{1}{\tau_{25}})$ and $d_{26} = {}^{26}\mathrm{Al}_0 - a_{26} - b_{26} - c_{26}$.

A Algorithms

Substitution into the ^{26}Mg equation gives

$$\frac{d^{26}\text{Mg}}{dt} + \frac{^{26}\text{Mg}}{\tau_{26}} = \frac{^{26}\text{Al}}{\tau_{\beta 26}} = a'_{26} + b'_{26}e^{-t/\tau_{24}} + c'_{26}e^{-t/\tau_{25}} + d'_{26}e^{-t/\tau'} \qquad (\text{A31})$$

where $a'_{26} = a_{26}/\tau_{\beta 26}$, $b'_{26} = b_{26}/\tau_{\beta 26}$, $c' = c_{26}/\tau_{\beta 26}$ and $d'_{26} = d_{26}/\tau_{\beta 26}$. So,

$$^{26}\text{Mg} = f_{26} + g_{26}e^{-t/\tau_{24}} + h_{26}e^{-t/\tau_{25}} + i_{26}e^{-t/\tau'} + j_{26}e^{-t/\tau_{26}} \qquad (\text{A32})$$

where $f_{26} = \tau_{26}a'_{26}$, $g_{26} = b'_{26}/(\frac{1}{\tau_{26}} - \frac{1}{\tau_{24}})$, $h_{26} = c'_{26}/(\frac{1}{\tau_{26}} - \frac{1}{\tau_{25}})$, $i_{26} = d'_{26}(\frac{1}{\tau_{26}} - \frac{1}{\tau'})$ and $j_{26} = ^{26}\text{Mg}_0 - f_{26} - g_{26} - h_{26} - i_{26}$. Finally for ^{27}Al

$$\frac{d^{27}\text{Al}}{dt} = \frac{^{26}\text{Mg}}{\tau_{26}} + \frac{^{26}\text{Al}}{\tau'_{26}} > 0 \qquad (\text{A33})$$

which is of a slightly different form to the other equations. This can be rewritten

$$\begin{aligned}
\frac{d^{27}\text{Al}}{dt} &= f'_{26} + g'_{26}e^{-t/\tau_{24}} + h'_{26}e^{-t/\tau_{25}} + i'_{26}e^{-t/\tau'} + j'_{26}e^{-t/\tau_{26}} + \\
&\quad a^*_{26} + b^*_{26}e^{-t/\tau_{24}} + c^*_{26}e^{-t/\tau_{25}} + d^*_{26}e^{-t/\tau'} \qquad (\text{A34})
\end{aligned}$$

where $f'_{26} = f_{26}/\tau_{26}$, $g'_{26} = g_{26}/\tau_{26}$, $h'_{26} = h_{26}/\tau_{26}$, $i'_{26} = i_{26}/\tau_{26}$, $j'_{26} = j_{26}/\tau_{26}$, $a^*_{26} = a_{26}/\tau'_{26}$, $b^*_{26} = b_{26}/\tau'_{26}$, $c^*_{26} = c_{26}/\tau'_{26}$ and $d^*_{26} = d_{26}/\tau'_{26}$. This can be further simplified to

$$\frac{d^{27}\text{Al}}{dt} = a_{27} + b_{27}e^{-t/\tau_{24}} + c_{27}e^{-t/\tau_{25}} + d_{27}e^{-t/\tau_{26}} + f_{27}e^{-t/\tau'} \qquad (\text{A35})$$

where $a_{27} = f'_{26} + a^*_{26}$, $b_{27} = g'_{26} + b^*_{26}$, $c_{27} = h'_{26} + c^*_{26}$, $d_{27} = j'_{26}$ and $f_{27} = i'_{26} + d^*_{26}$. Integration gives

$$^{27}\text{Al} = a_{27}t - (b_{27}\tau_{24}e^{-t/\tau_{24}} + c_{27}\tau_{25}e^{-t/\tau_{25}} + d_{27}\tau_{26}e^{-t/\tau_{26}} + f_{27}\tau'e^{-t/\tau'}) + \text{const} \qquad (\text{A36})$$

where the constant of integration is found from the initial value $^{27}\text{Al}_0$ so the full solution is

$$
\begin{aligned}
^{27}\text{Al} \;\;=\;\; & a_{27}t - (b_{27}\tau_{24}e^{-t/\tau_{24}} + c_{27}\tau_{25}e^{-t/\tau_{25}} + d_{27}\tau_{26}e^{-t/\tau_{26}} + f_{27}\tau' e^{-t/\tau'}) + \\
& {}^{27}\text{Al}_0 + (b_{27}\tau_{24} + c_{27}\tau_{25} + d_{27}\tau_{26} + f_{27}\tau')\,.
\end{aligned}
\tag{A37}
$$

Psychological help is available to readers who make it this far, but prepare your liver for it.

A3 The Portinari et al. (1998) Method

It is easy to remove the envelope from a star in the rapid nucleosynthesis model because the mass and composition of the envelope are known. After this however it is impossible to know the abundance of the matter in the CO core ejecta. The method of Portinari et al. (1998) is used to calculate the abundances in the ejecta of an exploding CO core according to the models of WW95. Such a method is required because the yields published by WW95 are for the entire star and do not include mass loss prior to the supernova. Portinari's notation is as follows:

M	total mass of the WW95 model
M_{CO}	mass of the CO-core of the model
Z	metallicity of the model
E_i	total ejected amount of species i, taken from WW95 tables
E_i^{new}	newly synthesized and ejected amount of species i
X_i^O	initial abundance of species i in the model
E_i^{ext}	amount of species i contained in the layers external to M_{CO}
E_i^{CO}	amount of species i ejected by the CO core
M_{env}	mass of the region unaffected by CNO burning (approximately the mass of the envelope)

A Algorithms

Firstly M_{CO} is derived. It is assumed that all expelled hydrogen and helium originates in the envelope and that the metallicity of the envelope is the same as the initial metallicity. Then

$$M - M_{CO} = E_H + E_{He} + Z(M - M_{CO}) \tag{A38}$$

which gives

$$M_{CO} = M - \frac{E_H + E_{He}}{1 - Z}. \tag{A39}$$

The origin of each isotope is then considered.

- ^{14}N and ^{13}C can only exist in the envelope because they are destroyed by helium burning and are not produced during the explosion. Thus $E_{C13}^{CO} = E_{N14}^{CO} = 0$.

- ^{12}C and ^{16}O are converted by CNO cycling to ^{13}C and ^{14}N. The amount of ^{13}C and ^{14}N formed during the life of the star are estimated from

$$E_{C13}^{new} = E_{C13} - X_{C13}^0 (M - M_{CO}) \tag{A40}$$

and

$$E_N^{new} = E_N - X_N^0 (M - M_{CO}). \tag{A41}$$

It is them assumed that new ^{14}N forms from ^{12}C and ^{16}O proportionally to the initial abundance $X_C^0 + X_O^0$ such that

$$E_C^{ext} = X_C^0 (M - M_{CO}) - E_{C13}^{new} - E_N^{new} \frac{X_C^0}{X_C^0 + X_O^0} \tag{A42}$$

where the first term is the ^{12}C present at stellar birth, the second is conversion to ^{13}C and the third to ^{14}N. A similar expression results for ^{16}O

$$E_O^{ext} = X_O^0 (M - M_{CO}) - E_N^{new} \frac{X_O^0}{X_C^0 + X_O^0}. \tag{A43}$$

The contribution to the yields from the CO core is then

$$E_C^{CO} = E_C - E_C^{ext} \tag{A44}$$

and

$$E_O^{CO} = E_O - E_O^{ext}. \tag{A45}$$

- ^{15}N is destroyed by the CNO cycle but can be produced by neutrino capture during the explosion. The envelope is treated as a CNO-cycled region and a region which has not experienced hydrogen burning of mass

$$M_{env} = \frac{E_H}{X^0}. \tag{A46}$$

The total ^{15}N ejecta is the made up of that from the unburned envelope and that created from neutrino capture which is assumed to scale with oxygen fraction in the CO core

$$E_{N15}^{CO} = (E_{N15} - M_{env}X_{N15}^0)\frac{E_O^{CO}}{E_O}. \tag{A47}$$

- No ^{17}O or ^{18}O survive helium burning, so $E_{O17}^{CO} = E_{O18}^{CO} = 0$.

- The α-capture isotopes ^{20}Ne, ^{24}Mg, ^{28}Si, ^{32}S and ^{40}Ca are produced during helium and carbon burning. Outside the CO core their abundance is the initial abundance and it is a simple matter to remove the hydrogen- and helium-rich envelopes:

$$E_{Ne}^{CO} = E_{Ne} - (M - M_{CO})X_{Ne}^0 \tag{A48}$$

etc.

- ^{56}Fe is produced during silicon burning and also results from the decay of ^{56}Ni:

$$E_{Fe}^{CO} = E_{Fe} - (M - M_{CO})X_{Fe}^0 + E_{Ni}. \tag{A49}$$

- Other isotopes are corrected in an identical way to the α-capture isotopes, the envelope is just removed from the ejecta.

The WW95 fits given below are to the mass fraction of an isotope in the ejecta, i.e. E^{CO}/M_{CO}, to allow various prescriptions for the remnant mass. This is incorrect because the fitted ejecta are strictly only true for the WW95 core/remnant masses, but is the best that can be done presently.

B Analytic Fits

B1 First Dredge Up

Stars which undergo first dredge-up during their first ascent of the giant branch have their abundances modified by

$$
\begin{aligned}
\Delta X \;=\;& a_{B1} + (b_{B1} + c_{B1}Z)\exp\left[-\frac{(M-2)^2}{d_{B1}}\right] + \\
& (e_{B1} + f_{B1}Z)\exp\left[-\frac{(M-5)^2}{g_{B1}}\right]
\end{aligned}
\tag{B1}
$$

Then $X'_{\mathrm{H1}} = X_{\mathrm{H1}} - \Delta X$ and $X'_{\mathrm{He4}} = X_{\mathrm{He4}} + \Delta X$ (i.e. $\Delta X_{\mathrm{He4}} = -\Delta X_{\mathrm{H1}}$). The CNO abundances are changed by

$$
g = \left(\frac{M}{a_{B2} + b_{B2}Z}\right) X_{\mathrm{C12}} \times \min(0.36, 0.21 + 0.05M/\mathrm{M}_\odot)
\tag{B2}
$$

if $M/\mathrm{M}_\odot < 1.0833 + 20.833Z$, otherwise

$$
g = X_{\mathrm{C12}} \times \min(0.36, 0.21 + 0.05M/\mathrm{M}_\odot)
\tag{B3}
$$

such that

$$
X'_{\mathrm{C12}} = X_{\mathrm{C12}} - g\,,
\tag{B4}
$$

and

B Analytic Fits

$$X'_{\text{N14}} = X_{\text{N14}} + \frac{7}{6}g \,. \tag{B5}$$

Also

$$
\begin{aligned}
X'_{\text{C13}} \;=\; & X_{\text{C13}} + a_{B6} + b_{B6}M_{B6} + c_{B6}Z + \\
& (d_{B6} + e_{B6}Z)\exp\left[-\frac{(M-1.67)^2}{f_{B6}}\right] \,,
\end{aligned}
\tag{B6}
$$

$$X'_{\text{N15}} = X_{\text{N15}} + (a_{B7} + b_{B7}Z^{c_{B7}}) \times (1 + d_{B7}M^{e_{B7}}) \,, \tag{B7}$$

if $M < 1.0833 + 20.833Z$

$$
\begin{aligned}
X'_{\text{O16}} \;=\; & X_{\text{O16}} + a_{B8}\min(b_{B8}, Z)\exp\left[-\frac{M + c_{B8} + d_{B8}Z}{e_{B8} + f_{B8}Z}\right] + \\
& g_{B8}(MZ)^{h_{B8}}
\end{aligned}
\tag{B8}
$$

otherwise there is no change in ^{16}O,

$$X'_{\text{O17}} = X_{\text{O17}} + (a_{B9}Z + b_{B9}\xi)\frac{M^{f_{B9}}}{1 + c_{B9}^{M - d_{B9} + e_{B9}Z}} \tag{B9}$$

$$
\begin{aligned}
X'_{\text{O18}} \;=\; & X_{\text{O18}} + (a_{B10} + b_{B10}M + c_{B10}M^2 + d_{B10}M^3) \times \\
& (1 + e_{B10}M + f_{B10}M^2) \,.
\end{aligned}
\tag{B10}
$$

Some NeNa and MgAl cycling leads to abundance changes

$$
\begin{aligned}
X'_{\text{Ne20}} \;=\;& X_{\text{Ne20}} + Z(a_{B11} + b_{B11}Z)\exp\left[-\frac{(M + c_{B11} + d_{B11}Z)^2}{e_{B11} + f_{B11}Z}\right] + \\
& g_{B11}(MZ)^{h_{B11}} ,
\end{aligned}
\tag{B11}
$$

$$
\begin{aligned}
X'_{\text{Ne21}} \;=\; X_{\text{Ne21}} +\;& Z(a_{B12} + b_{B12}Z)\exp\left[-\frac{(M + c_{B12} + d_{B12}Z)^2}{e_{B12} + f_{B12}Z}\right] + \\
& g_{B12}(MZ)^{h_{B12}} ,
\end{aligned}
\tag{B12}
$$

$$
\begin{aligned}
X'_{\text{Ne22}} \;=\;& X_{\text{Ne22}} + \min\left(0, Z(a_{B13} + b_{B13}Z)\exp\left[-\frac{(M + c_{B13} + d_{B13}Z)^2}{e_{B13} + f_{B13}Z}\right]\right. + \\
& \left. g_{B13}(MZ)^{h_{B13}}\right. ,
\end{aligned}
\tag{B13}
$$

$$
\begin{aligned}
X'_{\text{Na23}} \;=\; X_{\text{Na23}} +\;& \min\left(0, Z(a_{B14} + b_{B14}Z)\exp\left[-\frac{(M + c_{B14} + d_{B14}Z)^2}{e_{B14} + f_{B14}Z}\right]\right. + \\
& \left. g_{B14}(MZ)^{h_{B14}}\right. ,
\end{aligned}
\tag{B14}
$$

$$
\begin{aligned}
X'_{\text{Mg25}} \;=\;& X_{\text{Mg25}} + a_{B15}Z^{b_{B15}}M^{c_{B15}} + \\
& (d_{B15} + e_{B15}Z)\exp\left[-\frac{M + f_{B15} + g_{B15}Z^2}{h_{B15}}\right] ,
\end{aligned}
\tag{B15}
$$

$$
X'_{\text{Mg26}} = X_{\text{Mg26}} + \frac{Z}{0.02}(a_{B16} + b_{B16}M)
\tag{B16}
$$

and some *pp* chain burning gives

$$
\begin{aligned}
X'_{\text{He3}} \;=\;& (a_{B17} + b_{B17}M + c_{B17}M^2 + d_{B17}M^3 + e_{B17}M^4) \times \\
& (1 + f_{B18}M + g_{B18}M^2 + h_{B18}M^3) .
\end{aligned}
\tag{B17}
$$

All other isotopes do not change at first dredge-up.

	Eq. (B1)	Eq. (B2)	Eq. (B6)	Eq. (B7)	Eq. (B8)
a	2.6415×10^2	1.0833	-5.831×10^{-6}	4.6566×10^{-9}	-1.5238×10^{-2}
b	1.4576×10^{-3}	2.0833	8.2329×10^{-7}	-9.8197×10^{-5}	0.005
c	-6.5206×10^{-1}		2.5644×10^{-3}	9.6658×10^{-1}	-2.647
d	5.9183×10^{-1}		-1.1772×10^{-6}	-5.4293×10^{-1}	-4.5367×10^1
e	-3.1617×10^{-2}		1.4908×10^{-3}	-2.694	4.2393×10^{-2}
f	6.7782×10^{-1}		1.2685×10^{-1}		8.5491×10^1
g	8.5768				-3.2798×10^{-1}
h					3.1829

	Eq. (B9)	Eq. (B10)	Eq. (B11)	Eq. (B12)	Eq. (B13)
a	4.3423×10^{-3}	2.2212×10^{-6}	-1.5839×10^{-5}	1.7876×10^{-5}	-1.2129×10^{-3}
b	-4.7218×10^{-7}	-2.24360×10^{-6}	6.111×10^{-4}	-6.794×10^{-4}	3.4988×10^{-2}
c	2.33×10^{-3}	5.0478×10^{-7}	-2.6312	-2.6323	-2.6083
d	-1.7198	-3.6322×10^{-8}	-4.6861×10^1	-4.6303×10^1	-3.1764×10^1
e	-1.4425×10^1	5.35030×10^1	-3.5043×10^{-3}	4.0193×10^{-3}	1.0164
f	-1.3455	9.78910×10^3	5.9749×10^1	5.9438×10^1	4.0828×10^1
g			-5.0424×10^{-5}	6.4432×10^{-5}	-6.7756×10^{-4}
h			2.6416	2.7127	1.7639

	Eq. (B14)	Eq. (B15)	Eq. (B16)	Eq. (B17)
a	1.267×10^{-3}	-3.6335×10^{-3}	-5.1875×10^{-7}	-4.0811×10^{-4}
b	-3.4988×10^{-2}	2.9927	2.7474×10^{-7}	2.87570×10^{-4}
c	-2.6083	1.9803		-2.6118×10^{-4}
d	-3.1781×10^1	2.7008×10^{-8}		5.7827×10^{-5}
e	1.0167	-4.9247×10^{-5}		-3.9861×10^{-6}
f	4.0854×10^1	-2.5146		-5.6886×10^1
g	7.0726×10^{-4}	-1.1626×10^4		6.60510×10^3
h	1.7635	2.5723×10^{-1}		-2.05390×10^5

Table B1: 1st dredge up fitting coefficients.

B2 Second Dredge Up

Second dredge-up occurs in sufficiently massive stars ($M_{\rm c,bagb} \geq 0.8\,{\rm M_\odot}$ where $M_{\rm c,bagb}$ is the core mass of the star at the start of the (E)AGB) at the end of the EAGB when twin shell burning begins. Following Renzini & Voli (1981) and Groenewegen & de Jong (1993), with alterations to better fit the Monash models, the fraction of the envelope which is hydrogen rich is defined as

$$a = \frac{M - M_{\rm c,bagb}}{M - M_{\rm c}^A} \tag{B18}$$

while the fraction which is hydrogen-burned is

$$b = \frac{M_{\rm c,bagb} - M_{\rm c}^A}{M - M_{\rm c}^A} \,, \tag{B19}$$

where $M_{\rm c}^A$ is the core mass just after second dredge-up, which is assumed to be equal to the core mass at the first thermal pulse $M_{\rm c}^{\rm 1TP}$. Then the abundances after second dredge-up X_i' are given by

$$X_{\rm H1}' = X_{\rm H1} + \Delta X_{\rm H1} \,, \tag{B20}$$

and

$$X_{\rm He4}' = X_{\rm He4} - \Delta X_{\rm H1} \tag{B21}$$

where

$$\Delta X_{\rm H1} = \min\left[0, (a_{B22} + b_{B22}M) \times (1 + c_{B22}Z)\right] \,, \tag{B22}$$

$$X_{\rm C12}' = aX_{\rm C12} \,, \tag{B23}$$

$$X_{\rm C13}' = aX_{\rm C13} \,, \tag{B24}$$

$$
\begin{aligned}
X'_{\mathrm{N}14} \;=\;& aX_{\mathrm{N}14} + 14b \times \left(\frac{X_{\mathrm{C}12}}{12} + \frac{X_{\mathrm{C}13}}{13} + \frac{X_{\mathrm{N}14}}{14} + \right. \\
& \left. \frac{X_{\mathrm{N}15}}{15} + \frac{X_{\mathrm{O}16}}{16} + \frac{X_{\mathrm{O}17}}{17} + \frac{X_{\mathrm{O}18}}{18} + \frac{X_{\mathrm{F}17}}{17} \right) ,
\end{aligned}
\tag{B25}
$$

$$
X'_{\mathrm{N}15} = aX_{\mathrm{N}15} \,,
\tag{B26}
$$

$$
X'_{\mathrm{O}16} = aX_{\mathrm{O}16} \,,
\tag{B27}
$$

$$
X'_{\mathrm{O}17} = aX_{\mathrm{O}17} \,,
\tag{B28}
$$

$$
X'_{\mathrm{O}18} = aX_{\mathrm{O}18} \,,
\tag{B29}
$$

$$
X'_{\mathrm{F}17} = aX_{\mathrm{F}17} \,,
\tag{B30}
$$

$$
\begin{aligned}
X'_{\mathrm{Ne}20} \;=\;& X_{\mathrm{Ne}20} + (a_{B31} + b_{B31}Z + c_{B31}Z^2)\exp\left(-\frac{(M + d_{B31} + e_{B31}Z)^2}{f_{B31} + g_{B31}Z}\right) + \\
& h_{B31}(MZ)^{i_{B31}}
\end{aligned}
\tag{B31}
$$

$$
X'_{\mathrm{Ne}21} = X_{\mathrm{Ne}21} + (a_{B32} + b_{B32}Z)M^{c_{B32}} + d_{B32}(MZ)^{e_{B32}} \,,
\tag{B32}
$$

$$
\begin{aligned}
X'_{\mathrm{Ne}22} \;=\;& X_{\mathrm{Ne}22} + (a_{B33} + b_{B33}M + c_{B33}M^2 + d_{B33}M^3 + e_{B33}M^4) \times \\
& (1 + g_{B33}Z + h_{B33}Z^2 + i_{B33}Z^3) \,,
\end{aligned}
\tag{B33}
$$

$$
X'_{\mathrm{Na}22} = 0 \,,
\tag{B34}
$$

$$
X'_{\mathrm{Na}23} \;=\; X_{\mathrm{Na}23} + a_{B35} + b_{B35}M^{c_{B35}} + d_{B35}\exp\left(-\frac{(M + e_{B35})^2}{f_{B35}}\right) ,
\tag{B35}
$$

$$
X'_{\mathrm{Mg}25} \;=\; X_{\mathrm{Mg}25} + (a_{B36} + b_{B36}Z + c_{B36}Z^2) \times (1 + d_{B36}M + e_{B36}M^2) \,,
\tag{B36}
$$

$$
X'_{\mathrm{Mg}26} \;=\; X_{\mathrm{Mg}26} + (a_{B37} + b_{B37}Z + c_{B37}Z^2) \times (1 + d_{B37}M + e_{B37}M^2) \,,
\tag{B37}
$$

$$X'_{\text{Al26}} = X_{\text{Al26}} + \max\left[(a_{B38} + b_{B38}\zeta)(M - 3.5)^3, 10^{-8} + 10^{-9}(M - 4)\right], \tag{B38}$$

$$X'_{\text{Al27}} = X_{\text{Al27}} + (a_{B39} + b_{B39}M + c_{B39}M^2) \times (1 + d_{B39}Z + e_{B39}Z^2), \tag{B39}$$

$$X'_{\text{P31}} = X_{\text{P31}} + 1.0524 \times 10^{-7}, \tag{B40}$$

$$X'_{\text{S34}} = X_{\text{S34}} + 9.78 \times 10^{-8}, \tag{B41}$$

$$X'_{\text{S35}} = X_{\text{S35}} + 1.02 \times 10^{-7}, \tag{B42}$$

$$X'_{\text{Fe56}} = X_{\text{Fe56}} + (a_{B43} + b_{B43}M + c_{B43}M^2) \times (1 + d_{B43}Z + e_{B43}Z^2), \tag{B43}$$

$$X'_{\text{Fe57}} = X_{\text{Fe57}} + (a_{B44} + b_{B44}M + c_{B44}M^2) \times (1 + d_{B44}Z + e_{B44}Z^2) \tag{B44}$$

and

$$X'_{\text{Fe58}} = X_{\text{Fe58}} + 1.1828 \times 10^{-7}. \tag{B45}$$

	Eq. (B22)	Eq. (B31)	Eq. (B32)	Eq. (B33)
a	1.2682×10^{-1}	1.8626×10^{-9}	-7.4506×10^{-9}	3.58090×10^{-6}
b	-3.6696×10^{-2}	-1.6582×10^{-5}	3.7933×10^{-6}	-6.09360×10^{-6}
c	-2.1922×10^{1}	7.2624×10^{-4}	2.4538	3.0817×10^{-6}
d		-2.4443	-3.2682×10^{-4}	-6.25850×10^{-7}
e		-6.8824×10^{1}	2.055	4.09780×10^{-8}
g		-3.4425×10^{-1}		2.77350×10^{2}
f		1.2338×10^{2}		-1.07480×10^{4}
g		-4.436×10^{-5}		7.41730×10^{4}
h		2.5626		

	Eq. (B35)	Eq. (B36)	Eq. (B37)
a	4.191×10^{-8}	-8.475×10^{-8}	-2.32830×10^{-8}
b	6.7055×10^{-8}	-1.4843×10^{-4}	1.673×10^{-4}
c	2.8874	4.4544×10^{-3}	-5.0904×10^{-3}
d	3.295×10^{-6}	-1.2662	-1.2364
e	-1.6914	2.8752×10^{-1}	2.8173×10^{-1}
g	2.4136×10^{-2}		

	Eq. (B38)	Eq. (B39)	Eq. (B43)	Eq. (B44)
a	2.3283×10^{-8}	1.4994×10^{-7}	-4.4983×10^{-7}	3.7532×10^{-7}
b	4.048×10^{-1}	-1.4435×10^{-7}	2.1979×10^{-7}	-2.4214×10^{-7}
c		3.1665×10^{-8}	-2.6077×10^{-8}	3.3528×10^{-8}
d		-1.1753×10^{2}	3.2299×10^{2}	5.5655×10^{1}
e		3.6373×10^{3}	-3.5382×10^{3}	2.4978×10^{3}

Table B2: Second dredge up fitting coefficients.

Eq. (17)	$Z = 0.02$	$Z = 0.008$	$Z = 0.004$	$Z = 0.0001$
a_{17}	0.038515	0.057689	0.40538	0.40538
b_{17}	1.41379	1.42199	1.54656	1.54656
c_{17}	0.555145	0.548143	0.55076	0.55076
d_{17}	0.039781	0.045534	0.054539	0.054539
e_{17}	0.675144	0.652767	0.625886	0.625886
g_{17}	3.18432	2.90693	2.78478	$2.0^\dagger$
h_{17}	0.368777	0.287441	0.227620	0.227620

Table B3: Coefficients for the core mass at the first thermal pulse. The $\dagger$ indicates the value is not from the K02 fit but was introduced to fit the few $Z = 0.0001$ stars available.

Eq. (22)	$Z = 0.02$	$Z = 0.008$	$Z = 0.004$	$Z = 0.0001$
a_{22}	-3.821	-4.189	-4.255	-4.5
b_{22}	1.8926	1.8187	1.8141	1.79
$c_{22} = -2.080 - 0.353Z + 0.200(M_{\mathrm{env}}/\mathrm{M}_\odot + \alpha - 1.5)$				
$d_{22} = -0.626 - 70.30(M_{\mathrm{c,1TP}}/\mathrm{M}_\odot - \zeta)(\Delta M_{\mathrm{c}}/\mathrm{M}_\odot)$				

Table B4: Interpulse period coefficients.

B3 The TPAGB, Third Dredge-Up and HBB

The coefficients for eq. (17) are interpolated from table B3 (taken from Karakas et al., 2002). The coefficients for the fit to interpulse period (eq. 22) are shown in table B4. The coefficients for the fit to the TPAGB radius (eq. 29) are in table B5. The coefficients for the minimum mass for dredge-up $M_{\mathrm{c}}^{\mathrm{min}}$ (eq. 37) are in table B6. The coefficients for the fit to λ_{max} (eq. 40) are in table B7. The coefficients for eq. (42) are in table B8. Coefficients for the fit to HBB temperature (eqs. 61 and 62) and density (eq. 65) are in table B9.

$Z = 0.02$				$Z = 0.008$				$Z = 0.004$			
$M_{\rm 1TP}$	a	b	c	$M_{\rm 1TP}$	a	b	c	$M_{\rm 1TP}$	a	b	c
0.5	-0.2035	0.76686	-0.04375	0.5	-0.2911	0.7483	0.0909	0.5	-0.2134	0.6987	0.2606
1.0	-0.5329	0.8262	-0.1155	1.0	-0.5538	0.80213	-0.0107	1.0	-0.4634	0.7568	0.0379
1.5	-0.6605	0.8373	-0.1719	1.5	-0.8166	0.8559	-0.1124	1.5	-0.7134	0.8150	-0.1838
2.0	-0.5865	0.7955	-0.20114	2.0	-1.054	0.9037	-0.2091	2.0	-0.9633	0.8731	-0.4075
2.5	-0.6829	0.8113	-0.3111	2.5	-1.192	0.9273	-0.2860	2.5	-1.179	0.9140	-0.3109
3.0	-0.7794	0.8270	-0.4211	3.0	-1.232	0.9251	-0.3206	3.0	-1.426	0.9610	-0.2966
3.5	-0.8999	0.8471	-0.3653	3.5	-1.273	0.9229	-0.3552	3.5	-1.247	0.9060	-0.2734
4.0	-1.0203	0.8672	-0.3095	4.0	-1.314	0.9207	-0.3898	4.0	-1.068	0.8509	-0.2502
4.5	-0.9528	0.8435	-0.3492	4.5	-0.8763	0.8095	-0.3542	4.5	-0.7239	0.7619	-0.2970
5.0	-0.8853	0.8198	-0.3889	5.0	-0.4391	0.6983	-0.3188	5.0	-0.3803	0.6729	-0.3439
5.5	-0.7029	0.7701	-0.3836	5.5	-0.4893	0.7043	$-0.33^{\dagger}$	5.5	-0.4450	0.6829	$-0.33^{\dagger}$
6.0	-0.5205	0.7204	-0.3784	6.0	-0.5395	0.7102	$-0.33^{\dagger}$	6.0	-0.5096	0.6929	$-0.33^{\dagger}$
6.5	-0.2955	0.6692	-0.3451	6.5	-0.5896	0.7162	$-0.33^{\dagger}$	6.5	-0.5743	0.7028	$-0.33^{\dagger}$
7.0	-0.0705	0.6180	-0.3117	7.0	-0.6397	0.7222	$-0.33^{\dagger}$	7.0	-0.6389	0.7128	$-0.33^{\dagger}$
7.5	0.1545	0.5668	-0.2784	7.5	-0.6899	0.7282	$-0.33^{\dagger}$	7.5	-0.7036	0.7228	$-0.33^{\dagger}$
8.0	0.3796	0.5156	-0.2451	8.0	-0.7400	0.7341	$-0.33^{\dagger}$	8.0	-0.7682	0.7328	$-0.33^{\dagger}$
8.5	0.6046	0.4644	-0.2117	8.5	-0.7902	0.7401	$-0.33^{\dagger}$	8.5	-0.8329	0.7428	$-0.33^{\dagger}$

Table B5: TPAGB Radius coefficients (eq. 29). For masses outside the range of the Monash models the values are extrapolated. Values marked with $\dagger$ are put in manually because the Monash models break down before the envelope becomes small enough to fit them.

$M_{\rm c}^{\rm min}$	$Z = 0.02$	$Z = 0.008$	$Z = 0.004$
a	0.732759	0.672660	0.516045
b	-0.0202898	0.0657372	0.2411016
c	-0.0385818	-0.1080931	-0.1938891
d	0.0115593	0.0274832	0.0446382

Table B6: Coefficients for the fit to $M_{\rm c}^{\rm min}$, taken from Karakas et al. (2002).

$\lambda_{\rm max}$	$Z = 0.02$	$Z = 0.008$	$Z = 0.004$
a	-0.764199	-0.609465	-1.17696
b	0.70859	0.55430	0.76262
c	0.0058833	0.056787	0.026028
d	0.075921	0.069227	0.041019

Table B7: Coefficients for the fit to $\lambda_{\rm max}$, taken from Karakas et al. (2002).

a	2.7536	e	2.1213
b	6.3895	f	1.4655×10^2
c	2.416	g	5.4606
d	1.1732	h	2.2534

Table B8: Coefficients for eq. (42), the fit for N_{r}.

Eqs. (61) and (62)		Eq. (65)	
a_{61}	4.44290×10^{-2}	a_{65}	3.05860
a_{62}	-2.27390×10^{-2}	b_{65}	9.51050
b_{62}	-8.28510×10^{-2}	c_{65}	-7.20180×10^{-1}
c_{62}	1.67930	d_{65}	-3.65330
d_{62}	-1.161390×10^{-1}		
e_{62}	1.63740×10^{-1}		

Table B9: HBB temperature and density fit coefficients.

Eq.	(43)	(44)	(46)	(47)	(48)
Isotope	^{12}C	^{16}O	^{19}F	^{20}Ne	^{21}Ne
a	4.7318×10^{-1}	2.4845×10^{-2}	9.6488×10^{-5}	1.8208×10^{-3}	7.3832×10^{-5}
b	-2.3708×10^{-1}	-2.1839×10^{-2}	-1.5286×10^{-3}	-5.0381×10^{-5}	-7.1809×10^{-5}
c	5.1112	5.5602×10^{-1}	-2.498	8.5105×10^{-4}	-1.7287
d	6.0359×10^{-2}	6.0325×10^{-3}	-3.774×10^{-1}	4.8022×10	0.01
e	-2.0683	-2.3757×10^{-1}	1.1418×10^{-1}	-4.413×10^{-5}	1.0173×10^{1}
f	-4.0986×10^{-3}	-4.7830×10^{-4}	5.74×10^{1}		
g	1.8593×10^{-1}	2.3482×10^{-2}			

Table B10: Coefficients for the fit to intershell ^{12}C, ^{16}O, ^{19}F, ^{20}Ne and ^{21}Ne.

Eq.	(49)	(50)	(51)	(52)	(53)	(55)
Isotope	^{22}Ne	^{23}Na	^{24}Mg	^{25}Mg	^{26}Mg	^{27}Al
a	1.0003	3.4002×10^{-4}	2.6581×10^{-4}	1.6325×10^{-1}	4.0583×10^{-4}	1.7768×10^{-4}
b	-1.2107×10^{-8}	-6.8279×10^{-5}	8.6264×10^{-5}	1.6882×10^{-3}	-1.0221×10^{-3}	5.5616×10^{-5}
c	6.8356	2.7554×10^{-3}	1.099×10^{-3}	-1.658×10^{-1}	-2.1225×10^{-4}	1.6534×10^{-4}
d	3.477×10^{-2}	9.0052×10^{-4}	3.696×10^{-4}	1.8538×10^{-2}	1.9959	-3.5782
e	-1.1586	-1.5735×10^{-2}	8.1325×10^{-3}	-3.7719×10^{-4}		-6.3068×10^{1}
f	-2.5370	-3.1204	-3.1909			
g	-4.0209×10^{1}	6.7662	-3.78×10^{1}			
h	5.2392×10^{-1}	3.0857×10^{-1}				
i	-8.5182					
j	1.3321×10^{-2}					
k	-1.4586×10^{-3}					
l	1.0693×10^{2}					

Table B11: Coefficients for the fit to intershell ^{22}Ne, ^{23}Na, ^{24}Mg, ^{25}Mg, ^{26}Mg and ^{27}Al.

B4 Intershell Abundances

Tables B10 and B11 give the coefficients to the intershell abundance fits.

B5 Radius Truncation at the AGB Tip

The `SSE` algorithm provides a method for ensuring a smooth transition from the tip of the AGB to the WD track in the HR diagram by truncation of the stellar radius. This is required because as the stellar envelope is lost on the AGB the radius increases quickly and the star becomes very red. However, when the envelope is small the star becomes blue and eventually, when the envelope is lost, is a white dwarf. The following is a method to simulate this behaviour. A parameter

$$\mu = \frac{M_{\mathrm{env}}}{M} \min\left(5.0, \max\left[1.2, \left\{\frac{L}{L_0}\right\}^{\kappa}\right]\right) \tag{B46}$$

is defined where $L_0 = 7.0 \times 10^4$ and $\kappa = -0.5$. Then if $\mu < 1.0$ the luminosity and radius are perturbed according to

$$L' = L_{\mathrm{c}} \left(\frac{L}{L_{\mathrm{c}}}\right)^{s} \tag{B47}$$

and

$$R' = R_{\mathrm{c}} \left(\frac{R}{R_{\mathrm{c}}}\right)^{r}, \tag{B48}$$

where

$$s = \frac{(1 + b^3)(\mu/b)^3}{1 + (\mu/b)^3}, \tag{B49}$$

and

$$r = \frac{(1 + c^3)(\mu/c)^3 \mu^{0.1/q}}{1 + (\mu/c)^3}, \tag{B50}$$

with

$$b = 0.002 \max\left(1, \frac{2.5}{M}\right), \tag{B51}$$

$$c = 0.006 \max\left(1, \frac{2.5}{M}\right) \tag{B52}$$

and

$$q = \ln\left(\frac{R}{R_{\mathrm{c}}}\right). \tag{B53}$$

The values of L_{c} and R_{c} are the luminosity and radius in the absence of a stellar envelope.

	Eq. (107)	Eq. (108)	Eq. (109)	Eq. (110)	Eq. (111)
a	2.298	-2.74	-7.914	-7.5×10^{-1}	1.1705
b	1.9	173.0	4.157×10^{-2}	2.3×10^{-1}	0.4743
c	0.4	160.0	1.8933		-1.8762×10^{-2}
d	3.0	4.937	-5.3736×10^{-1}		6.7386×10^{-1}
e	143.7	0.1	4.9012×10^{-3}		3.3929×10^{-1}
f	1.1212×10^{-3}	$\begin{cases} 0.5\sqrt{Z} & Z < 10^{-3} \\ 1 & \text{otherwise} \end{cases}$	6.0426		2.37380×10^{-2}
g	7.2913×10^{-2}	$\begin{cases} 1+\xi & \xi \geq 1 \\ 1 & 0.1 \leq \xi < 1 \\ 4\xi & \xi < 0.1 \end{cases}$	9.5713×10^{-2}		-2.2379×10^{-1}
h	1.8796	10^{-5}	0.39818		
i	-2.2871×10^{-2}		0.75613		
j	10^{-5}		-2.0772		
k			-0.73418		

Table B12: Coefficients for the fits to Y, Ba, Pb and Kr.

For AGB stars these are the luminosity and radius of a white dwarf, as defined by the `SSE` model. The stellar luminosity and radius are then given by L' and R'.

B6 The S-process

See tables B12 and B13.

Element A	Fitted to isotope...(B)	a_{112}	b_{112}
Ce	Ba	1.0839	-0.79546
Dy	Ba	1.0153	-1.4938
Er	Ba	0.98322	-1.7823
Eu	Ba	1.0558	-2.8742
Gd	Ba	1.043	-1.8747
Hf	Ba	0.95175	-1.3953
Hg	Ba	0.85404	-0.74736
La	Ba	1.0547	-1.2285
Lu	Ba	0.94413	-2.4119
Nd	Ba	1.0817	-1.0742
Os	Ba	0.99086	-1.6381
Pr	Ba	1.0858	-1.8215
Re	Ba	0.98727	-2.3456
Sb	Ba	0.92138	-1.6938
Sm	Ba	1.0591	-1.7621
Sn	Ba	0.89942	-0.18915
Ta	Ba	0.96036	-2.4097
Te	Ba	1.0389	-0.53706
Tl	Ba	0.87297	-1.1273
Tm	Ba	0.97431	-2.6813
W	Ba	0.97918	-1.5259
Xe	Ba	0.8605	-0.45371
Yb	Ba	0.95063	-1.1202
Rb	Kr	0.99092	-0.62874
Bi	Pb	0.92089	-1.68050
Ag	Y	0.93724	-1.8116
Cd	Y	0.92210	-0.60916
In	Y	0.91670	-1.7001
Mo	Y	0.94158	-0.42414
Pd	Y	0.94622	-0.76471
Ru	Y	0.95103	-0.89359
Sr	Y	0.99743	0.69429
Tc	Y	0.93201	-1.9894
Zr	Y	0.97750	0.41723

Table B13: Coefficients for eq. (112).

	$M_{\mathrm{ZAMS}} \leq 25\,\mathrm{M}_\odot$	$25 < M_{\mathrm{ZAMS}}/\mathrm{M}_\odot \leq 38$	$38 < M_{\mathrm{ZAMS}}/\mathrm{M}_\odot \leq 55$	$M_{\mathrm{ZAMS}} > 55\,\mathrm{M}_\odot$
δ_1	1	1	0	0
δ_2	0	1	0	0
δ_3	0	0	1	1
δ_4	0	0	1	0

Table B14: δ factors for eq. (B54).

B7 Massive Hydrogen Stars

B7.1 Hydrogen $Z = 0.02$

The surface hydrogen abundance is given over the entire mass range by a set of Fermi-like functions

$$
\begin{aligned}
X_{\mathrm{H1}} &= X_{\mathrm{i,H1}} - \delta_1 \frac{dX_1}{1 + s_1^{\Delta M - dM_1}} - \delta_2 \frac{dX_2}{1 + s_2^{\Delta M - dm_2}} - \\
&\quad \delta_3 \frac{dX_1}{1 + s_1^{\log \Delta M - \log dM_1}} - \delta_4 \frac{dX_2}{1 + s_2^{\log \Delta M - \log dM_2}} + \Delta X_{\mathrm{H1}}
\end{aligned}
\tag{B54}
$$

where $\Delta M = M_{\mathrm{ZAMS}} - M$ is the mass lost (also referred to as depth) by the star relative to its main-sequence mass. The various Fermi functions are activated over certain mass ranges by the factors $\delta_1 ... \delta_4$ as given in table B14. The break depth for each function is given by the dM_i factors, the slope factors s_i determine the steepness of the break and the dX_i determine the magnitude of the drop relative to the MS abundance. ΔX_{H1} is defined below.

First define a Fermi function which is 0 at low mass and 1 at high mass with the break at around $M = 75\,\mathrm{M}_\odot$

$$
f_{\mathrm{M75}} = F(M_{\mathrm{i}}, 1, 1, 0.2, 75)
\tag{B55}
$$

	Eq. (B57)	Eq. (B58)	Eq. (B59)
a	2.5977	2.8655×10^{-1}	2.6759×10^{-2}
b	-3.053×10^{-1}	-1.1037×10^{-1}	3.5589×10^{-3}
c	1.1911×10^{-2}	8.8883×10^{-3}	
d	1.4044×10^{-5}		
e	1.6137×10^{2}		
f	-2.3087		
g	1.1335×10^{-4}		

	Eq. (B60)	Eq. (B63)	Eq. (B64)
a	2.7291×10^{-1}	7.543×10^{1}	0.32
b	-6.4511×10^{-3}	2.0927	0.18
c	7.4506×10^{-8}	-2.9313×10^{1}	0.3
d	0.74	2.7694×10^{2}	-42.5
e	6.9329×10^{-1}	-2.7142×10^{1}	
f	2.062×10^{-2}	5.2789×10^{-1}	
g		-2.5971×10^{-3}	

	Eq. (B65)	Eq. (B66)	Eq. (B67)	Eq. (B76)	Eq. (B77)	Eq. (B82)
a	1.4174×10^{-1}	-7.5216×10^{1}	-7.0918×10^{-1}	6.357×10^{-1}	9.4401	9.527×10^{-3}
b	5.5388×10^{-1}	1.3218	5.6122×10^{-2}	30.479	514.99	-1.1142×10^{-4}
c			-1.25×10^{1}	109.61		-1.3925×10^{1}
d			3.5×10^{-1}			0.16

Table B15: Massive hydrogen star fitting coefficients.

where F is a Fermi-like function

$$F(x, a, b, c, d) \;=\; a \left[1 - \frac{1}{b + c^{d-x}} \right] \tag{B56}$$

then

$$
\begin{aligned}
dM_1^{(0)} \;=\; & (1 - f_{\mathrm{M75}})(a_{B57} - b_{B57}M_{\mathrm{ZAMS}} + c_{B57}M_{\mathrm{ZAMS}}^2 + d_{B57}M_{\mathrm{ZAMS}}^3) + \\
& f_{\mathrm{M75}}(e_{B57} + f_{B57}M_{\mathrm{ZAMS}} + g_{B57}M_{\mathrm{ZAMS}}^3)\,.
\end{aligned} \tag{B57}
$$

For $M_{\mathrm{ZAMS}} < 20\,\mathrm{M_\odot}$ this is corrected to $dM_1^{(1)}$

$$
dM_1^{(1)} = \max\left[0.2, \min\left(dM_1^{(0)}, a_{B58} - b_{B58}M_{\mathrm{ZAMS}} + c_{B58}M_{\mathrm{ZAMS}}^2\right)\right] \tag{B58}
$$

otherwise $dM_1^{(1)} = dM_1^{(0)}$.

For $M_{\mathrm{ZAMS}} < 31\,\mathrm{M_\odot}$ $dX_1^{(0)}$ is given by

$$
dX_1^{(0)} \;=\; a_{B59} + b_{B59}M_{\mathrm{ZAMS}} \tag{B59}
$$

otherwise

$$
\begin{aligned}
dX_1^{(0)} \;=\; & f_{\mathrm{Z31}} \times f_{\mathrm{M55}} \times \Big[(1 - f_1) \times (a_{B60} + b_{B60}M_{\mathrm{ZAMS}} + c_{B60}M_{\mathrm{ZAMS}}^4) + \\
& f_1 \max(d_{B60}, e_{B60} + \frac{f_{B60}}{M_{\mathrm{ZAMS}}})\Big]
\end{aligned} \tag{B60}
$$

where

$$
f_{\mathrm{Z31}} = 1 + 0.3\max(0, Z_t/0.02 - 1) \tag{B61}
$$

is a metallicity-correction factor, Z_t is the instantaneous metallicity and

$$
f_{\mathrm{M55}} = \begin{cases} (1 + \frac{62 - M_{\mathrm{ZAMS}}}{12}) & 55 < M_{\mathrm{ZAMS}}/\mathrm{M_\odot} < 62 \\ 1 & \text{otherwise} \end{cases} \tag{B62}
$$

creates a smooth transition in the 55 to $62\,\mathrm{M_\odot}$ mass range.

The slope factor s_1 is given by

$$
\log_{10} s_1^{(0)} =
\begin{cases}
-100 & M_{\text{ZAMS}} < 25\,\text{M}_\odot\,, \\
\max\left(-10, \min(-a_{B63} + b_{B63} M_{\text{ZAMS}}, -2)\right) & 25 \leq \frac{M_{\text{ZAMS}}}{M_\odot} < 38\,, \quad (\text{B63}) \\
-\left(c_{B63} + \frac{d_{B63}}{M_{\text{ZAMS}} + e_{B63}} + f_{B63} M_{\text{ZAMS}} + g_{B63} M_{\text{ZAMS}}^2\right) & M \geq 38\,\text{M}_\odot\,.
\end{cases}
$$

The factors ΔX_2, dM_2 and s_2 are only required over a limited mass range defined by δ_2 and δ_4

$$
dX_2^{(0)} = a_{B64} + \frac{b_{B64}}{1 + c_{B64}^{M_{\text{ZAMS}} - d_{B64}}}\,, \tag{B64}
$$

$$
dM_2^{(0)} = a_{B65} + b_{B65} M_{\text{ZAMS}} \tag{B65}
$$

and

$$
\log_{10} s_2^{(0)} = \max(-10, a_{B66} + b_{B66} M_{\text{ZAMS}})\,. \tag{B66}
$$

B7.2 Wind Loss

To cope with wind loss define

$$
\begin{aligned}
dM_1^{(a)} &= (M_{\mathrm{ZAMS}} - M_{\mathrm{HG}}) + \\
&\quad \max(0, a_{B67} + b_{B67}M_{\mathrm{ZAMS}},\, c_{B67} + d_{B67}M_{\mathrm{ZAMS}})
\end{aligned}
\tag{B67}
$$

which forces the drop in hydrogen when the star leaves the MS and changes for $M \lesssim 54\,\mathrm{M}_\odot$ and $M \gtrsim 54\,\mathrm{M}_\odot$

$$
f_{54} = F(M_{\mathrm{ZAMS}}, 1, 1, 0.01, 54)\,,
\tag{B68}
$$

$$
f_{\mathrm{X1}} = 1 + (1 - f_{54})\frac{(dM_1^{(a)} - dM_1^{(1)})}{20}
\tag{B69}
$$

so

$$
dX_1^{(1)} = f_{\mathrm{X1}}dX_1^{(0)} + \frac{2f_{54}}{M - M_{\mathrm{c}} + 10^{-14}}\,,
\tag{B70}
$$

$$
dX_2^{(1)} = f_{\mathrm{X1}}dX_2^{(0)}
\tag{B71}
$$

and

$$
dM_1^{(2)} = (1 - f_{54})dM_1^{(a)} + f_{54}dM_1^{(1)}\,.
\tag{B72}
$$

For small X_{H1} such that $X_{\mathrm{H1}} - dX_1^{(1)} < 0.1$ a correction is applied

$$
\Delta X_{\mathrm{H1}} = \max\left[1, \frac{Z_t}{0.02}\right] \times \max\left[0, 5 \times 10^{-3}(\Delta M - dM_2^{(1)})X_{\mathrm{i,H1}}\right]
\tag{B73}
$$

otherwise

$$
\Delta X_{\mathrm{H1}} = 0\,.
\tag{B74}
$$

B7.3 Metallicity Corrections

Metallicity corrections are then applied. A function f_Z which is 1 below $Z_t = 0.01$ and 0 above $Z_t = 0.02$ with a smooth transition is defined by

$$f_Z = \frac{1}{1 + 0.1^{10^3(0.015 - Z_t)}} \, . \tag{B75}$$

The slope s_1 may be redefined because of metallicity affecting the convection zones

$$s_1^a = f_Z a_{B76} \exp\left[-\frac{(M_{\mathrm{ZAMS}} - b_{B76})^2}{c_{B76}}\right] \tag{B76}$$

and a metallicity dependent mass

$$M_{\mathrm{low}} = a_{B77} + b_{B77} Z \tag{B77}$$

such that

$$dX_1 = dX_1^{(1)}(1 + \delta X_1 f_Z) \tag{B78}$$

$$dM_1 = dM_1^{(2)} + \delta M_1 f_z \, , \tag{B79}$$

$$dX_2 = dX_2^{(1)} + \delta X_2 \tag{B80}$$

and

$$dM_2 = dM_2^{(0)} + \delta M_2 \tag{B81}$$

where the δX and δM are given in table B16. The surface hydrogen abundance $X_{\mathrm{XH1}}^{(0)}$ is then calculated from eq. (B54).

There are further slight complications owing to metallicity, a minimum hydrogen abundance prior to the helium star phase in low-Z stars

Mass Range	δX_1	δM_1
$M_{\mathrm{ZAMS}} > M_{\mathrm{low}}$ $M_{\mathrm{ZAMS}} < 45\,\mathrm{M}_\odot$	$0.75 + 0.05 M_{\mathrm{ZAMS}}$	$-3.08 + 0.35 M_{\mathrm{ZAMS}}$
$M_{\mathrm{ZAMS}} > M_{\mathrm{low}}$ $M_{\mathrm{ZAMS}} \geq 45\,\mathrm{M}_\odot$	-0.1	0
$M_{\mathrm{ZAMS}} < M_{\mathrm{low}}$ $\Delta M \leq 1.5$	$\dfrac{-2(\frac{Z}{0.01})^3}{(M_{\mathrm{low}} - M_{\mathrm{ZAMS}})^2}$	0
$M_{\mathrm{ZAMS}} < M_{\mathrm{low}}$ $\Delta M > 1.5$	$0.2(0.75 + 0.05 M_{\mathrm{ZAMS}})$	$-3.08 + 0.35 M_{\mathrm{ZAMS}}$

Mass Range	δX_2	δM_2	s_1 change
$M_{\mathrm{ZAMS}} > M_{\mathrm{low}}$ $M_{\mathrm{ZAMS}} < 45\,\mathrm{M}_\odot$	0	0	$s_1 = s_1^a$ if $s_1^a > 0.1$ otherwise no change
$M_{\mathrm{ZAMS}} > M_{\mathrm{low}}$ $M_{\mathrm{ZAMS}} \geq 45\,\mathrm{M}_\odot$	$-0.5 f_Z dX_2^{(1)}$	$-9.515 - 472 Z_t$	$s_1 = s_1^a$ if $s_1^a > 0.1$ otherwise no change
$M_{\mathrm{ZAMS}} < M_{\mathrm{low}}$ $\Delta M \leq 1.5$	0	0	no change
$M_{\mathrm{ZAMS}} < M_{\mathrm{low}}$ $\Delta M > 1.5$	0	0	$s_1 = s_1^a$

Table B16: Metallicity-correction terms for massive hydrogen stars.

$$X_{\text{XH1}}^{(1)} = \max\left(\min\left[0.2, (1 + a_{B82}M_{\text{ZAMS}} + b_{B82}M_{\text{ZAMS}}^2)(1 + c_{B82}Z_t)d_{B82}f_Z\right], X_{\text{XH1}}^{(0)}\right)$$
(B82)

and the final bump as the helium core approaches the surface for stars with $dM_2 > 0$, $\Delta M > dM_2$ and $M_{\text{ZAMS}} < 45(Z/0.02)$

$$X_{\text{XH1}}^{(2)} = X_{\text{XH1}}^{(1)} - \max\left[0, 0.5X_{\text{XH1}}^{(1)}(\Delta M - dM_2)\right].$$
(B83)

Finally,

$$X_{\text{XH1}} = \max\left[0, \min(X_{\text{XH1}}^{(2)}, X_{\text{i,XH1}})\right]$$
(B84)

because X_{XH1} cannot increase and cannot fall below zero.

B7.4 Helium and Metals

Surface helium is calculated from

$$X_{\text{He4}} = \begin{cases} 1 - X_{\text{H1}} - Z_t & M - M_c \geq 1\,\text{M}_\odot \\ \min\left[1 - Z_t, \max\left\{1 - Z_t - (M - M_c), 1 - X_{\text{H1}} - Z_t\right\}\right] & M - M_c < 1\,\text{M}_\odot \end{cases}$$
(B85)

where the correction for $M - M_c < 1\,\text{M}_\odot$ ensures a smooth transition to the helium star phase (for which $X_{\text{He4}} \approx 0.95$). This is particularly important in binary stars where the star may jump from the HG to the HeMS because of enhanced mass loss.

The coefficients for the ^{16}O and ^{12}C fits are given in tables B17 and B18. The constant c_{124} is given by

$$c_{124} = \begin{cases} 4.3012 \times 10^{-1} - 8.3078 \times 10^{-1}b_{124} & b_{124} < -0.423 \\ 4.6923s \times 10^{-1} - 1.3706b_{124} & b_{124} \geq 0.423\,. \end{cases}$$
(B86)

	Eq. (123)		
a	$-9.4 \times 10^{-2} + 1.1468 \times 10^{-1}/0.01^{0.19394 M_{\mathrm{ZAMS}} - 6.8227}$	g	8.48070×10^{-1}
b	$3.2732 - 4.8939 \times 10^{-2} M_{\mathrm{ZAMS}} + 3.7616 \times 10^{-4} M_{\mathrm{ZAMS}}^2$	h	1.974×10^{-2}
c	$18.88 - 1.1831 \exp(-(\ln M_{\mathrm{ZAMS}} - \ln 17.8)^2/0.5076)$	i	-4.3243×10^{-4}
d	$-13.936 - 0.68025 \exp(-(\ln M_{\mathrm{ZAMS}} - \ln 16)^2/0.97626)$	j	2.5574×10^{-6}
e	$0.8064 - 0.81104/(1 + 1.4638^{-1.1967 M_{\mathrm{ZAMS}} + 55.336}) + 1.7509 \times 10^{-7} M_{\mathrm{ZAMS}}^3$	k	-4.4266×10^{-1}
f	$0.70766 + \exp\left[3.7462 \times 10^{-2}(M_{\mathrm{ZAMS}} - 82.122)\right]$	l	1.146×10^2

Table B17: Coefficients for ψ_{O16}.

Eq. (124)	a	b
$M_{\mathrm{ZAMS}}/\mathrm{M_\odot} < 25.19$	$3.8576 - 3.0414 \times 10^{-1} M_{\mathrm{ZAMS}}$ $+6.295 \times 10^{-3} M_{\mathrm{ZAMS}}^2$	$-1.2725 \times 10^1 + 1.0165 M_{\mathrm{ZAMS}}$ $-2.1193 \times 10^{-2} M_{\mathrm{ZAMS}}^2$
$25.19 \leq M_{\mathrm{ZAMS}}/\mathrm{M_\odot} < 46.21$	-1.4495×10^{-2} $+6.7851 \times 10^{-4} M_{\mathrm{ZAMS}}$	$-6.3494 \times 10^{-1} + 5.5562 \times 10^{-2} M_{\mathrm{ZAMS}}$ $-9.4467 \times 10^{-4} M_{\mathrm{ZAMS}}^2$
$46.21 \leq M_{\mathrm{ZAMS}}/\mathrm{M_\odot} < 66.32$	1.119×10^{-2} $+6.7851 \times 10^{-4} M_{\mathrm{ZAMS}}$	$2.3992 \times 10^{-1} - 7.6394 \times 10^{-3} M_{\mathrm{ZAMS}}$ $+3.0795 \times 10^{-5} M_{\mathrm{ZAMS}}^2$
$M_{\mathrm{ZAMS}}/\mathrm{M_\odot} \geq 66.32$	$-2.325 \times 10^{-2} + 1.0086 \times 10^{-3} M_{\mathrm{ZAMS}}$ $-5.467 \times 10^{-6} M_{\mathrm{ZAMS}}^2$	$2.3992 \times 10^{-1} - 7.6394 \times 10^{-3} M_{\mathrm{ZAMS}}$ $+3.0795 \times 10^{-5} M_{\mathrm{ZAMS}}^2$

Table B18: Coefficients for a and b ψ_{C12}.

The factor γ_{13} is given by

$$\gamma_{13} = \frac{Z\gamma_{14}}{0.02} \min\left\{0.1, \max\left[10^{-4}, 1.1254 \times 10^{-1}\left(1 - \frac{1.009}{1 + 0.8^{M_{\mathrm{ZAMS}} - 32.051}}\right)\right]\right\}. \quad \text{(B87)}$$

The factor γ_{14} is positive when there is little $^{14}\mathrm{N}$, negative when $^{14}\mathrm{N}$ constitutes the majority of the CNO present representing the decline of $^{13}\mathrm{C}$ when CN burning approaches equilibrium and zero when there is little hydrogen left to burn,

$$\gamma_{14} = \begin{cases} -2.0 & X_{\mathrm{XH1}} > 0.3 \,\text{and}\, X_{\mathrm{N14}}/X_{\mathrm{CNO}} > 0.5 \\ 1 & X_{\mathrm{XH1}} > 0.3 \,\text{and}\, X_{\mathrm{N14}}/X_{\mathrm{CNO}} \leq 0.5 \\ 0 & X_{\mathrm{XH1}} \leq 0.3. \end{cases} \quad \text{(B88)}$$

Note that the initial ^{13}C abundance must be doubled in order to match the MM94 models. The reason is unclear.

B Analytic Fits

B8 WW95 Fits

Figures B1 to B6 show the comparison of the analytic fits to the WW95 CO core collapse (model A) SNe ejecta abundances after the envelope is removed according to the method of Portinari et al. (1998), see appendix A3. The fitting formulae are shown below. ^{56}Ni is grouped with ^{56}Fe prior to fitting. The fits are made to all the WW95 isotopes, however some are not currently used in the synthetic model or are expected to decay rapidly. For this reason ^{56}Co is treated as ^{56}Fe, ^{52}Fe is treated as ^{52}Cr, ^{48}Cr as ^{48}Ti, ^{44}Ti as ^{44}Ca, ^{61}Ni as ^{60}Ni, ^{31}S as ^{32}Si, ^{30}Si as ^{28}Si. Other trace elements are dealt with in appendix B10.

$$
\begin{aligned}
X_{\text{Be7}} \;=\;\; & \max(0, -1.6578 \times 10^{-7} + \frac{1}{\log_{10} Z}(1.9828 \times 10^{-6} - \\
& 2.2016 \times 10^{-6} \exp(-9.1326 \times 10^{-2}(M_{\text{CO}} - 13)^2) - \\
& 6.0303 \times 10^{-6}/M_{\text{CO}}))
\end{aligned}
\tag{B89}
$$

$$
X_{\text{Li7}} = \max(0, 9.4064 \times 10^{-8} - 4.6566 \times 10^{-9} M_{\text{CO}} + 6.1132 \times 10^{-6} M_{\text{CO}}^{-4.0742})
\tag{B90}
$$

$$
X_{\text{Be9}} = \max(0, (-9.3132 \times 10^{-10} + 4.61 \times 10^{-7} Z) M_{\text{CO}}^{-3.022})
\tag{B91}
$$

$$
X_{\text{B10}} = \max(0, (-8.3819 \times 10^{-9} + 4.2869 \times 10^{-6} Z) M_{\text{CO}}^{-3.0202})
\tag{B92}
$$

$$
\begin{aligned}
X_{\text{C11}} \;=\;\; & \max(0, (1.4063 \times 10^{-6} + 2.4038 \times 10^{-5} Z) M_{\text{CO}}^{-1.7376} + \\
& (9.3132 \times 10^{-10} + 1.7416 \times 10^{-7} Z) M_{\text{CO}})
\end{aligned}
\tag{B93}
$$

$$
\begin{aligned}
X_{\text{B11}} \;=\;\; & \max(0, -9.7789 \times 10^{-8} + \frac{1}{\log_{10} Z}(-4.7563 \times 10^{-6}/M_{\text{CO}} + \\
& 9.3132 \times 10^{-9} - 6.5193 \times 10^{-9} M_{\text{CO}}))
\end{aligned}
\tag{B94}
$$

$$
X_{\text{C12}} = \max(0, (0.21486 - 2.9967 \times 10^{-2} \log_{10} Z) M_{\text{CO}}^{-0.77067})
\tag{B95}
$$
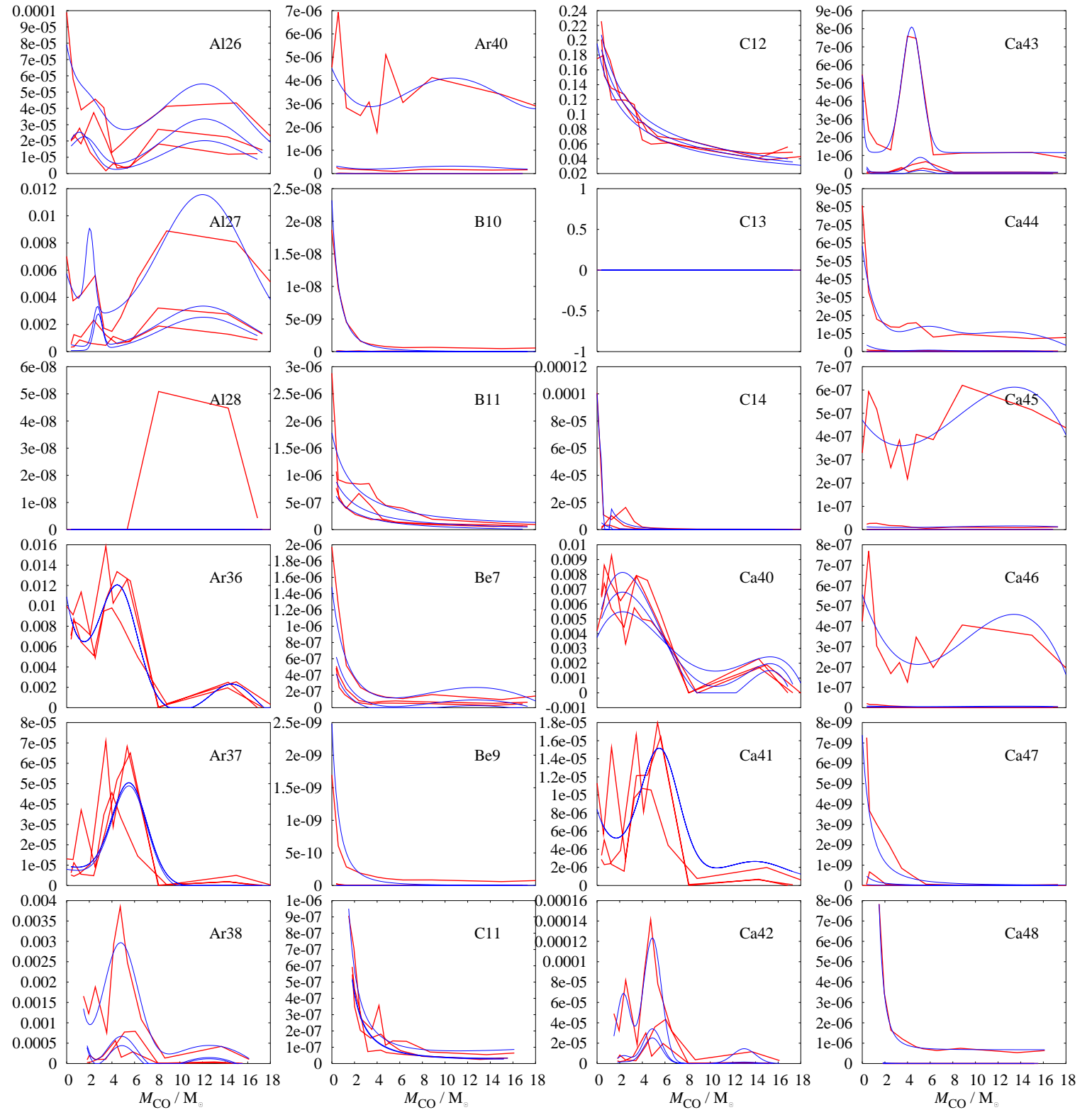
Figure B1: Mass-fraction fits to the WW95 CO core-collapse yields (in alphanumeric order) for ^{26}Al to ^{48}Ca. Red lines show the WW95 data, corrected for envelope removal, the blue lines show the fits.
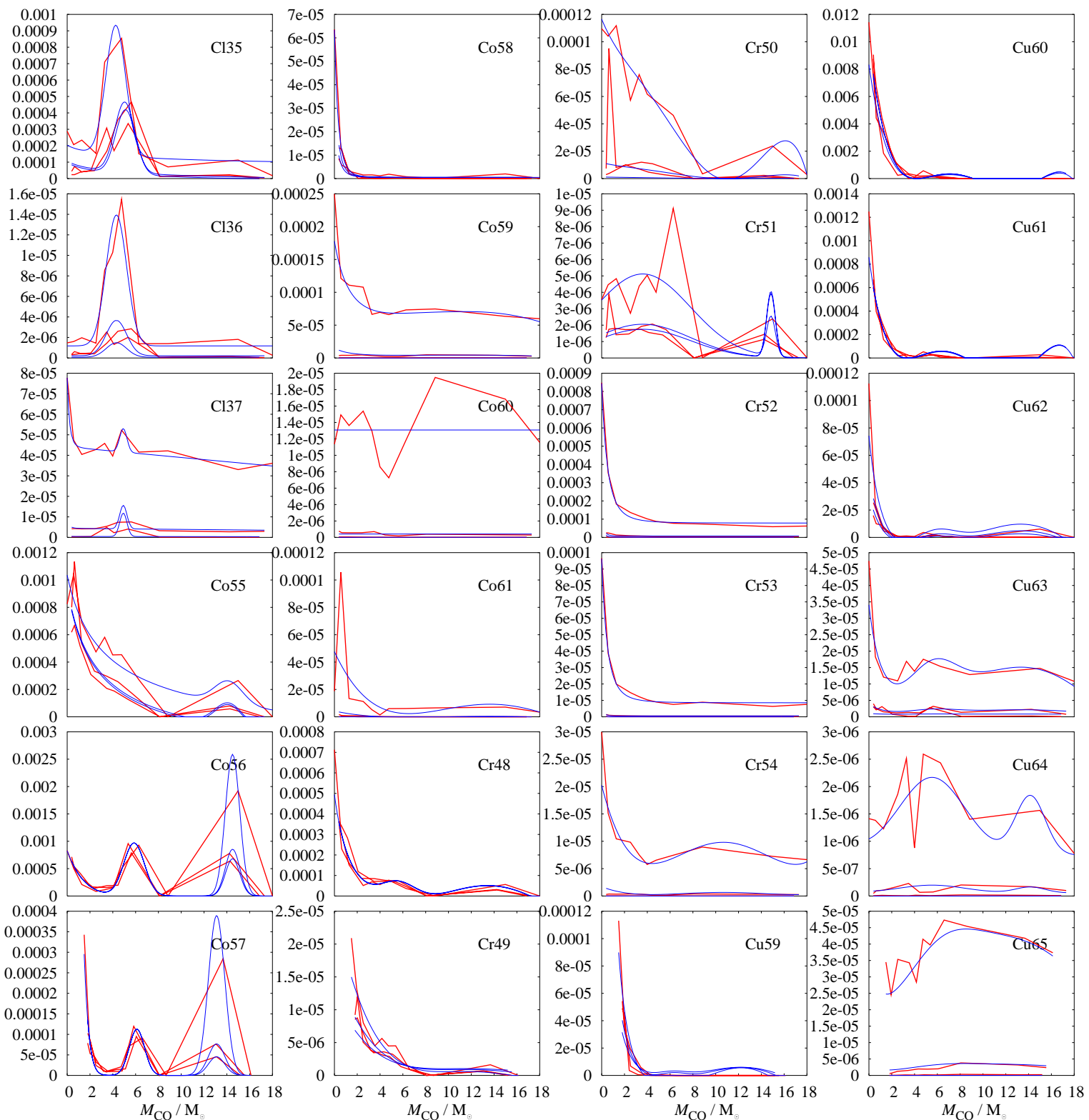
Figure B2: As figure B1 for ^{35}Cl to ^{65}Cu.
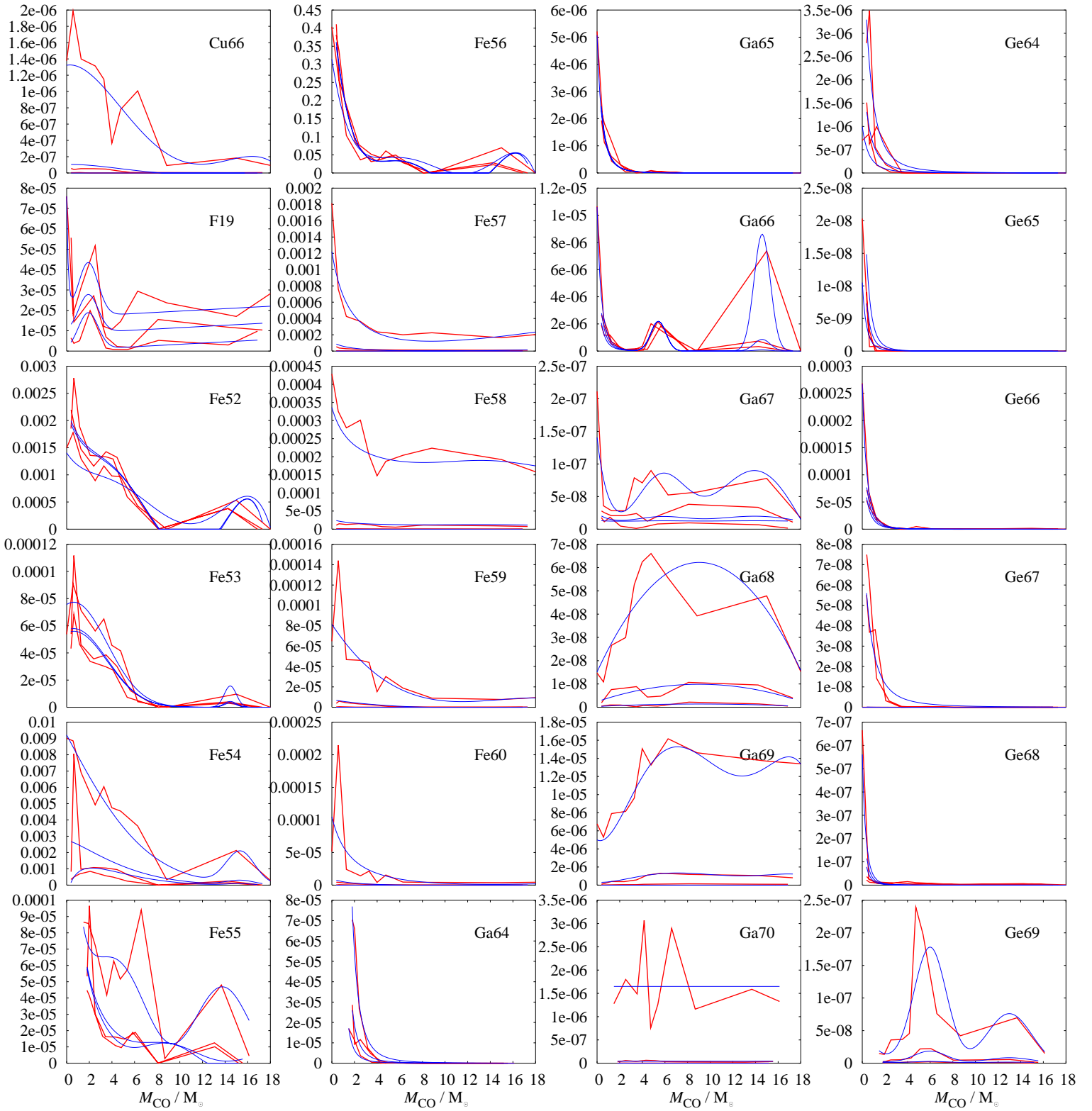
Figure B3: As figure B1 for ^{66}Cu to ^{69}Ge.
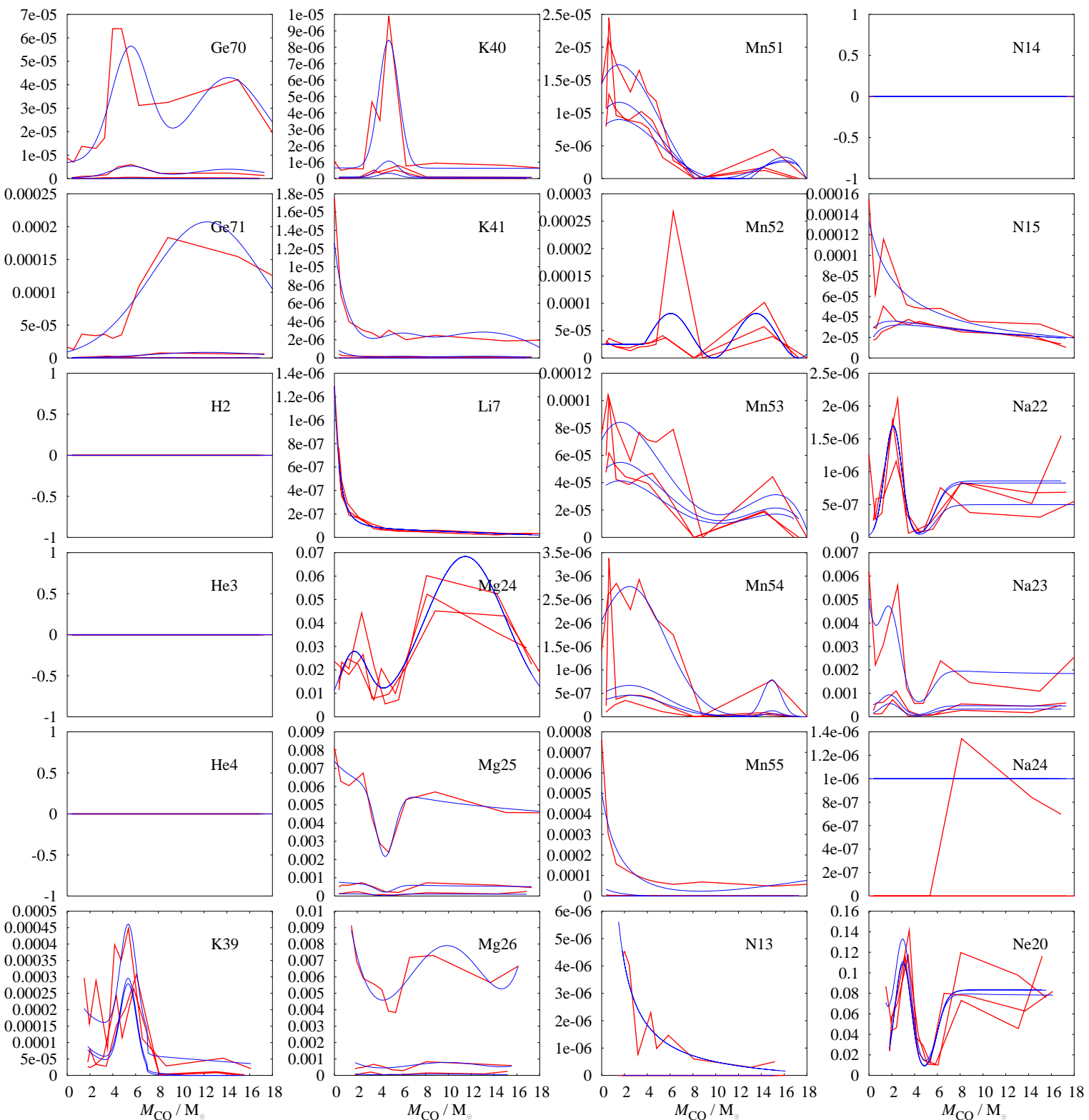
Figure B4: As figure B1 for ^{70}Ge to ^{20}Ne.
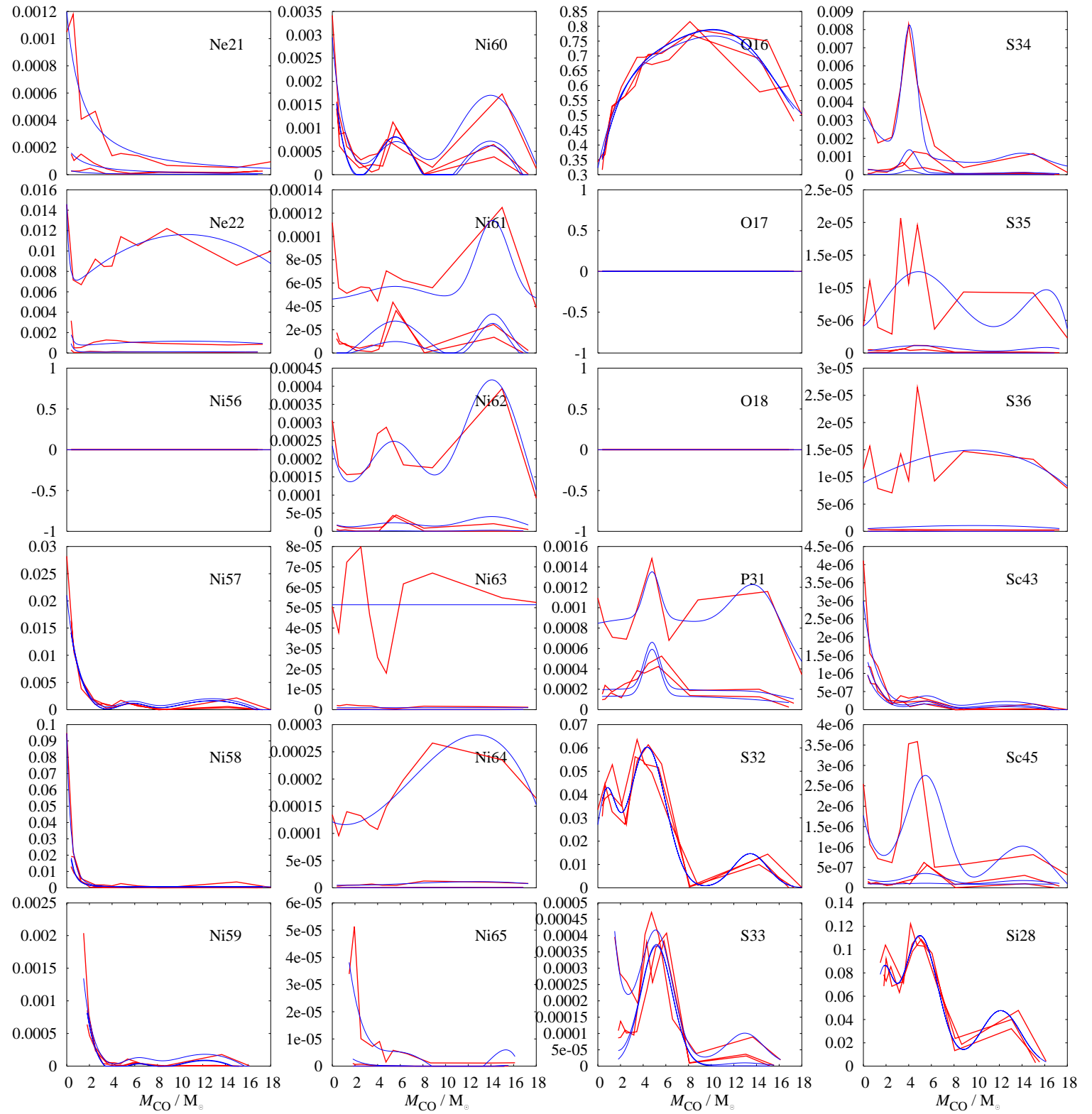
Figure B5: As figure B1 for ^{21}Ne to ^{28}Si.
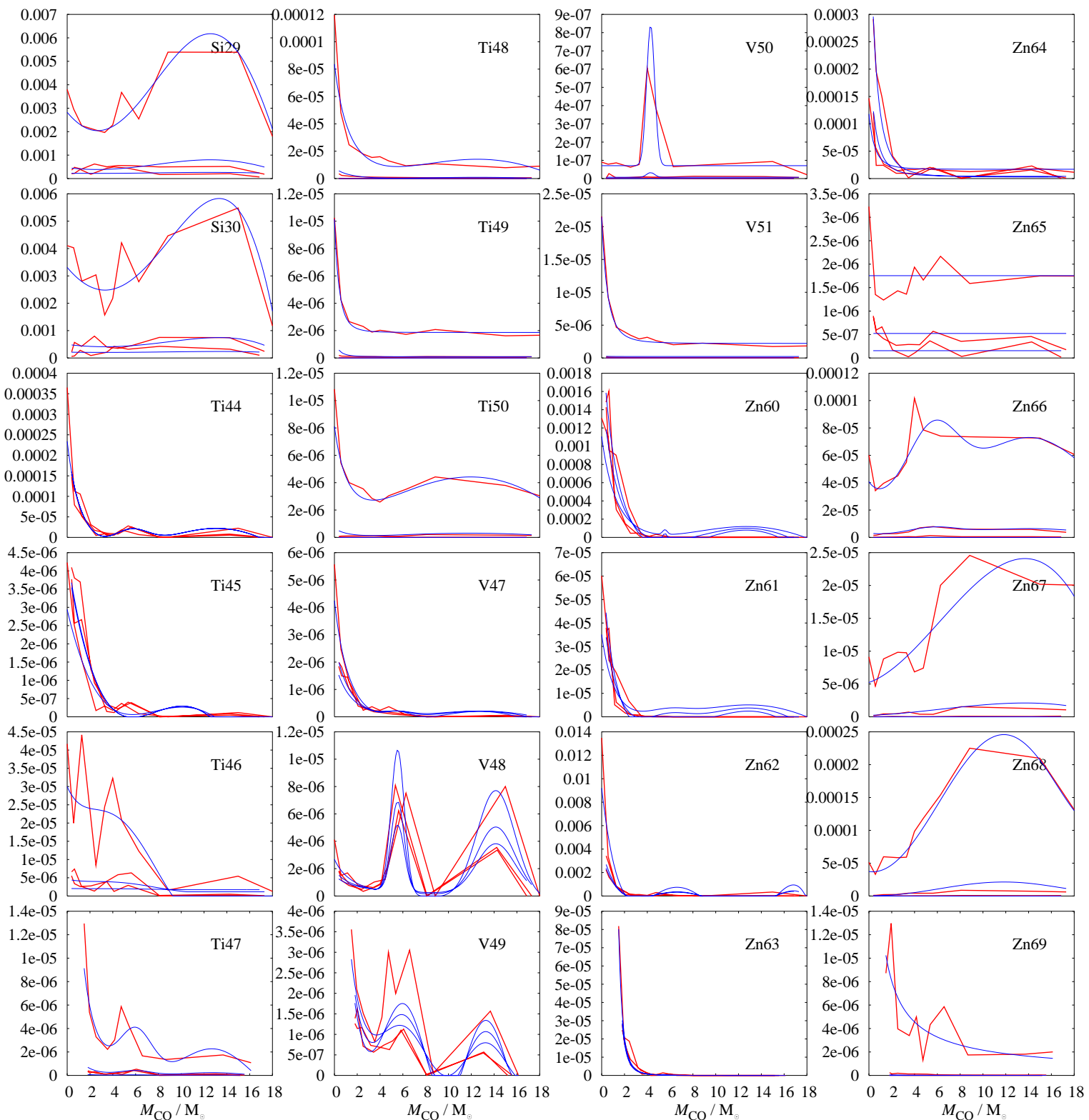
Figure B6: As figure B1 for ^{29}Si to ^{69}Zn.

$$X_{\mathrm{N13}} \quad = \quad \max(0, \min(1, \max(0, (Z - 0.0002)/1.8 \times 10^{-3}))$$
$$(-3.9861 \times 10^{-7} + 8.9584 \times 10^{-6}/M_{\mathrm{CO}})) \tag{B96}$$

$$X_{\mathrm{C13}} = X_{\mathrm{N14}} = 0 \tag{B97}$$

$$X_{\mathrm{C14}} \quad = \quad \max(0, 2.0684 \times 10^{-2} Z M_{\mathrm{CO}}^{-3.5578} - 3.9593 \times 10^{-3}$$
$$\exp(-M_{\mathrm{CO}} - 2.8975 + 36.874 Z^2/8.9678 \times 10^{-3})) \tag{B98}$$

$$X_{\mathrm{N15}} \quad = \quad \max(0, -7.5772 \times 10^{-6} + (-3.5698 \times 10^{-4} + 1.7455 \times 10^{-2} Z)/M_{\mathrm{CO}} +$$
$$(3.3997 \times 10^{-4} - 7.335 \times 10^{-3} Z)/M_{\mathrm{CO}}^{0.70029}) \tag{B99}$$

$$X_{\mathrm{O16}} \quad = \quad \max(0, 0.6179 + (1 - 6.5924 Z)(-0.88519 + 0.50179 M_{\mathrm{CO}} - 0.10799 M_{\mathrm{CO}}^2 +$$
$$1.2249 \times 10^{-2} M_{\mathrm{CO}}^3 - 6.853 \times 10^{-4} M_{\mathrm{CO}}^4 + 1.4418 \times 10^{-5} M_{\mathrm{CO}}^5)) \tag{B100}$$

$$X_{\mathrm{O17}} = X_{\mathrm{O18}} = 0 \tag{B101}$$

$$X_{\mathrm{F19}} \quad = \quad \max(0, 2.9942 \times 10^{-5} + 8.1509 \times 10^{-6} \log_{10} Z + 0.61495 Z M_{\mathrm{CO}}^{-13.484} +$$
$$(1.7899 \times 10^{-5} + 4.1949 \times 10^{-4} Z) \exp(-(M_{\mathrm{CO}} - 3.0389)^2) +$$
$$3.6787 \times 10^{-7} M_{\mathrm{CO}}) \tag{B102}$$

$$X_{\mathrm{Ne20}} \quad = \quad \max(0, (8.359 \times 10^{-2} - 0.28975 Z)/(1 + 0.1^{M_{\mathrm{CO}} - 6}) +$$
$$(0.10872 + 0.47628 Z) \exp(-M_{\mathrm{CO}} - 3^2/1) + 6.5491 Z M_{\mathrm{CO}}^{-2}) \tag{B103}$$

$$X_{\mathrm{Ne21}} = \max(0, 4.027 \times 10^{-2} Z^{0.75936} M_{\mathrm{CO}}^{-1.3673}) \tag{B104}$$

$$
\begin{aligned}
X_{\mathrm{Na22}} \;=\; & \max(0, 1.6997 \times 10^{-6} \exp(-(M_{\mathrm{CO}} - 3.2211)^2/0.74294) + \\
& (8.6427 \times 10^{-7} - 1.8283 \times 10^{-5} Z)/(1 + 0.1^{M_{\mathrm{CO}} - 6.2539}))
\end{aligned} \tag{B105}
$$

$$
\begin{aligned}
X_{\mathrm{Ne22}} \;=\; & \max(0, 0.18885 Z (1 + 0.41251 M_{\mathrm{CO}} - 2.0495 \times 10^{-2} M_{\mathrm{CO}} M_{\mathrm{CO}}) + \\
& 0.48702 Z^{0.15151} M_{\mathrm{CO}}{}^{-8.6199})
\end{aligned} \tag{B106}
$$

$$
\begin{aligned}
X_{\mathrm{Na23}} \;=\; & \max(0, 3.1171 \times 10^{-4} + 7.4621 \times 10^{-2} Z)/(1 + 0.1^{M_{\mathrm{CO}} - 6}) + \\
& (5.2008 \times 10^{-4} + 0.15019 Z) \exp(-(M_{\mathrm{CO}} - 3)^2/1) + \\
& 0.51976 Z M_{\mathrm{CO}}{}^{-2})
\end{aligned} \tag{B107}
$$

$$
\begin{aligned}
X_{\mathrm{Mg24}} \;=\; & \max(0, 2.6277 \times 10^{-2} \exp(-(M_{\mathrm{CO}} - 2.8538)^2/2.1509) + \\
& 6.8362 \times 10^{-2} \exp(-(M_{\mathrm{CO}} - 10.823)^2/16.875))
\end{aligned} \tag{B108}
$$

$$
X_{\mathrm{Na24}} = 0 \tag{B109}
$$

$$
\begin{aligned}
X_{\mathrm{Mg25}} \;=\; & \max(0, 5.3532 \times 10^{-5} + 0.39669 Z M_{\mathrm{CO}}{}^{-0.19653} - (5.5216 \times 10^{-5} + 0.17976 Z) \\
& \exp(-(M_{\mathrm{CO}} - 5.0875)^2/0.87357))
\end{aligned} \tag{B110}
$$

$$
\begin{aligned}
X_{\mathrm{Al26}} \;=\; & \max(0, 5.7129 \times 10^{-3} Z/M_{\mathrm{CO}} - 6.6934 \times 10^{-6} \times \\
& \log_{10} Z \exp(-M_{\mathrm{CO}} - 3.8609 - 0.39476 \log_{10} Z^2/1.7666) + (6.6046 \times 10^{-5} + \\
& 1.2425 \times 10^{-5} \log_{10} Z) \exp(-(M_{\mathrm{CO}} - 11.407)^2/17.018))
\end{aligned} \tag{B111}
$$

$$
\begin{aligned}
X_{\mathrm{Mg26}} \;=\; & \max(0, Z(0.8209 - 0.33616 M_{\mathrm{CO}} + 5.9571 \times 10^{-2} M_{\mathrm{CO}}^2 - \\
& 2.9439 \times 10^{-3} M_{\mathrm{CO}}{}^3 - 6.3509 \times 10^{-5} M_{\mathrm{CO}}{}^4 + 5.5777 \times 10^{-6} M_{\mathrm{CO}}{}^5))
\end{aligned} \tag{B112}
$$

$$
\begin{aligned}
X_{\mathrm{Al27}} \;=\; & \max(0, 0.42196 Z/M_{\mathrm{CO}} + (2.5901 \times 10^{-3} + 0.17301 Z) \times \\
& \exp(-M_{\mathrm{CO}} - 3.7616 + 30.045 Z^2/0.1805) + (2.4404 \times 10^{-3} + 0.41877 Z) \times \\
& \exp(-M_{\mathrm{CO}} - 11.308^2/19.571))
\end{aligned}
\tag{B113}
$$

$$
X_{\mathrm{Al28}} = 0
\tag{B114}
$$

$$
\begin{aligned}
X_{\mathrm{Si28}} \;=\; & \max(0, 7.2177 \times 10^{-2} \exp(-(M_{\mathrm{CO}} - 1.72)^2/1.324) + \\
& 0.11199 \exp(-M_{\mathrm{CO}} - 4.9998^2/4.9635) + 4.7649 \times 10^{-2} \\
& \exp(-(M_{\mathrm{CO}} - 12.116)^2/6.2636))
\end{aligned}
\tag{B115}
$$

$$
\begin{aligned}
X_{\mathrm{Si29}} \;=\; & \max(0, (2.0326 \times 10^{-4} + Z((0.1975 - 5.1798 \times 10^{-2} M_{\mathrm{CO}} + \\
& 3.2181 \times 10^{-3} M_{\mathrm{CO}}{}^2 + 1.276 \times 10^{-3} M_{\mathrm{CO}}{}^3 - 1.3227 \times 10^{-4} M_{\mathrm{CO}}{}^4 + \\
& 3.2 \times 10^{-6} M_{\mathrm{CO}}{}^5))))
\end{aligned}
\tag{B116}
$$

$$
\begin{aligned}
X_{\mathrm{Si30}} \;=\; & \max(0, 1.8135 \times 10^{-4} + Z(0.21305 - 4.472 \times 10^{-2} M_{\mathrm{CO}} + \\
& 4.0417 \times 10^{-3} M_{\mathrm{CO}}{}^2 + 3.7584 \times 10^{-4} M_{\mathrm{CO}}{}^3 - 3.0211 \times 10^{-5} M_{\mathrm{CO}}{}^4))
\end{aligned}
\tag{B117}
$$

$$
\begin{aligned}
X_{\mathrm{P31}} \;=\; & \max(0, (1.3211 \times 10^{-3} + 0.39615 Z)(8.589 \times 10^{-2} + 4.5103 \times 10^{-3} M_{\mathrm{CO}} - \\
& 4.5734 \times 10^{-4} M_{\mathrm{CO}} M_{\mathrm{CO}}) + 4.5711 \times 10^{-4} \exp(-(M_{\mathrm{CO}} - 5.3796)^2/0.63588) + \\
& 0.5 \times 0.16913 Z^{1.2699} \exp(-(M_{\mathrm{CO}} - 12.915)^2/6))
\end{aligned}
\tag{B118}
$$

$$
\begin{aligned}
X_{\mathrm{S32}} \;=\; & \max(0, 3.7549 \times 10^{-2} \exp(-(M_{\mathrm{CO}} - 2.0771)^2/0.8852) + \\
& 6.0379 \times 10^{-2} \exp(-(M_{\mathrm{CO}} - 5.0281)^2/3.4905) + 1.465 \times 10^{-2} \times \\
& \exp(-(M_{\mathrm{CO}} - 12.424)^2/30.0432))
\end{aligned}
\tag{B119}
$$

B Analytic Fits

$$
\begin{aligned}
X_{\mathrm{S}33} \;=\;& \max(0, 3.6815 \times 10^{-4} \exp(-(M_{\mathrm{CO}} - 5.1833)^2/3.8048) + \\
& 4.5482 \times 10^{-3} Z \exp(-(M_{\mathrm{CO}} - 13)^2/5) + 3.9742 \times 10^{-2} Z M_{\mathrm{CO}}^{-1.7012}) \quad\text{(B120)}
\end{aligned}
$$

$$
\begin{aligned}
X_{\mathrm{S}34} \;=\;& \max(0, 0.13275 Z^{0.7497} \exp(-M_{\mathrm{CO}} - 4.8027^2/0.56836) + \\
& 3.6367 \times 10^{-2} Z \exp(-M_{\mathrm{CO}} - 13^2/5) + 0.27296 Z M_{\mathrm{CO}}^{-0.96893}) \quad\text{(B121)}
\end{aligned}
$$

$$
\begin{aligned}
X_{\mathrm{Cl}35} \;=\;& \max(0, (-5.9742 \times 10^{-5} + 5.4213 \times 10^{-3} Z + 1.8366 \times 10^{-4} M_{\mathrm{CO}}^{-0.43502}) + \\
& (3.8797 \times 10^{-4} + 2.0306 \times 10^{-2} Z) \exp(-(M_{\mathrm{CO}} - 5.6587 + 35.18 Z)^2)) \quad\text{(B122)}
\end{aligned}
$$

$$
\begin{aligned}
X_{\mathrm{S}35} \;=\;& \max(0, -1.3132 \times 10^{-7} + Z(3.7111 \times 10^{-4} - 3.5211 \times 10^{-4} M_{\mathrm{CO}} + \\
& 2.1899 \times 10^{-4} M_{\mathrm{CO}}^2 - 4.0579 \times 10^{-5} M_{\mathrm{CO}}^3 + 2.942 \times 10^{-6} M_{\mathrm{CO}}^4 - \\
& 7.3574 \times 10^{-8} M_{\mathrm{CO}}^5)) \quad\text{(B123)}
\end{aligned}
$$

$$
\begin{aligned}
X_{\mathrm{Ar}36} \;=\;& \max(0, -2.5457 \times 10^{-3} + 1.0799 \times 10^{-2} \exp(-0.53427(M_{\mathrm{CO}} - 5.2381)^2) + \\
& 3.3881 \times 10^{-3} \exp(--0.43453(M_{\mathrm{CO}} - 13.415)^2) + \\
& 1.9731 \times 10^{-2}/M_{\mathrm{CO}}) \quad\text{(B124)}
\end{aligned}
$$

$$
\begin{aligned}
X_{\mathrm{S}36} \;=\;& \max(0, (-4.7404 \times 10^{-7} + Z((3.6823 \times 10^{-4} + 7.035 \times 10^{-5} M_{\mathrm{CO}} - \\
& 1.3262 \times 10^{-6} M_{\mathrm{CO}}^2 - 1.7136 \times 10^{-7} M_{\mathrm{CO}}^3)))) \quad\text{(B125)}
\end{aligned}
$$

$$
\begin{aligned}
X_{\mathrm{Cl}36} \;=\;& \max(0, 3.0722 \times 10^{-5} Z + 2.5118 \times 10^{-6} - \log_{10} Z^{-2.8228} \\
& (1 + 22.691 \exp(-(M_{\mathrm{CO}} - 5)^2/1.0614))) \quad\text{(B126)}
\end{aligned}
$$

$$
\begin{aligned}
X_{\mathrm{Ar37}} \;=\; & \max(0, (0.33039 + ((1 + 2.4937 \times 10^{-4} Z))(-0.33037 + \\
& 4.6862 \times 10^{-5} \exp(-0.56232(M_{\mathrm{CO}} - 6)^2) - 2.1183 \times 10^{-5} \times \\
& \exp(--7.2928 \times 10^{-2}(M_{\mathrm{CO}} - 13)^2)))) \qquad\qquad \text{(B127)}
\end{aligned}
$$

$$
\begin{aligned}
X_{\mathrm{Cl37}} \;=\; & \max(0, 2.2537 \times 10^{-3} Z(1 - 1.4143 \times 10^{-2} M_{\mathrm{CO}}) + 1.1438 \times 10^{-5} \times \\
& \exp(-M_{\mathrm{CO}} - 5.4905^2/0.13329) + 6.4414 \times 10^{-2} Z M_{\mathrm{CO}}^{-9.1447}) \qquad \text{(B128)}
\end{aligned}
$$

$$
\begin{aligned}
X_{\mathrm{Ar38}} \;=\; & \max(0, -5.771 \times 10^{-3} + (1.221 \times 10^{-3} + 0.11642 Z) \times \\
& \exp(-0.43682(M_{\mathrm{CO}} - 4.6935)^2) + (5.4536 \times 10^{-3} + 1.6611 \times 10^{-2} Z) \times \\
& \exp(-7.1143 \times 10^{-2}(M_{\mathrm{CO}} - 13.231)^2) + 5.5681 \times 10^{-3}/M_{\mathrm{CO}})
\end{aligned}
$$

$$
\begin{aligned}
X_{\mathrm{K39}} \;=\; & \chi_{39}(2.6397 \times 10^{-5} + 5.6705 \times 10^{-3} Z + 1.0578 \times 10^{-4}/M_{\mathrm{CO}}) + (2.5639 \times 10^{-4} + \\
& 3.5011 \times 10^{-3} Z) \exp(-M_{\mathrm{CO}} - 5.3582^2) - 4.6268 \times 10^{-6} M_{\mathrm{CO}}) \qquad \text{(B129)}
\end{aligned}
$$

$$
\text{(B130)}
$$

where $\chi_{39} = 1$ if $M < 7\,\mathrm{M_\odot}$, 0.5 otherwise,

$$
\begin{aligned}
X_{\mathrm{K40}} \;=\; & \max(0, (4.0047 \times 10^{-8} + 3.0579 \times 10^{-5} Z) + (2.1607 \times 10^{-7} + \\
& 3.7918 \times 10^{-4} Z) \exp(-(M_{\mathrm{CO}} - 5.3619)^2) - 1.8626 \times 10^{-9} M_{\mathrm{CO}}) \quad \text{(B131)}
\end{aligned}
$$

$$
\begin{aligned}
X_{\mathrm{Ca40}} \;=\; & \max(0, (3.2196 \times 10^{-3} + (\log_{10} Z)((2.8027 \times 10^{-3} - 3.0256 \times 10^{-3} M_{\mathrm{CO}} + \\
& 7.16 \times 10^{-4} M_{\mathrm{CO}}^2 - 5.9506 \times 10^{-5} M_{\mathrm{CO}}^3 + 1.6391 \times 10^{-6} M_{\mathrm{CO}}^4)))) \qquad \text{(B132)}
\end{aligned}
$$

B Analytic Fits

$$
\begin{aligned}
X_{\mathrm{Ar40}} \;=\; & \max(0, -1.0151 \times 10^{-7} + Z(3.8561 \times 10^{-4} - 1.4072 \times 10^{-4} M_{\mathrm{CO}} + \\
& 2.7806 \times 10^{-5} M_{\mathrm{CO}}{}^2 - 2.0517 \times 10^{-6} M_{\mathrm{CO}}{}^3 + 5.0291 \times 10^{-8} M_{\mathrm{CO}}{}^4)) \quad \text{(B133)}
\end{aligned}
$$

$$
\begin{aligned}
X_{\mathrm{K41}} \;=\; & \max(0, (-1.0058 \times 10^{-7} + Z(-6.335 \times 10^{-4} + 9.1181 \times 10^{-5} \times \\
& \exp(-0.46868(M_{\mathrm{CO}} - 6)^2) + 6.531 \times 10^{-4} \exp(-9.5955 \times 10^{-2}(M_{\mathrm{CO}} - 13)^2) + \\
& 1.6003 \times 10^{-3}/M_{\mathrm{CO}}))) \quad \text{(B134)}
\end{aligned}
$$

$$
\begin{aligned}
X_{\mathrm{Ca41}} \;=\; & \max(0, (0.25003 + (1)(-0.25003 + 1.3091 \times 10^{-5} \exp(-0.52349(M_{\mathrm{CO}} - 6)^2) + \\
& 1.6894 \times 10^{-6} \exp(--0.357(M_{\mathrm{CO}} - 13)^2) + 1.2462 \times 10^{-5}/M_{\mathrm{CO}}))) \quad \text{(B135)}
\end{aligned}
$$

$$
\begin{aligned}
X_{\mathrm{Ca42}} \;=\; & \max(0, (8.6986 \times 10^{-7} + 3.3701 \times 10^{-3} Z) \exp(-(M_{\mathrm{CO}} - 2.3283)^2/0.75542) + \\
& (2.4213 \times 10^{-5} + 4.9544 \times 10^{-3} Z) \exp(-(M_{\mathrm{CO}} - 4.8862)^2/1.2788) + \\
& (7.2903 \times 10^{-4} Z) \exp(-(M_{\mathrm{CO}} - 13)^2/2)) \quad \text{(B136)}
\end{aligned}
$$

$$
\begin{aligned}
X_{\mathrm{Ca43}} \;=\; & \max(0, -5.2154 \times 10^{-8} + 6.0534 \times 10^{-5} Z + 1.0154 \times 10^{-3} M_{\mathrm{CO}}{}^{-13.728} + \\
& (1.4715 \times 10^{-7} + 3.3948 \times 10^{-4} Z) \exp(-(M_{\mathrm{CO}} - 5.7289 + 34.454 Z)^2)) \quad \text{(B137)}
\end{aligned}
$$

$$
\begin{aligned}
X_{\mathrm{Sc43}} \;=\; & \max(0, -3.4459 \times 10^{-8} + (1/\log_{10} Z)(5.9921 \times 10^{-6} - 7.3016 \times 10^{-7} \\
& \exp(-0.61822(M_{\mathrm{CO}} - 6)^2) - 5.3374 \times 10^{-6} \exp(-8.6405 \times 10^{-2}(M_{\mathrm{CO}} - 13)^2) - \\
& 1.3611 \times 10^{-5}/M_{\mathrm{CO}})) \quad \text{(B138)}
\end{aligned}
$$

$$
\begin{aligned}
X_{\mathrm{Ca44}} \; = \;\; & \mathrm{max}(0, -6.482 \times 10^{-7} + Z(-3.577 \times 10^{-3} + 5.2375 \times 10^{-4} \times \\
& \exp(--0.42545(M_{\mathrm{CO}} - 6)^2) + 3.5446 \times 10^{-3} \exp(-8.3893 \times 10^{-2}(M_{\mathrm{CO}} - 13)^2) + \\
& 7.6211 \times 10^{-3}/M_{\mathrm{CO}})) \quad\quad\quad\quad\quad\quad\quad\quad\quad\quad\quad\quad\quad\quad\text{(B139)}
\end{aligned}
$$

$$
\begin{aligned}
X_{\mathrm{Ti44}} \; = \;\; & \mathrm{max}(0, 0.24988 - 0.25018 + 4.3198 \times 10^{-5} \exp(-0.55151(M_{\mathrm{CO}} - 6)^2) + \\
& 2.6702 \times 10^{-4} \exp(-0.10078(M_{\mathrm{CO}} - 13)^2) + 6.92 \times 10^{-4}/M_{\mathrm{CO}}) \quad\quad \text{(B140)}
\end{aligned}
$$

$$
\begin{aligned}
X_{\mathrm{Ca45}} \; = \;\; & \mathrm{max}(0, (3.183 \times 10^{-4} - 7.4008 \times 10^{-5} M_{\mathrm{CO}} + 1.1601 \times 10^{-5} M_{\mathrm{CO}} M_{\mathrm{CO}} - \\
& 4.6287 \times 10^{-7} M_{\mathrm{CO}}{}^3) Z^{1.585}) \quad\quad\quad\quad\quad\quad\quad\quad\quad\quad\quad\quad\quad\quad\quad\text{(B141)}
\end{aligned}
$$

$$
\begin{aligned}
X_{\mathrm{Ti45}} \; = \;\; & \mathrm{max}(0, 2.0955 \times 10^{-7} + (1 - 17.648 Z)(9.2611 \times 10^{-6} - 4.3083 \times 10^{-6} M_{\mathrm{CO}} + \\
& 6.8359 \times 10^{-7} M_{\mathrm{CO}}{}^2 - 4.3772 \times 10^{-8} M_{\mathrm{CO}}{}^3 + 9.3132 \times 10^{-10} M_{\mathrm{CO}}{}^4)) \quad\quad \text{(B142)}
\end{aligned}
$$

$$
\begin{aligned}
X_{\mathrm{Sc45}} \; = \;\; & \mathrm{max}(0, 8.475 \times 10^{-8} + Z(-4.1524 \times 10^{-5} + 1.43 \times 10^{-4} \times \\
& \exp(-0.50195(M_{\mathrm{CO}} - 6)^2) + 7.3904 \times 10^{-5} \exp(--0.30076(M_{\mathrm{CO}} - 13)^2) + \\
& 1.8636 \times 10^{-4}/M_{\mathrm{CO}})) \quad\quad\quad\quad\quad\quad\quad\quad\quad\quad\quad\quad\quad\quad\quad\quad\text{(B143)}
\end{aligned}
$$

$$
\begin{aligned}
X_{\mathrm{Ti46}} \; = \;\; & \mathrm{max}(0, 1.7881 \times 10^{-6} + Z(2.7772 \times 10^{-3} - 1.5644 \times 10^{-3} \mathrm{min}(M_{\mathrm{CO}}, 10) + \\
& 5.5381 \times 10^{-4} \mathrm{min}(M_{\mathrm{CO}}, 10)^2 - 8.9342 \times 10^{-5} \mathrm{min}(M_{\mathrm{CO}}, 10)^3 + \\
& 6.1318 \times 10^{-6} \mathrm{min}(M_{\mathrm{CO}}, 10)^4 - 1.4808 \times 10^{-7} \mathrm{min}(M_{\mathrm{CO}}, 10)^5)) \quad\quad\quad \text{(B144)}
\end{aligned}
$$

$$
\begin{aligned}
X_{\mathrm{Ca46}} \; = \;\; & \mathrm{max}(0, 2.794 \times 10^{-9} + 2.3051 \times 10^{-3} Z^2 (1 - 0.33082 M_{\mathrm{CO}} + 4.3534 \times 10^{-2} M_{\mathrm{CO}}^2 - \\
& 1.6247 \times 10^{-3} M_{\mathrm{CO}}^3)) \quad\quad\quad\quad\quad\quad\quad\quad\quad\quad\quad\quad\quad\quad\quad\quad\quad\text{(B145)}
\end{aligned}
$$

B Analytic Fits

$$
\begin{aligned}
X_{\text{Ti47}} \;=\; & \max(0,\, 1.0245 \times 10^{-8} + Z(-2.1705 \times 10^{-4} + 2.1569 \times 10^{-4} \times \\
& \exp(-0.48117(M_{\text{CO}} - 6)^2) + 2.5242 \times 10^{-4} \exp(-0.19382(M_{\text{CO}} - 13)^2) + \\
& 9.9758 \times 10^{-4}/M_{\text{CO}}))
\end{aligned}
\tag{B146}
$$

$$
\begin{aligned}
X_{\text{V47}} \;=\; & \max(0,\, (2.2165 \times 10^{-7} + \frac{1}{\log_{10} Z}(6.5267 \times 10^{-6} - 5.8208 \times 10^{-7} \\
& \exp(-0.70109(M_{\text{CO}} - 6)^2) - 5.0208 \times 10^{-6} \exp(-0.10639(M_{\text{CO}} - 13)^2) - \\
& 1.8238 \times 10^{-5}/M_{\text{CO}})))
\end{aligned}
\tag{B147}
$$

$$
X_{\text{Ca47}} = \max(0,\, 1.0002 \times 10^{-6} Z^1 M_{\text{CO}}^{-2.5})
\tag{B148}
$$

$$
X_{\text{Ca48}} = \max(0,\, 1.6886 \times 10^{-3} Z^2 + 7.282 \times 10^{-2} Z^2 M_{\text{CO}}^{-3.5235})
\tag{B149}
$$

$$
\begin{aligned}
X_{\text{Cr48}} \;=\; & \max(0,\, (0.32965 + ((1 - 2.6197 \times 10^{-4} Z))(-0.32994 + 9.8321 \times 10^{-5} \times \\
& \exp(-0.54506(M_{\text{CO}} - 6)^2) + 2.4945 \times 10^{-4} \exp(-0.15862(M_{\text{CO}} - 13)^2) + \\
& 1.152 \times 10^{-3}/M_{\text{CO}})))
\end{aligned}
\tag{B150}
$$

$$
\begin{aligned}
X_{\text{Ti48}} \;=\; & \max(0,\, (-5.5786 \times 10^{-7} + Z(-4.339 \times 10^{-3} - 8.9494 \times 10^{-4} \times \\
& \exp(--2.5976 \times 10^{-2}(M_{\text{CO}} - 6)^2) + 5.1282 \times 10^{-3} \times \\
& \exp(-7.065 \times 10^{-2}(M_{\text{CO}} - 13)^2) + 1.0106 \times 10^{-2}/M_{\text{CO}})))
\end{aligned}
\tag{B151}
$$

$$
\begin{aligned}
X_{\text{V48}} \;=\; & \max(0,\, 5.2061 \times 10^{-7} + \frac{1}{\log_{10} Z}(2.047 \times 10^{-6} - 1.7869 \times 10^{-5} \times \\
& \exp(-1.4953(M_{\text{CO}} - 6)^2) - 1.3599 \times 10^{-5} \exp(-0.52025(M_{\text{CO}} - 13)^2) - \\
& 8.5179 \times 10^{-6}/M_{\text{CO}}))
\end{aligned}
\tag{B152}
$$

$$
X_{\text{V49}} = \max(0,\, 4.6799 \times 10^{-6} M_{\text{CO}}^{-1.0229} + (2.7288 \times 10^{-7} - \log_{10} Z)\sin(0.87475 M_{\text{CO}} + 2.4944))
\tag{B153}
$$

$$X_{\text{Cr49}} = \max(0, 1.4156 \times 10^{-6} + \frac{1}{\log_{10} Z}(-4.0769 \times 10^{-5} + 1.4344 \times 10^{-5} M_{\text{CO}} - 1.7853 \times 10^{-6} M_{\text{CO}}{}^2 + 9.5926 \times 10^{-8} M_{\text{CO}}{}^3 - 1.8626 \times 10^{-9} M_{\text{CO}}{}^4)) \quad \text{(B154)}$$

$$X_{\text{Ti49}} = \max(0, -1.0058 \times 10^{-7} + 1.4146 \times 10^{-3} Z^{0.84649} M_{\text{CO}}{}^{-4.587} + 9.8378 \times 10^{-5} Z) \quad \text{(B155)}$$

$$X_{\text{Ti50}} = \max(0, (-1.4901 \times 10^{-7} + Z(-5.0397 \times 10^{-4} + 5.988 \times 10^{-5} \times \\ \exp(-0.18137(M_{\text{CO}} - 6)^2) + 6.3748 \times 10^{-4} \exp(-8.432 \times 10^{-2}(M_{\text{CO}} - 13)^2) + \\ 9.4991 \times 10^{-4}/M_{\text{CO}})) \quad \text{(B156)}$$

$$X_{\text{Cr50}} = \max(0, Z(8.6358 \times 10^{-3} - 2.7397 \times 10^{-3} M_{\text{CO}} + 7.3554 \times 10^{-4} M_{\text{CO}}^2 - 1.2169 \times 10^{-4} M_{\text{CO}}{}^3 + 9.045 \times 10^{-6} M_{\text{CO}}{}^4 - 2.3562 \times 10^{-7} M_{\text{CO}}{}^5)) \quad \text{(B157)}$$

$$X_{\text{V50}} = \max(0, 2.4748 \times 10^{-4} Z^{1.4761} \exp(-(M_{\text{CO}} - 4.9803)^2/0.16529) + 3.5334 \times 10^{-6} Z) \quad \text{(B158)}$$

$$X_{\text{Mn51}} = \max(0, 1.8999 \times 10^{-6} + \frac{1}{\log_{10} Z}(2.9597 \times 10^{-6} - 2.503 \times 10^{-5} M_{\text{CO}} + 6.7046 \times 10^{-6} M_{\text{CO}}{}^2 - 5.7463 \times 10^{-7} M_{\text{CO}}{}^3 + 1.5832 \times 10^{-8} M_{\text{CO}}{}^4)) \quad \text{(B159)}$$

$$X_{\text{V51}} = \max(0, 1.1101 \times 10^{-4} Z + 1.7499 Z^{2.5417} M_{\text{CO}}{}^{-3.6957}) \quad \text{(B160)}$$

$$X_{\text{Cr51}} = \max(0, (1.7146 \times 10^{-6} + 1.7017 \times 10^{-4} Z) \exp(-(M_{\text{CO}} - 4.4201)^2/23.081) + (4.0317 \times 10^{-6} - 8.0697 \times 10^{-5} Z) \exp(-(M_{\text{CO}} - 13.557)^2/0.19604)) \quad \text{(B161)}$$

$$X_{\text{Fe52}} = \max(0, 6.5481 \times 10^{-4} + ((1 - 26.113 Z))((3.85 \times 10^{-3} - 2.4642 \times 10^{-3} M_{\text{CO}} + \\ 7.9771 \times 10^{-4} M_{\text{CO}}{}^2 - 1.2733 \times 10^{-4} M_{\text{CO}}{}^3 + 8.9742 \times 10^{-6} M_{\text{CO}}{}^4 - \\ 2.2538 \times 10^{-7} M_{\text{CO}}{}^5))) \quad \text{(B162)}$$

B Analytic Fits

$$X_{\mathrm{Cr}52} = \max(0, (-3.8091 \times 10^{-7} + 3.9504 \times 10^{-3}Z + 3.296 \times 10^{-3}M_{\mathrm{CO}}{}^{-9.7837+3.0616\times10^2 Z}))$$
$$\text{(B163)}$$

$$X_{\mathrm{Mn}52} = \max(0, 8.1407 \times 10^{-5}(\sin(0.51574\max(M_{\mathrm{CO}}, 4.5) + 1.4096)^2 + 10^{-5})) \quad \text{(B164)}$$

$$\begin{aligned} X_{\mathrm{Cr}53} &= \max(0, -2.6263 \times 10^{-7} + 4.4046 \times 10^{-4}Z + 4.0249 \times 10^{-4} \times \\ & \quad M_{\mathrm{CO}}{}^{-11.49+3.8341\times10^2 Z}) \end{aligned} \quad \text{(B165)}$$

$$\begin{aligned} X_{\mathrm{Mn}53} &= \max(0, 5.0263 \times 10^{-6} + \frac{1}{\log_{10} Z}(-1.5165 \times 10^{-5} - 9.9844 \times 10^{-5}M_{\mathrm{CO}} + \\ & \quad 2.6331 \times 10^{-5}M_{\mathrm{CO}}{}^2 - 2.2817 \times 10^{-6}M_{\mathrm{CO}}{}^3 + 6.4261 \times 10^{-8}M_{\mathrm{CO}}{}^4)) \quad \text{(B166)} \end{aligned}$$

$$\begin{aligned} X_{\mathrm{Fe}53} &= \max(0, (5.5767 \times 10^{-5} + 1.0795 \times 10^{-3}Z)\exp(-(M_{\mathrm{CO}} - 1.9967)^2/11.602) + \\ & \quad (3.0128 \times 10^{-6} + 6.3525 \times 10^{-4}Z)\exp(-(M_{\mathrm{CO}} - 13.243)^2/0.38068)) \quad \text{(B167)} \end{aligned}$$

$$\begin{aligned} X_{\mathrm{Fe}54} &= \max(0, (4.1293 \times 10^{-3} + 0.59975Z)\exp(-(M_{\mathrm{CO}} + 4.7831)^2/70.719) + \\ & \quad (8.2181 \times 10^{-5} + 9.5626 \times 10^{-2}Z)\exp(-(M_{\mathrm{CO}} - 13.965)^2/2.1023) - \\ & \quad 1.3905 \times 10^{-6}M_{\mathrm{CO}}{}^{-2}/Z) \quad \text{(B168)} \end{aligned}$$

$$\begin{aligned} X_{\mathrm{Cr}54} &= \max(0, -3.6135 \times 10^{-7} + Z(2.067 \times 10^{-3} - 9.179 \times 10^{-4}M_{\mathrm{CO}} + \\ & \quad 1.6529 \times 10^{-4}M_{\mathrm{CO}}{}^2 - 1.1805 \times 10^{-5}M_{\mathrm{CO}}{}^3 + 2.8964 \times 10^{-7}M_{\mathrm{CO}}{}^4)) \quad \text{(B169)} \end{aligned}$$

$$\begin{aligned} X_{\mathrm{Mn}54} &= \max(0, (4.3586 \times 10^{-7} + 1.1709 \times 10^{-4}Z)\exp(-(M_{\mathrm{CO}} - 3.4779)^2/13.024) + \\ & \quad (5.5879 \times 10^{-8} + 3.654 \times 10^{-5}Z)\exp(-(M_{\mathrm{CO}} - 13.614)^2/0.8564)) \quad \text{(B170)} \end{aligned}$$

$$
\begin{aligned}
X_{\mathrm{Mn55}} \;=\; & \max(0, -6.482 \times 10^{-6} + Z(5.3055 \times 10^{-2}/M_{\mathrm{CO}} - 1.0986 \times 10^{-2} + \\
& 7.3427 \times 10^{-4} M_{\mathrm{CO}}))
\end{aligned} \tag{B171}
$$

$$
\begin{aligned}
X_{\mathrm{Fe55}} \;=\; & \max(0, (-1.171 \times 10^{-5} + 2.5273 \times 10^{-3} Z)\sin(0.34111 M_{\mathrm{CO}})^2 + \\
& 1.1096 \times 10^{-4}/M_{\mathrm{CO}})
\end{aligned} \tag{B172}
$$

$$
\begin{aligned}
X_{\mathrm{Co55}} \;=\; & \max(0, -3.7361 \times 10^{-4} + 1.7239 \times 10^{-3} M_{\mathrm{CO}}{}^{-0.68637 + 9.0351 Z} + \\
& 1.6495 \times 10^{-4} \exp(-(M_{\mathrm{CO}} - 13)^2/2))
\end{aligned} \tag{B173}
$$

$$
\begin{aligned}
X_{\mathrm{Co56}} \;=\; & \max(0, 9.4078 \times 10^{-3} \exp(-(M_{\mathrm{CO}} + 4.3821)^2/14.174) + 9.6675 \times 10^{-4} \times \\
& \exp(-(M_{\mathrm{CO}} - 6.2599)^2/1.0877) + (6.6154 \times 10^{-4} + 9.6361 \times 10^{-2} Z) \times \\
& \exp(-(M_{\mathrm{CO}} - 13.278)^2/0.52483))
\end{aligned} \tag{B174}
$$

$$
\begin{aligned}
X_{\mathrm{Fe56}} \;=\; & \max(0, 5.8588 \times 10^{-2} + (1 - 19.256 Z) \times (1.3941 - 0.9707 M_{\mathrm{CO}} + 0.2534 M_{\mathrm{CO}}{}^2 - \\
& 3.1295 \times 10^{-2} M_{\mathrm{CO}}{}^3 + 1.8128 \times 10^{-3} M_{\mathrm{CO}}{}^4 - 3.9517 \times 10^{-5} M_{\mathrm{CO}}{}^5))
\end{aligned} \tag{B175}
$$

$$
X_{\mathrm{Ni56}} = 0 \tag{B176}
$$

$$
X_{\mathrm{Fe57}} = \max(0, (-9.519 \times 10^{-6} + Z(0.11965/M_{\mathrm{CO}} - 2.1258 \times 10^{-2} + 1.6133 \times 10^{-3} M_{\mathrm{CO}})) \tag{B177}
$$

$$
\begin{aligned}
X_{\mathrm{Ni57}} \;=\; & \max(0, 0.3152 + (1 - 6.4787 \times 10^{-2} Z)(-0.34595 + 2.6003 \times 10^{-3} \times \\
& \exp(-0.58657(M_{\mathrm{CO}} - 6)^2) + 2.7454 \times 10^{-2} \exp(-8.6268 \times 10^{-2}(M_{\mathrm{CO}} - 13)^2) + \\
& 6.1326 \times 10^{-2}/M_{\mathrm{CO}}))
\end{aligned} \tag{B178}
$$

B Analytic Fits

$$
\begin{aligned}
X_{\text{Co57}} &= \max(0, 8.6579 \times 10^{-3} \exp(-M_{\text{CO}} + 1.3351^2/2.3631) + 1.1253 \times 10^{-4} \times \\
&\quad \exp(-M_{\text{CO}} - 6.1126^2/0.89975) + (4.1985 \times 10^{-5} + 1.7376 \times 10^{-2}Z) \times \\
&\quad \exp(-M_{\text{CO}} - 13.102^2/1.0372))
\end{aligned}
\tag{B179}
$$

$$
X_{\text{Co58}} = \max(0, 4.936 \times 10^{-7} + 1.2275 \times 10^{-3} Z^{0.18099} M_{\text{CO}}{}^{-5.6769})
\tag{B180}
$$

$$
\begin{aligned}
X_{\text{Fe58}} &= \max(0, -7.0939 \times 10^{-6} + Z(7.1429 \times 10^{-3} + 1.5213 \times 10^{-3} \times \\
&\quad \exp(-0.20179(M_{\text{CO}} - 13)^2) + 1.4908 \times 10^{-2}/M_{\text{CO}}))
\end{aligned}
\tag{B181}
$$

$$
X_{\text{Ni58}} = \max(0, 6.2091 \times 10^{-4} + (0.36944 + 20.281Z)/M_{\text{CO}}{}^{5.2934})
\tag{B182}
$$

$$
\begin{aligned}
X_{\text{Ni59}} &= \max(0, 0.32885 + (1 - 1.5171 \times 10^{-2}Z)(-0.33067 + 2.4491 \times 10^{-4} \times \\
&\quad \exp(--0.48058(M_{\text{CO}} - 6)^2) + 1.5852 \times 10^{-3} \exp(-0.10387(M_{\text{CO}} - 13)^2) \\
&\quad +3.9969 \times 10^{-3}/M_{\text{CO}}))
\end{aligned}
\tag{B183}
$$

$$
\begin{aligned}
X_{\text{Cu59}} &= \max(0, 6.3134 \times 10^{-6} + ((1/\log_{10} Z))(1.8652 \times 10^{-4} - \\
&\quad 2.0008 \times 10^{-5} \exp(-0.48434(M_{\text{CO}} - 6)^2) - 1.4974 \times 10^{-4} \times \\
&\quad \exp(-0.11287(M_{\text{CO}} - 13)^2) - 4.4787 \times 10^{-4}/M_{\text{CO}}))
\end{aligned}
\tag{B184}
$$

$$
\begin{aligned}
X_{\text{Fe59}} &= \max(0, -8.6986 \times 10^{-7} + Z((5.8629 \times 10^{-3} - 1.3175 \times 10^{-3}M_{\text{CO}} + \\
&\quad 1.0159 \times 10^{-4}M_{\text{CO}}{}^2 - 2.5118 \times 10^{-6}M_{\text{CO}}{}^3)))
\end{aligned}
\tag{B185}
$$

$$
\begin{aligned}
X_{\text{Co59}} &= \max(0, -2.9448 \times 10^{-6} + Z(-2.5593 \times 10^{-3} + 4.5253 \times 10^{-4} \times \\
&\quad \exp(-0.24621(M_{\text{CO}} - 6)^2) + 4.9644 \times 10^{-3} \exp(-9.5259 \times 10^{-2}(M_{\text{CO}} - 13)^2) + \\
&\quad 1.4861 \times 10^{-2}/M_{\text{CO}}))
\end{aligned}
\tag{B186}
$$

286

$$\begin{aligned}
X_{\mathrm{Zn60}} \;=\; &\max(0, 1.5225 \times 10^{-4} + \log_{10} Z(6.6008 \times 10^{-4} - 3.0585 \times 10^{-5} \\
&\exp(--4.187(M_{\mathrm{CO}} - 6)^2) - 5.118 \times 10^{-4} \exp(-9.7036 \times 10^{-2}(M_{\mathrm{CO}} - 13)^2) - \\
&1.601 \times 10^{-3}/M_{\mathrm{CO}})))
\end{aligned} \tag{B187}$$

$$X_{\mathrm{Co60}} = \max(0, 4.6252 \times 10^{-3} Z^{1.5}) \tag{B188}$$

$$\begin{aligned}
X_{\mathrm{Fe60}} \;=\; &\max(0, -7.851 \times 10^{-7} + Z(9.8426 \times 10^{-3}/M_{\mathrm{CO}} - 1.4094 \times 10^{-3} + \\
&5.7954 \times 10^{-5} M_{\mathrm{CO}})
\end{aligned} \tag{B189}$$

$$\begin{aligned}
X_{\mathrm{Cu60}} \;=\; &\max(0, -3.9837 \times 10^{-5} + ((1 - 8.9127Z))((3.1126 \times 10^{-2} - 2.0375 \times 10^{-2} M_{\mathrm{CO}} + \\
&5.0437 \times 10^{-3} M_{\mathrm{CO}}{}^2 - 5.856 \times 10^{-4} M_{\mathrm{CO}}{}^3 + 3.1933 \times 10^{-5} M_{\mathrm{CO}}{}^4 - \\
&6.5845 \times 10^{-7} M_{\mathrm{CO}}{}^5)))
\end{aligned} \tag{B190}$$

$$\begin{aligned}
X_{\mathrm{Ni60}} \;=\; &\max(0, (-3.3104 \times 10^{-3} + 2.6334 \times 10^{-2} Z + 8.4455 \times 10^{-3}/M_{\mathrm{CO}}) + \\
&(2.3476 \times 10^{-3} - 3.4932 \times 10^{-2} Z) \exp(-(M_{\mathrm{CO}} - 6)^2/5.7333) + (3.265 \times 10^{-3} + \\
&2.838 \times 10^{-2} Z) \exp(-(M_{\mathrm{CO}} - 13)^2/22.522))
\end{aligned} \tag{B191}$$

$$\begin{aligned}
X_{\mathrm{Cu61}} \;=\; &\max(0, 2.4884 \times 10^{-4} + (1 + 1.4075Z)(2.7586 \times 10^{-3} - 2.1834 \times 10^{-3} M_{\mathrm{CO}} + \\
&5.9052 \times 10^{-4} M_{\mathrm{CO}}{}^2 - 7.3633 \times 10^{-5} M_{\mathrm{CO}}{}^3 + 4.2431 \times 10^{-6} M_{\mathrm{CO}}{}^4 - \\
&9.127 \times 10^{-8} M_{\mathrm{CO}}{}^5))
\end{aligned} \tag{B192}$$

$$\begin{aligned}
X_{\mathrm{Ni61}} \;=\; &\max(0, 0.33021 + (1 - 8.3345 \times 10^{-3} Z)(-0.33022 + (1.184 \times 10^{-5} + \\
&0.5 \times 10^{-8}/Z) \exp(-0.33469(M_{\mathrm{CO}} - 6)^2 + 3.4356 \times 10^{-5} \times \\
&(1 + Z/0.02) \exp(-0.59448(M_{\mathrm{CO}} - 13)^2)))
\end{aligned} \tag{B193}$$

B Analytic Fits

$$\begin{aligned} X_{\text{Co61}} \;=\;\; & \max(0, -6.0908 \times 10^{-7} + Z((4.5014 \times 10^{-3} - 1.7287 \times 10^{-3} M_{\text{CO}} + \\ & 2.3732 \times 10^{-4} M_{\text{CO}}{}^2 - 1.3014 \times 10^{-5} M_{\text{CO}}{}^3 + \\ & 2.4308 \times 10^{-7} M_{\text{CO}}{}^4))) \end{aligned} \tag{B194}$$

$$\begin{aligned} X_{\text{Zn61}} \;=\;\; & \max(0, 7.3435 \times 10^{-6} + \log_{10} Z(3.7124 \times 10^{-5} - 2.441 \times 10^{-6} \times \\ & \exp(-0.44437(M_{\text{CO}} - 6)^2) - 3.0977 \times 10^{-5} \exp(-8.1119 \times 10^{-2}(M_{\text{CO}} - 13)^2) - \\ & 6.0245 \times 10^{-5}/M_{\text{CO}})) \end{aligned} \tag{B195}$$

$$\begin{aligned} X_{\text{Cu62}} \;=\;\; & \max(0, -3.3509 \times 10^{-6} + \frac{1}{\log_{10} Z}(1.9745 \times 10^{-4} - \\ & 3.2678 \times 10^{-5} \exp(-0.42344(M_{\text{CO}} - 6)^2) - 1.8603 \times 10^{-4} \times \\ & \exp(-0.10484(M_{\text{CO}} - 13)^2) - 4.2485 \times 10^{-4}/M_{\text{CO}})) \end{aligned} \tag{B196}$$

$$\begin{aligned} X_{\text{Zn62}} \;=\;\; & \max(0, 7.2528 \times 10^{-5} + (1 + 88.911Z)((1.2906 \times 10^{-2} - 9.7666 \times 10^{-3} M_{\text{CO}} + \\ & 2.6775 \times 10^{-3} M_{\text{CO}}{}^2 - 3.3416 \times 10^{-4} M_{\text{CO}}{}^3 + 1.9155 \times 10^{-5} M_{\text{CO}}{}^4 - \\ & 4.0885 \times 10^{-7} M_{\text{CO}}{}^5))) \end{aligned} \tag{B197}$$

$$\begin{aligned} X_{\text{Ni62}} \;=\;\; & \max(0, -1.1763 \times 10^{-6} + Z(-7.3365 \times 10^{-3} + 1.5037 \times 10^{-2} \times \\ & \exp(-0.33164(M_{\text{CO}} - 6)^2) + 2.6194 \times 10^{-2} \exp(-0.29156(M_{\text{CO}} - 13)^2) + \\ & 2.6171 \times 10^{-2}/M_{\text{CO}})) \end{aligned} \tag{B198}$$

$$X_{\text{Ni63}} = \max(0, 4.4969 \times 10^{-2} Z^{1.7314}) \tag{B199}$$

$$X_{\text{Zn63}} = \max(0, 5.7624 \times 10^{-4} M_{\text{CO}}{}^{-4.5673} Z^{3.8754 \times 10^{-2}}) \tag{B200}$$

$$\begin{aligned} X_{\text{Cu63}} \;=\; & \max(0, 7.0129 \times 10^{-7} + Z(-2.0903 \times 10^{-3} + 6.2356 \times 10^{-4} \times \\ & \exp(-0.41043(M_{\text{CO}} - 6)^2) + 2.454 \times 10^{-3}\exp(-9.7155 \times 10^{-2}(M_{\text{CO}} - 13)^2) + \\ & 4.5247 \times 10^{-3}/M_{\text{CO}})) \end{aligned}$$

(B201)

$$X_{\text{Zn64}} = \max(0, 2.5732 \times 10^{-6} + 9.8341 \times 10^{-5} Z^{-0.38212} M_{\text{CO}}{}^{-3.6853} + 7.2031 \times 10^{-4} Z)$$ (B202)

$$X_{\text{Ga64}} = \max(0, 1.0581 \times 10^{-5} Z^{-0.46221} M_{\text{CO}}{}^{-3.3291})$$

(B203)

$$\begin{aligned} X_{\text{Cu64}} \;=\; & \max(0, -2.0489 \times 10^{-8} + Z(3.7803 \times 10^{-5} + 7.0552 \times 10^{-5} \times \\ & \exp(-0.30149(M_{\text{CO}} - 6)^2) + 5.3909 \times 10^{-5}\exp(-0.67062(M_{\text{CO}} - 13)^2) + \\ & 6.3572 \times 10^{-6}/M_{\text{CO}})) \end{aligned}$$

(B204)

$$\begin{aligned} X_{\text{Ni64}} \;=\; & \max(0, 2.3888 \times 10^{-3} Z^{1.3959}(15.17 - 3.3035 M_{\text{CO}} + 0.82123 M_{\text{CO}}^2 \\ & -3.8254 \times 10^{-2} M_{\text{CO}}^3)) \end{aligned}$$

(B205)

$$X_{\text{Ge64}} = \max(0, 7.7393 \times 10^{-7} Z^{-0.39108} M_{\text{CO}}{}^{-3.2087})$$

(B206)

$$\begin{aligned} X_{\text{Ni65}} \;=\; & \max(0, -3.9302 \times 10^{-7} + Z((5.5209 \times 10^{-3} - 3.5727 \times 10^{-3} M_{\text{CO}} + \\ & 9.3786 \times 10^{-4} M_{\text{CO}}{}^2 - 1.1642 \times 10^{-4} M_{\text{CO}}{}^3 + 6.7139 \times 10^{-6} M_{\text{CO}}{}^4 - \\ & 1.4435 \times 10^{-7} M_{\text{CO}}{}^5))) \end{aligned}$$

(B207)

$$X_{\text{Ge65}} = \max(0, 2.794 \times 10^{-8} Z^{-0.29218} M_{\text{CO}}{}^{-5.3194})$$

(B208)

$$X_{\text{Zn65}} = \max(0, 1.374 \times 10^{-5} Z^{0.52602})$$

(B209)

B Analytic Fits

$$X_{\text{Cu65}} = \max(0, -9.2108 \times 10^{-7} + Z(2.2031 \times 10^{-4} + 7.7515 \times 10^{-4} \times$$
$$\exp(-0.22287(M_{\text{CO}} - 6)^2) + 1.7971 \times 10^{-3} \exp(-0.10853(M_{\text{CO}} - 13)^2) +$$
$$6.0481 \times 10^{-4}/M_{\text{CO}})) \tag{B210}$$

$$X_{\text{Ga65}} = \max(0, 2.6841 \times 10^{-5} Z^{-2.2215 \times 10^{-2}} M_{\text{CO}}^{-4.3977}) \tag{B211}$$

$$X_{\text{Ga66}} = \max(0, 1.4629 \times 10^{-4} Z^{0.1421} M_{\text{CO}}^{-5.1875} + 2.183 \times 10^{-6} \times$$
$$\exp(-(M_{\text{CO}} - 5.8965)^2/0.57897) + 4.3048 \times 10^{-4} Z \times$$
$$\exp(-(M_{\text{CO}} - 13.348)^2/0.68231)) \tag{B212}$$

$$X_{\text{Cu66}} = \max(0, -3.0734 \times 10^{-8} + Z(5.6063 \times 10^{-5} + 1.491 \times 10^{-5} M_{\text{CO}} -$$
$$5.4799 \times 10^{-6} M_{\text{CO}}^2 + 4.8149 \times 10^{-7} M_{\text{CO}}^3 - 1.3039 \times 10^{-8} M_{\text{CO}}^4) \tag{B213}$$

$$X_{\text{Ge66}} = \max(0, 3.0963 \times 10^{-3} Z^{0.13255} M_{\text{CO}}^{-4.8438}) \tag{B214}$$

$$X_{\text{Zn66}} = \max(0, -9.5926 \times 10^{-7} + Z(3.6081 \times 10^{-4} + 2.6664 \times 10^{-3}$$
$$\exp(-0.38998(M_{\text{CO}} - 6)^2) + 3.1659 \times 10^{-3} \exp(-0.16104(M_{\text{CO}} - 13)^2) +$$
$$2.2357 \times 10^{-3}/M_{\text{CO}}))) \tag{B215}$$

$$X_{\text{Ga67}} = \max(0, 1.2107 \times 10^{-8} + Z(-9.4119 \times 10^{-6} + 7.2764 \times 10^{-6} \times$$
$$\exp(-0.35611(M_{\text{CO}} - 6)^2) + 1.1531 \times 10^{-5} \exp(-0.18887(M_{\text{CO}} - 13)^2) +$$
$$2.2628 \times 10^{-5}/M_{\text{CO}})) \tag{B216}$$

$$X_{\text{Zn67}} = \max(0, (-3.39 \times 10^{-7} + Z((2.6072 \times 10^{-4} - 1.7072 \times 10^{-5} M_{\text{CO}} +$$
$$2.0857 \times 10^{-5} M_{\text{CO}}^2 - 1.0673 \times 10^{-6} M_{\text{CO}}^3)))) \tag{B217}$$

$$X_{\text{Ge67}} = \max(0, 10^{-8} \times 6.5193 \times 10^{-9} Z^{-2.6111} M_{\text{CO}}{}^{-2.8434}) \tag{B218}$$

$$
\begin{aligned}
X_{\text{Ga68}} \;=\;& \max(0, 10^{-8}(-1.5873 \times 10^{-3} + 8.4323 Z^{0.79001}) \times \\
& (-1.5288 + 4.0354 M_{\text{CO}} - 0.22847 M_{\text{CO}}^2))
\end{aligned}
\tag{B219}
$$

$$X_{\text{Ge68}} = \max(0, 1.2595 \times 10^{-5} Z^{0.18288} M_{\text{CO}}{}^{-6.0096}) \tag{B220}$$

$$
\begin{aligned}
X_{\text{Zn68}} \;=\;& \max(0, -3.6098 \times 10^{-6} + Z((2.9337 \times 10^{-3} - 9.8971 \times 10^{-4} M_{\text{CO}} + \\
& 2.3653 \times 10^{-4} M_{\text{CO}}{}^2 + 2.5966 \times 10^{-5} M_{\text{CO}}{}^3 - 4.4061 \times 10^{-6} M_{\text{CO}}{}^4 + \\
& 1.3504 \times 10^{-7} M_{\text{CO}}{}^5)))
\end{aligned}
\tag{B221}
$$

$$
\begin{aligned}
X_{\text{Ga69}} \;=\;& \max(0, -2.0396 \times 10^{-7} + Z(6.2491 \times 10^{-4} - 5.0702 \times 10^{-4} M_{\text{CO}} + \\
& 2.2036 \times 10^{-4} M_{\text{CO}}{}^2 - 3.2652 \times 10^{-5} M_{\text{CO}}{}^3 + 2.02 \times 10^{-6} M_{\text{CO}}{}^4 - \\
& 4.4703 \times 10^{-8} M_{\text{CO}}{}^5))
\end{aligned}
\tag{B222}
$$

$$
\begin{aligned}
X_{\text{Ge69}} \;=\;& \max(0, 9.3132 \times 10^{-10} + Z(-5.5041 \times 10^{-7} + 9.0543 \times 10^{-6} \times \\
& \exp(-0.48928(M_{\text{CO}} - 6)^2) + 4.1453 \times 10^{-6} \exp(-0.3509(M_{\text{CO}} - 13)^2) + \\
& 2.0796 \times 10^{-6}/M_{\text{CO}}))
\end{aligned}
\tag{B223}
$$

$$X_{\text{Zn69}} = \max(0, 0.10419 Z^{2.2754} M_{\text{CO}}{}^{-0.81877}) \tag{B224}$$

$$
\begin{aligned}
X_{\text{Ge70}} \;=\;& \max(0, (-3.4925 \times 10^{-7} + Z(3.9595 \times 10^{-4} + 2.4171 \times 10^{-3} \\
& \exp(-0.52855(M_{\text{CO}} - 6)^2) + 1.7799 \times 10^{-3} \exp(-0.2796(M_{\text{CO}} - 13)^2) - \\
& 6.8349 \times 10^{-5}/M_{\text{CO}}))
\end{aligned}
\tag{B225}
$$

$$X_{\text{Ga70}} = \max(0, 8.6158 \times 10^{-4} Z^{1.5999}) \tag{B226}$$

$$X_{\text{Ge71}} = \max(0, 4.6168 \times 10^{-2} Z^{1.3819} \exp(-(M_{\text{CO}} - 11.468)^2/31.855)) \qquad \text{(B227)}$$

B9 Belczynski et al. (2002) BH Mass Prescription

The Belczynski et al. (2002) BH mass is coded according to a prescription provided by Jarrod Hurley.

First, M_{cx} is set

$$M_{cx} = \begin{cases} 0.161767 M_c + 1.067055 & M_c < 2.5\,\mathrm{M_\odot} \\ 0.314154 M_c + 0.686088 & M_c \geq 2.5\,\mathrm{M_\odot} \end{cases} \tag{B228}$$

then the remnant mass is given by

$$M_{\mathrm{NS/BH}} = \begin{cases} M_{cx} & M_c < 5\,\mathrm{M_\odot} \\ M_{cx} + (M_c - 5)(M - M_{cx}) & 5 \leq M_c/\mathrm{M_\odot} < 7.6 \\ M & M \geq 7.6\,\mathrm{M_\odot} \end{cases} \quad . \tag{B229}$$

B10 Trace Isotopes

In order to increase the speed of the code some rare isotopes are considered to behave as their more abundant cousins with the same proton number. This is dealt with easily in the code at compile time and is treated in a way that can easily be extended to include these trace elements for particular studies at a later date. There is also a high speed option in the code to bin all the trace isotopes into one isotope and quietly ignore it. Table B19 shows the conversions.

Isotope(s)	Treated as	Isotope(s)	Treated as
^{11}C,^{14}C	^{13}C	^{51}Mn,^{53}Mn,^{54}Mn	^{55}Mn
^{24}Na	^{23}Na	^{53}Fe,^{55}Fe,^{59}Fe	^{56}Fe
^{28}Al	^{27}Al	^{57}Ni	^{56}Ni
^{35}S	^{32}S	^{55}Co,^{58}Co,^{60}Co	^{59}Co
^{36}Cl	^{35}Cl	^{63}Ni,^{65}Ni	^{64}Ni
^{37}Ar	^{38}Ar	^{60}Zn,^{61}Zn, ^{62}Zn^{63}Zn,^{65}Zn	^{64}Zn
^{41}Ca,^{45}Ca,^{47}Ca	^{44}Ca	^{60}Cu,^{62}Cu,^{64}Cu,^{66}Cu	^{65}Cu
^{45}Ti	^{44}Ti	^{69}Zn	^{68}Zn
^{43}Sc	^{45}Sc	^{65}Ga, ^{66}Ga,^{67}Ga,^{68}Ga,^{70}Ga	^{69}Ga
^{49}Cr,^{51}Cr	^{48}Cr	^{64}Ge,^{65}Ge, ^{66}Ge,^{67}Ge, ^{68}Ge, ^{69}Ge,^{71}Ge	^{70}Ge
^{48}V,^{49}V	^{51}V		

Table B19: Trace isotopes.

Isotope	a	b	c	d
^{4}He	1.885×10^{-2}	1.919×10^{-1}	-1.90040×10^{-1}	7.398×10^{-1}
^{12}C	3.2448×10^{-1}	-7.5668×10^{-1}	4.4693×10^{-1}	-2.5692
^{16}O	7.9324×10^{-1}	-1.4184	6.7159×10^{-1}	-2.2394
^{20}Ne	5.6865×10^{-2}	-1.1574×10^{-1}	6.0577×10^{-2}	-2.4772
^{24}Mg	6.8268×10^{-2}	-1.8269×10^{-2}	-5.339×10^{-2}	-1.9527
^{28}Si	1.9537×10^{-2}	4.9225×10^{-1}	-4.2238×10^{-1}	-1.229
^{32}S	3.3483×10^{-1}	-7.4649×10^{-1}	5.2431×10^{-1}	-1.0288
^{36}Ar	1.553×10^{-1}	-4.2591×10^{-1}	3.0771×10^{-1}	5.0104×10^{-1}
^{40}Ca	4.7899×10^{-2}	-1.3997×10^{-1}	1.0286×10^{-1}	3.8396×10^{1}
^{44}Ti	1.5964×10^{-1}	-3.9855×10^{-1}	2.5757×10^{-1}	-2.4052
^{48}Cr	1.2483×10^{-1}	-3.1778×10^{-1}	2.0946×10^{-1}	-2.2352
^{52}Fe	3.5674×10^{-1}	-9.9596×10^{-1}	7.0243×10^{-1}	-2.2407×10^{-1}
^{56}Fe	-7.9924×10^{-1}	2.2283	-1.2529	1.3922×10^{1}

Table B20: Coefficients to the fits to the SNIa yields of Livne & Arnett (1995).

Isotope	Yield	Isotope	Yield
^{4}He	0.17	^{36}Ar	6.6×10^{-4}
^{12}C	1.3×10^{-3}	^{40}Ca	3.9×10^{-4}
^{16}O	1.5×10^{-6}	^{44}Ti	8.9×10^{-3}
^{20}Ne	2.3×10^{-6}	^{48}Cr	9.4×10^{-3}
^{24}Mg	6.4×10^{-6}	^{52}Fe	1.8×10^{-2}
^{28}Si	7.3×10^{-5}	^{56}Ni	0.45
^{32}S	3.0×10^{-4}		

Table B21: Yields from an exploding $0.664\,\mathrm{M_\odot}$ WD as calculated by Woosley et al. (1986).

B11 Binary Star Explosions - SNeIa and Novae

The coefficients for the fits to the alpha elements from Livne & Arnett (1995) are in table B20. The yields of Woosley et al. (1986) and Iwamoto et al. (1999) are shown in tables B21 and B22 respectively.

Mass fractions in ejecta fitted to the nova models of José & Hernanz (1998) for accretion on to COWDs are

Isotope	Yield	...								
^{12}C	8.99×10^{-3}	^{25}Mg	2.66×10^{-5}	^{36}Ar	2.41×10^{-2}	^{48}Ti	6.11×10^{-4}	^{58}Fe	3.23×10^{-3}
^{13}C	3.30×10^{-7}	^{26}Mg	2.59×10^{-5}	^{38}Ar	9.90×10^{-4}	^{49}Ti	4.39×10^{-5}	^{59}Co	6.25×10^{-4}
^{14}N	2.69×10^{-4}	^{27}Al	2.47×10^{-4}	^{40}Ar	5.19×10^{-9}	^{50}Ti	3.51×10^{-4}	^{58}Ni	4.29×10^{-2}
^{15}N	5.32×10^{-7}	^{28}Si	2.06×10^{-1}	^{39}K	5.67×10^{-5}	^{50}V	9.33×10^{-9}	^{60}Ni	1.15×10^{-2}
^{16}O	6.58×10^{-2}	^{29}Si	3.40×10^{-4}	^{41}K	4.52×10^{-6}	^{51}V	1.16×10^{-4}	^{61}Ni	3.58×10^{-4}
^{17}O	4.58×10^{-6}	^{30}Si	6.41×10^{-4}	^{40}Ca	2.43×10^{-2}	^{50}Cr	3.53×10^{-4}	^{62}Ni	3.69×10^{-3}
^{18}O	6.35×10^{-7}	^{31}P	1.60×10^{-4}	^{43}Ca	2.22×10^{-7}	^{52}Cr	1.37×10^{-2}	^{64}Ni	2.31×10^{-4}
^{19}F	4.50×10^{-10}	^{32}S	1.22×10^{-1}	^{44}Ca	2.95×10^{-5}	^{53}Cr	1.38×10^{-3}	^{63}Cu	4.88×10^{-6}
^{20}Ne	6.22×10^{-4}	^{33}S	1.92×10^{-4}	^{46}Ca	4.73×10^{-9}	^{54}Cr	1.60×10^{-3}	^{65}Cu	2.04×10^{-6}
^{21}Ne	1.39×10^{-6}	^{34}S	2.04×10^{-3}	^{48}Ca	1.64×10^{-6}	^{55}Mn	7.05×10^{-3}	^{64}Zn	3.10×10^{-5}
^{22}Ne	4.21×10^{-4}	^{36}S	1.31×10^{-7}	^{45}Sc	2.09×10^{-7}	^{54}Fe	5.91×10^{-2}	^{66}Zn	6.42×10^{-5}
^{23}Na	2.61×10^{-5}	^{35}Cl	7.07×10^{-5}	^{46}Ti	1.12×10^{-5}	^{56}Fe	7.13×10^{-1}	^{67}Zn	6.55×10^{-7}
^{24}Mg	4.47×10^{-3}	^{37}Cl	2.26×10^{-5}	^{47}Ti	1.56×10^{-6}	^{57}Fe	1.67×10^{-2}	^{68}Zn	8.81×10^{-8}

Table B22: M_{Ch} SNIa yields of Iwamoto et al. (1999)'s DD2 model.

$$^{1}\mathrm{H} = 10^{-5} \times \max(0.0, ((-7.0188 \times 10^{+2}) \times f_{\mathrm{nov}} + (-1.0192 \times 10^{+4}) \times M_{\mathrm{WD}} + (7.6612 \times 10^{+4})))$$
(B230)

$$^{3}\mathrm{He} = 10^{-5} \times \max(0.0, ((4.0714 \times 10^{-3}) \times f_{\mathrm{nov}} + (-1.66430) \times M_{\mathrm{WD}} + (2.00320)))$$ (B231)

$$^{4}\mathrm{He} = 10^{-5} \times \max(0.0, ((-3.1323 \times 10^{+2}) \times f_{\mathrm{nov}} + (8.8501 \times 10^{+3}) \times M_{\mathrm{WD}} + (2.2102 \times 10^{+4})))$$
(B232)

$$^{7}\mathrm{Be} = 10^{-5} \times \max(0.0, ((1.52750) \times M_{\mathrm{WD}} + (-1.16350)))$$
(B233)

$$^{11}\mathrm{B} = 10^{-5} \times \max(0.0, ((-3.1665 \times 10^{-8}) \times f_{\mathrm{nov}} + (6.4289 \times 10^{-6}) \times M_{\mathrm{WD}} + (-4.0634 \times 10^{-6})))$$
(B234)

$$^{12}\mathrm{C} = 10^{-5} \times \max(0.0, ((9.0502 \times 10^{+1}) \times f_{\mathrm{nov}} + (1.0682 \times 10^{+3}) \times M_{\mathrm{WD}} + (-1.0916 \times 10^{+3})))$$
(B235)

$$^{13}\mathrm{C} = 10^{-5} \times \max(0.0, ((-2.6658 \times 10^{+1}) \times M_{\mathrm{WD}} + (3.3122 \times 10^{+2})) \times (f_{\mathrm{nov}} + (-1.2685 \times 10^{+1})))$$
(B236)

$$^{14}\mathrm{N} = 10^{-5} \times \max(0.0, ((1.2205 \times 10^{+2}) \times f_{\mathrm{nov}} + (-3.0464 \times 10^{+3}) \times M_{\mathrm{WD}} + (8.0772 \times 10^{+3})))$$
(B237)

$$^{15}\text{N} = 10^{-5} \times \max(0.0, ((8.5541 \times 10^{+3}) \times M_{\text{WD}} + (-6.9567 \times 10^{+3}))) \tag{B238}$$

$$^{16}\text{O} = 10^{-5} \times \max(0.0, ((5.05 \times 10^{+2}) \times f_{\text{nov}} + (-1.1864 \times 10^{+4}) \times M_{\text{WD}} + (9.751 \times 10^{+3})))$$
$$\tag{B239}$$

$$^{17}\text{O} = 10^{-5} \times \max(0.0, ((3.1153 \times 10^{+1}) \times M_{\text{WD}} + (-2.2047 \times 10^{+1})) \times (f_{\text{nov}} + (7.1595 \times 10^{+1})))$$
$$\tag{B240}$$

$$^{18}\text{O} = 10^{-5} \times \max(0.0, ((-1.42700) \times f_{\text{nov}} + (9.8591 \times 10^{+2}) \times M_{\text{WD}} + (-6.7039 \times 10^{+2})))$$
$$\tag{B241}$$

$$^{19}\text{F} = 10^{-5} \times \max(0.0, ((8.7752 \times 10^{-4}) \times M_{\text{WD}} + (-6.6271 \times 10^{-4})) \times (f_{\text{nov}} + (8.7528 \times 10^{+2})))$$
$$\tag{B242}$$

$$^{20}\text{Ne} = 10^{-5} \times \max(0.0, ((-1.72370) \times f_{\text{nov}} + (4.8452 \times 10^{+1}) \times M_{\text{WD}} + (1.2615 \times 10^{+2})))$$
$$\tag{B243}$$

$$^{21}\text{Ne} = 10^{-5} \times \max(0.0, ((-1.8884 \times 10^{-4}) \times f_{\text{nov}} + (3.8205 \times 10^{-2}) \times M_{\text{WD}} + (-2.0585 \times 10^{-2})))$$
$$\tag{B244}$$

$$^{22}\text{Na} = 10^{-5} \times \max(0.0, ((-4.9237 \times 10^{-4}) \times f_{\text{nov}} + (1.0045 \times 10^{-3}) \times M_{\text{WD}} + (4.7887 \times 10^{-2})))$$
$$\tag{B245}$$

$$^{22}\text{Ne} = 10^{-5} \times \max(0.0, ((1.011 \times 10^{+1}) \times f_{\text{nov}} + (-8.5547 \times 10^{+1}) \times M_{\text{WD}} + (7.1204 \times 10^{+1})))$$
$$\tag{B246}$$

$$^{23}\text{Na} = 10^{-5} \times \max(0.0, ((-2.6158 \times 10^{-2}) \times M_{\text{WD}} + (4.0585 \times 10^{-2})) \times (f_{\text{nov}} + (1.5067 \times 10^{+2})))$$
$$\tag{B247}$$

$$^{24}\text{Mg} = 10^{-5} \times \max(0.0, ((9.0846 \times 10^{-3}) \times f_{\text{nov}} + (-1.4289 \times 10^{+1}) \times M_{\text{WD}} + (1.6798 \times 10^{+1})))$$
$$\tag{B248}$$

$$^{25}\text{Mg} = 10^{-5} \times \max(0.0, ((-5.0879 \times 10^{+1}) \times M_{\text{WD}} + (7.297 \times 10^{+1}))) \tag{B249}$$

$$^{26}\text{Al} = 10^{-5} \times \max(0.0, ((-2.6911 \times 10^{-3}) \times f_{\text{nov}} + (9.06690) \times M_{\text{WD}} + (-6.71080))) \tag{B250}$$

$$^{26}\text{Mg} = 10^{-5} \times \max(0.0, ((-9.79150) \times M_{\text{WD}} + (1.2496 \times 10^{+1}))) \tag{B251}$$

$$^{27}\text{Al} = 10^{-5} \times \max(0.0, ((-1.3868 \times 10^{-1}) \times f_{\text{nov}} + (2.4911 \times 10^{+1}) \times M_{\text{WD}} + (-1.1496 \times 10^{+1})))$$
$$\tag{B252}$$

$$^{28}\text{Si} = 10^{-5} \times \max(0.0, ((-1.34920) \times f_{\text{nov}} + (8.1937 \times 10^{+1}) \times M_{\text{WD}} + (2.4719 \times 10^{+1})))$$
$$(\text{B253})$$

$$^{29}\text{Si} = 10^{-5} \times \max(0.0, ((2.6524 \times 10^{-2}) \times M_{\text{WD}} + (-4.9313 \times 10^{-2})) \times (f_{\text{nov}} + (-1.1586 \times 10^{+2})))$$
$$(\text{B254})$$

$$^{30}\text{Si} = 10^{-5} \times \max(0.0, ((-5.7586 \times 10^{-2}) \times M_{\text{WD}} + (1.7187 \times 10^{-2})) \times (f_{\text{nov}} + (-8.7219 \times 10^{+1})))$$
$$(\text{B255})$$

$$^{31}\text{P} = 10^{-5} \times \max(0.0, ((-8.3059 \times 10^{-3}) \times f_{\text{nov}} + (8.2235 \times 10^{-1}))) \qquad (\text{B256})$$

$$^{32}\text{S} = 10^{-5} \times \max(0.0, ((-3.8675 \times 10^{-1}) \times f_{\text{nov}} + (-1.62480) \times M_{\text{WD}} + (4.0831 \times 10^{+1})))$$
$$(\text{B257})$$

$$^{33}\text{S} = 10^{-5} \times \max(0.0, ((-2.8742 \times 10^{-2}) \times M_{\text{WD}} + (1.8421 \times 10^{-2})) \times (f_{\text{nov}} + (-7.8546 \times 10^{+1})))$$
$$(\text{B258})$$

$$^{34}\text{S} = 10^{-5} \times \max(0.0, ((-1.8795 \times 10^{-2}) \times f_{\text{nov}} + (-9.8219 \times 10^{-3}) \times M_{\text{WD}} + (1.87800)))$$
$$(\text{B259})$$

$$^{35}\text{Cl} = 10^{-5} \times \max(0.0, ((-3.2658 \times 10^{-3}) \times f_{\text{nov}} + (8.5558 \times 10^{-2}) \times M_{\text{WD}} + (2.1291 \times 10^{-1})))$$
$$(\text{B260})$$

$$^{36}\text{S} = 10^{-5} \times \max(0.0, ((-9.0210^{-5}) \times f_{\text{nov}} + (-4.4866 \times 10^{-4}) \times M_{\text{WD}} + (9.6037 \times 10^{-3})))$$
$$(\text{B261})$$

$$^{36}\text{Ar} = 10^{-5} \times \max(0.0, ((-7.7522 \times 10^{-2}) \times f_{\text{nov}} + (-4.2416 \times 10^{-2}) \times M_{\text{WD}} + (7.79590)))$$
$$(\text{B262})$$

$$^{37}\text{Cl} = 10^{-5} \times \max(0.0, ((-1.0046 \times 10^{-3}) \times f_{\text{nov}} + (1.8348 \times 10^{-2}) \times M_{\text{WD}} + (7.6208 \times 10^{-2})))$$
$$(\text{B263})$$

$$^{38}\text{Ar} = 10^{-5} \times \max(0.0, ((-1.6591 \times 10^{-2}) \times f_{\text{nov}} + (1.6964 \times 10^{-2}) \times M_{\text{WD}} + (1.59170)))$$
$$(\text{B264})$$

$$^{39}\text{K} = 10^{-5} \times \max(0.0, ((-3.4934 \times 10^{-3}) \times f_{\text{nov}} + (2.969 \times 10^{-3}) \times M_{\text{WD}} + (3.4329 \times 10^{-1})))$$
$$(\text{B265})$$

while for ONeWDs

$$^1\text{H} = 10^{-5} \times \max(0.0, ((-7.0198 \times 10^{+2}) \times f_{\text{nov}} + (-2.1871 \times 10^{+4}) \times M_{\text{WD}} + (8.9608 \times 10^{+4})))$$
$$\text{(B266)}$$

$$^3\text{He} = 10^{-5} \times \max(0.0, ((2.8285 \times 10^{-4}) \times f_{\text{nov}} + (-8.8654 \times 10^{-3}))) \qquad \text{(B267)}$$

$$^4\text{He} = 10^{-5} \times \max(0.0, ((-2.9356 \times 10^{+2}) \times f_{\text{nov}} + (1.7871 \times 10^{+4}) \times M_{\text{WD}} + (1.4567 \times 10^{+4})))$$
$$\text{(B268)}$$

$$^7\text{Be} = 10^{-5} \times \max(0.0, ((1.1681 \times 10^{-2}) \times M_{\text{WD}} + (-1.1033 \times 10^{-2})) \times (f_{\text{nov}} + (-2.4826 \times 10^{+1})))$$
$$\text{(B269)}$$

$$^{11}\text{B} = 10^{-5} \times \max(0.0, ((3.4842 \times 10^{-5}) \times M_{\text{WD}} + (-4.0007 \times 10^{-5})) \times (f_{\text{nov}} + (-4.7973 \times 10^{+1})))$$
$$\text{(B270)}$$

$$^{12}\text{C} = 10^{-5} \times \max(0.0, ((2.8398 \times 10^{+3}) \times M_{\text{WD}} + (-1.2506 \times 10^{+3}))) \qquad \text{(B271)}$$

$$^{13}\text{C} = 10^{-5} \times \max(0.0, ((7.20260) \times f_{\text{nov}} + (1.9999 \times 10^{+3}))) \qquad \text{(B272)}$$

$$^{14}\text{N} = 10^{-5} \times \max(0.0, ((6.6635 \times 10^{-1}) \times M_{\text{WD}} + (-3.6999 \times 10^{-1})) \times (f_{\text{nov}} + (7.1937 \times 10^{+3})))$$
$$\text{(B273)}$$

$$^{15}\text{N} = 10^{-5} \times \max(0.0, ((5.1408 \times 10^{+2}) \times M_{\text{WD}} + (-5.4313 \times 10^{+2})) \times (f_{\text{nov}} + (1.4193 \times 10^{+1})))$$
$$\text{(B274)}$$

$$^{16}\text{O} = 10^{-5} \times \max(0.0, ((3.7238 \times 10^{+2}) \times f_{\text{nov}} + (-4.8613 \times 10^{+4}) \times M_{\text{WD}} + (4.8786 \times 10^{+4})))$$
$$\text{(B275)}$$

$$^{17}\text{O} = 10^{-5} \times \max(0.0, ((7.2463 \times 10^{+1}) \times f_{\text{nov}} + (-9.5368 \times 10^{+2}))) \qquad \text{(B276)}$$

$$^{18}\text{O} = 10^{-5} \times \max(0.0, ((-3.6582 \times 10^{+1}) \times M_{\text{WD}} + (5.1806 \times 10^{+1})) \times (f_{\text{nov}} + (4.61820)))$$
$$\text{(B277)}$$

$$^{19}\text{F} = 10^{-5} \times \max(0.0, ((3.1613 \times 10^{-2}) \times f_{\text{nov}} + (6.08890) \times M_{\text{WD}} + (-7.44170))) \quad \text{(B278)}$$

$$^{20}\text{Ne} = 10^{-5} \times \max(0.0, ((3.3536 \times 10^{+2}) \times f_{\text{nov}} + (-7.9159 \times 10^{+3}) \times M_{\text{WD}} + (9.8141 \times 10^{+3})))$$
$$\text{(B279)}$$

B Analytic Fits

$$^{21}\text{Ne} = 10^{-5} \times \max(0.0, ((2.5073 \times 10^{-1}) \times M_{\text{WD}} + (-2.2038 \times 10^{-1})) \times (f_{\text{nov}} + (-7.27060)))$$

$$\text{(B280)}$$

$$^{22}\text{Na} = 10^{-5} \times \max(0.0, ((3.16800) \times M_{\text{WD}} + (-3.36720)) \times (f_{\text{nov}} + (-4.18600))) \quad \text{(B281)}$$

$$^{22}\text{Ne} = 10^{-5} \times \max(0.0, ((-1.4955 \times 10^{+1}) \times M_{\text{WD}} + (2.0984 \times 10^{+1})) \times (f_{\text{nov}} + (-1.1821 \times 10^{+1})))$$

$$\text{(B282)}$$

$$^{23}\text{Na} = 10^{-5} \times \max(0.0, ((3.8757 \times 10^{+1}) \times M_{\text{WD}} + (-3.8618 \times 10^{+1})) \times (f_{\text{nov}} + (-1.6515 \times 10^{+1})))$$

$$\text{(B283)}$$

$$^{24}\text{Mg} = 10^{-5} \times \max(0.0, ((3.4114 \times 10^{-1}) \times M_{\text{WD}} + (2.61060)) \times (f_{\text{nov}} + (-3.6483 \times 10^{+1})))$$

$$\text{(B284)}$$

$$^{25}\text{Mg} = 10^{-5} \times \max(0.0, ((1.4668 \times 10^{+1}) \times f_{\text{nov}} + (-1.4336 \times 10^{+3}) \times M_{\text{WD}} + (1.4242 \times 10^{+3})))$$

$$\text{(B285)}$$

$$^{26}\text{Al} = 10^{-5} \times \max(0.0, ((4.00780) \times f_{\text{nov}} + (-5.1138 \times 10^{+2}) \times M_{\text{WD}} + (5.2138 \times 10^{+2})))$$

$$\text{(B286)}$$

$$^{26}\text{Mg} = 10^{-5} \times \max(0.0, ((2.02750) \times f_{\text{nov}} + (-8.682 \times 10^{+1}) \times M_{\text{WD}} + (5.597 \times 10^{+1}))) \quad \text{(B287)}$$

$$^{27}\text{Al} = 10^{-5} \times \max(0.0, ((1.7186 \times 10^{+1}) \times f_{\text{nov}} + (-2.8691 \times 10^{+3}) \times M_{\text{WD}} + (3.0188 \times 10^{+3})))$$

$$\text{(B288)}$$

$$^{28}\text{Si} = 10^{-5} \times \max(0.0, ((7.3982 \times 10^{+1}) \times f_{\text{nov}} + (8.9046 \times 10^{+2}))) \quad \text{(B289)}$$

$$^{29}\text{Si} = 10^{-5} \times \max(0.0, ((1.3145 \times 10^{+1}) \times M_{\text{WD}} + (-1.3624 \times 10^{+1})) \times (f_{\text{nov}} + (-1.1926 \times 10^{+1})))$$

$$\text{(B290)}$$

$$^{30}\text{Si} = 10^{-5} \times \max(0.0, ((1.0588 \times 10^{+2}) \times M_{\text{WD}} + (-1.1518 \times 10^{+2})) \times (f_{\text{nov}} + (-1.6289 \times 10^{+1})))$$

$$\text{(B291)}$$

$$^{31}\text{P} = 10^{-5} \times \max(0.0, ((1.2395 \times 10^{+1}) \times f_{\text{nov}} + (-3.5799 \times 10^{+2}))) \quad \text{(B292)}$$

$$^{32}\text{S} = 10^{-5} \times \max(0.0, ((6.761 \times 10^{+1}) \times M_{\text{WD}} + (-7.4808 \times 10^{+1})) \times (f_{\text{nov}} + (3.8548 \times 10^{+1})))$$

$$\text{(B293)}$$

$$^{33}\text{S} = 10^{-5} \times \max(0.0, ((3.38080) \times f_{\text{nov}} + (1.3794 \times 10^{+1}))) \quad \text{(B294)}$$

$$^{34}\text{S} = 10^{-5} \times \max(0.0, ((1.2892 \times 10^{+3}) \times M_{\text{WD}} + (-1.429 \times 10^{+3}))) \quad \text{(B295)}$$

$$^{35}\text{Cl} = 10^{-5} \times \max(0.0, ((-3.6338 \times 10^{-1}) \times f_{\text{nov}} + (1.3213 \times 10^{+2}))) \tag{B296}$$

$$^{36}\text{S} = 10^{-5} \times \max(0.0, ((-1.2405 \times 10^{-2}) \times M_{\text{WD}} + (1.7831 \times 10^{-2}))) \tag{B297}$$

$$^{36}\text{Ar} = 10^{-5} \times \max(0.0, ((1.5232 \times 10^{-1}) \times M_{\text{WD}} + (-1.68 \times 10^{-1})) \times (f_{\text{nov}} + (4.0688 \times 10^{+3})))$$
$$\tag{B298}$$

$$^{37}\text{Cl} = 10^{-5} \times \max(0.0, ((-4.965 \times 10^{-2}) \times f_{\text{nov}} + (6.82040))) \tag{B299}$$

$$^{38}\text{Ar} = 10^{-5} \times \max(0.0, ((-2.334 \times 10^{-2}) \times f_{\text{nov}} + (2.56750))) \tag{B300}$$

$$^{39}\text{K} = 10^{-5} \times \max(0.0, ((-5.8502 \times 10^{-3}) \times f_{\text{nov}} + (9.7249 \times 10^{-1}) \times M_{\text{WD}} + (-6.0058 \times 10^{-1}))) \,.$$
$$\tag{B301}$$

C HBB Calibration

Previous authors (e.g. Groenewegen & de Jong, 1993) have used constant values for f_{HBB}, f_{burn}, f_{DUP} and $f_{\mathrm{DUP,burn}}$, with a different prescription for the temperature (not requiring N_{rise}). Here these values are fitted to M_{1TP} and Z.

C1 Calibration method

A Monte-Carlo (MC) method is used to test the above free parameters with ranges $0.0 < f_{\mathrm{HBB}} < 1.0$, $0.0 < 10^6 f_{\mathrm{burn}} < 10.0$ and $0 < N_{\mathrm{Trise}} < 20$. The parameters f_{DUP} and $f_{\mathrm{DUP,burn}}$ are chosen to be zero and are only increased when necessary.

A weighted sum of squares is constructed from the Monash model nucleosynthesis data vs the corresponding synthetic nucleosynthesis data to enable comparison between MC model runs. A score $= (\sum_i w_i s_i)^{-1}$ is defined such that higher numbers mean a better fit where the weights are $w_i = (w_{\mathrm{C12}}, w_{\mathrm{C13}}, w_{\mathrm{N14}}, w_{\mathrm{O16}}, w_{\mathrm{C/O}}, w_{\mathrm{C12/C13}}) = (1, 10, 1, 1, 5, 5)$ and s_i is the sum of squares difference between the Monash model and synthetic model for the isotope (or ratio) i. The ratios $X_{\mathrm{C12}}/X_{\mathrm{C13}}$ and $X_{\mathrm{C}}/X_{\mathrm{O}}$ are weighted preferentially because these are important observed nucleosynthetic constraints on AGB stars. ^{13}C is also boosted because its abundance is small. 1D slices and 2D projections of the resulting parameter space are then examined and compared with the best fit obtained by this method. Human intervention comes last but proves invaluable when trying to fit the details.

C2 $M_{\mathrm{i}} \gtrsim 5\,\mathrm{M}_\odot$

The Monash models for $M_{\mathrm{i}} \gtrsim 5\,\mathrm{M}_\odot$ show strong hot-bottom burning at all metallicities. This is modelled with a high value for both f_{burn} and f_{HBB}. When CNO reaches equilibrium there is degeneracy between f_{burn} and f_{HBB} because it is possible to increase the amount of envelope burned at the expense of the burning time and obtain roughly the same amount of hot-bottom burning. This can be quantified in the following way: define the mass exposed to hot-bottom burning in an interpulse period as

$$M_{\mathrm{exp}} = \frac{1}{\tau_{\mathrm{ip}}} \int_0^{\tau_{\mathrm{ip}}} \Delta M_{\mathrm{burn}} dt \,, \tag{C1}$$

where ΔM_{burn} is the amount of matter burned in time dt. This can be approximated as

$$M_{\mathrm{exp}} \approx \frac{1}{\tau_{\mathrm{ip}}} \Delta M_{\mathrm{burn}} \Delta t \,, \tag{C2}$$

where Δt is the burning time. In the synthetic model f_{HBB} is used to parameterize the burning such that $\Delta M_{\mathrm{burn}} = M_{\mathrm{env}} f_{\mathrm{HBB}}$ and $\Delta t = \tau_{\mathrm{ip}} f_{\mathrm{burn}}$ giving

$$M_{\mathrm{exp}} = M_{\mathrm{env}} f_{\mathrm{HBB}} f_{\mathrm{burn}} \,, \tag{C3}$$

from which it can be seen that increasing f_{HBB} while decreasing f_{burn} will give the same M_{exp}.

An approximate value for M_{exp} can be calculated from the Monash models. Let $\Delta t = \tau_{\mathrm{c}}(\Delta M_{\mathrm{HBB}}/M_{\mathrm{env}})$, where τ_{c} is the convective turnover time, and $\Delta M_{\mathrm{burn}} = \Delta M_{\mathrm{HBB}}$ which correspond to the true values expected for Δt and ΔM_{burn}. ΔM_{HBB} is about $10^{-4}\,\mathrm{M}_\odot$ (see section 2.7), while τ_{c} can be found from the Monash models and is of the order of $1\,\mathrm{year}$ for $M_{\mathrm{i}} = 5\,\mathrm{M}_\odot$, $Z = 0.02$. Substituting into eq. (C2) gives
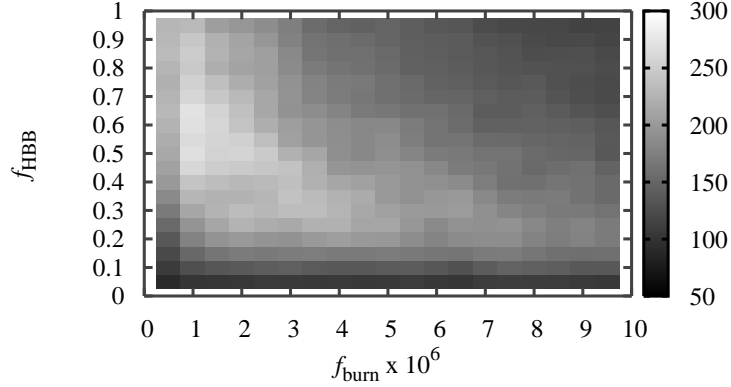
Figure C1: Monte Carlo score (light is best, dark is worst) for varying f_{HBB} and f_{burn} when $M_{\mathrm{i}} = 6\,\mathrm{M}_\odot$, $Z = 0.02$. The relation $f_{\mathrm{HBB}} \approx (10^6 f_{\mathrm{burn}})^{-1}$ can be seen to be approximately true.

$$M_{\mathrm{exp}}/\mathrm{M}_\odot \quad \approx \quad \frac{1}{\tau_{\mathrm{ip}}} \frac{\Delta M_{\mathrm{HBB}}}{M_{\mathrm{env}}} \tau_{\mathrm{c}} \Delta M_{\mathrm{HBB}} \tag{C4}$$

$$\approx \quad \frac{1}{10^4} \times \frac{10^{-4}}{5} \times 1 \times 10^{-4} \approx 10^{-5} \,. \tag{C5}$$

A comparison with eq. (C3) with $M_{\mathrm{env}} \approx 5\,\mathrm{M}_\odot$ gives

$$f_{\mathrm{HBB}} f_{\mathrm{burn}} \approx 10^{-6} \,. \tag{C6}$$

This is not accurate enough to use as a constraint, because the values for τ_{ip}, τ_{c}, ΔM_{HBB}, M_{env} etc. change from pulse to pulse and star to star, but does explain the results of the MC runs. The expected $f_{\mathrm{HBB}} \approx (10^6 f_{\mathrm{burn}})^{-1}$ behaviour can be seen in the plot of f_{HBB} vs f_{burn} in figure C1.

The values of f_{burn} and f_{HBB} are extracted from the one dimensional plots of MC score vs f_{burn} and f_{HBB}. An additional term is included in the score to match the shape of the abundance curve for $^{13}\mathrm{C}$. This is a useful constraint because this shape (figure C4) is very dependent on the burn time f_{burn}. If f_{burn} is too high the smooth bell-shape across the interpulse period is lost while, if it is too low, not enough $^{13}\mathrm{C}$ is converted to $^{14}\mathrm{N}$
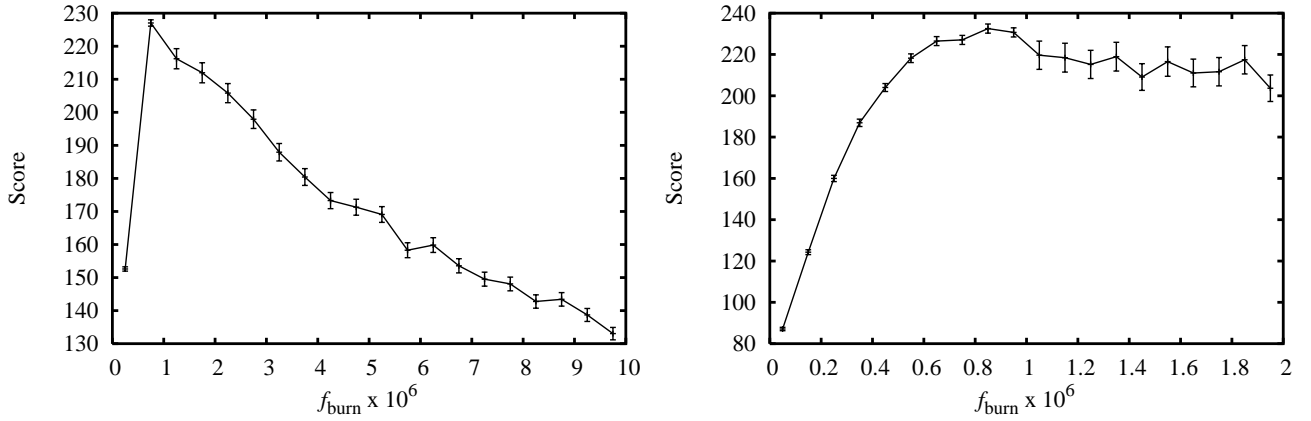
Figure C2: MC score vs the fraction of the interpulse period for which hot-bottom burning is active, f_{burn}, for 20 bins in the range $0 < 10^6 f_{\text{burn}} < 10$ (left panel) and 0 bins in the range $0 < 10^6 f_{\text{burn}} < 2$ (right panel) when $M_{\text{i}} = 6.0\,\text{M}_{\odot}$, $Z = 0.02$. Error bars are Poisson (statistical) errors.

during each interpulse period. Figure C2 shows the MC score distribution of f_{burn} for $M_{\text{i}} = 6\,\text{M}_{\odot}$, $Z = 0.02$. The peak is at $10^6 f_{\text{burn}} \approx 0.8$. For $M_{\text{i}} = 5\,\text{M}_{\odot}$, $Z = 0.02$, f_{HBB} and $10^6 f_{\text{burn}}$ drop to about 0.3 because there is less hot-bottom burning. This drop-off occurs somewhere between $M_{\text{i}} = 4\,\text{M}_{\odot}$ and $M_{\text{i}} = 5\,\text{M}_{\odot}$ for $Z = 0.008$ and at $M_{\text{i}} = 4\,\text{M}_{\odot}$ for $Z = 0.004$ reflecting the fact that the lower metallicity stars are more compact so the convective turnover time is smaller, more mixing occurs and the temperature and density are higher at the base of the convective envelope.

The temperature-rise factor N_{rise} is of order 1–2 for these strongly hot-bottom burning stars. The effect of this factor is seen mainly in ^{13}C with a spike in the surface abundance as shown in figure C4. An initial rise in ^{12}C is not visible at $M_{\text{i}} = 6\,\text{M}_{\odot}$ but is by $M_{\text{i}} = 5\,\text{M}_{\odot}$ indicative of HBB beginning only after a few pulses. No dredged-up material is immediately burned ($f_{\text{DUP}} = 0$, $f_{\text{DUP,burn}} = 0$).
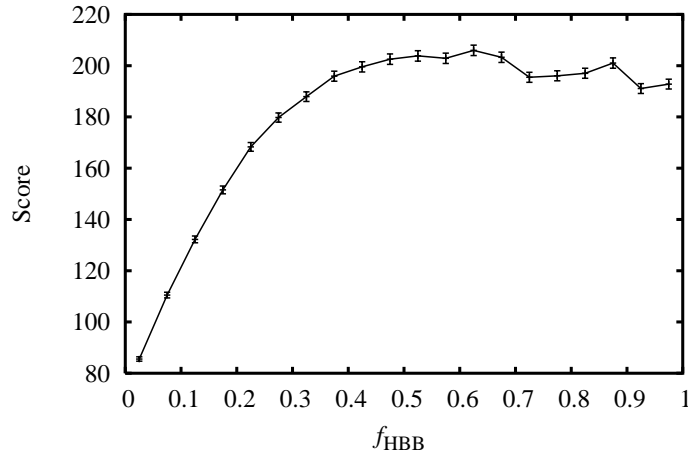
Figure C3: MC score vs the fraction of the envelope which undergoes hot-bottom burning, f_{HBB}, for $M_{\mathrm{i}} = 6.0\,\mathrm{M}_\odot$, $Z = 0.02$. While this shows that $f_{\mathrm{HBB}} \gtrsim 0.4$, the true value is not well constrained. Error bars are Poisson (statistical) errors.
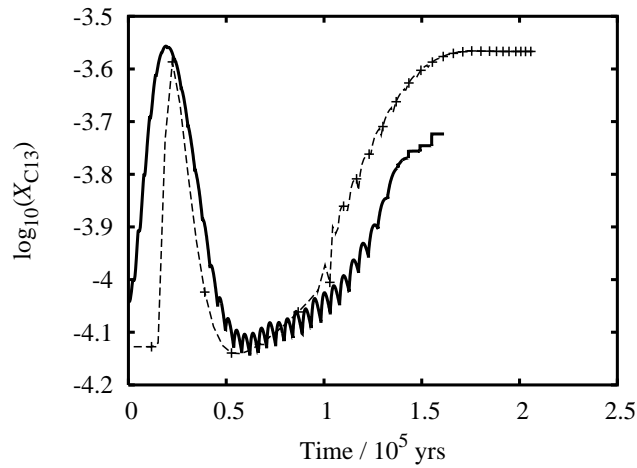

Figure C4: Variation of the surface ^{13}C abundance with time from the first pulse for the TPAGB phase of a $M_{\mathrm{i}} = 6\,\mathrm{M}_\odot$, $Z = 0.02$ star. The position of the ^{13}C spike at about $20,000$ years is controlled mainly by the N_{rise} parameter. The full stellar evolution model is shown by the solid line, the synthetic model by the dashed line.
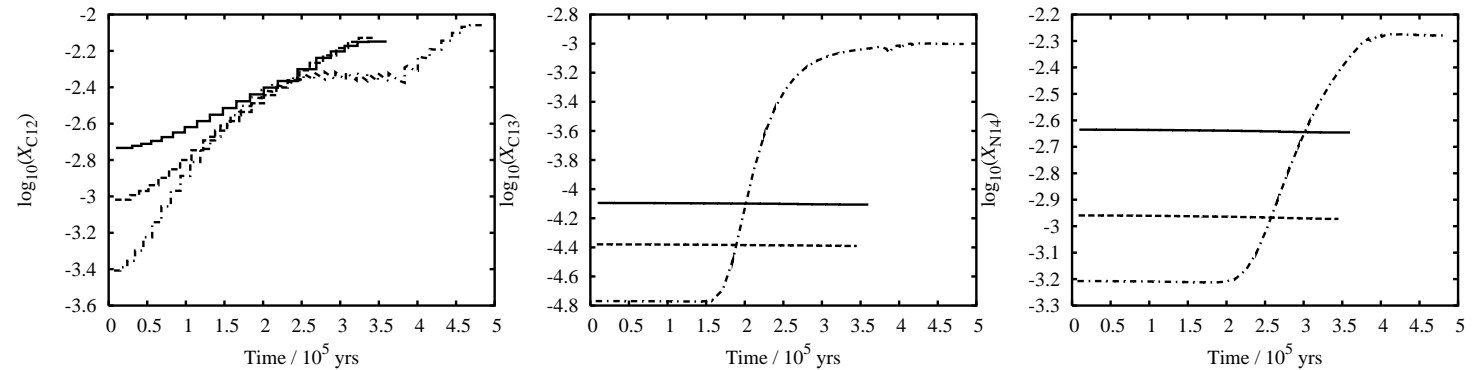
Figure C5: Synthetic model output showing the surface ^{12}C, ^{13}C and ^{14}N abundance for $M_{\mathrm{i}} = 4\,\mathrm{M}_\odot$, $Z = 0.004$ (dot-dashes), 0.012 (dashes) and 0.02 (solid line). For $Z = 0.004$ there is HBB after a delay of about 15 pulses but for higher metallicity there is no HBB at all.

C3 $M_{\mathbf{i}} \approx 4\,\mathrm{M}_\odot$

Stars around $M_{\mathrm{i}} = 4\,\mathrm{M}_\odot$ are in a transition zone where hot-bottom burning is not very effective but does occur at low metallicity. There is no immediate drop in ^{12}C and associated peak in ^{13}C at the onset of pulses, rather if HBB occurs at all it occurs after many pulses (see figure C5). Large amounts of CNO-processed products can still be produced.

For $M_{\mathrm{i}} = 4\,\mathrm{M}_\odot$ $f_{\mathrm{HBB}} \approx 0.1$ and $10^6 f_{\mathrm{burn}} \approx 0.1$ but the MC technique cannot isolate regions of parameter space for stars in which little or no HBB occurs ($Z > 0.008$). A large value of $N_{\mathrm{rise}} \geq 3 - 6$ simulates the late start of HBB. No dredged-up material is immediately burned ($f_{\mathrm{DUP}} = 0.0$, $f_{\mathrm{DUP,burn}} = 0.0$).

C4 $M_{\mathbf{i}} \lesssim 3.5\,\mathrm{M}_\odot$

No HBB occurs in stars with $M_{\mathrm{i}} \leq 3.5\,\mathrm{M}_\odot$ with the exception of $Z = 0.0001$. Thus for $M_{\mathrm{i}} \leq 3.5\,\mathrm{M}_\odot$, $f_{\mathrm{burn}} = f_{\mathrm{HBB}} = 0$ and $N_{\mathrm{rise}} = 0$. In the low-mass and low-Z stars there is production of ^{13}C and ^{14}N *at each pulse.* This indicates CNO burning during dredge-up or incomplete mixing during the He-shell flash. To simulate this, for $Z < 0.004$,

$f_{\mathrm{DUP,burn}} = 3 \times 10^{-6}$ and

$$f_{\mathrm{DUP}} = 10^{-3} \max(1 - 250Z, 0)(1 + \frac{3.7}{1 + 0.1^{27-21M_\mathrm{i}}}) \tag{C7}$$

to give a value about 3.5 times larger for $M_\mathrm{i} > 1.5\,\mathrm{M}_\odot$ than for $M_\mathrm{i} < 1.5\,\mathrm{M}_\odot$.

$Z \downarrow M_{1TP}/M_\odot \rightarrow$	3.5	4.0	5.0	6.0	6.5
0.02	-	-	0.1-0.5	0.5-0.6	0.4-1.0
			0.3	0.55	0.7
0.008	0	<0.2	0.6-1.0	0.8-1.0	
	0	0.1	0.8	0.9	
0.004	0	0.15-0.5	0.5-1.0	0.8-10	
	0	0.3	0.75	0.9	

Table C1: Burning time $10^6 f_{burn}$ as a fraction of the interpulse period for different masses and metallicities. The top numbers (black) are the ranges narrowed down by the MC runs. The numbers below (red) are used to fit a relation to M_{1TP} and Z. $f_{burn} = 0$ for $M_{1TP} < 3.5\,M_\odot$.

$Z \downarrow M_{1TP}/M_\odot \rightarrow$	3.5	4.0	5.0	6.0	6.5
0.02	-	-	0.1-0.4	0.65	0.3-1.0
			0.25	0.65	0.7
0.008	0	0.1-0.2	0.4-1.0	0.7-1.0	
	0	0.15	0.7	0.85	
0.004	<0.1	0.1-0.5	0.8-1.0	0.75-1.0	
	0.1	0.3	0.9	0.85	

Table C2: Envelope mass fraction exposed to HBB, f_{HBB} for different masses and metallicities. The top numbers (black) are the ranges narrowed down by the MC runs. The numbers below (red) are used to fit a relation to M_{1TP} and Z. $f_{HBB} = 0$ for $M_{1TP} < 3.5\,M_\odot$.

C5 Free Parameter Heaven or Hell

The results of the Monte-Carlo runs for each star are shown in tables C1, C2 and C3. Ranges are given when the MC technique cannot distinguish a unique solution. In such cases a value is chosen that aids the fit of the free parameter to M_{1TP} and Z or such that $10^6 f_{burn} \approx f_{HBB}$. The chosen value is shown under the range. If the value is "-" then there is no HBB so $f_{DUP} = f_{burn} = 0.0$. Where no value is given there is no Monash model with which to compare. It is not possible to use the best MC values for every star because there is too much non-systematic scatter.

The values for f_{HBB} and f_{burn} are zero for $M_{1TP} < 3.5\,M_\odot$ with a step up to about 0.9 at $M_{1TP} \approx 4.5\,M_\odot$ and a slight metallicity dependence. These can be reasonably well fitted

$Z \downarrow M_{\mathrm{1TP}}/\mathrm{M}_\odot \rightarrow$	3.5	4.0	5.0	6.0	6.5
0.02	-	-	~ 3	<1	1-2
			3	0.5	1.5
0.008	≥ 6	~ 6	~ 2.5	~ 2	
	6	6	2.5	2	
0.004	~ 6	~ 3	< 2	< 1	
	6	3	2	1	

Table C3: Temperature rise factor N_{rise} for different masses and metallicities. The top numbers (black) are the ranges narrowed down by the MC runs. The numbers below (red) are used to fit a relation to M_{1TP} and Z. N_{rise} is undefined for $M_{\mathrm{1TP}} < 3.5\,\mathrm{M}_\odot$ (because $f_{\mathrm{burn}} = f_{\mathrm{HBB}} = 0$).

to a function f_{C8} similar to a Fermi function

$$f_{C8} = \frac{(a_{C8}Z + b_{C8})}{1 + (c_{C8}Z + d_{C8})^{(e_{C8}Z + g_{C8} - M_{\mathrm{1TP}}/\mathrm{M}_\odot)}} . \tag{C8}$$

Coefficients are given in table C4. The f_{C8} parameter for f_{HBB} or $10^6 f_{\mathrm{burn}}$ is then given by $\max(f_{C8}, 0.0)$. N_{rise} is fitted to a quadratic in M_{1TP} and $z = \min(Z, 0.02)$

$$\begin{aligned} N_{\mathrm{rise}} = \max \quad & (a_{C9}(M_{\mathrm{1TP}}/\mathrm{M}_\odot)^2 + b_{C9}(M_{\mathrm{1TP}}/\mathrm{M}_\odot) + \\ & c_{C9}z + d_{C9}z^2 + e_{C9},\, 0) . \end{aligned} \tag{C9}$$

Coefficients are given in table C5. The maximum value for Z is necessary to maintain the behaviour of the function at higher metallicity. Equation (C9) reaches a minimum value at around $M_{\mathrm{1TP}} = 6\,\mathrm{M}_\odot$ and is assumed to be valid for masses higher than this. For $Z < 0.004$ some immediate burning of dredge-up material is included.

	Eq. (C8) for f_{burn}	Eq. (C8) for f_{HBB}
a	4.4174	-0.10852
b	0.83381	0.93068
c	-6967.1	-1072.4
d	143.62	40.997
e	96.155	65.438
f	3.7466	3.9181

Table C4: Coefficients for f_{burn} and f_{HBB} Fermi functions.

	Eq. (C9)
a_{C9}	0.51
b_{C9}	-6.6
c_{C9}	169
d_{C9}	5800
e_{C9}	21

Table C5: Coefficients for N_{rise} fitting function.

C6 Sensitivity to f_HBB, f_burn and N_rise

With the model described above and an appropriate choice of f_HBB, f_burn and N_rise it is possible to match the Monash models to the synthetic models quite accurately. Problems occur with the fitted values of f_HBB, f_burn and N_rise because minor deviations in the fit of the free parameters produce very different output. The sensitivity does not help us pin down unique values for f_burn and f_HBB owing to their inherent degeneracy. For example if N_rise is too small then ^{13}C rises and falls too early in the $M_\text{i} = 6\,\text{M}_\odot$ stars. If f_burn is even slightly too small the ON cycle does not get switched on[1]. If f_burn is slightly too large then more ^{14}N is produced at the expense of ^{12}C and ^{13}C. A slight rise in f_HBB causes a large rise in HBB products, especially ^{14}N. The sensitivity to f_HBB and f_burn is compounded when both are erroneous in the same direction.

A change to f_HBB affects the ^{12}C surface abundance evolution for $M_\text{i} = 5\,\text{M}_\odot$, $Z = 0.02$ (see figure C6). An increased f_HBB better fits the drop in ^{12}C which occurs when HBB sets in but by the end of the evolution the surface abundances are not very different. At most X_C12 is wrong by a factor of 1.4 at any point over the entire evolution, while overall it changes by a factor of 5. Final ^{13}C and ^{14}N have a similar scatter in $\log_{10} X$ of about 0.15. These effects are hardly visible in the case of the $M_\text{i} = 6\,\text{M}_\odot$, $Z = 0.02$ star and, because no burning occurs at all at $M_\text{i}/\text{M}_\odot = 4$.

Alteration of the burning time, f_burn, has essentially the same effect as a similar change in f_HBB. The exception is oxygen which is burned in the ON cycle when f_burn is long enough. The amount of ^{16}O burned for $M_\text{i} = 6\,\text{M}_\odot$, $Z = 0.02$ is small in the Monash models ($\Delta \log_{10} X_\text{O16} = -0.04$). This is about twice the size of the spread with $\Delta f_\text{burn} = \pm 0.13$ so is not significant. Significant oxygen burning occurs for $M_\text{i} = 6\,\text{M}_\odot$, $Z = 0.004$ but the standard synthetic model deals quite well with this (see figure C7). The carbon and nitrogen abundances are weakly affected at $M_\text{i} = 6\,\text{M}_\odot$ but at the transition mass

---

[1] This is not a huge problem (except for $M_\text{i} > 6\,\text{M}_\odot$) because most stars do not change their surface oxygen abundance significantly over their lifetime. For $M_\text{i} > 6\,\text{M}_\odot$ and low Z this could be a source of worry.

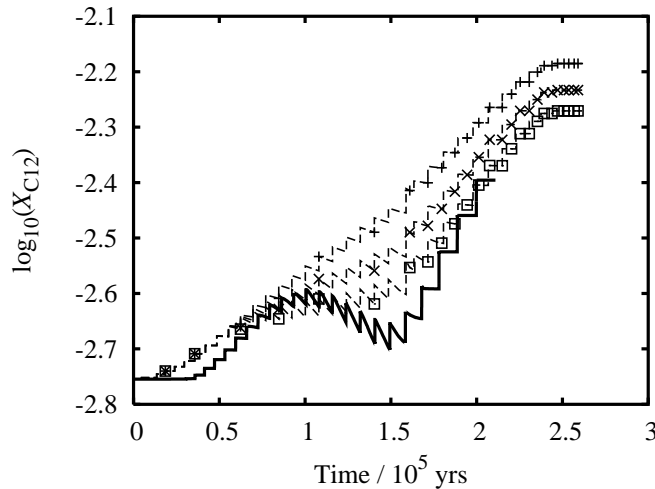Figure C6: ^{12}C abundance vs time for $M_i = 5\,M_\odot$, $Z = 0.02$ with varying $f_{HBB} = f_{HBB}^{fit} + \Delta f$, with $-0.13 < \Delta f < 0.13$. The fitted value of f_{HBB} is slightly wrong, but this only gives a maximum error of 0.15. The solid line is the Monash model, the other three lines are $\Delta f = -0.13$, 0 and $+0.13$ with symbols $+$, $\times$ and $\square$ respectively.

($M_i = 5\,M_\odot$ for $Z = 0.02$, $M_i = 4\,M_\odot$ for $Z = 0.004$) the surface abundance is sensitive to f_{burn}.

In summary, stars in the zone of transition between non-HBB and HBB ($M_i = 4\,M_\odot$ for $Z = 0.004$, $M_i = 5\,M_\odot$ for $Z = 0.02$) are the most troublesome when it comes to errors in the fit to f_{HBB} and f_{burn}. However this transition is quite sharp, so not too many stars in a population would have the wrong surface abundances.

C6.1 Temperature sensitivity

If the fit to the temperature of the HBB layer is allowed to vary even by a tiny amount, while the other free parameters are kept constant, CNO element production varies significantly. To show this $\log_{10} T_{max}$ is allowed to vary from the fitted value by a factor $0.98 < f_T < 1.02$, just 2 per cent variations (5% in T_{max}), and the abundance vs time profiles are compared for the case $M_i = 6\,M_\odot$, $Z = 0.02$ which would ordinarily undergo large amounts of HBB (see figure C8). It should not be expected that $f_T = 1.00$ is the best fit because in reality
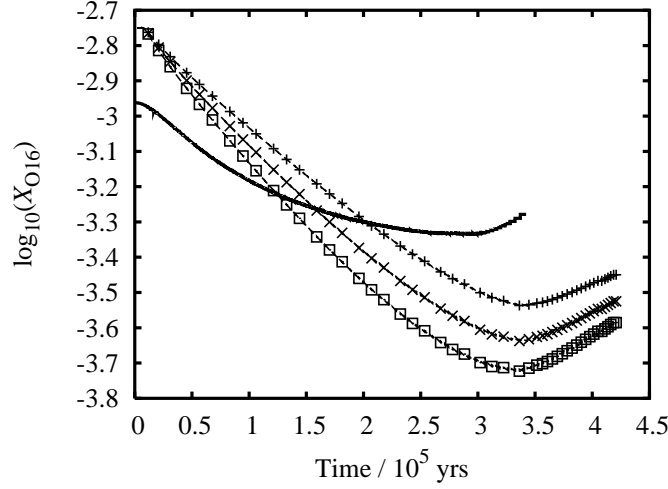
Figure C7: ^{16}O abundance vs time for the $M_i = 6\,M_\odot$, $Z = 0.004$ models, f_{burn} set to $f_{burn}^{fit} + \Delta f$, where $-0.13 < \Delta f < 0.13$. The standard synthetic model ($\Delta f = 0$) does a reasonable job of reproducing the Monash model. The solid line is the Monash model, the others from top to bottom are $\Delta f = -0.13, 0$ and $+0.13$ with symbols $+$, $\times$ and $\square$ respectively.

the HBB layer has a temperature profile while in the synthetic model it does not. Note that the $\log_{10} T_{max}$ limit of 7.95 is disabled for these tests leading to numerical problems at $f_T = 1.02$.

- The final ^{12}C is not greatly affected by temperature changes but $f_T = 0.98$ effectively switches off HBB. Paradoxically $f_T = 1.02$ burns less ^{12}C than $f_T = 1.01$ during most of the evolution. This is because $f_T = 1.02$ puts the temperature above the $\log_{10}(T/K) = 7.95$ limit of applicability of the burning code. The best fit is for $f_T = 1.0$.

- ^{13}C is affected in a more subtle way. At low temperature more ^{13}C is produced by incomplete CNO cycling. At the higher temperatures this ^{13}C is converted to ^{14}N. The final abundances for $f_T > 1.0$ are all similar because CN equilibrium is achieved, while for $f_T < 1.00$ there has not been enough conversion of ^{13}C to ^{14}N. Again $f_T = 1.00$ is the best fit.
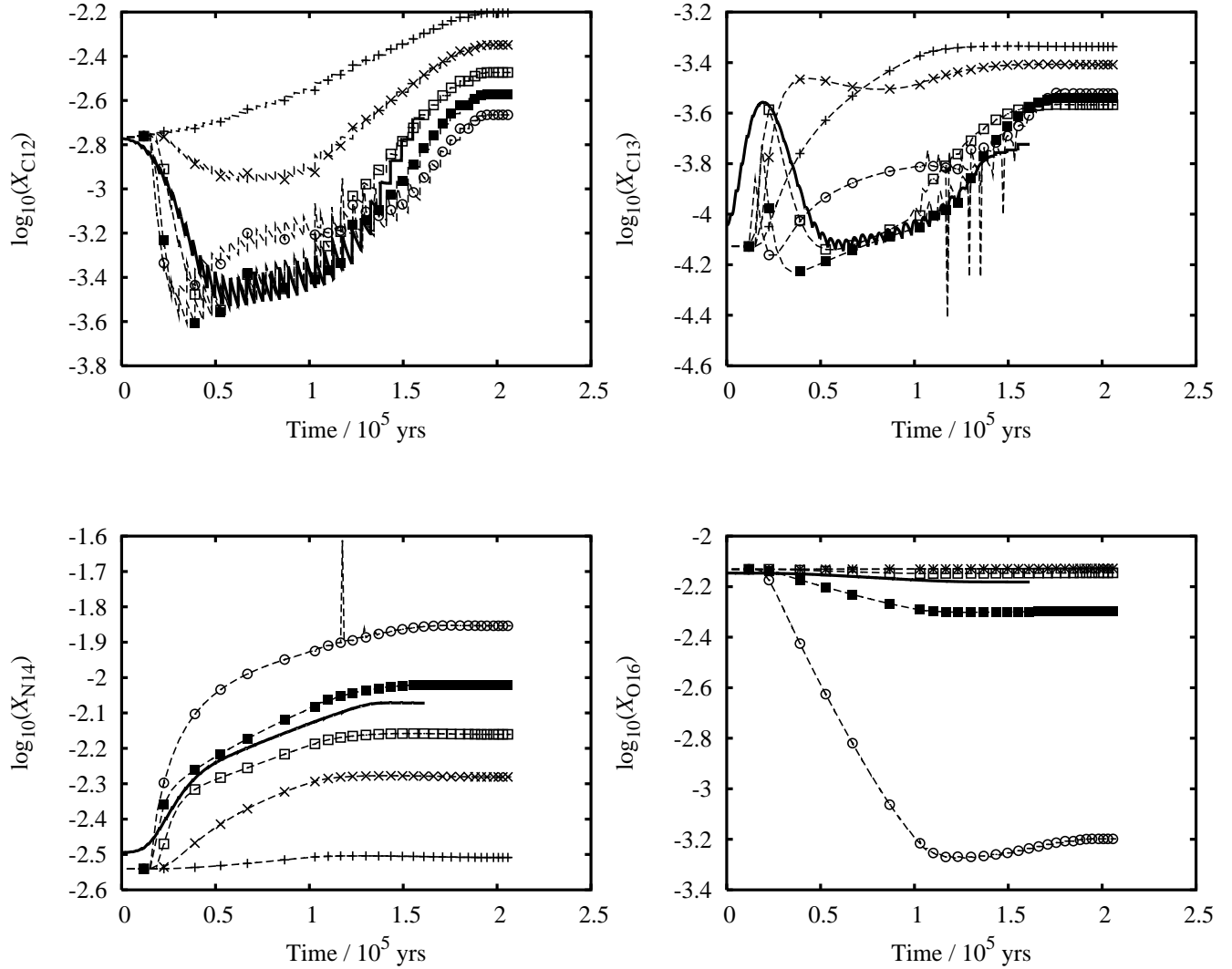
Figure C8: ^{12}C, ^{13}C, ^{14}N and ^{16}O surface abundances vs time for $M_{\rm i} = 6\,M_{\odot}$, $Z = 0.02$ with varying temperature factor $0.98 < f_{\rm T} < 1.02$. The solid line is the corresponding Monash model. The dashed lines represent $f_{\rm T} = 0.98$ to 1.02 in 0.01 increments, from top to bottom ($+$, $\times$, $\square$, $\blacksquare$ and $\circ$ respectively). See text for details.

- The log of the final surface abundance of nitrogen varies from -2.55 at $f_{\mathrm{T}} = 0.98$ (the same as the abundance at the start of the TPAGB) to -1.85 at $f_{\mathrm{T}} = 1.02$. The best fit is $f_{\mathrm{T}} = 1.01$ although $f_{\mathrm{T}} = 1.00$ is not too bad. For $f_{\mathrm{T}} \geq 1.01$ nitrogen abundances are high owing to excessive ON cycling.

- Of the CNO elements, surface oxygen abundance varies the most with temperature. For $f_{\mathrm{T}} \leq 1.00$ there is little change in oxygen abundance, just as in the Monash models. An increase in the value of f_{T} to just 1.02 causes the surface oxygen abundance to drop by a factor of 10. This is not seen in the Monash models so a value of $f_{\mathrm{T}} = 1.00$ is certainly justified while $f_{\mathrm{T}} = 1.01$ also gives too large a drop.

D Mass-Loss Prescriptions

The following mass-loss prescriptions are included here for completeness. No justification to the terms is given, for such details see Hurley et al. (2002), Dray et al. (2003) and/or references included below.

D1 H02

GB and post-GB stars The formula of Kudritzki & Reimers (1978) is used

$$\dot{M}_{\mathrm{R}} = \eta\, 4 \times 10^{-13} \frac{(L/\mathrm{L}_\odot)(R/\mathrm{R}_\odot)}{(M/\mathrm{M}_\odot)}\, \mathrm{M}_\odot\, \mathrm{yr}^{-1} \tag{D1}$$

with $\eta = 0.5$.

AGB stars The Vassiliadis & Wood (1993) rate

$$\log \dot{M}_{\mathrm{VW}} = -11.4 + 0.0125\left[P_0 - 100\max\left(M/\mathrm{M}_\odot - 2.5, 0.0\right)\right] \tag{D2}$$

is applied where P_0 is the Mira period pulsation given by

$$\log(P_0/\mathrm{d}) = \min\left[3.3,\, -2.07 - 0.9\log(M/\mathrm{M}_\odot) + 1.94\log(R/R_\odot)\right]. \tag{D3}$$

A cap (the $\min\left[3.3, ...\right]$ term) is applied at $\dot{M}_{\mathrm{VW}} = 1.36 \times 10^{-9}(L/\mathrm{L}_\odot)\,\mathrm{M}_\odot\,\mathrm{yr}^{-1}$ to model the superwind phase.

D Mass-Loss Prescriptions

Massive Stars The rates of Nieuwenhuijzen & de Jager (1990) are applied over the entire HR diagram by

$$\dot{M}_{\mathrm{NJ}} = \left(\frac{Z}{Z_\odot}\right)^{0.5} 9.6 \times 10^{-15} (R/\mathrm{R}_\odot)^{0.81} (L/L_\odot)^{1.24} (M/\mathrm{M}_\odot)^{0.16}\,\mathrm{M}_\odot\,\mathrm{yr}^{-1}\,, \qquad \text{(D4)}$$

for $L > 4000\,\mathrm{L}_\odot$, modified by the factor $Z^{0.5}$.

Small envelopes For $\mu < 1.0$ (see eq. B46 for the definition of μ) a Wolf-Rayet-like mass loss is included in the form

$$\dot{M}_{\mathrm{WR}} = 10^{-13} L^{1.5} (1.0 - \mu)\,\mathrm{M}_\odot\,\mathrm{yr}^{-1}\,. \qquad \text{(D5)}$$

The total mass-loss rate is the dominant rate from the above choices

$$\dot{M} = \max(\dot{M}_{\mathrm{R}}, \dot{M}_{\mathrm{VW}}, \dot{M}_{\mathrm{NJ}}, \dot{M}_{\mathrm{WR}})\,. \qquad \text{(D6)}$$

A Luminous-Blue-Variable-like mass loss is added for stars beyond the Humphreys-Davidson limit (Humphreys & Davidson, 1994),

$$\dot{M}_{\mathrm{LBV}} = 0.1(10^{-5}(R/\mathrm{R}_\odot)(L/\mathrm{L}_\odot)^{0.5} - 1.0)^3 \times \left(\frac{L}{6 \times 10} - 1.0\right)\,\mathrm{M}_\odot\,\mathrm{yr}^{-1} \qquad \text{(D7)}$$

which is added to $\dot{M}$ if $L > 6 \times 10^5\,\mathrm{L}_\odot$ and $10^{-5}(R/\mathrm{R}_\odot)(L/\mathrm{L}_\odot)^{0.5} > 1.0$.

For naked helium stars the WR mass-loss rate is used with $\mu = 0$ to give

$$\dot{M} = \max\left(\dot{M}_{\mathrm{R}}, \dot{M}_{\mathrm{WR}}(\mu = 0)\right)\,. \qquad \text{(D8)}$$

D2 MM

The MM rates are similar to the enhanced mass-loss rates of Maeder & Meynet (1994).

Pre-WR evolution The empirical mass-loss rate of de Jager, Nieuwenhuijzen & van der Hucht (1988) is used, but note the extra factor of 2,

$$-\log(-\dot{M}/\mathrm{M}_\odot\,\mathrm{yr}^{-1}) = \sum_{n=0}^{N}\sum_{1=0,\,j=n-1}^{i=n} a_{ij}T_i\left(\frac{\log(T_{\mathrm{eff}}/\mathrm{K})-4.05}{0.75}\right)T_j\left(\frac{\log(L/\mathrm{L}_\odot)-4.6}{2.1}\right),$$
(D9)

where

$$T_j(x) = 2\cos(j\arccos x)$$
(D10)

and a_{ij} are tabulated in de Jager et al. (1988).

WNL phase A constant rate of $8\times 10\,\mathrm{M}_\odot\,\mathrm{yr}^{-1}$ is used (Conti et al., 1988).

WNE, WC and WO phases The theoretical mass-loss rate of Langer (1989),

$$\dot{M}_{\mathrm{WR}} = (0.6-1.0)\times 10^{-7}\left(\frac{M_{\mathrm{WR}}}{\mathrm{M}_\odot}\right)^{2.5}\mathrm{M}_\odot\,\mathrm{yr}^{-1},$$
(D11)

is used.

D3 NL

Pre-WR evolution As with the MM mass-loss rate above the de Jager et al. (1988) rates are used, although without the factor of 2 in eq. (D10).

WNL and WNE phases The mass-loss rate of Nugis & Lamers (2000) is used:

$$\log(\dot{M}_{\mathrm{WN}}/\mathrm{M}_\odot\,\mathrm{yr}^{-1}) = -13.6 + 1.63\log(\mathrm{L}/L_\odot) + 2.22\log Y$$
(D12)

where Y is the surface helium abundance (by mass fraction).

WC phase The Nugis & Lamers (2000) mass-loss rate

$$\log(\dot{M}_{\mathrm{WC}}/\mathrm{M}_\odot\,\mathrm{yr}^{-1}) = -8.3 + 0.84\log(L/\mathrm{L}_\odot) + 2.04\log Y + 1.04\log Z$$
(D13)

is used.

WO phase A constant rate of 1.9×10^{-5} is used.

D4 KTG93 Initial Mass Function

According to Kroupa et al. (1993) the probability of finding a star with initial mass $m < M_{\mathrm{i}} \le m + dm$ is given by $\xi(M_{\mathrm{i}})dm$ where

$$
\xi(m) = \begin{cases}
0 & m \le m_0 \\
a_1 m^{-1.3} & m_0 < m \le 0.5 \\
a_2 m^{-2.2} & 0.5 < m \le 1.0 \\
a_2 m^{-2.7} & 1.0 < m < \infty
\end{cases} \, .
\tag{D14}
$$

With $m_0 = 0.1 \, \mathrm{M_\odot}$, and the normalization condition

$$
\int_0^\infty \xi(m)dm = 1 \, ,
\tag{D15}
$$

gives $a_1 = 0.29055$ and $a_2 = 0.1557$.

E Prescription for λ_{CE}

The latest version of `BSE`, released after the Hurley et al. (2002) paper, contains a prescription for the free parameter λ_{CE} calculated by Onno Pols. He used a method similar to that of Dewi & Tauris (2000) to calculate λ_{CE} by fitting to detailed Eggleton-code models. The following is taken directly from the code – it has not yet been published.

For helium stars a value of $\lambda_{\mathrm{CE}} = 0.5$ is assumed (no fit is yet available). For MS, HG or GB stars

$$m_1 = M \tag{E1}$$

while for CHeB or EAGB

$$m_1 = 100 \tag{E2}$$

then

$$\lambda_1 = \min\left(\frac{3}{2.4 + \frac{1}{m_1^{3/2}}} - 0.15 \log_{10} L, 0.80 \right) . \tag{E3}$$

TPAGB stars have

$$\lambda_1 = -3.5 - 0.75 \log_{10} M + \log_{10} L . \tag{E4}$$

For CHeB, EAGB or TPAGB stars then define

$$\lambda_2 = \min\left(-0.9, 0.58 + 0.75\log_{10}M\right) - 0.08\log_{10}L \tag{E5}$$

while for all other stellar types

$$\lambda_2 = 0\,.$$

Then

$$\lambda_1 = \begin{cases} 2\lambda_1 & \text{MS, GB}\,, \\ 2\min(\lambda_1,\lambda_2) & \text{CHeB, EAGB}\,, \\ 2\min\left[1.0, \max(\lambda_1,\lambda_2)\right] & \text{TPAGB}\,. \end{cases}$$

A fraction of the ionization energy f_{ion}, the `BSE` default is $f_{\text{ion}} = 0.5$, can then be introduced into the envelope. Define

$$a = \begin{cases} \min\left(1.2(\log_{10}M - 0.25)^2 - 0.7, -0.5\right) & \text{MS, GB,} \\ \max\left(-0.2 - \log_{10}M, 0.5\right) & \text{CHeB, EAGB, TPAGB,} \end{cases} \tag{E6}$$

$$b = \max(3 - 5\log_{10}M, 1.5)\,, \tag{E7}$$

$$c = \max(3.7 + 1.6\log_{10}M, 3.3 + 2.1\log_{10}M)\,, \tag{E8}$$

redefine λ_2 such that

$$\lambda_2 = a + \arctan\left[b(c - \log_{10}L)\right]\,, \tag{E9}$$

$$d = \max\left(0, \min\left[0.15, 0.15 - 0.25\log_{10}M\right]\right)\,, \tag{E10}$$

fudge λ_2 for pre-helium-burning stars

$$\lambda_2 = \begin{cases} \lambda_2 + d \times (\log_{10} L - 2) & \text{MS, HG, GB,} \\ \lambda_2 & \text{CHeB, EAGB, TPAGB} \end{cases} \tag{E11}$$

then

$$\lambda_2 = \max\left(1/\max(\lambda_2, 0.01), \lambda_1\right) . \tag{E12}$$

Now let

$$\lambda_1 = \lambda_1 + f_{\text{ion}}(\lambda_2 - \lambda_1) . \tag{E13}$$

If the envelope mass is $\leq 1\,\text{M}_\odot$ then override the above definitions to give

$$\lambda_2 = 0.84 \left(\frac{R_{\text{ZAMS}}}{R}\right)^{0.4} . \tag{E14}$$

Then calculate λ_{CE}

$$\lambda_{\text{CE}} = \begin{cases} \lambda_2 & M_{\text{env}} = 0\,\text{M}_\odot , \\ \lambda_2 + M_{\text{env}}^{0.5}(\lambda_1 - \lambda_2) & 0 \leq M_{\text{env}}/\text{M}_\odot \leq 1 , \\ \lambda_1 & M_{\text{env}} \geq 1\,\text{M}_\odot . \end{cases}$$

Typically $\lambda_{\text{CE}} \approx 1.0 - 2.0$ for GB or AGB stars, is $0.25 - 0.75$ for HG stars and is 0.5 for helium stars.

F How Fast is `binary_c/nucsyn`?

Table F1 gives the reader some idea of the runtime of `binary_c/nucsyn` on a 1.4 GHz AMD *Athlon* PC running *Linux* 2.4.20. One thousand stars were evolved at $Z = 0.02$ over the low- and intermediate-mass range and the entire mass range. The intermediate-mass stars are the slowest to evolve because they experience more thermal pulses.

For comparison, a $7 \, M_\odot$, $Z = 0.02$ model takes 36 minutes to evolve from pre-MS to TPAGB using 199 mesh points with the full Eggleton code (Stancliffe, private communication). To evolve properly on the TPAGB takes about an hour per pulse with 999 mesh points (Stancliffe, private communication). This is just the evolution code with the same nucleosynthesis as the Dray models, not the full nucleosynthesis of the K02 models which can take days or weeks to calculate (Karakas, private communication). These figures are for a 550 MHz *Sun-Blade-100,* scaled to an equivalent 1400 GHz CPU. Note that *Athlons* give better performance per GHz and per unit currency. The speed-up factor the synthetic code provides can be conservatively estimated as

$$\frac{2 \, \text{weeks}}{0.1 \, \text{s}} \approx 1.2 \times 10^7 \, .$$

Not bad!

Mass Range	Single Stars	Binary Stars
$0.1 \leq M_{1,2} \leq 8$	0.081	0.143
$0.1 \leq M_{1,2} \leq 100$	0.046	0.076

Table F1: `binary_c/nucsyn` runtimes (in seconds). See text for details.